TUDelft

Delft University of Technology

Mimicking the nuclear pore complex using nanopores

Ananth, Adithya

Important note
To cite this publication, please use the final published version (if applicable).
Please check the document version above.

MIMICKING THE NUCLEAR PORE COMPLEX USING NANOPORES

Adithya N. Ananth

Mimicking the nuclear pore complex using nanopores

Proefschrift

ter verkrijging van de graad van doctor
aan de Technische Universiteit Delft,
op gezag van de Rector Magnificus Prof.dr.ir. T.H.J.J. van der Hagen,
voorzitter van het College voor Promoties,
in het openbaar op dinsdag 10 april 2018 om 12:30 uur

door

Adithya Nagarakodige ANANTH

Master of Science in de Nanobiophysics
Technische Universität Dresden, Germany
geboren te Hosanagar, India.

This dissertation has been approved by the
promotor: Prof. dr. C. Dekker

Composition of the doctoral committee:
  Rector Magnificus   Chairman
  Prof. dr. C. Dekker   Technische Universiteit Delft, promotor

Independent members:
Prof. dr. A. Engel   Technische Universiteit Delft
Prof. dr. H. Bayley   University of Oxford, England
Prof. dr. C. Storm   Technische Universiteit Eindhoven
dr. L.M. Veenhoff   Rijksuniversiteit ,Groningen
Prof. dr.M. Dogterom   Technische   Universiteit   Delft,   *reserve*
member

Other members:
  Prof. dr. P. Onck   Rijksuniversiteit ,Groningen
  Prof. dr. H. Dietz   Technische Universität München, Germany

Cover Image: Front and back-artistic impression of NPC mimics, designed by A.N.Ananth & P. Ketterer (front page illustration)

An electronic version of this dissertation is available at http://repository.tudelft.nl/

Contents

1.
Introduction

In this chapter, I present the basic elements underlying this research which is aimed at mimicking the nuclear pore complex using solid-state nanopore and DNA origami.

The remarkable success of eukaryotic cells is attributed to its ability to store the genetic information in a membrane compartment called the nucleus (aka. the brain of the cell). Also, the contents of nucleus enables the regulation of gene expression and thereby the controlling the cellular functions [1-3]. A direct outcome of compartmentalization of cells demands for a selective, modular, and efficient transport system between the nucleus and cytoplasm. The transport channel of the nucleus are called the nuclear pore complex (NPC) [1-3] provides the path fort transport. The NPCs have shown to regulate cellular processes and plays a significant role in immune response. Thus, making its study relevant for understanding origin and cause of many disease such as cancers and ALS [2,4] .

The objective of this thesis is the construction of a minimalistic NPC using solid-state nanopores and DNA origami. The study is aimed in the direction of addressing some of the challenges of transport through the nuclear pore complex. Nanopores is a small pore in a membrane that serve as a biosensing technique, especially developed for DNA and protein detection. Nanopore enables a label-free single-molecule sensing. DNA origami is a relatively new fields of research, where the DNA is folded into desired nanostructures, and offers control over the geometry and chemical functionality at nanoscale. These two techniques are extensively put into use in this thesis.

1.1 The Nuclear Pore Complex

The Nuclear Pore Complex (NPC) is a macromolecular protein assembly embedded in the nuclear envelope of eukaryotic cell, which plays a central role in forming a selective barrier between the cytoplasm and nucleus. NPCs not only regulate nucleocytoplasmic transport, but also have a critical role in various cellular processes such as gene expression, DNA repair, cell cycle regulation and kinetochore organization. Nucleocytoplasmic transport comprises passive diffusion of small molecules and ions, as well as signal- and receptor-mediated translocation of proteins and ribonucleoprotein complexes that are larger than ~40 kDa.

The structure of the NPC is a repetition of structural components. The components form hierarchical modules (rings) with eight-fold symmetry of nups arranged radially around the central channel (see Figure 1.1). The precise composition of the NPC varies between different organisms, cells, and the phase of the cell cycle. The NPCs are organized into an hourglass-shaped central transport channel, that dynamically undergoes conformational changes during the molecule translocation[5,3,1] . A core scaffold consisting of an inner ring, central-

spoke ring, and outer ring are embedded in the nuclear envelope, which forms the structural core of the NPC. The core scaffold and outer rings anchors the NPC to the nuclear envelope and NPCs also provide stability to the lipid membrane [3,6]. Cytoplasmic filaments are attached to the cytoplasmic ring, while the nuclear ring is decorated with eight filaments that join into a distal ring to form the NPC's nuclear basket. The NPCs from different organisms share a global architecture but variations in sizes were reported. For example, human NPC has a height of ~ 85 nm and an outer diameter of ~ 120 nm [7,8], *Xenopus laevis* are ~ 95 nm high with an outer diameter of ~ 125 nm [9], **whereas the yeast NPC's is slightly smaller with** ~ 60 nm in height and an outer diameter of ~ 120 nm[9–11] . Species-specific variations in the arrangements and compositions of nups arise in the size difference (Frenkiel-Krispin et al., 2010). Despite these differences in the dimensions the diameter of the central channel of the NPC is about 40 nm[3,7,9,12] which is close to the size limit of 39 nm in diameter for cargo translocation[6,13,14] .
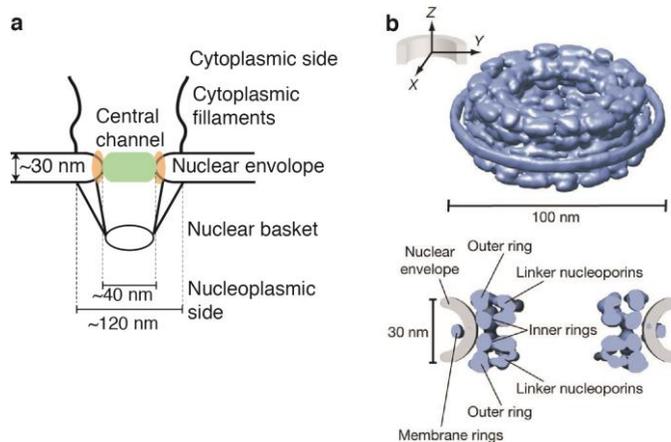
Figure 1.1- The structure of nuclear pore complex. a. Schematic overview of nuclear pore complex structure cross-section. b. The top and cross-section view of structured nucleoporin domains of the NPC, represented by a density volume contour (blue) of all the nucleoporins. [Image b. used with permission from ref 2.

Individual NPCs are constituted of approximately 34 different proteins called nucleoporins or nups. Nups are present in multiple copy numbers in forming a NPC with 456 nups in yeast cells. The nups are broadly conserved across different species. The secondary structure predictions of nups allowed their classification into three major groups [3,15]. The first group of nups is characterized by the **presence of transmembrane α-helices**, which facilitate the tethering of NPCs to the nuclear envelope and thereby stabilizes the interaction between the inner nuclear membrane and the outer nuclear membrane. The second class of nups **consists of nucleoporins comprising α-solenoid and β-propeller folds and**

functions mainly as architectural and scaffold nups. The scaffold nups connect the transmembrane nucleoporins to FG-nucleoporins, The third and the most important class of nucleoporins are called as FG-nups containing phenylalanine-glycine (FG)-repeats[1,16]. The core scaffold forms an anchoring point for FG-nups. The FG-nups are anchored between the outer and inner rings and forms two 16-membered rings[3,17]. FG-nups fill up the inner volume of the central channel and represents about one third of all the nucleoporins. The FG-nups consist of a minor structured region functioning as NPC anchor domain, while the remaining structure is natively unfolded and belongs to intrinsically disordered class of proteins[5,3,15]. FG-nup unstructured regions usually consists of 20-30 repetitive hydrophobic sequence motifs linked by hydrophilic spacer regions of variable length[1]. The subsequent FG-regions in FG-nups are separated by linker sequences consisting of charged and polar amino acids and are the source of "disorder" for FG-nups[18–20]. These sequence motifs are characterized by tandem repeated cluster of FG-repeats (Phenylalanine (Phe)-Glycine (Gly) residues) or FXFG-repeats where X can be a variable amino acid residue. The most abundantly found classes of FG-repeats are FxFG , GLFG (L- leucine), and FG. Other motifs include PSFG, PAFG and SAFG[15,16]. These unstructured regions form a disordered cloud around **the attachment sites, filling the central transport channel of the NPC and** extending into the cyto- and nucleoplasm[3].

1.1.1 Permeability barrier of NPC and functions of FG-Nucleoporins

The FG-nups are the key component of NPC to form the selective permeability barrier of the NPC and transport receptor-mediated translocation of molecules through the central channel. This selective barrier prohibits the passage of large particles, while small molecules ($< \sim 40$KDa or < 5nm) can freely diffuse through the central channel at high rates [21–23]. Numerous studies in the past decades have concluded that FG-nups are essential for establishing the selective permeable barrier across the NPC. Furthermore, FG-nups are essential for a proper **functioning of NPC and removal or deletion of specific FG**-nups or FG-motifs yield leaky nuclear pores. Leaky NPCs translocate unsuitable molecules in and out of nucleus resulting in malfunction and eventually cell mortality [5]. The presence of tightly packed FG-Nups networks in central channel restricts the effective diameter to <10 nm. This effective diameter indicates that the transport of larger molecules must be facilitated to translocate through the NPC. The nuclear transport factors assists in translocation of larger cargos through central channel.

1.1.2 Transport factors

The transport factors or cargo carriers (karyopherins (Kaps)) mediate nuclear transport by providing binding sites for both cargo molecules and the FG-nups. Nuclear transport factors include two classes of transport factors called as importins and exportins. In order to pass the NPC barrier, Kaps must posses a

nuclear localization signals (NLSs) for cargo entering the nucleus or a nuclear export signals (NESs) for cargo that is exported out of the nucleus. The directionality of nucleocytoplasmic transport is controlled by the concentration gradient of a small protein called as Ran-GTPase [1,24–26]. Ran-GTPase has GTP- and GDP-bound states. RanGTP is concentrated on the nuclear side and upon binding to importins receptors-cargo complex, releases the cargo from the importins [1,25]. GTP hydrolysis results in the unbinding of the RanGTP-importin complex in cytoplasm. The importin is recycled for the next transport cycle. RanGTP also binds to exportins and export cargoes molecules during nuclear export cycle. The most well-known transport pathways is import cycle involving importin and RanGTP. The import cycle is organized in three parallel phases, consisting of cargo-carrier import, recycling of the transport factors and regeneration of RanGTP. After translocation through the NPC, cytoplasmic GTP hydrolysis allows the dissociation of the exportin-cargo-Ran GTP complex and releasing the cargo[27]. It is critical to note that export of cargoes demands the input of energy (GTP), since GTP hydrolysis is necessary for export. In contrast, the import of cargo does not require input of GTP.

The transport receptors possess multiple hydrophobic patches on surface and can recognize FG-domains of central channel. The interaction between FG-domains and transport receptors of the NPC are key for nucleocytoplasmic transport. Studies show that interactions of the cargo-carrier with the FG-nups are essential for nuclear transport, where mutants with different affinity for the FG-repeats fail nucleocytoplasmic transport[5,6,24,28]. Cargo translocation through NPCs is a rapid process with hundreds of molecules passing through NPC each second and the mechanism of translocation is unclear and under debate[22,29–31]. The NPC translocate approximately 1000 molecules per second, with at least 10 parallel transport events at any given time with dwell times of 1 and 15 ms[6,21,32]. The nucleocytoplasmic exchange is a vital process and hence, any malfunctioning of NPC components or nucleocytoplasmic transport have a critical impact on cell functioning and survival. The nucleoporins are associated in a large number of disorders, especially, cancer and autoimmune disease[4,33] .

1.1.3 The transport process and transport models
The FG-nups and transport carrier's interactions are vital for transport across the NPC, but the mechanism of transport is lack general consensus [5,1]. The transport process resembles bidirectional-facilitated diffusion. Effective transport depends on the, cargo size, carrier concentration and RanGTP gradient across the nuclear envelope. There are various mechanisms to regulate nucleocytoplasmic transport, such as variation in the binding affinity of transport factors, alterations in FG-nups compositional and interaction strength between cargo and nuclear localization signal. To understand how transport receptops (Kaps) interacts with

the FG-repeats of the Nups we look more closely at the central channel of the NPC [1,32,34]. It is important to know how the spatial arrangement of the Nups inside this central channel. Various biophysical models have been proposed the organization of FG-Nups and its interaction with transport factors. None of the models completely account for all known properties of the NPC, and studies support elements from each model. In all models, the FG-repeat domains are central to inhibit the free diffusion of molecules depending on their surface properties and size. The cargo-carrier complex overcomes the selective barrier through interactions with FG-repeats, either by locally disrupting a physical barrier formed by the FG-repeat network (sieve models) or enthalpy of binding that compensates entropic barrier (crowding models)[1,6,35].

Virtual gate model
NPC lacks motor proteins that are normally needed for mechano-chemical transport [36]. Brownian motion was believed to be the driving force for translocation of cargoes, because no energy investment seems to be involved in the actual translocation step. It was predicted that the narrow channel in the centre of the NPC is important for gating and forms a barrier for passive diffusion of molecules. The model proposes an entropic barrier formed by the confined volume of the central transport channel (virtual gate) together with steric hindrance from the brush like FG-**nup's unstructured domains**[37]. Diffusion and thermal motion of macromolecules is therefore restricted in the central channel, and translocating particles must overcome a size-dependent entropic penalty. Above a certain size the probability of translocation by free diffusion becomes negligible due to increase in entropic barrier. However, transport factors have specific binding sites that interact with the FG-domain regions and increase the dwell time near the central channel. Thereby, the entropic barrier is lowered with the enthalpy of binding and favouring the transport [3, 37].

Polymer brush model
The polymer brush model or reversible collapse model is built on the premise that the unstructured FG-nups form a brush-like structure in the central channel. The FG-nup brush structure causes steric repulsion to any molecule that approaches it. [39,40]The FG-repeat regions form a collapsed hydrophobic layer coats the inner surface of the transport channel, while hydrophilic sequences fill the volume of the channel. Small particles can freely diffuse through the central channel; while diffusion of large macromolecules is restricted by FG-Nups filter. Transport factors enable translocation of cargo-carrier complexes through the barrier using interactions with the FG-repeat domains with their hydrophobic binding sites. These interactions reduce the translocation through the central channel to a two dimensional walk.
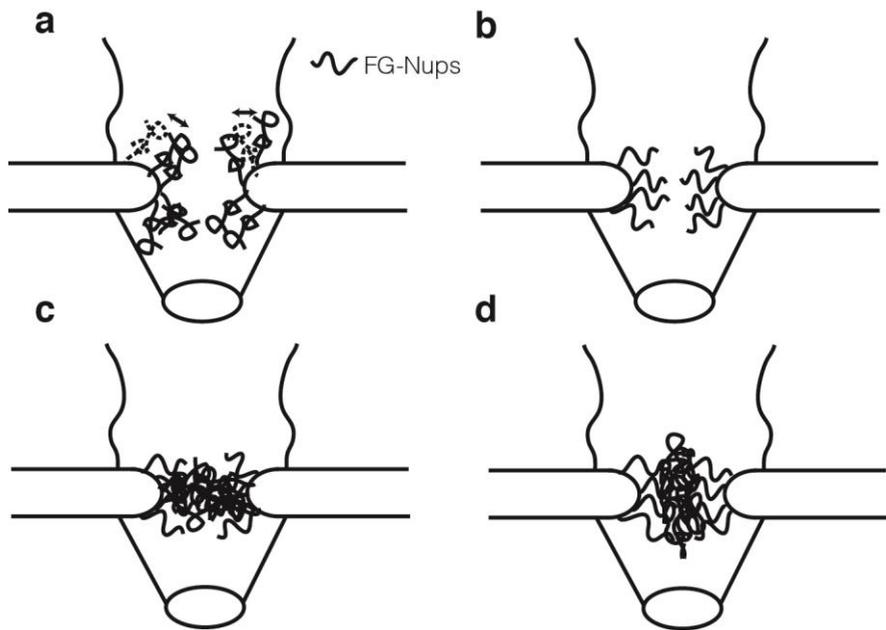
Figure 1.2 Schematic representation of proposed nuclear transport models with FG-Nups a) The virtual gate model b) Polymer brush model. c) The selective phase or hydrogel model d) The forest or central plug model.

Selective phase/hydrogel model
In the selective phase model, the FG-repeats form a meshwork or a sieve-like hydrogel that covers the inner channel of the NPC. Hydrophobic FG-repeats forms FG-FG interactions to form meshwork[41–43]. This meshwork acts as a selective filter to allow translocation of for molecules that are smaller than mesh size, thereby excluding the bigger from central channel. Transport receptors carrying cargos interact with FG-FG cross-linked regions, and transiently melt or disrupt the FG-FG crosslinks. The hydrophobic interaction creates a gap in the meshwork that allows the transport passage. S.Frey. et al. showed that purified FG-Nups forms **macroscopic hydrogels and selectivity of NPC's wer**e mimicked [42].

Forest model
A more recent forest model proposes a segregation of FG-nups into two discrete phases depending on the amino acid composition of Fg-Nups[44]. The model, propose two separate zones of traffic across the NPC (figure 1.2d). A gel-phase, with collapsed coil FG regions with low charge and rich hydrophobic region yielding a central plug structure. While, a region closer to the NPC channel wall occupied with hydrophilic and high charge content. Small molecules translocate through the periphery whereas the larger molecules interacts with central plug

to pass though the pore. The model takes into account the role of both charge and hydrophobicity of FG-Nups and subtly combines the critical aspects of other models [35,44].

1.2 DNA origami for programmable structures

The synthesis of well-defined complex and functional nanoscale objects has long been a challenge for chemists and material scientists. Famously, the genetic material in cells is stored in the form of deoxyribonucleic acid (DNA). DNA forms a double helical structure by hybridization of two complementary single stranded DNA. DNA strands are made up of four different bases adenine (A), guanine (G), cytosine (C), and thymine (T). The bases bind using hydrogen bonds via Watson-Crick base-pairing. The base pair A bonds with T and C with G, yielding two complementary strands of DNA forming double-helix structure [45]. Harnessing the base pairing of DNA is well suited for use in specific binding interactions, which has led to the tremendous control over nanoscale DNA bonds [46]. The most common method is to weave a long single-stranded scaffold DNA with small oligonucleotides to create complex and rigid structures using hybridization of DNA bases. Numerous cross-over junctions between helical domains constrain the conformational flexibility and yield a thermodynamically favorable nanostructure with a well-defined shape[47]. This 'DNA origami' technique folds a long single-stranded DNA 'scaffold' (viral genome) molecule using hybridization with suitable complementary short ssDNA. The scaffold and staple strands are mixed and annealed after synthesis without the need of precise stoichiometry or purified strands. An excess of staples together with strand invasion and cooperative effects replace unintended secondary structures and guide the self-assembly of the thermodynamically favorable nanostructure [47]. Practically any DNA origami structure with twists and turns can be constructed using honey comb lattice .[48,49]
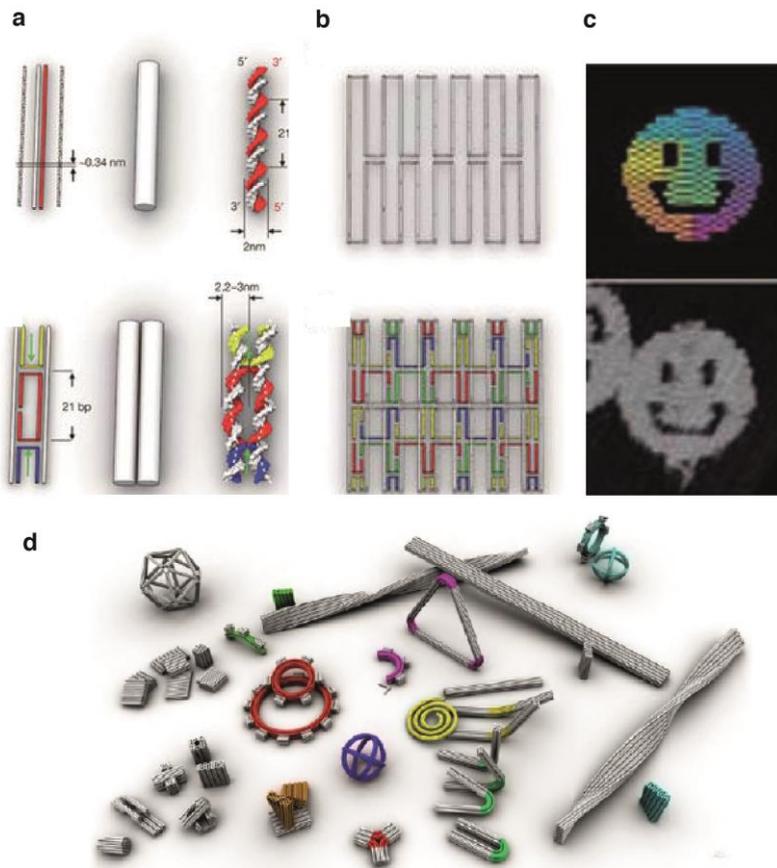
Figure 1.3: DNA origami design fundamentals. a. DNA double helix depicted as a barrel. b. Scaffold routing for 2D DNA nanostucture. c. Example of 2D origami structure. d. Example of complex and 3D DNA nanostructures from scaffold DNA-origami techniques. (a-c reproduced with permission from ref 50 and for d credited to Dietz lab)

The main restrictions of the DNA origami techniques are working requirement of high Mg^{2+} to keep the stable structures, prone to nucleases, long annealing times for complex objects, and the formation of undesired thermodynamically stable products [46]. Various studies has shown that the optimization of staple strand and design is critical to obtain thermodynamically favorable structure and increased folding yields [47,51]. DNA origami nanostructures have huge potential applications such as cargo delivery in the cell,, DNA based sensors, and platform for biophysical studies [46,52,53].

1.3 Nanopores

A nanopore is a tiny, few nanometer-sized hole made up of proteins or fabricated in materials such as glass, polymers, silicon nitride, or graphene. In the past decade, nanopore technology has gained tremendous traction both from scientific community and industries for their applications in bio-sensing. Historically, the predecessor of nanopore are Coulter counter, the pioneering work to count blood cells based on current blockade was developed by Wallace **Coulter in 1940's** [54]. The working principle of nanopores can be briefly summarized as follows, a pore separates two compartments containing an **electrolyte solution (salt solution), and an electric field is** applied through the pore while measuring the ionic current through the pore. Any particle dwelling or passing through the pore blocks the equivalent fraction of ions in the pore volume, and a characteristic current drop and time spent in the pore by that particle is observed (see Figure 1.4).
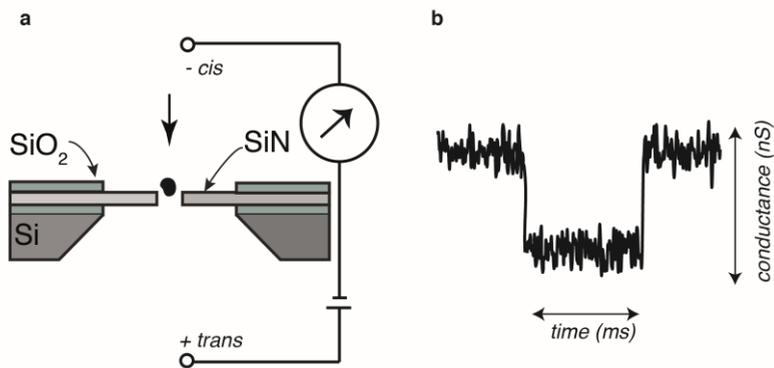
Figure 1.4 A scheme of nanopore setup. a. Experimental set up of a solid-state nanopore with a molecule translocation b. Typical signal from a nanopore translocation event showing signature conductance blockade level as a function of time for translocating particle.

The study of nanopores for sensing applications started with biological pores, where alpha-haemolysin and MspA are among the most studied pores [54,55]. α-haemolysin pore is a toxin produced by S. *aureus* bacteria that embeds itself into lipid membranes naturally. These properties were later exploited for sensing applications of nucleic acids through membrane proteins. Kasianowicz and colleagues first demonstrated the sensing of single-stranded DNA (ssDNA) and RNA molecules through a biological pore [56]. The striking features of biological pores are they can biologically engineered with mutagenesis and ease of adding

specific-binding sites. **The major drawbacks are the fixed di**ameter, and sensitive to conditions such as pH, salt concentration and temperature [57]. With advances in **technology the nanopore field is seen as a promise for label**-free low-cost sequencing of DNA based on a current blockades[55].

The development of solid-state nanopores enabled stable pores with controlled diameters as small as 1nm by drilling a hole in typically in a silicon nitride (SiN) membrane, glass[58], or graphene [59–61] with a ion or electron beam [54,57,62]. The solid state nanopores have been used for widely for single-molecule sensing such as nucleic acids and proteins [62] . The Recent advance allow control over their geometry and chemical functionalization [63]. These nanopores also offers the ease of integration into solid-state devices and scale-up possibilities for commercialization. The current solid-state nanopores technology severely suffers from relatively low signal-to-noise ratio (SNR) for DNA sequencing[54,55,57,64].

The translocation process of charged biopolymers through nanopore is started by capturing the molecule in the close vicinity of the pore opening region is called as capture radius, where the diffusion and the electrophoretic force on the polymer is balanced. Once captured, the end of the polymer chain enters the pore by overcoming the free-energy barrier due to their conformational entropy. Finally, the polymer translocates through the nanopore. Several physical **properties influence particle translocation, mainly the charge of the polymer,** charge on the pore surface, salt concentration, pore diameter, the entropic barrier and frictional forces [62].

The measured ionic current of the solid-state nanopore can be modeled using the theoretical characteristics of the pore. A common mathematical description is given in terms of the nanopore conductance. The conductance (G) **is defined as** the inverse of the resistance (R) of an object ($G = 1/R = I/V$), given by the measured ionic current I **due to ion flow divided by the applied voltage** V between the electrodes. Considering the hourglass shape for nanopore the conductance versus diameter was modelled of the pore can be written as [65]-

$$G_{pore} = \kappa \left[\frac{4l_{pore}}{\pi d^2} + \frac{1}{d} \right]^{-1}$$

where κ is the bulk conductivity of the buffer, l_{pore} is the effective thickness of the solid-state nanopore, and d is its diameter [65].

1.4 NPC mimics and hybrid nanopores

Hybrid nanopore were first reported by docking alpha-hemolysin pore on the solid-state nanopore using a DNA tail[66]. In this work, the possibility to incorporate a chemical functionality to solid-state nanopore was envisioned

In recent years, multiple groups have reported the possibilities of building NPC mimics in nanopore pores arrays and single pores. Talisman et al. [67] reconstructed the transport selectivity of the NPC by coating a track etched polycarbonate porous membrane layer of FG-nups. The pore size was kept close to the actual NPC. The fluorescence imaging techniques was implemented to investigate translocation of transport factors. Most importantly, they showed the size-dependent hindrance of non-importin proteins transportation with through FG-pores. The seminal work reported the possibility to construct minimal NPC mimic system and reproduced the essential properties of NPC selective barrier [67]. Later, responsive polymer based synthetic NPC mimics were built to show the polymer brush mechanism of FG-nups [68]. In 2011, Kowalczyk et al.[69] constructed a biomimetic NPC by covalently anchoring FG-nups to a solid-.state nanopore. Extensive conductance blockade measurements showed the selective translocation of transport factors, while the translocation of inert proteins (BSA) proteins was severely inhibited.

The DNA origami field was embraced by multiple biophysical research groups. The solid-state nanopore community was attracted by control over shape, size , and functional options offered by DNA origami [70]. and Bell et al[71]. independently docked origami structures with a central aperture to form a hybrid between DNA origami and solid-state nanopores. . They showered DNA and proteins translocation through the hybrid pores, and demonstrated chemical selectivity using a bait-prey system (ssDNA motifs on the plate aperture). Wei et al. trapped translocating DNA with the baits and showed the dwell times were dependent on the binding energy controlled by the number of base pairs between the bait-prey DNA. They concluded that single-molecule sensing with a DNA-origami bait-prey system enables sequence-specific detection of DNA and biomolecular interaction studies. Bell et al.[71] demonstrated the controlled insertion of DNA origami nanopore funnel like structures (see figure 1.5a) into solid-state nanopores. Since, these two pioneering papers, many studies have reported the DNA origami nanopore hybrids. A few examples of DNA origami nanopore system are depicted in the figure 1.5. The formation of hybrid pores using captured biological pores or DNA origami with solid-state nanopores allows the construction of nanopores with desired geometry, chemical functionality and integrated binding sites.
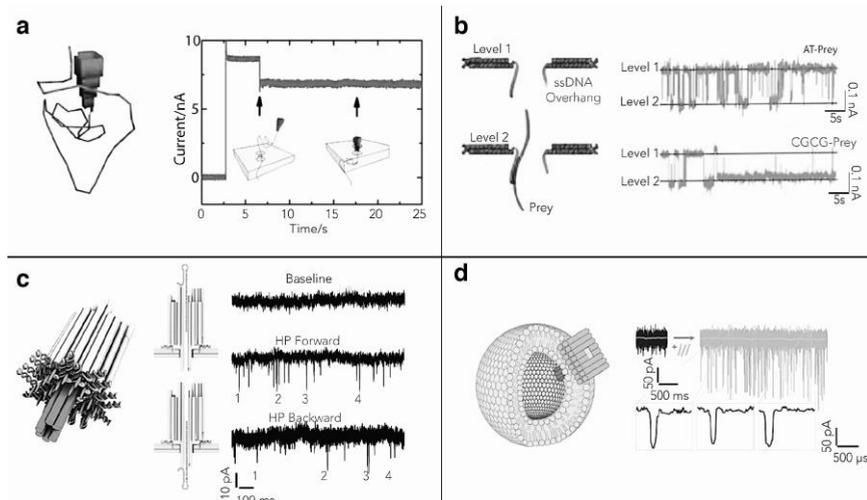
Figure 1.5 Examples of DNA origami pores. a Funnel-like origami structure with a tail and a current-versus-time graph of origami insertion into a solid-state nanopore [71]. b. Origami nanoplate on a nanocapillary with predator strands (top left) for capturing prey strands (bottom left). Current traces show that CGCG prey strands (top right) are captured for a significantly longer time than AT prey strands (bottom right) [72]. c. Small origami nanopore embedded into lipid bilayer and current traces (right) showing the translocation of a single DNA hairpin [73]. d. Large origami nanopore incorporated into lipid bilayer and current traces (right) showing the translocation of dsDNA[74]. (image reproduced with permission from ref 75)

1.5 Outline of this thesis

The primary objective of this dissertation is to build a minimal NPC and understand the intriguing nuclear pore transport phenomena. Hybrid and designer nanopores with custom functionalities may enable biophysical experiments that have the potential to understand biomolecular interactions and processes. Earlier studies on nuclear pores mimics, hybrid pores, and DNA origami pores has inspired the elegant study on cellular transport systems and the translocation of molecules [54,52,76,77]. However, the specific combination of all of the above components into a biophysical experiment with a selective pore was not demonstrated yet. The aim of this thesis is to establish, characterize, and carryout biophysical experiments on a minimalistic selective NPC as controllable macromolecular object.

In this thesis, we construct NPC mimics based on SiN and DNA origami. We utilize purified yeast FG-nups (Nsp1) to attach to nanopore surfaces. In chapter 2, we follow previous biomimetic NPC approaches [67,76] to investigate the biophysical properties and relevance of hydrophobic amino acids residues in FG-Nups (Nsp1). We probe the ion transport properties and transporter receptor selectivity through Nsp1 coated pores. Subsequently, we compare Nsp1 with its mutant Nsp1-S, where hydrophobic amino acid residues F,I,L,V are replaced by hydrophilic serine (S). In chapter 3, we present a novel and reversible surface chemistry technique for immobilizing proteins based on *his-tags*. We also present orthogonal chemistry for attachment of proteins on gold and silicon planar surfaces simultaneously. We report real time attachment and detachment of proteins to both the planar surface and to nanopores.

In chapter 4, we switch our focus to DNA origami and solid-state nanopore hybrid. First, we characterize different types and thickness of DNA-nanoplates for ion permeability and mechanical stability when docked onto the nanopores. In this work, single layered, 2-layered, 3-layered, and honeycomb lattice based nanoplates with dimensions of approximately 50 nm*50 nm were used. We test the ion permeability under varying salt conditions and nanopore diameters. This study yielded interesting and counter institutive observations. The results from this study were taken into account for designing the structures used in chapter 5.

In chapter 5, a DNA origami ring with specific binding sites (ssDNA with 21 nucleotides) on the inner channel surface was constructed to act as the scaffold for NPC mimics. The minimalistic pore is completed by attachment of FG-nucleoporins on the channel surface with well-defined stoichiometries (8 and 32 binding sites). Complementary oligos to DNA-origami binding sites were chemically decorated to proteins to form oligo-protein complex. Oligo-Nsp1 and oligo-Nsp1-S complexes were used to build minimal NPC's with DNA origami ring scaffolds. We utilized solid-state nanopores, gels, TIRF, (cryo) EM, and molecular dynamics simulations to characterize our system. Our current study is aimed at identifying the assembly and stability of the origami ring with FG-nups. The scope for use of these NPC mimics is tremendous and with this thesis we hope to have laid a solid platform for future studies on NPC mimics.

References

(1)   Stewart, M. Molecular Mechanism of the Nuclear Protein Import Cycle. *Nat. Rev. Mol. Cell Biol.* 2007, *8*, 195–208.

(2)   Alberts, B.; Johnson, A.; Lewis, J.; Raff, M.; Roberts, K.; Walter, P. *Molecular Biology of the Cell*; 2002.

(3)   Alber, F.; Dokudovskaya, S.; Veenhoff, L. M.; Zhang, W.; Kipper, J.; Devos, D.; Suprapto, A.; Karni-Schmidt, O.; Williams, R.; Chait, B. T.; *et al.* The Molecular Architecture of the Nuclear Pore Complex. *Nature* 2007, *450*, 695–701.

(4)   Lim, R. Y. H.; Aebi, U.; Fahrenkrog, B. Towards Reconciling Structure and Function in the Nuclear Pore Complex. *Histochem. Cell Biol.* 2008, *129*, 105–116.

(5)   Terry, L. J.; Wente, S. R. Flexible Gates: Dynamic Topologies and Functions for FG Nucleoporins in Nucleocytoplasmic Transport. *Eukaryotic Cell*, 2009, *8*, 1814–1827.

(6)   Musser, S. M.; Grünwald, D. Deciphering the Structure and Function of Nuclear Pores Using Single Molecule Fluorescence Approaches. *J. Mol. Biol.* 2016.

(7)   Bui, K. H.; Von Appen, A.; Diguilio, A. L.; Ori, A.; Sparks, L.; Mackmull, M. T.; Bock, T.; Hagen, W.; Andrés-Pons, A.; Glavy, J. S.; *et al.* Integrated Structural Analysis of the Human Nuclear Pore Complex Scaffold. *Cell* 2013, *155*, 1233–1243.

(8)   Maimon, T.; Elad, N.; Dahan, I.; Medalia, O. The Human Nuclear Pore Complex as Revealed by Cryo-Electron Tomography. *Structure* 2012, *20*, 998–1006.

(9)   Frenkiel-Krispin, D.; Maco, B.; Aebi, U.; Medalia, O. Structural Analysis of a Metazoan Nuclear Pore Complex Reveals a Fused Concentric Ring Architecture. *J. Mol. Biol.* 2010, *395*, 578–586.

(10)   Beck, M.; Hurt, E. The Nuclear Pore Complex: Understanding Its Function through Structural Insight. *Nat. Rev. Mol. Cell Biol.* 2016, *18*, 73–89.

(11)   **Beck, M.; Lucić, V.; Förster, F.; Baumeister, W.; Medalia, O. Snapshots of Nuclear** Pore Complexes in Action Captured by Cryo-Electron Tomography. *Nature* 2007, *449*, 611–615.

(12)   Adams, R. L.; Wente, S. R. Uncovering Nuclear Pore Complexity with Innovation. *Cell* 2013, *152*, 1218–1221.

(13)   Pante, N.; Kann, M. Nuclear Pore Complex Is Able to Transport Macromolecules with Diameters of 39 Nm. *Mol. Biol. Cell* 2002, *13*, 425–434.

(14)   Lowe, A. R.; Siegel, J. J.; Kalab, P.; Siu, M.; Weis, K.; Liphardt, J. T. Selectivity Mechanism of the Nuclear Pore Complex Characterized by Single Cargo Tracking. *Nature* 2010, *467*, 600–603.

(15)   Devos, D.; Dokudovskaya, S.; Williams, R.; Alber, F.; Eswar, N.; Chait, B. T.; Rout, M.
        P.; Sali, A. Simple Fold Composition and Modular Architecture of the Nuclear Pore
        Complex. *Proc. Natl. Acad. Sci.* 2006, *103*, 2172–2177.

(16)   Patel, S. S.; Belmont, B. J.; Sante, J. M.; Rexach, M. F. Natively Unfolded Nucleoporins
        Gate Protein Diffusion across the Nuclear Pore Complex. *Cell* 2007, *129*, 83–96.

(17)   Lin, D. H.; Stuwe, T.; Schilbach, S.; Rundlet, E. J.; Perriches, T.; Mobbs, G.; Fan, Y.;
        Thierbach, K.; Huber, F. M.; Collins, L. N.; *et al.* Architecture of the Symmetric Core
        of the Nuclear Pore. *Science* 2016, *352*, aaf1015.

(18)   Hoelz, A.; Debler, E. W.; Blobel, G. The Structure of the Nuclear Pore Complex. *Annu.
        Rev. Biochem.* 2011, *80*, 613–643.

(19)   Denning, D. P.; Rexach, M. F. Rapid Evolution Exposes the Boundaries of Domain
        Structure and Function in Natively Unfolded FG Nucleoporins. *Mol. Cell. Proteomics*
        2007, *6*, 272–282.

(20)   Dunker, A. K.; Lawson, J. D.; Brown, C. J.; Williams, R. M.; Romero, P.; Oh, J. S.;
        Oldfield, C. J.; Campen, A. M.; Ratliff, C. M.; Hipps, K. W.; *et al.* Intrinsically Disordered
        Protein. *J. Mol. Graph. Model.* 2001, *19*, 26–59.

(21)   Yang, W.; Musser, S. M. Nuclear Import Time and Transport Efficiency Depend on
        Importin Beta Concentration. *J. Cell Biol.* 2006, *174*, 951–961.

(22)   Milles, S.; Mercadante, D.; Aramburu, I. V.; Jensen, M. R.; Banterle, N.; Koehler, C.;
        Tyagi, S.; Clarke, J.; Shammas, S. L.; Blackledge, M.; *et al.* Plasticity of an Ultrafast
        Interaction between Nucleoporins and Nuclear Transport Receptors. *Cell* 2015,
        163, 734–745.

(23)   Quimby, B. B.; Leung, S. W.; Bayliss, R.; Harreman, M. T.; Thirumala, G.; Stewart, M.;
        Corbett, a H. Functional Analysis of the Hydrophobic Patch on Nuclear Transport
        Factor 2 Involved in Interactions with the Nuclear Pore in Vivo. *J. Biol. Chem.* 2001,
        276, 38820–38829.

(24)   Weis, K. The Nuclear Pore Complex: Oily Spaghetti or Gummy Bear? *Cell* 2007, *130*,
        405–407.

(25)   Görlich, D.; Panté, N.; Kutay, U.; Aebi, U.; Bischoff, F. R. Identification of Different
        Roles for RanGDP and RanGTP in Nuclear Protein Import. *EMBO J.* 1996, *15*, 5584–
        5594.

(26)   Ribbeck, K.; Kutay, U.; Paraskeva, E.; Görlich, D. The Translocation of Transportin-
        Cargo Complexes through Nuclear Pores Is Independent of Both Ran and Energy.
        Curr. Biol. 1999, *9*, 47–50.

(27)   Grünwald, D.; Singer, R. H.; Rout, M. Nuclear Export Dynamics of RNA-"protein

Complexes. *Nature*, 2011, *475*, 333–341.

(28)   **Zahn, R.; Osmanović, D.; Ehret, S.; Araya Callis, C.; Frey, S.; Stewart, M.; You, C.;** Görlich, D.; Hoogenboom, B. W.; Richter, R. P. A Physical Model Describing the Interaction of Nuclear Transport Receptors with FG Nucleoporin Domain Assemblies. *Elife* 2016, *5*, e14119.

(29)   Yang, W.; Gelles, J.; Musser, S. M. Imaging of Single-Molecule Translocation through Nuclear Pore Complexes. *Proc Natl Acad Sci U S A* 2004, *101*, 12887–12892.

(30)   Ribbeck, K.; Görlich, D. Kinetic Analysis of Translocation through Nuclear Pore Complexes. *EMBO J.* 2001, *20*, 1320–1330.

(31)   Kubitscheck, U.; Grünwald, D.; Hoekstra, A.; Rohleder, D.; Kues, T.; Siebrasse, J. P.; Peters, R. Nuclear Transport of Single Molecules: Dwell Times at the Nuclear Pore Complex. *J. Cell Biol.* 2005, *168*, 233–243.

(32)   Tran, E. J.; Wente, S. R. Dynamic Nuclear Pore Complexes: Life on the Edge. *Cell*, 2006, *125*, 1041–1053.

(33)   Köser, J.; Maco, B.; Aebi, U.; Fahrenkrog, B.; Genes, H.; Solid, L.; Deep, T. C.; Portal, I.; Maco, B.; Aebi, U.; *et al.* The Nuclear Pore Complex Becomes Alive : New Insights into Its Dynamics and Involvement in Different Cellular Processes. *Components* 2007, 1–29.

(34)   Timney, B. L.; Raveh, B.; Mironska, R.; Trivedi, J. M.; Kim, S. J.; Russel, D.; Wente, S. R.; Sali, A.; Rout, M. P. Simple Rules for Passive Diffusion through the Nuclear Pore Complex. *J. Cell Biol.* 2016, *215*.

(35)   Tagliazucchi, M.; Peleg, O.; Kröger, M.; Rabin, Y.; Szleifer, I. Effect of Charge, Hydrophobicity, and Sequence of Nucleoporins on the Translocation of Model Particles through the Nuclear Pore Complex. *Proc. Natl. Acad. Sci. U. S. A.* 2013, *110*, 3363–3368.

(36)   Rout, M. P.; Aitchison, J. D.; Magnasco, M. O.; Chait, B. T. Virtual Gating and Nuclear Transport: The Hole Picture. *Trends in Cell Biology*, 2003, *13*, 622–628.

(37)   Ando, D.; Zandi, R.; Kim, Y. W.; Colvin, M.; Rexach, M.; Gopinathan, A. Nuclear Pore Complex Protein Sequences Determine Overall Copolymer Brush Structure and Function. *Biophys. J.* 2014, *106*, 1997–2007.

(38)   Rout, M. Virtual Gating and Nuclear Transport: The Hole Picture. *Trends Cell Biol.* 2003, *13*, 622–628.

(39)   Lim, R. Y. H.; Fahrenkrog, B.; Köser, J.; Schwarz-Herion, K.; Deng, J.; Aebi, U. Nanomechanical Basis of Selective Gating by the Nuclear Pore Complex. *Science* 2007, *318*, 640–643.

(40)   Schleicher, K. D.; Dettmer, S. L.; Kapinos, L. E.; Pagliara, S.; Keyser, U. F.; Jeney, S.; Lim, R. Y. H. Selective Transport Control on Molecular Velcro Made from Intrinsically Disordered Proteins. *Nat. Nanotechnol.* 2014, *9*, 525–530.

(41)   Frey, S.; Görlich, D. A Saturated FG-Repeat Hydrogel Can Reproduce the Permeability Properties of Nuclear Pore Complexes. *Cell* 2007, *130*, 512–523.

(42)   Frey, S.; Richter, R. P.; Görlich, D. FG-Rich Repeats of Nuclear Pore Proteins Form a Three-Dimensional Meshwork with Hydrogel-like Properties. *Science* 2006, *314*, 815–817.

(43)   Ader, C.; Frey, S.; Maas, W.; Schmidt, H. B.; Görlich, D.; Baldus, M. Amyloid-like Interactions within Nucleoporin FG Hydrogels. *Proc. Natl. Acad. Sci. U. S. A.* 2010, *107*, 6281–6285.

(44)   Yamada, J.; Phillips, J. L.; Patel, S.; Goldfien, G.; Calestagne-Morelli, A.; Huang, H.; Reza, R.; Acheson, J.; Krishnan, V. V; Newsam, S.; *et al.* A Bimodal Distribution of Two Distinct Categories of Intrinsically Disordered Structures with Separate Functions in FG Nucleoporins. *Mol. Cell. Proteomics* 2010, *9*, 2205–2224.

(45)   Watson, J.; Crick, F. Molecular Structure of Nucleic Acids. *Nature.* 1953, *171*, 737–738.

(46)   Jones, M. R.; Seeman, N. C.; Mirkin, C. A. Programmable Materials and the Nature of the DNA Bond. *Science*, 2015, *347*.

(47)   Rothemund, P. W. K. Folding DNA to Create Nanoscale Shapes and Patterns. *Nature* 2006, *440*, 297–302.

(48)   Douglas, S. M.; Marblestone, A. H.; Teerapittayanon, S.; Vazquez, A.; Church, G. M.; Shih, W. M. Rapid Prototyping of 3D DNA-Origami Shapes with caDNAno. *Nucleic Acids Res.* 2009, *37*, 5001–5006.

(49)   Dietz, H.; Douglas, S. M.; Shih, W. M. Folding DNA into Twisted and Curved Nanoscale Shapes. *Science* 2009, *325*, 725–730.

(50)   Castro, C. E.; Kilchherr, F.; Kim, D. N.; Shiao, E. L.; Wauer, T.; Wortmann, P.; Bathe, M.; Dietz, H. A Primer to Scaffolded DNA Origami. *Nat. Methods* 2011, *8*, 221–229.

(51)   Wagenbauer, K. F.; Engelhardt, F. A. S.; Stahl, E. K.; Hechtl, V. K.; Stömmer, P.; Seebacher, F.; Meregalli, L.; Ketterer, P.; Gerling, T.; Dietz, H. How We Make DNA Origami. *ChemBioChem* 2017.

(52)   Hernández-Ainsa, S.; Keyser, U. F. DNA Origami Nanopores: Developments, Challenges and Perspectives. *Nanoscale* 2014, *6*, 14121–14132.

(53)   Linko, V.; Dietz, H. The Enabled State of DNA Nanotechnology. *Curr. Opin.*

Biotechnol. 2013, 1–7.

(54)   Wanunu, M. Nanopores: A Journey towards DNA Sequencing. *Physics of Life Reviews*, 2012, *9*, 125–158.

(55)   Branton, D.; Deamer, D. W.; Marziali, A.; Bayley, H.; Benner, S. A.; Butler, T.; Di Ventra, M.; Garaj, S.; Hibbs, A.; Huang, X.; *et al.* The Potential and Challenges of Nanopore Sequencing. *Nature Biotechnology*, 2008, *26*, 1146–1153.

(56)   Kasianowicz, J. J.; Brandin, E.; Branton, D.; Deamer, D. W. Characterization of Individual Polynucleotide Molecules Using a Membrane Channel. *Proc. Natl. Acad. Sci. U. S. A.* 1996, *93*, 13770–13773.

(57)   Dekker, C. Solid-State Nanopores. *Nat. Nanotechnol.* 2007, *2*, 209–215.

(58)   Steinbock, L. J.; Otto, O.; Chimerel, C.; Gornall, J.; Keyser, U. F. Detecting DNA Folding with Nanocapillaries. *Nano Lett.* 2010, *10*, 2493–2497.

(59)   Merchant, C. A.; Healy, K.; Wanunu, M.; Ray, V.; Peterman, N.; Bartel, J.; Fischbein, M. D.; Venta, K.; Luo, Z.; Johnson, A. T. C.; *et al.* DNA Translocation through Graphene Nanopores. *Nano Lett.* 2010, *10*, 2915–2921.

(60)   Siwy, Z. S.; Davenport, M. Nanopores: Graphene Opens up to DNA. *Nature Nanotechnology*, 2010, *5*, 697–698.

(61)   Schneider, G. F.; Dekker, C. DNA Sequencing with Nanopores. *Nature Biotechnology*, 2012, *30*, 326–328.

(62)   Muthukumar, M.; Plesa, C.; Dekker, C. Single-Molecule Sensing with Nanopores. *Phys. Today* 2015, *68*, 40–46.

(63)   Wanunu, M.; Meller, A. Chemically Modified Solid-State Nanopores. *Nano Lett.* 2007, *7*, 1580–1585.

(64)   Smeets, R. M. M.; Keyser, U. F.; Dekker, N. H.; Dekker, C. Noise in Solid-State Nanopores. *Proc. Natl. Acad. Sci. U. S. A.* 2008, *105*, 417–421.

(65)   Kowalczyk, S. W.; Grosberg, A. Y.; Rabin, Y.; Dekker, C. Modeling the Conductance and DNA Blockade of Solid-State Nanopores. *Nanotechnology* 2011, *22*, 315101.

(66)   Hall, A. R.; Scott, A.; Rotem, D.; Mehta, K. K.; Bayley, H.; Dekker, C. Hybrid Pore Formation by Directed Insertion of α-Haemolysin into Solid-State Nanopores. *Nat. Nanotechnol.* 2010, *5*, 874–877.

(67)   Jovanovic-Talisman, T.; Tetenbaum-Novatt, J.; McKenney, A. S.; Zilman, A.; Peters, R.; Rout, M. P.; Chait, B. T. Artificial Nanopores That Mimic the Transport Selectivity of the Nuclear Pore Complex. *Nature* 2009, *457*, 1023–1027.

(68)   Caspi, Y.; Zbaida, D.; Cohen, H.; Elbaum, M. Synthetic Mimic of Selective Transport through the Nuclear Pore Complex. *Nano Lett.* 2008, *8*, 3728–3734.

(69)   Kowalczyk, S. W.; Kapinos, L.; Blosser, T. R.; Magalhães, T.; van Nies, P.; Lim, R. Y. H.; Dekker, C. Single-Molecule Transport across an Individual Biomimetic Nuclear Pore Complex. *Nat. Nanotechnol.* 2011, *6*, 433–438.

(70)   Wei, R.; Martin, T. G.; Rant, U.; Dietz, H. DNA Origami Gatekeepers for Solid-State Nanopores. *Angew. Chem. Int. Ed. Engl.* 2012, *51*, 4864–4867.

(71)   Bell, N. a W.; Engst, C. R.; Ablay, M.; Divitini, G.; Ducati, C.; Liedl, T.; Keyser, U. F. DNA Origami Nanopores. *Nano Lett.* 2012, *12*, 512–517.

(72)   Hernández-Ainsa, S.; Misiunas, K.; Thacker, V. V.; Hemmig, E. A.; Keyser, U. F. Voltage-Dependent Properties of DNA Origami Nanopores. *Nano Lett.* 2014, *14*, 1270–1274.

(73)   Langecker, M.; Arnaut, V.; Martin, T. G.; List, J.; Renner, S.; Mayer, M.; Dietz, H.; Simmel, F. C. Synthetic Lipid Membrane Channels Formed by Designed DNA Nanostructures. *Science* 2012, *338*, 932–936.

(74)   Krishnan, S.; Ziegler, D.; Arnaut, V.; Martin, T. G.; Kapsner, K.; Henneberg, K.; Bausch, A. R.; Dietz, H.; Simmel, F. C. Molecular Transport through Large-Diameter DNA Nanopores. 2016, *7*, 12787.

(75)   Wang, P.; Meyer, T. A.; Pan, V.; Dutta, P. K.; Ke, Y. The Beauty and Utility of DNA Origami. *Chem*, 2017, *2*, 359–382.

(76)   Kowalczyk, S. W.; Blosser, T. R.; Dekker, C. Biomimetic Nanopores: Learning from and about Nature. *Trends Biotechnol.* 2011, *29*, 607–614.

(77)   Howorka, S. Building Membrane Nanopores. *Nat Nano* 2017, *12*, 619–630.

2.

Spatial structure of disordered proteins dictates conductance and selectivity in Nuclear Pore Complex mimics

Nuclear pore complexes (NPCs) lined with intrinsically disordered FG-domains act as selective gatekeepers for molecular transport between the nucleus and the cytoplasm in eukaryotic cells. The underlying physical mechanism of the intriguing selectivity is still under debate. Here, we probe the transport of ions and transport receptors through biomimetic NPCs consisting of Nsp1 domains attached to the inner surface of solid-state nanopores. We examine both wildtype FG-domains and hydrophilic SG-mutants. FG-nanopores showed a clear selectivity as transport receptors can translocate across the pore whereas other proteins cannot. SG mutant pores lack such selectivity. To unravel this striking difference, we present coarse-grained molecular dynamics simulations that reveal that FG-pores exhibit a high-density, nonuniform protein distribution, in contrast to a uniform and significantly less-dense protein distribution in the SG-mutant. We conclude that the sequence-dependent density distribution of disordered proteins inside the NPC plays a key role for its conductivity and selective permeability.

2.1 Introduction

The nuclear envelope (NE) separates the nucleus of eukaryotic cells from the cytosol. NE-embedded nuclear pore complexes (NPCs) allow for the exchange of molecules such as RNA, metabolites, and proteins between the two compartments. NPCs are giant structures with a molecular mass of around 100 MDa, composed of about 30 different types of proteins named nucleoporins (Nups) [1–3]. NPCs are equipped with a barrier that is permeable for molecules of up to 30 kDa or ~5 nm in diameter, but blocks the passage of larger ones [4–6]. Shuttling nuclear transport receptors (NTRs) can overcome this size-limit and traverse the NPC, carrying along cargoes with diameters of up to 40 nm [7,8], thus endowing the pore with a selective permeability barrier. Nups that contain phenylalanine-glycine (FG) repeats (FG-Nups) [9] are crucial for this remarkable selectivity, suggesting that the NTR transport is mediated by hydrophobic interactions. The FG-repeat domains are intrinsically disordered, bind NTRs during facilitated translocation [10,11], and form the NPC permeability barrier [12,13]. The question of how FG domains create a permeability barrier and at the same time greatly favor the passage of NTRs is one of the central questions in molecular cell biology.

Many different models have been proposed to explain the selective transport of NTRs through NPCs, including the virtual-gate model [14,15], the reversible-collapse (or polymer-brush) model [16], the reduction-of-dimensionality [17] and 'molecular velcro' [18] model, the hydrogel model [12,19] , the Kap-centric model [20,21], and the forest model [22]. However, no consensus has been reached on one prevailing model.

A typical NPC comprises about 10-12 different FG Nups (in copy numbers of 8 to 32), yielding about 5000 FG motifs per NPC. One of the most abundant and best-studied FG Nups is *S. cerevisiae* Nsp1[9]. Here, we specifically address the importance of FG domains for NPCs by comparing the transport properties of Nsp1-coated biomimetic NPCs with analogs that employ an Nsp1 mutant in which the hydrophobic amino acids F, I, L and V are replaced by hydrophilic serines (S), thus creating an 'SG' Nsp1 variant. To realize this, we employ an approach that combines biophysics experiments and coarse-grained molecular dynamics (MD) simulations. For the experiments, we utilize the approach of biomimetic NPCs [23,24] based on the solid-state-nanopore platform [25]. Solid-state nanopores, basically small holes in a silicon nitride membrane, are single-molecule sensors based on ion-current readout. As a robust, modular, and label-free technique [26], nanopores provide a powerful platform to study NPCs in a bottom-up approach. Using these nanopore-based biomimetic NPCs, we here

investigate the ion transport through such pores at various diameters as well as compare the selectivity of NPCs with Nsp1-FG domains with those made of the Nsp1-SG mutant.

Important insight in the nanoscopic structure of these biomimetic NPCs is obtained by complementing the *in-vitro* measurements with *in-silico* simulation results of an experimentally-calibrated one-bead-per-amino-acid MD model [27,28]. The key feature of the model is that it is fine enough to represent the amino-acid sequence of each Nsp1-FG domain and its SG-mutant, but coarse enough to capture the collective behavior of all FG-domains inside the biomimetic nanopore (that contains over 80,000 amino-acids altogether). The model is used to establish the nonhomogeneous density distribution inside the pores of different diameters and to shed light on the relation between ion conductance and FG-domain density. Furthermore, using umbrella sampling, the energy barrier of inert cargos and transport receptors is calculated to address the difference in selectivity and permeability between nanopores lined with Nsp1 and its mutant. The *in-vitro* and *in-silico* data agree very well and highlight the role of hydrophobic interactions in nuclear transport. Our findings identify how the sequence-dependent spatial structure of the disordered FG domains affects the conductance and establishes **the NPC's selective perme**ability.

2.2 Results

2.2.1 Conductance of Nup-coated biomimetic NPCs

To study the structural and transport properties of FG domains within biomimetic NPCs, we used self-assembled-monolayer chemistry to graft the domains to the surface of the solid-state nanopore, using a C-terminal cysteine for surface attachment. A scheme of the attachment chemistry is shown in SI 2.1. To build the minimal NPC mimic, we first examined the important and well-studied FG domain [9] from S. cerevisiae: Nsp1$^{1-601}$ (65.7 kDa) (Figure 2.1A), which has a highly cohesive N-terminus and a charged non-cohesive C-terminal part [22,29]. Additionally, we studied an Nsp1 mutant, in which the hydrophobic amino acids F, I, L, V have been replaced by the hydrophilic amino acid serine (S). Given the abundance of F compared to I, L and V, the major change in sequence is the replacement of the FG and FxFG motifs into SG and SxSG motifs, thus converting the Nsp1 FG-domain into a Nsp1 SG-domain (see SI 1 for the exact amino-acid sequence of the wildtype and mutant Nsp1). In earlier studies, it was shown that the mutated Nsp1-SG domain was unable to form a hydrogel-like structure [13,29,30].

Here, we study how this affects the conductance of the biomimetic NPCs as well as their selective properties. Once the nanopore was coated with the Nsp1-FG domains (further called Nsp1 in short) and Nsp1-SG domains (further called Nsp1-

S), current (I) versus voltage (V) curves for each pore were recorded at physiological salt conditions and applied voltages from -200 mV to 200 mV. All pores showed a linear IV response, see Figure 2.1C, D for examples. The IV characteristics of both the Nsp1 and Nsp1-S grafted pores are linear but with a lower slope than for the bare pores, indicating, as expected, a reduced ion conductance due to the presence of the Nups. The attachment of Nups to the nanopore also increased the low-frequency $1/f$ noise compared to bare pores (See SI 2.6). Transmission electron micrographs of Nsp1-coated pores further supported the presence of Nups within the nanopores (SI 3). The linearity of the IV curves indicates that the Nsp1 and Nsp1-S coat was not significantly affected by the applied voltage. For the Nsp1-coated pores, the conductance $G = I/V$ dropped about 80% after coating Nsp1 (Fig. 2.1C). For pores coated with Nsp1-S, the current drop was lower, about 50% when compared with bare pores (Fig. 2.1D). The difference in the current blockade points towards a different volumetric arrangement of the proteins inside the nanopore, thus emphasizing the difference in the amino acid sequence of Nsp1 and Nsp1-S.

Biomimetic NPCs have the advantage that, unlike natural NPCs, the pore diameter can be varied as a free parameter. We compared the ionic conductance $G=I/V$ of bare pores with Nsp1 and Nsp1-S coated pores for various pore diameters d (Fig. 2.1B). For bare pores, a conductance of $G=6$-88 nS was measured for pore diameters ranging from 5-60 nm. We observed a slightly non-linear increase of conductance at small pore sizes, followed by a near-linear relation for wide pores. This is in accordance with the well-established non-linear $G(d)$ relation for cylindrical SiN pores [31,32]:

$$G(d) = \sigma_{\mathrm{bare}}[4l/(\pi d^2) + 1/d]^{-1}, \qquad (1)$$

where the first term in the denominator accounts for the pore resistance and the second for the access resistance (the latter being dominant at large pore diameters). Here, $l = 20$ nm is the height of the pore and σ_{bare} is the conductivity of the ions through the bare pore, which was fitted to be equal to 2.2 ± 0.2 nS/nm (average ± standard deviation), in close agreement with the experimental value of 2.3 ± 0.3 nS/nm from bulk conductivity measurements.

For Nsp1-coated pores, the conductance data show a radically different behaviour, with two rather distinct regimes of ion conductivity above and below an apparent threshold diameter of $d_{\mathrm{Nsp1}} = 41 ± 2$ nm. The current measured for pores with a diameter ranging from 5 nm to 41 nm showed a very low conductance of $G = 0.2$ to 4 nS (see SI 5). Nsp1-coated pores with a diameter larger than 41 nm conduct ions with a much larger conductance. These observations are

consistent with previously published results for biomimetic NPC's with human FG domains [25]. When we coat the pores with the Nsp1-S mutant, we observed a qualitatively similar non-linear $G(d)$ behaviour as for the Nsp1-coated pores, but with a much lower threshold diameter $d_{Nsp1-S} = 23 \pm 3$ nm.

2.2.2 Molecular dynamics calculations of the FG domain density distribution

In order to gain a microscopic understanding of the FG domain structures that underlie these nonlinear *in vitro* conductance data, we developed a coarse-grained MD model of the biomimetic nanopores with embedded FG domains. The MD model of the domains is based on a one-bead-per-amino-acid representation that distinguishes between all 20 amino acids (see Fig. 2.2A) [28]. The model takes into account hydrophobic and electrostatic interactions between the amino acids, as well as the screening effect of free ions and the polarity of the solvent. The model has been shown to accurately predict (within 20% error) the Stokes radii of a wide range of FG domains and FG domain segments [28], including the low-charge Nsp1$^{1-172}$ and high-charge Nsp1$^{173-603}$ FG segments [22]. Nanopores were modeled as cylinders of height 20 nm (see SI 2.4) constructed from inert beads of 3 nm diameter as depicted in Fig. 2.2B. The Nsp1 and Nsp1-S were anchored in a close-packed triangular lattice with an average grafting density of 1 per 28 nm^2, corresponding to an average grafting distance of 5.7 nm. This grafting distance was experimentally estimated using two independent techniques (see SI 2.4), and further confirmed in experiments on denatured proteins in guanidinium HCl (SI 2.8). The 1 per 28 nm^2 grafting density matches well with the surface area per FG Nup in a yeast NPC of about 24 to 32 nm^2 and is close to the density that was reported for Nsp1 assembled *in vitro* on a planar surface [33].

To further explore the partitioning of Nsp1 in the pore based on amino-acid sequence, we study the localization of its head and tail groups inside the nanopore. Nsp1 has a collapsed coil N-terminal segment that is hydrophobic, low in charge and rich in FG-repeats, forming a small cohesive 'head'. The C-terminus domain – which is bound to the nanopore surface – has a high charge-to-hydrophobicity ratio and has a repulsive, extended coil ('stalk') conformation [22] (see Fig. S2.10 in SI 2.9). Our results show that for Nsp1 the heads are rather localized, forming a cohesive structure around the central pore axis for the 45 (see SI Movie 1) and 60 nm pores. In contrast, the Nsp1-S heads show a much more widespread distribution (see SI Movie 2), reflecting their higher charge-to-hydrophobicity ratio.

In terms of amino acid sequence and pore partitioning it is interesting to compare these Nsp1 pores also with nanopores lined with the Nup98 FG domain (498 amino acids), studied before [25]. The Nup98 FG domain has a low charge-to-hydrophobicity ratio, resulting in a collapsed structure, and it is grafted on the pore surface at a density of 1 per 49 nm^2 [25]. The 2D (r,z) and radial density distribution, depicted in Fig. S2.12 (SI 2.10), show a profoundly different behaviour: the Nup98 FG pore shows a very dense (300 mg/ml) ring-like structure that forms already at relatively small pore sizes (25 – 30 nm), while the protein density vanishes towards the pore centre. In contrast, Nsp1 and its mutant form a pore-filling Nup network that is retained up to pore diameters larger than 60 nm. The key observation is that, consistent with experiments [25], the ionic conductance through the Nup98 pores only commences when a central conduit has opened up in the nonconductive high-density ring structure, which contrast Nsp1 and Nsp1-S pores that are filled by a uniform protein network of relative low density that supports ion flow throughout.
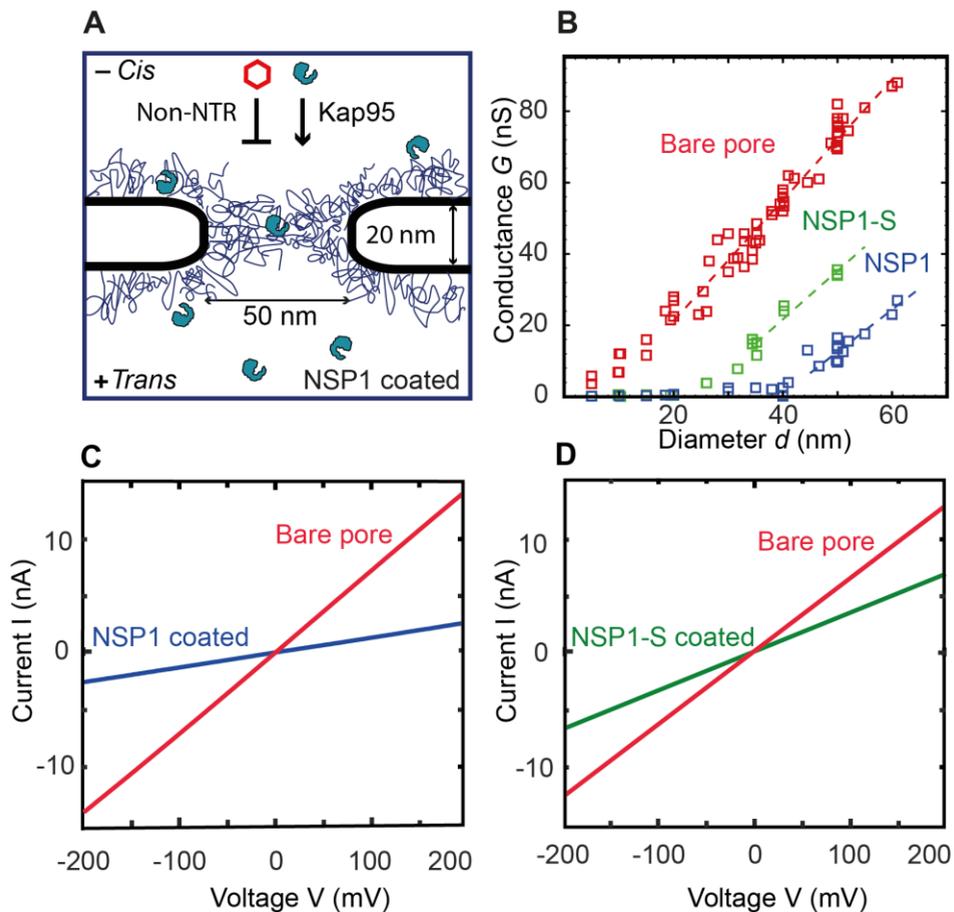
Figure 2.1 Coating a nanopore with FG-Nups reduces the pore conductivity. A. Schematic of the biomimetic NPC where yeast FG-Nup Nsp1 is coated onto a solid-state nanopore of diameter 50 nm and thickness of 20 nm. Kap95, a yeast importer, can pass through the barrier, whereas most other proteins such as tCherry fail to pass through the pores. B. Conductance versus pore diameter for bare pores (red), Nsp1-coated pores (blue), and Nsp1-S-coated pores (green). The conductance is low (<4nS) for small-diameter biomimetic pores, below a threshold diameter 41±2 nm and 26 ±3 nm, for Nsp1 and Nsp1-S respectively. Above this threshold diameter, the conductance increases linearly with slope similar to that of the bare pore conductance. Dashed lines are linear guides to the eye. C & D. Current vs voltage curves for a 50 nm pore before (blue) and after Nsp1 coating (red). The conductance drops by about 80% after coating, confirming a high density of Nsp1 inside the nanopore. C. Current vs voltage curves for a mutant Nsp1-S-coated (green) 50 nm pore. Here the conductance drops by about 50% conductance compared to the bare pore (blue).

A

head

Nsp1

tail

B

20 nm

C
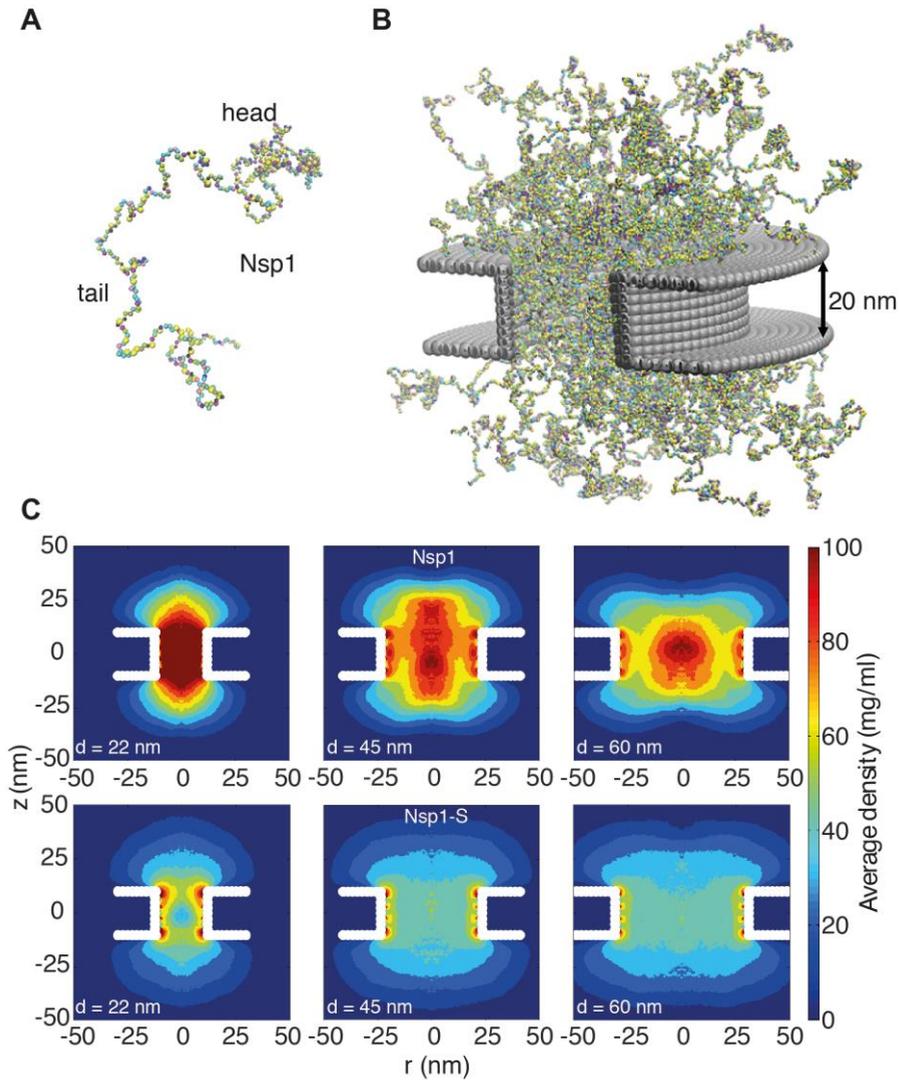
Figure 2.2 Coarse-grained molecular dynamics results of Nup density distributions in Nsp1 and Nsp1-S pores of varying diameter. A. Coarse-grained one-bead-per-amino-acid representation of Nsp1; the different colors of the beads represent the 20 different amino acids. The collapsed-coil N-**terminal 'head' region is visible at the top right.** B. Multiple Nsp1s tethered inside a cylindrical pore of height 20 nm and a diameter of 45 nm with anchor points spaced according to a fully triangulated (close-packed) distribution with a spacing of 5.7 nm. C. Time-averaged r-z density distribution of Nsp1-coated nanopores (top row) with diameters 22 nm, 45 nm and 60 nm; and similarly, for

Nsp1-S (bottom row). These data show denser structures for the smaller pores and much lower densities for Nsp1-S compared to the wildtype Nsp1. The nups are coated on the inner surface of the cylindrical nanopores at a close-packed triangular spacing of 5.7 We thus computed the time-averaged amino acid mass density distribution of the nanopores that were coated with Nsp1 or Nsp1-S, for pore diameters ranging from 22 to 60 nm. Fig. 2.2C shows the axisymmetric (r, z) density distribution in the pores, averaged in the circumferential direction. The mass density inside the central cylindrical region of the larger Nsp1 pores is much higher (70 – 100 mg/ml), than that for the mutant (50 mg/ml), as can also be seen in the z-averaged (-10 nm < z < 10 nm) radial density distribution in Fig. 2.3A. Interestingly, we observed that the Nsp1 pores clearly feature a maximum density at the central axis (r = 0, see Fig.2.3), which is possibly related to the high percentage of hydrophobic residues, relative to charged residues, in the head group of the wildtype Nsp1. The Nsp1-S data show a striking difference in density distribution: much more uniform and less dense, which is likely to be caused by the lower number of hydrophobic residues compared to the wildtype Nsp1 (see Fig. 2C and Fig. 2.3A).

Figure 2.3B shows a dependence of G on d that is strikingly similar to that of the experimental data (cf. Fig. 2.1B), featuring two distinct regimes of ion conductance, at low and high pore diameters. Below a critical pore diameter, the conductance is very low, whereas above it, it rises nearly linearly with diameter. Furthermore, the mutant shows a larger conductance than the native Nsp1. Gratifyingly, the experimental and theoretical data are even in good quantitative agreement (see inset Fig. 2.3B). Note that this correspondence is remarkable, given the simplicity of the model that merely assumes a critical FG domain density. In order to generate a closed-form, continuous function for the conductance $G(d)$, we fit the conductivities in Fig. S2.11 (SI 2.10) with smooth sigmoidal functions, substitute these in Eq. 2, and plot the results together with the experimental and numerical data points in Fig. 2.3C. The figure clearly illustrates that both the non-linear increase at small pore diameters as well as the near-linear increase in conductance at large pore sizes are nicely captured by the theoretical conductance relation, in close agreement with the numerical and experimental data points. Some deviations remain in the crossover region, e.g., near 20-30 nm in the Nsp1-S mutant data.

 It is of interest to put the conductance values that we report here for biomimetic NPCs in perspective. Early patch clamp studies of whole NPCs in vivo showed that NPCs are permeable to ions [34,35], and all papers on NPCs since then have mentioned the good permeability of NPCs to ions and small molecules. However, the conductance of a single NPC is actually quite low, with values of only 0.3-2 nS, which is roughly two orders of magnitude lower than unhindered ionic transport [34,35]. It is noteworthy that our biomimetic NPC, with only 1 type of Nups, viz. Nsp1,

has a conductance of ~4 nS for 35 nm pores, which is quite close to the in vivo value of 0.3-2 nS, certainly in view of the simplicity of our biomimetic NPC. Real NPCs consists of several types of Nups with a varying charge and FG content that all may affect the ion flux.

2.2.4 Nsp1-pores are selective whereas Nsp1-S-pores are not selective for transport receptors

A critical question is to determine whether the NPC biomimetic pores are functional and selective regarding the transport of proteins. We compared the translocation of yeast NTR Kap95 (95 kDa) and a non-NTR tetrameric protein tCherry of similar size (104kDa, see SI. 14) through Nsp1-coated pores of size 48 ± 3 nm (as measured by TEM) [12,30]. First, we show the control experiment where we added either Kap95 or tCherry to the *cis* side of a bare (uncoated) pore. We observed clear translocation events as blockade peaks in the conductance (Fig. 2.4A). Each downward spike is a single protein translocation event with a characteristic translocation time (τ) and conductance blockade (ΔG, the amplitude of the spikes in Fig. 2.4A and B). We use a custom-made Matlab script to analyze our data as described elsewhere [36]. In Fig. 2.4C-F, each translocation event was represented as a dot in the scatter diagram, which shows the conductance blockade versus translocation time. A log-normal fit of the translocation times yields an average τ = 0.29 ± 0.16 ms and 0.19 ± 0.11 ms (mean ± standard deviation, for N=3 pores), for Kap95 (100 nM) and tCherry (100 nM), respectively. The conductance blockade for Kap95 was 0.22 ± 0.07 nS and for tCherry 0.28 ±0.11 nS. We thus conclude that, as expected from their similar size, the Kap95 and tCherry proteins translocate the bare nanopore with quite similar characteristics.

Next, we address the translocation though nanopores that were coated with Nsp1. Kap95 translocate through such pores with a most likely translocation time of τ = 5.2 ms ± 2.4 ms and an average conductance blockade of 0.31 ± 0.10 nS (N=3). The conductance blockade is, as expected, of similar magnitude as for the bare pore. The most noteworthy difference is the significant increase in translocation time of Kap95 as it moves through the Nsp1-coated pore, indicating interactions between Nsp1 and Kap95. To probe whether these biomimetic NPCs also allow large non-NTR proteins to pass through, Kap95 was replaced by tCherry, a protein that is expected not to interact with the FG domains of NPCs. We found that passage of tCherry through the Nsp1-coated pores was essentially blocked: The tCherry translocation experiments yielded a significantly lower number of events (n=90, compared to n=917 for Kap95 in the same time window and at the same concentration; see Figure 2.4E). From these measurements, we conclude that the Nsp1-coated pore is selective: it does not allow tCherry to pass through efficiently, in contrast to the transport observed for Kap95.
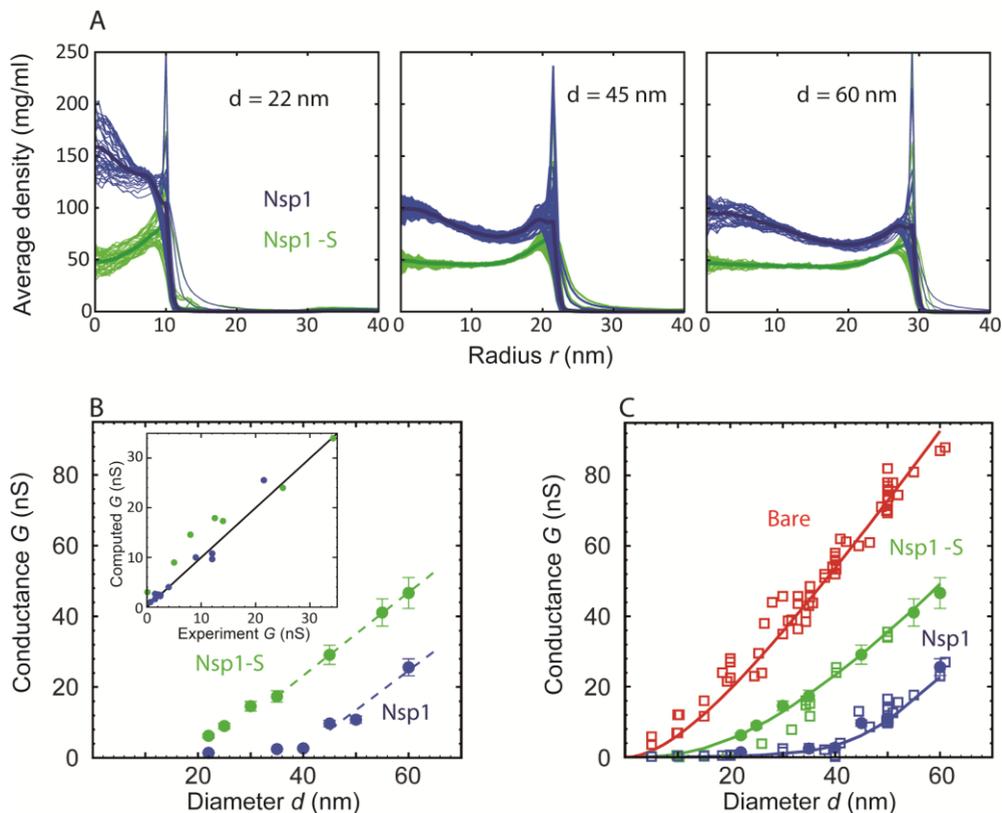
Figure 2.3. Radial density distribution and conductance data for Nsp1 and Nsp1-S biomimetic pores. A. Radial protein density distribution for biomimetic nuclear pores with pore diameters of 22 nm, 45 nm, and 60 nm, for pores coated with Nsp1 (blue) and Nsp1-S (green). All data are taken within the height of the cylinder (20 nm; -10 nm < z < 10 nm) that is divided into 20 equally spaced discs of thickness 1 nm each. Each of the 20 curves represented in each panel shows the radial density distribution for that specific z location. B. Modeling results for the conductance as a function of pore diameter for Nsp1-coated pores (blue) and Nsp1-S-coated pores (green). The dashed lines are linear guides to the eye. The inset shows a comparison between the computed and the experimental conductance. C. Conductance versus pore diameter for the experimental (open symbols) and modeling data (closed symbols). For Nup-coated pores, the conductance is low (G<4nS) for small diameters, but it increases strongly with a non-linear dependence on pore diameter beyond ~40 nm for Nsp1 and beyond ~20 nm for Nsp1-S. At larger diameters the conductance increases almost linearly with a slope slightly smaller than that of the bare pore, with G-values of tens of nS. The red solid line corresponds to Eq. (1) for the bare pore and the green and blue solid lines correspond to Eq. (2) with the

conductivities for the access and pore regions obtained by fitting the numerical results using sigmoidal functions (see Fig. S2.11 in SI 2.10).

One of the main objectives of this research was to address the importance of FG motifs in Nups such as Nsp1. Specifically, we ask ourselves whether the mutation of the hydrophobic FG motifs to the much less hydrophobic SG motifs affects the selective permeability barrier. To investigate this, we carried out translocation measurements with both Kap95 and tCherry on the Nsp1-S-coated nanopores. We successfully performed such experiments (Fig.2.4D and 2.4F), yielding an average translocation time for Kap95 of τ = 0.23 ± 0.13 ms (Fig. 4D) and τ = 0.45 ±0.23 ms for tCherry (Fig. 2.4F), and a conductance blockade of 0.24 ±0.10 nS and 0.32 ± 0.09 nS, respectively (N=3). Figure 2.4G and 2.4H compare the translocation times for all cases. Fig. 2.4G clearly shows the longer translocation time for Kap95 through Nsp1-coated pores, compared to both bare and Nsp1-S coated pores. Figure 2.4H shows that the tCherry translocation times are similar for bare and Nsp1-S-coated pores. We thus find that the Kap95 and tCherry actually translocate mutant-coated pores very well with short translocation times, similar to those for bare pores. The data show that the selectivity of the Nsp1-coated pores is lost when the hydrophobic FG-domains are replaced by the hydrophilic SG-domains.

The event frequency, i.e., the number of translocation events per unit time, can be used as a figure of merit to quantify the selective behavior of Nsp1-coated and Nsp1-S-coated pores. Figure 2.5A compares the event frequency of Kap95 (blue, 100 nM) and tCherry (red, 100nM) for translocations through 48 nm pores. The measured event rate of Kap95 was 1.7 ± 0.2 Hz for a bare pore, 1.4 ± 0.3 Hz for Nsp1-coated pores, and 1.4 ± 0.1 Hz for Nsp1-S-coated pores, i.e., Kap95 thus translocates through all pore types with a similar event rate. Additionally, we performed translocation measurements for varying Kap95 concentration (50-500 nM) through a Nsp1-coated pore, where we observed a constant baseline current at all Kap95 concentrations (SI 13), contrasting to what would have been expected if large numbers of Kap95 would accumulate within the pore.[20,21] Furthemore, we observed , as expected, a linear increase in the event frequency (see SI 13). Notably, in contrast to the finite 1.4 Hz event rate measured for Kap95, tCherry virtually fails to pass through the Nsp1-coated pores with an event frequency as low as 0.02 ±0.04 Hz (at the same 100 nM concentration), while it translocates easily through the bare and Nsp1-S pores, with frequencies of 1.3 ± 0.2 Hz and 1.2 ± 0.3 Hz, respectively. Event frequencies for translocation through Nsp1-S-coated pores were also tested for various pore sizes in the range of 32 nm to 50 nm (Fig. 2.S9 in SI 2.7) for both Kap95 and tCherry. No clear diameter dependence of the selectivity was noted.

2.2.5 Probing the NPC selectivity through MD simulations

To understand the mechanism behind the selectivity of the nanopores, we carried out coarse-grained MD simulations to calculate the energy barrier that the tCherry and Kap95 proteins have to overcome for transport through a 45nm-diameter pore that is lined with Nsp1 or with Nsp1-S. More specifically, we use the umbrella sampling method to calculate the potential of mean force (PMF) at every location along the central transport channel of the 45nm nanopore [37]. The PMF is the effective potential that the tCherry and Kap95 experiences due to the presence of the FG or SG domains, averaged over all conformations of the system. tCherry is simulated by using an inert [38] sphere of radius 7.4 nm (see Table S2.1 in SI 2.2) while for Kap95 we use a sphere of radius 8.5 nm that is covered by 10 hydrophobic binding spots and a total charge of -43e [39] homogeneously distributed on the surface [40].

Figure 2.6 shows the potential of mean force (PMF) for tCherry and Kap95 particles at different z-positions along the central axis (r=0) for the wildtype Nsp1 and mutant Nsp1-S pores. The energy barrier that the particles encounter can be seen as the work required for transport through the transport channel and is defined as the difference between the maximum and minimum value of the PMF curve. In order to obtain the energy barrier, the PMF curves for positive and negative z-values are smoothened with a 6th-order polynomial function and these functions are used for further analysis. The PMF curves and the associated energy barriers can be understood in terms of the molecular interactions between the translocating particle and the FG-nups, which can be categorized into steric repulsion, hydrophobic/hydrophilic interactions, and electrostatic interactions [37,40]. Being an inert particle, tCherry only faces steric repulsion when entering the pore, whereas Kap95 is subjected to a higher steric repulsion (because it has a larger surface area [37]), but this is compensated by additional favorable hydrophobic and weak electrostatic interactions.
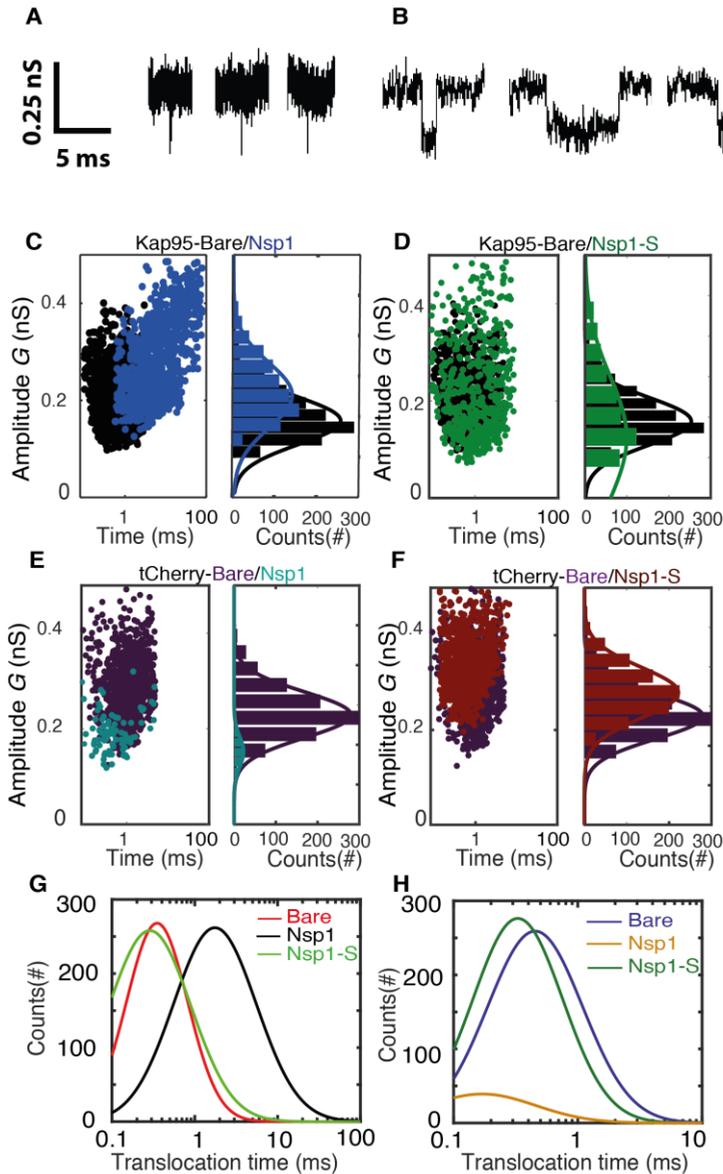
Figure 2.4 Transport and selectivity of the biomimetic NPCs A. Typical translocation event of Kap95 through a bare pore. Each spike signals a single kap95 that translocate the pore. B. Examples of translocation events through the Nsp1-coated pores. Note that the events in panel B show translocation times of a few ms, in contrast to the sub-ms events of panel A. C. Scatter plot comparing the translocation events of Kap95 through a bare pore (black; N=1193) and through Nsp1-coated pores (blue; N=917). The larger dwell time through the Nsp1-coated pore indicates a much slower transport than that through the

bare pore. In C-F, the panels on the right show histograms of the conductance blockade. D. Scatter diagram for Kap95 translocating through mutant Nsp1-S pores (green) (N=505). The conductance blockade histograms show that the average conductance blockade level after Nsp1-S modification is comparable to that of bare pores. E. Scatter plot comparing the translocation events of tCherry through a bare pore (Purple; N=1000) and Nsp1 (Cyan; N=90) coated pores. Note the low number of translocations of tCherry through Nsp1-coated pores. F. Scatter plot comparing the translocation events of tCherry through a bare pore (Purple; N=1000) and Nsp1-S (Red; N=1000)-coated pores. G. Translocation time distribution in lognormal format for translocation of Kap95 through bare, Nsp1-coated, and Nsp1-S-coated pores. H. Same as G, but for tCherry translocations through bare pore, Nsp1-, and Nsp1-S coated pores. Kap95 and tCherry concentrations were 100 nM.

If we focus on the wild-type Nsp1 pores, we see that the energy barrier for tCherry is high, 12 kJ mol^{-1}, i.e. almost 5 k_BT. This is entirely due to the strong steric hindrance that the inert tCherry particle experiences when it aims to pass through the high-density Nsp1 pore (100 mg/ml density, see Fig. 2.2C and 2.3A). In contrast, the PMF curve for Kap95 in the wild-type pore shows a drastically different behavior. Due to the hydrophobic binding sites and negative charge, the Kap95 particle is strongly attracted by the hydrophobic and weakly positively-charged Nsp1 meshwork, resulting in an energy well around $|z| = 30$ nm, which co-localizes with the high concentration of Nsp1 hydrophobic head groups (see Fig. S2.10 in SI 2.9 and Table S2.2 in SI 2.11). In order to complete translocation, the Kap95 has to overcome the energy barrier associated with the well, being equal to 6 kJ/mol^{-1} [41], viz., a strong reduction compared to the steric Nsp1-barrier of tCherry of 12 kJ/mol^{-1}. Such an energy barrier is reminiscent of the entropic barrier reported by Rout et al [15].

In contrast to the big difference between tCherry and Kap95 in the Nsp1 energy landscape, there is almost no difference in the energy barriers for the two particles in Nsp1-S. Both curves show a rising energy profile when entering, with the Kap95 PMF rising stronger than tCherry for $|z| > 20$ nm, due to its bigger size. Around $z = 0$, Kap95 features a sharp drop in the potential of mean force, whereas the PMF for tCherry shows a small peak. This is associated with a higher (hydrophobic) protein density at $z = 0$, resulting in an increased steric repulsion for tCherry and an increased attraction for Kap95. Despite the fact that their specific energy profiles are different, the energy barriers calculated from the PMF curves are similar, 6.5 kJ mol^{-1} and 6.4 kJ mol^{-1} for tCherry and Kap95, respectively. Clearly, from an energetic point of view, the Nsp1-S pore thus is non-selective for the two particles.

In order to characterize the experimental translocation event frequency of tCherry and Kap95, we used an Arrhenius relation. The event frequency Γ can be expressed as

$$\Gamma = \Gamma_0 \exp[-\Delta E / k_B T], \tag{4}$$

in which ΔE is the energy barrier that the translocating particle has to overcome and Γ_0 is a proportionality constant that resembles the event frequency of the bare pore. The computed event rates are compared to the experimental event rates in Fig. 2.5B, showing excellent agreement (for details see Fig. S2.15 in SI 2.12): Kap95 translocates through the nanopore coated with Nsp1 at a rate of 1.5 ± 0.3 Hz, while tCherry features a much lower rate of 0.13 ± 0.03 Hz. In contrast, for the mutated pore, the frequencies are very similar: 1.3 ± 0.3 Hz for Kap95 and at 1.2 ± 0.1 Hz for tCherry. These results show that the permeability barrier of Nsp1-S is compromised, while Nsp1 allows Kap95 but not tCherry, featuring a clear transport selectivity

2.3 Discussion

The NPC central conduit, which controls all transport between nucleus and cytosol, is guarded by a barrier made up of intrinsically disordered Nups with FG-repeats [42]. In this study, we examined the behavior of a minimalistic biomimetic NPC assembly with either Nsp1 or Nsp1-S domains tethered onto the inner surface of a solid-state nanopore. Our results provide the first experimental data for the ion conductance as a function of nanopore diameter (5 to 65 nm) for Nsp1 pores. Nsp1 pores are found to block the conductance stronger than Nsp1-S mutant pores. For small pore sizes the conductance is low (< 4nS), similar but slightly larger than natural NPCs (~1 nS) [34,35]. While these values are in fact remarkably close, the difference is not unexpected since we use only one type of FG-Nup domain, whereas the NPC consists of more than 10 different FG Nups with multiple copies. Beyond a non-linear transition regime at pore sizes of around 40 and 20 nm for Nsp1 and Nsp1-S, respectively, the conductance rises strongly, leading to a near-linear slope at larger pore sizes.
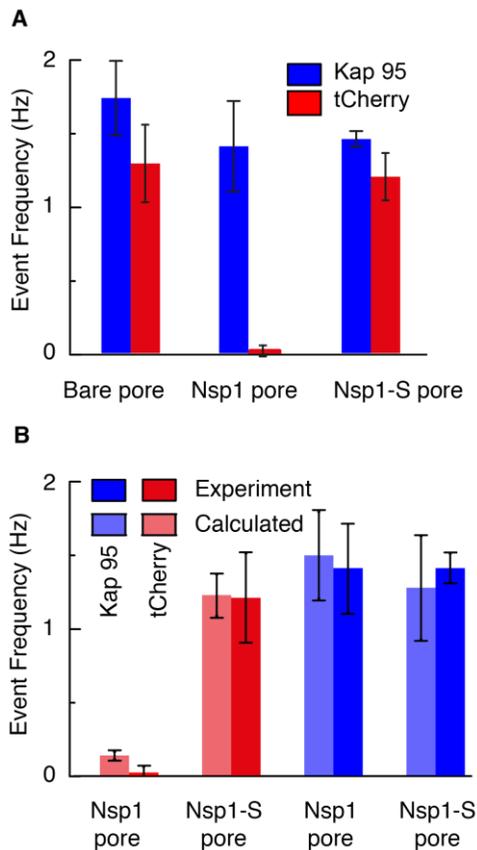
Figure 2.5 Selectivity for Nsp1, but not for Nps1-S biomimetic NPCs. A. Event frequencies for Kap95 (blue) and tCherry (red) through bare pores, Nsp1-coated pores, and Nsp1-S-coated pores. The data show an NPC-like selectivity for Nsp1-coated pores where the passage of tCherry is inhibited whereas Kap95 can pass well through the pore, with an event frequency that is similar to the case of bare pore. Note that the Nsp1-S mutant pores allow both Kap95 and tCherry to pass through with a similar rate. The pore diameter was in all cases 48 ± 2 nm. Kap95 and tCherry concentrations were 100 nM. B. A comparison between experimental event rate and calculated event rate using Eq. 4. The error bar in the calculated event rate is computed based on the error in the energy barrier for the respective particle and pore combination.
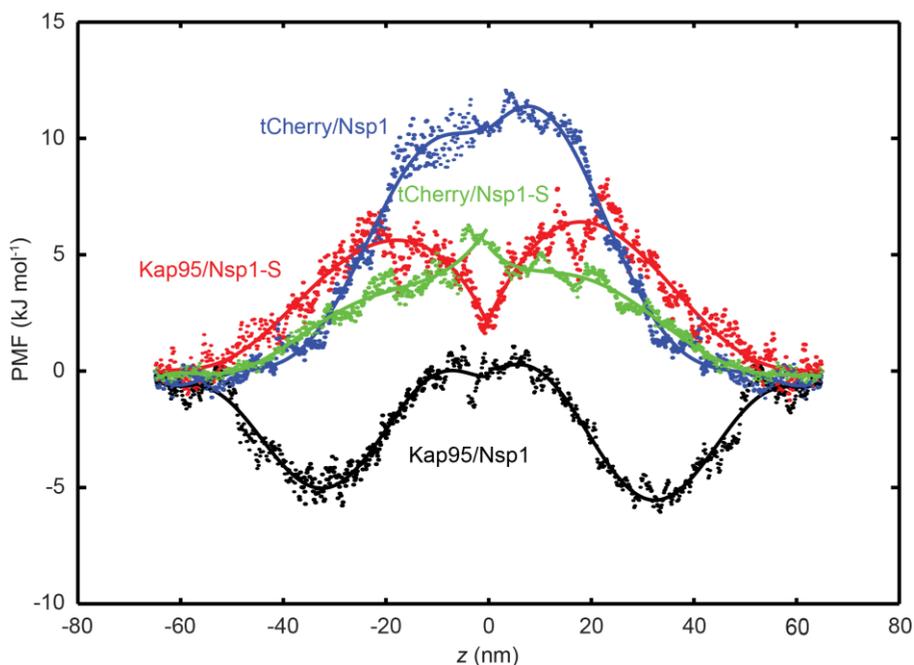
Figure 2.6. Potential of mean force (PMF) curves associated with transport of tCherry and Kap95 through Nsp1 and Nsp1-S coated pores. PMF values for tCherry and Kap95 particles at different positions along the central axis (r=0). Kap95 in the Nsp1 and in Nsp1-S pore is represented in black and red, respectively, and tCherry in Nsp1 and Nsp1-S is shown in blue and green, respectively. Solid lines represent polynomial fits of 6th order for $z < 0$ and $z > 0$. The data show that the energy barrier that tCherry needs to overcome to move across the Nsp1-lined pore is approximately 12 kJ/mol, while for Kap95, it is much lower, 6 kJ/mol. For the Nsp1-S pore however, the barriers are very similar for Kap95 and tCherry, viz., 6.5 kJ/mol and 6.4 kJ/mol, respectively.

To shed light on these experimental findings, we carried out coarse-grained molecular dynamics simulations on nanopores of different sizes. As the model contains the exact amino-acid sequence of the FG domains, it captures the difference in cohesiveness between the mutant and wildtype Nsp1 and predicts their distribution inside the pore. Interestingly, the density in the Nsp1 pores exhibits a maximum at the pore center and remains significantly high throughout (see Fig 2.2C and Fig. 2.3A), even for pore radii that are much larger than two times the Stokes radius of Nsp1 ($2R_S \sim 15$ nm). This can be partly attributed to the cohesive, sticky nature of the low-charge N-terminal 'head' segments of Nsp1 that

are rich in hydrophobic FG-repeats and partly to the geometric confinement of the closely-spaced Nups in the channel (the grafting distance of 5.7 nm is considerably smaller than twice the Stokes radius ($2R_S$ ~15 nm). This is consistent with the work of Zahn et al. [43] who found Nsp1 brush heights of approximately 27 nm for similar grafting densities and with the work of Vovk et al., who found that for surface-tethered FG domains the brush height increases with decreasing grafting distance [44]. The Nsp1-S mutant lacks the large percentage of hydrophobic residues required for cohesive interactions (see Table S2 in SI 11) leading to a remarkably uniform density distribution across the pore area (Fig. 2.3A). The spatial structure of the FG and SG domains in the wildtype and mutant Nsp1 pores shows a striking difference with that of (non-glycosylated) Nup98 pores that exhibit a high-density, donut-like structure that are fully open at the center already at pore diameters of ~25 nm. This is due to the lower geometric confinement (the grafting distance was measured to be approximately equal to $2R_S$=8.2 nm) and the much larger Nup98 cohesiveness. The latter reflects the smaller ratio of charged over hydrophobic residues (0.2 for Nup98 versus 0.9 and 1.6 for Nsp1 and Nsp1-S, respectively), resulting in characteristic protein densities of 344, 74, and 52 mg/ml, respectively (see Table S2 in SI 11).

To link protein density to ionic conductance, we developed a phenomenological relation for the nanopore conductance $G(d)$ which connects the *in-silico* time-averaged protein density distribution $\rho(r)$ to the effective ionic conductivity σ. By adopting a single critical protein concentration, the model successfully predicts the very low conductance at small pore sizes and the non-linear transition to an access-resistance-dominated conductance for larger pores. The conductance of the Nsp1-coated pores was found to be lower than those coated with Nsp1-S, which is a direct consequence of the sequence-dependent difference in spatial FG-domain distribution as discussed above. We also used the density-based conductance relation (Eq. 2) to predict the conductance of the Nup98 nanopores published before [25] (see Fig. S2.13 in SI 2.10). Also in this case the experimental and computational data are in excellent agreement, demonstrating the broad applicability of the $G(d)$ relation for Nup-nanopores that feature profoundly different protein density distributions.

The differences between the Nsp1 and Nsp1-S biomimetic pores testify to the importance of the hydrophobic residues for barrier-formation by FG domains. The formation of hydrogels [19,30] and surface-grafted FG domains [33] similarly showed evidence of the FG motifs' role in establishing the cohesiveness of Nsp1 relative to Nsp1-S. Hexanediols have been shown to disrupt the permeability barrier of either human or yeast NPCs [13,16,24]. Moreover, the FG motifs not only establish a cohesive structure [13,22,30,45], they also assist transport of NTRs through the NPC channel [11,46–49].

To explore the role of Nsp1 cohesiveness in assisting transport, we tested our Nsp1 biomimetic NPCs for the selective permeability for Kap95 and tCherry. We observed that Kap95 translocates well through Nsp1-coated pores, with sizeable (few ms) dwell times, compared to the fast translocation through bare and Nsp1-S-coated pores. Note that the dwell time of ~5 ms is close to the 3 to 10 ms NTR passage times observed through the NPC [50,51], which is remarkable given the simplicity of our biomimetic NPCs. Contrary to Kap95, tCherry did hardly translocate through Nsp1-coated pores, indicating a clear selectivity of these biomimetic NPCs. Kap95 transport through Nsp1 was tested before as a model reporter for selective permeability in a variety of studies [12,24,33]. In a previous report, Nsp1-based artificial NPCs were tested for selective behavior of various NTRs and NTR-cargo complexes which translocated effortlessly whereas the mutant version of NTR (with reduced binding affinity to the FG repeats) transported at a much lower rate [24]. We observed a similar reduction in transport rate for tCherry compared to Kap95 translocations through the Nsp1-coated pores.

The molecular dynamics simulations provide clear mechanistic insight into the permeability and selectivity of the Nsp1 pores. The tCherry is an inert (i.e. non-interacting with FG repeats) particle, subject to steric repulsion from the FG domains and unable to counteract the barrier-forming hydrophobic interactions between the FG domains. Since the protein density in the Nsp1-pores (~100 mg/ml) is significantly higher than that in the Nsp1-S pore (~ 50 mg/ml), the energy barrier is almost two times as high (~12 kJ mol^{-1} versus ~6.5 kJ mol^{-1}), resulting in Arrhenius-converted event rates that differ by an order of magnitude (0.13 and 1.22 Hz, respectively). In contrast to tCherry, Kap95 has hydrophobic binding sites and features a strong attraction to the hydrophobic residues of the Nsp1 FG domains. There is also a weak electrostatic attraction between the strongly negative Kap95 and the weakly positive FG domain. This together lowers the energy barrier from ~12 kJ mol^{-1} for tCherry to ~6 kJ mol^{-1} for Kap95 in the Nsp1 pore, associated with an increase in event rate from 0.13 to 1.50 Hz. We thus find that the Nsp1 pores are clearly selective, repelling inert particles but allowing transport receptors to pass through. The Nsp1-S pore, on the other hand, does not feature such a selective permeability barrier, allowing both tCherry as well as Kap95 to pass through, with event rates of 1.2 and 1.3 Hz, respectively. Clearly, when hydrophobic residues are replaced by hydrophilic residues, the permeability barrier is compromised, and the selectivity vanishes.

To conclude, we have successfully built and modeled minimal NPCs based on solid-state nanopores with yeast Nsp1 and mutant Nsp1-S domains. We demonstrated a clear difference in the conductance characteristics conferred by either Nsp1 or Nsp1-S. Translocation time and event rate analyses showed that Nsp1 is selective for the yeast importer Kap95 over tCherry, while Nsp1-S-coated

pores lack this selective barrier, verifying that cohesive inter FG repeat interactions are required for transport selectivity. Major new biophysics insights into the underlying structural cause of all these experimental observations were obtained from coarse-grained molecular dynamics simulations of the FG Nup density distributions. It was shown that Nsp1 forms a high-density protein distribution with a pronounced maximum at the pore center, in contrast to a uniform and significantly less-dense protein distribution for Nsp1-S. The computed density-dependent conductance and translocation times of Kap95 and tCherry for the Nsp1 and Nsp1-S nanopores were found to be in excellent agreement with the experimental results. Our results identify a sequence-dependent spatial structure of the disordered FG-Nups that affects the **conductance and highlights its key role in establishing the NPC's selective** permeability.

2.4 Materials and methods

Solid-state nanopores

Solid-state nanopores were fabricated on free standing Silicon Nitride (SiN) membrane deposited on Silicon wafer as mentioned elsewhere in detail [52]. In brief, nanopore chips are built-up on a silicon wafer (100) with supporting deposited layers of Silicon dioxide and low-stress SiN. By employing UV-lithography, chemical etching and reactive-ion etching, the layers were etched away to end up with ~10μm window of freestanding silicon nitride of 20 nm thickness. In this layer, a nanopore was drilled by electron beam using Transmission Electron Microscopy (TEM) operated at 300 kV. The focused electron beam was used to control the diameter of pore with a nanometer precision. After drilling with TEM, the pores were stored in a solution containing 50% (v/v) ethanol in Milli-Q water until usage. In our current work, we used pore diameter from 5 to 65 nm. Prior to measurement, each pores were painted with a layer of polydimethylsiloxane (PDMS) and baked for 2 hours at 70 °C. PDMS layer reduce capacitive noise and offer better signal-to-noise properties [53]. Nanopore chips were mounted on a custom made poly(methyl methacrylate) (PMMA) flow cell, after which the flow cell was filled with 150 mM KCl, 10 mM Tris- EDTA (1 mM) buffer at pH 7.6. The current was recorded with a electrophysiology patch clamp setup Axopatch 200B amplifier with a digitizer Digidata 1322A DAQ. We probe the transport electrically by monitoring the translocation of single proteins through 50 nm pores with a conductance of $G = 10\text{-}16$ nS. The concentration of Kap95 and tCherry used in translocation experiments was 100 nM unless stated otherwise. Note that measurements on nanopores with a diameter below the

threshold are difficult due to a low signal-to-noise ratio at physiological salt conditions. The data was analyzed in a custom Transalyzer package in MatLab [36].

Chemical modification of solid-state nanopore

The surface chemistry used to attach Nsp1 and Nsp1-S to the nanopore surface is shown in SI 1. The nanopore chip was rinsed with water and Ethanol and treated with oxygen plasma for 60 s. The process cleans the surface from organic contaminants and makes the surface hydrophilic. The membranes were then (step 1) incubated with a 1% solution of APTES (3-aminopropyl-triethoxysilane) (Sigma) in pure methanol for 1 h, followed by rinsing for 15 min in pure methanol. The chip was blow-dried under N_2 and baked at 100 °C for 60 min in order to fix the silane monolayer [54]. The exposed amines were cross-linked with sulfo-SMCC (sulphosuccinimidyl-4-(N-maleimidomethyl)-cyclohexane-1-carboxylate) (2 mg no-weight capsules (Pierce)). Sulfo-SMCC has an amine-reactive NHS-ester and a maleimide group. A capsule of Sulfo-SMCC was dissolved in 1.5 ml PBS at pH 7.4 and nanopores were incubated in sulfo-SMCC solution overnight. The nanopores were rinsed with PBS to wash-off free sulfo-SMCC. The Nsp1 WT and mutant were stored in 7.3M guanidinium HCl and buffer exchanged to PBS, pH 7.4 and both the Nsp1 and Nsp1-S-mutants were treated with 1mM TCEP for 30 mins to reactivate the SH-groups. The nanopores with maleimide were incubated with 120nM Nsp1 and Nsp1-S for 1 hr. The C-terminal cysteine covalently bonds with the maleimide group to form a self-assembled layer of Nsp1 or Nsp1-S-mutant on the nanopore surface. The proteins Nsp1, Nsp1-S, Kap95, and tCherry were purified by the methods described previously; for further details the reader is referred to ref [12,30].

Coarse-grained molecular dynamics simulations

The one-bead-per-amino-acid MD model used here accounts for the exact amino-acid sequence of the FG-nups, with each bead centered at the C_α positions of the polypeptide chain [27,28]. The average mass of the beads is 120 Da. Each bond is represented by a stiff harmonic spring potential with a bond length of 0.38 nm. The bending and torsion potentials for this model were extracted from the Ramachandran data of the coiled regions of protein structures [27]. Solvent molecules are not accounted for explicitly; we account for the solvent polarity and screening effect of ions through a modified Coulomb law. Solvent polarity is incorporated through a distance-dependent dielectric constant, and ionic screening is accounted for through Debye screening with a screening constant k = 1.27 nm^{-1} corresponding to a 150mM KCl solution. The hydrophobic interactions

among the amino-acids are incorporated through a modified Lennard-Jones potential accounting for hydrophobicity scales of all 20 amino-acids through normalized experimental partition energy data renormalized in a range of 0 to 1. For details of the method and its parametrization, the reader is referred to ref. [28]

MD simulations for the nanopores with diameters ranging from 22-60 nm were carried out using GROMACS 4.5.1. First, the systems were energy minimized to remove any overlap of the amino acid beads. Then all long-range forces were gradually switched on. The simulations were carried out for over 5×10^7 steps (with the first 5×10^6 steps ignored for extracting the end-result data), which was found to be long enough to have converged results in the density distribution inside the pores.

The time-average density calculations presented in the main text and supporting information (see SI 9 and SI 10) were carried out by centering the nanopore in a 100 nm x 100 nm x 140 nm box, which was divided into discrete cells of volume $(0.5 \text{ nm})^3$ and the number density in each cell was recorded as a function of simulation time. Finally, the number density was averaged over the simulation time and multiplied with the mass of each bead to get the time-averaged 3D density profile. The 3D density was averaged in the circumferential direction to obtain two-dimensional (2D) (r, z) density plots (as shown in Fig. 2.2C). Finally, the radial density distribution $\rho(r)$ was obtained by averaging these 2D density maps in the vertical direction (as shown in Fig. 2.3A).

To estimate the energy barrier for translocation of transport factors through the biomimetic NPC, we calculate potential–of-mean-force (PMF) curves along the transport channel of the nanopores using the umbrella sampling method [37]. In the current study, the cargo molecule is fixed at regularly spaced positions along the reaction coordinate (the central axis) of the pore by means of a harmonic spring. The spacing between the axial positions is chosen to be 1.3 nm and the spring constant is set to 10 kJ/nm^2/mole. For each position, 2 different starting configurations of the proteins are used to obtain statistically meaningful results. CG molecular dynamics simulations were performed for each particle position and the spring extension was recorded. The obtained distance histograms were used to calculate the PMF curves through a weighted histogram analysis. For further details on the umbrella sampling method, the reader is referred to ref. [37]

2.5 Supporting Information

SI 2.1. Surface chemistry for protein attachment to nanopore surface, and amino acid sequences of Nsp1 and Nsp1-S
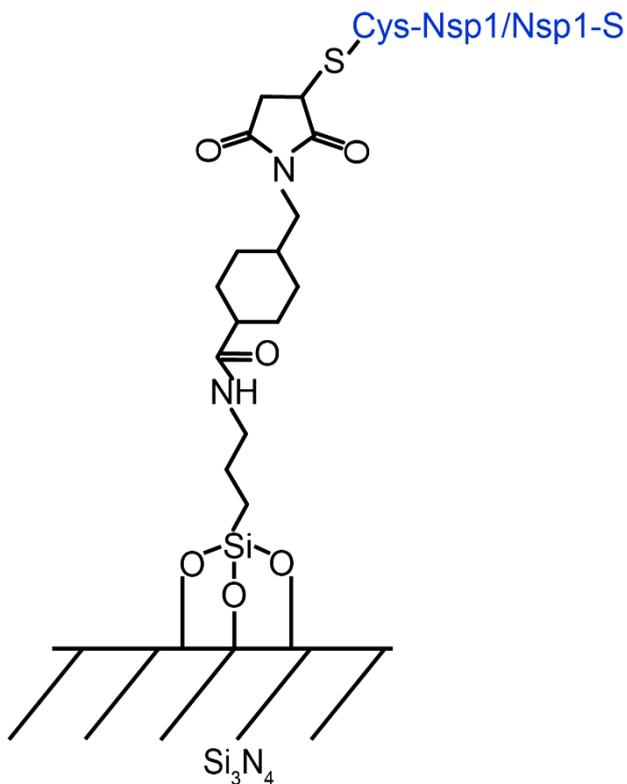
Figure S2.1: Self-assembled monolayer surface chemistry for covalently attaching Nsp1 and Nsp1-S to Silicon Nitride membrane. APTES layer was used as a primary monolayer through silanization. Next, NHS-ester with a maleimide reactive group (Sulfo-SMCC) was coupled to the APTES monolayer. Exposed maleimide functions as a binding group to C-terminal cysteine.

The exact amino-acid sequence of Nsp1 and Nsp1-S:

MSKHHHHSGHHHTGHHHHSGSHHHTGENLYFQGSNFNTPQQNKTPFSFGTANNNSNTTNQNSSTGAGAF
GTGQSTFGFNNSAPNNTNNANSSITPAFGSNNTGNTAFGNSNPTSNVFGSNNSTTNTFGSNSAGTSLFGSSS
AQQTKSNGTAGGNTFGSSSLFNNSTNSNTTKPAFGGLNFGGGNNTTPSSTGNANTSNNLFGATANANKPAF
SFGATTNDDKKTEPDKPAFSFNSSVGNKTDAQAPTTGFSFGSQLGGNKTVNEAAKPSLSFGSGSAGANPAGA
SQPEPTTNEPAKPALSFGTATSDNKTTNTTPSFSFGAKSDENKAGATSKPAFSFGAKPEEKKDDNSSKPAFSFG
AKSNEDKQDGTAKPAFSFGAKPAEKNNNETSKPAFSFGAKSDEKKDGDASKPAFSFGAKPDENKASATSKPA
FSFGAKPEEKKDDNSSKPAFSFGAKSNEDKQDGTAKPAFSFGAKPAEKNNNETSKPAFSFGAKSDEKKDGDA
SKPAFSFGAKSDEKKDSDSSKPAFSFGTKSNEKKDSGSSKPAFSFGAKPDEKKNDEVSKPAFSFGAKANEKKES
DESKSAFSFGSKPTGKEEGDGAKAAISFGAKPEEQKSSDTSKPAFTFGAQKDNEKKTETSC

MSKHHHHSGHHHTGHHHHSGSHHHTGENLYFQGSNSNTPQQNKTPSSSGTANNNSNTTNQNSSTGAGAS
GTGQSTSGSNNSAPNNTNNANSSSTPASGSNNTGNTASGNSNPTSNSSGSNNSTTNTSGSNSAGTSSSGSSS
AQQTKSNGTAGGNTSGSSSSSNNSTNSNTTKPASGGSNSGGGNNTTPSSTGNANTSNNSSGATANANKPAS
SSGATTNDDKKTEPDKPASSSNSSSGNKTDAQAPTTGSSSGSQSGGNKTSNEAAKPSSSSGSGSAGANPAGA
SQPEPTTNEPAKPASSSGTATSDNKTTNTTPSSSSGAKSDENKAGATSKPASSSGAKPEEKKDDNSSKPASSSG
AKSNEDKQDGTAKPASSSGAKPAEKNNNETSKPASSSGAKSDEKKDGDASKPASSSGAKPDENKASATSKPA
SSSGAKPEEKKDDNSSKPASSSGAKSNEDKQDGTAKPASSSGAKPAEKNNNETSKPASSSGAKSDEKKDGDA
SKPASSSGAKSDEKKDSDSSKPASSSGTKSNEKKDSGSSKPASSSGAKPDEKKNDESSKPASSSGAKANEKKES
DESKSASSSGSKPTGKEEGDGAKAASSSGAKPEEQKSSDTSKPASTSGAQKDNEKKTESTSC

SI 2.2. Dynamic light scattering (DLS) measurement of hydrodynamic diameter

DLS measurements are performed in 70µl standard cuvettes from Brand GMBH® with a light path of 10mm. Both Nsp1 (1µM) and Nsp1-S (1µM) were treated with 5 mM dithiothreitol (DTT) for 30 minutes at room temperature to reduce cystine and to prevent formation of dimers. 1µM of Kap95 or tCherry, treated with 1mM of TCEP in PBS at pH 7.4 for 30 minutes was used for DLS measurement. All the samples were measured in buffer containing 150 mM KCl, 10 mM Tris, and 1mM EDTA at pH 7.6. For the measurements, a Zetasizer Nano ZS (Malvern) was used at room temperature. DLS recordings (Table S2.1) were repeated at least three times for each protein and the result reported is the average over these recordings where errors represent the standard deviation. Dynamic light scattering experiments were also performed under denatured conditions (6M Guanidinium hydrochloride) for both Nsp1 and Nsp1-S yielding hydrodynamic diameters of 19.2 ± 5.3 nm and 19.4 ± 6.6 nm respectively.

Protein	Hydrodynamic Diameter (nm)
kap95	8.5 ± 0.8
tCherry	7.4 ± 1.4
Nsp1	14.6 ± 2.1
Nsp1-S	13.5 ± 3.1

Table S2.1. Measured hydrodynamic diameters (nm) of proteins from dynamic light scattering (DLS) experiment.

SI 2.3. Transmission electron microscopy images of coated nanopores

A

B

C

D
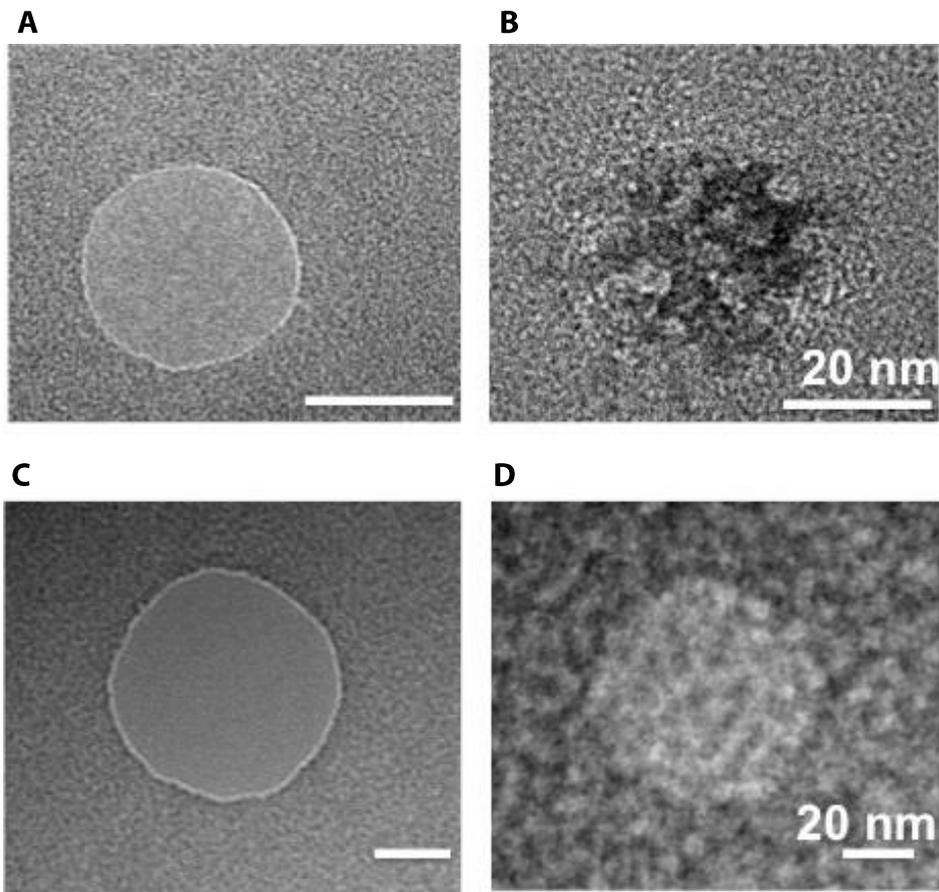
Figure S2.2: Transmission electron microscopy (TEM) images of bare pore and Nsp1 coated pores. A, B are the 30 nm pores and C,D are 50 nm pore before and after Nsp1 coating respectively. From the contrast, we can observe the presence of Nsp1 in both B and D. These TEM images e show a higher density of Nsp1 in the 30 nm nanopores, which is in agreement with the conductance measurement with nanopore. As these TEM were obtained by drying the samples, the actual structural information of Nsp1 might be hard to confirm. This is still an important piece of information as it corroborates the connection between the conductance measured and the material present in the pores.

SI2. 4. Grafting density estimates of Nsp1 and Nsp1-S

We estimated the grafting density of the FG-Nups on the surface, and its importance for our results, in different ways:

SI2.4-1: Estimate of the surface grafting density of the FG-Nups based on conductance

The idea of this approach is that one can estimate the number of, say, Nsp1 proteins that coat the pore from the drop in the conductance upon coating the pore, using the, independently measured, conductance blockade that is caused by a single protein as a reference. To pursue such an estimate, we translocated individual Nsp1 proteins through a bare pore (49 nm diameter) to estimate the ion blockade caused by a single Nsp1. The average conductance blockade of Nsp1 was found to be 0.54 ± 0.15 nS (cf. Fig. S2.3A) with corresponding translocation times in the range of 0.1-5 ms. The average conductance blockade can be used to estimate the number of Nsp1 proteins that are blocking the ion flow through a nanopore of e.g. 48 nm size where the conductance dropped from 70 nS to 12 nS. This yields an estimate of 107 ± 32 for the number of Nsp1 proteins for this 48 nm pore. Assuming that a cylindrical pore volume of $\pi * (24nm)^2 * 20\,nm$ confined these proteins, this line of reasoning provides a grafting density of about 1 Nsp1 per 28 ± 8 nm² (107 Nsp1 proteins per pore surface area of $2\pi * 24 * nm * 20\,nm$), resulting in a grafting distance of 5.7 ± 0.8 nm (assuming a close-packed triangular lattice).
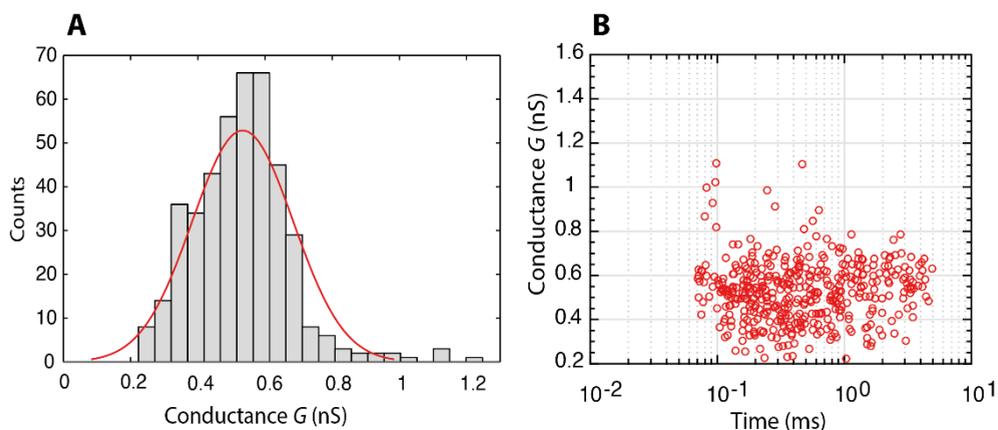
Figure S2.3: Histogram of the conductance of individual Nsp1 molecules translocating through a bare pore, and the associated scatter plot of conductance versus translocation time.

These numbers yield an estimated Nsp1 density of about 320 mg/ml (107 Nsp1 proteins, each with a molecular weight of 65.7 kDa, in the cylindrical pore volume of $\pi * (24nm)^2 * 20\,nm$). It is important to realize that this number is only a rough estimate based on a simplified geometry. For example, our MD simulations **show that the Nps1 proteins 'spill out' out of the** cylindrical nanopores such that an additional layer of Nsp1 is present above and below the nanopores, thus lowering the protein density in the cylindrical pore. Furthermore, the estimate neglects any intrinsic heterogeneities such as differences between the N-terminal part and C-terminal part of Nsp1. More accurate estimates for the Nsp1 density are provided by the MD simulations, see elsewhere in the paper.
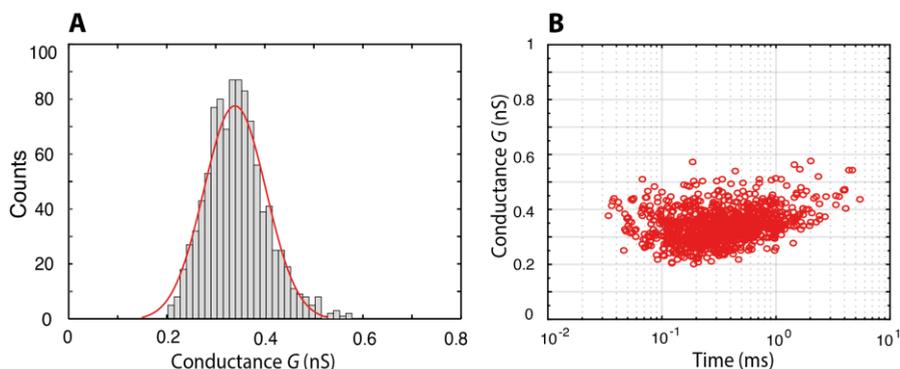
Figure S2.4: Histogram of the conductance of individual Nsp1-S molecules translocating through a bare pore, and the associated scatter plot of conductance versus translocation time.

Similarly, in independent experiments, individual Nsp1-S proteins were translocated through a bare pore (49 nm) to estimate the conductance blockade by single Nsp1-S proteins. The average conductance blockade of Nsp1-S was found to be 0.34 ± 0.09 nS (cf. Fig. S2.4A). From the average conductance blockade, we again estimate the number of Nsp1-S proteins that were blocking the ion flow through a 50 nm nanopore where the conductance dropped from 70.3 nS to 34.6 nS. This yields an estimate of 105 ± 30 for the number of Nsp1-S proteins for a 50 nm pore. Assuming that a cylindrical pore volume of $\pi * (25 * nm)^2 * 20\,nm$ confined these proteins, yields a surface coverage of about 1 Nsp1-S per 30 ± 8 nm^2 and a grafting distance of 5.9 ± 0.8 nm (assuming a close-packed triangular lattice).

SI2.4-2: Estimate of the surface grafting density of the FG-Nups based on QCM-D surface coating experiments

An independent estimate of the grafting density can be obtained using QCM-D, a method that measures the accumulated mass upon coating a surface. The binding of FG-Nups through its C-terminal cysteine group to maleimide (Suflo-SMCC) on the surface was monitored versus time using QCM-D (QSense –QE401, Biolin Scientific AB, Sweden). The QCM-D shift upon exposure of Nsp1 (1 µM) or Nsp1-S (1 µM) to the functionalized silicon nitride surface is shown in Fig. S2.5. QCM-D measures the shift in resonance frequency Δf and the dissipation ΔD of the crystal due to the increased mass. The frequency shift was recorded for more than 5000 s, and no change in the frequency was observed upon flushing PBS to wash away any unbound proteins (flow rates 20 µl/min). The frequency shifts, Δf = -60 ± 5 Hz (N=3) for Nsp1 and Δf =-56 ± 15 Hz (N=3) for Nsp1-S, are, within errors, equal to each other. Ignoring dissipation, we can use the Sauerbrey relation Δm = - (C*p* Δf) [where p=3 is the crystal overtone, C = 17.7e-9 kg s/m^2 at f = 5 MHz is the Sauerbrey constant, and Δm is the areal mass (kg/m^2) that is added due to the protein coverage] to estimate the surface grafting distance as 5.6 ± 0.2 nm for Nsp1 and 5.8 ± 0.9 nm for Nsp1-S. The finite dissipation indicates some viscoelastic behavior in the adsorbed layers, and hence the mass will not couple 100% to the oscillatory motion of the sensor. Accordingly, the mass will be somewhat underestimated by the above calculation, which would make the numbers for the grafting densities slightly larger. Overall, however, we conclude that the surface coverage of Nsp1 and Nsp1-S is very similar, as well as close to the estimates obtained from the conductance experiments (SI4-1).
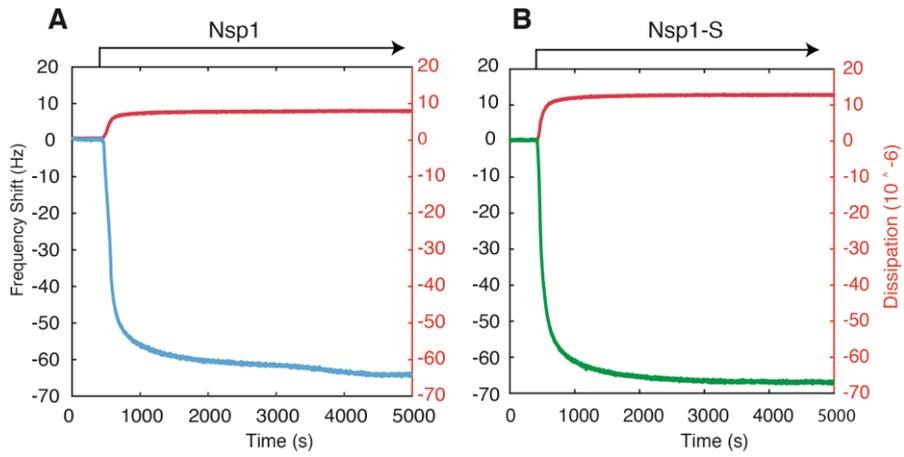
Figure S2.5: Example QCM-D traces for surface functionalization of Nsp1 (A) and Nsp1-S (B) on silicon nitride coated with APTES and Sulfo-SMCC.

SI 2.4-3: Estimate of the importance of the grafting density of the FG-Nups from MD simulations

The translocation analysis and the QCM-D measurements show that the grafting density for Nsp1 and Nsp1-S are almost the same. We adopted an average value of 5.7 nm for the grafting distance for the MD simulations for both Nsp1 and Nsp1-S pores. We performed a sensitivity analysis for Nsp1-S, to probe how sensitive our results depend on the grafting density. Fig. S2.6 depicts the density profiles of a 45 nm pore for grafting spacings 5.7 and 5.9 nm, showing that the density inside the pore only changes marginally. Using the density-based conductance relation (Eqn. 2) a conductance of 29.1± 2.7 nS and 30.6± 2.8 nS results for the grafting distances of 5.7 nm and 5.9 nm, respectively, showing that also the effect on the conductance data is negligible.
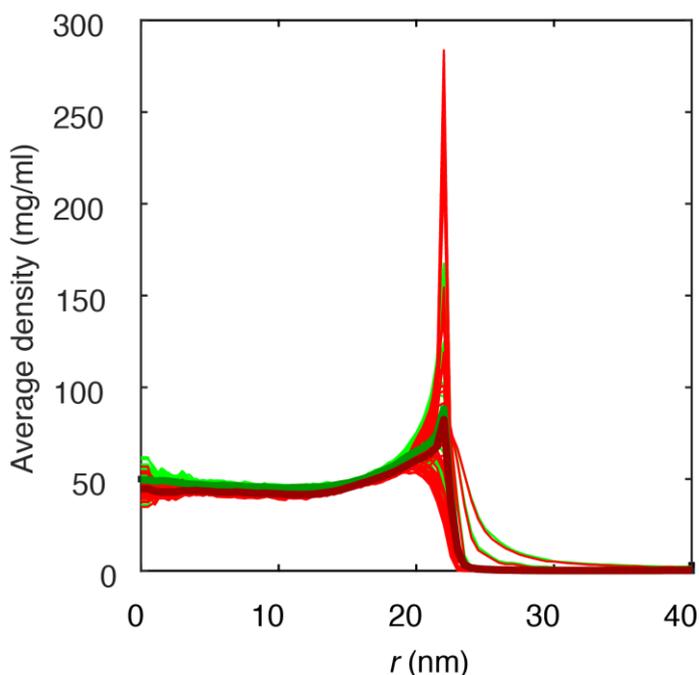
Figure S2.6: Average protein densities of a Nsp1-S coated solid-state nanopore of diameter 45 nm with grafting distance 5.7 nm (green) and 5.9 nm (red).

SI 2.5. Conductance blockade of Nsp1 coated pores below the threshold diameter
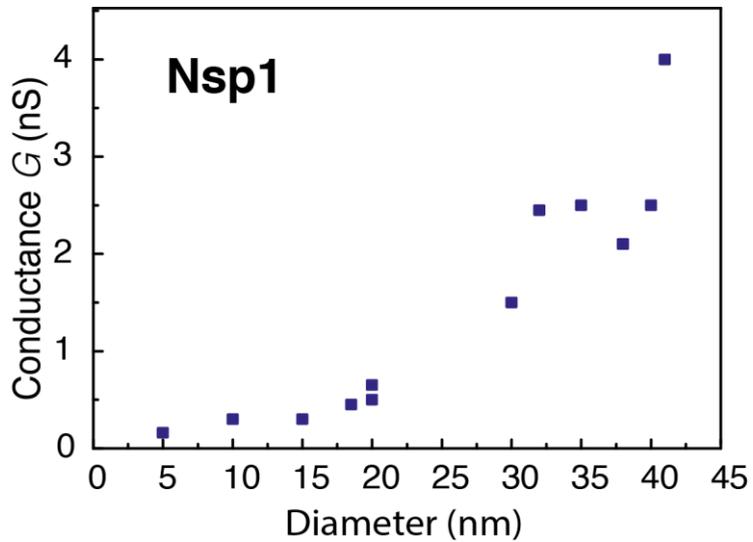
Figure S2.7: Conductance as a function of pore diameter below 40 nm. The conductance change versus the diameter of Nsp1 coated pores is plotted. The measured conductance of the NPC falls in the range of 0.3-2 nS for monovalent salt, which is comparable to the values measured here (0.2 – 4 nS) for pore sizes in the range from 5 to 40 nm (Bustamante, Hanover and Liepins, 1995; Tonini *et al.*, 1999).

SI 2.6. Power spectrum density (PSD) comparison of bare pore with Nsp1 and Nsp1-S coated pores
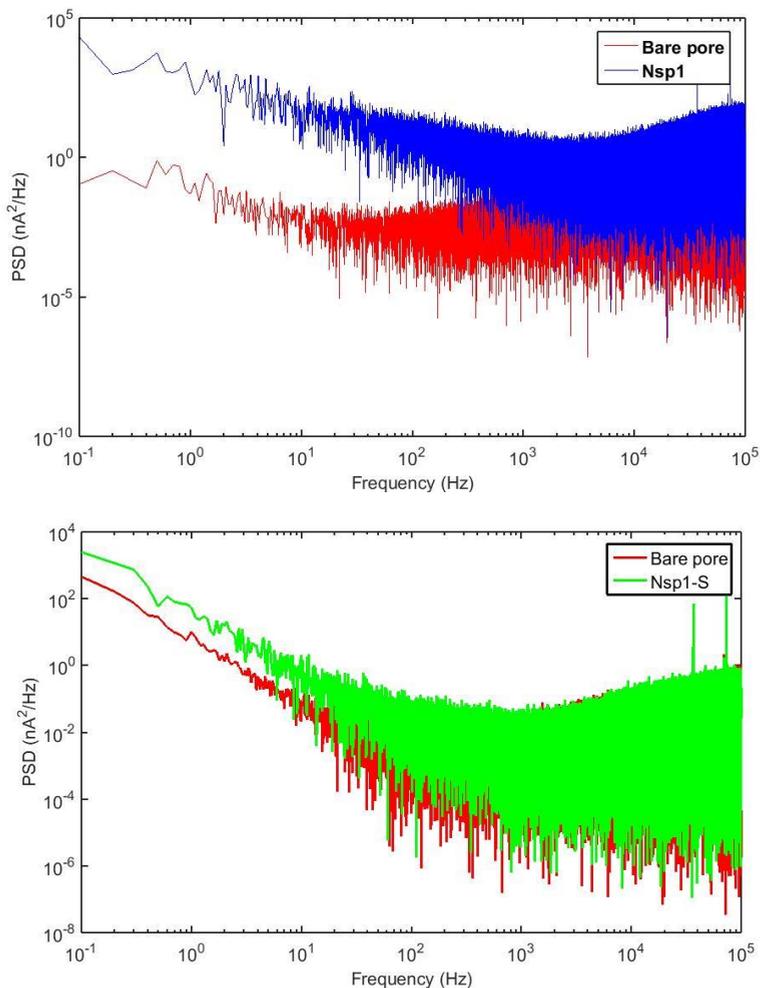
Figure S2.8: Power spectrum density of a bare pore and nanopores coated with Nsp1 and Nsp1-S are plotted. From the spectrum of the nsp1 pore it is evident that the noise in 1/f increases drastically compared to the bare pore (Smeets *et al.*, 2008). This is a clear indication of the fluctuations of Nsp1. A similar trend is observed for Nsp1-S coated pores.

SI 2.7. Event frequency of kap95 and tCherry translocation events in Nsp1-S modified nanopores

The Kap95 and tCherry were both translocated through the Nsp1-S coated pores similar to the data in figure 2.5A in the main text. The observed event frequencies were plotted below as a function of nanopore diameter (nm). Measured event frequencies for both Kap95 (blue) and tCherry (red) versus diameter for pores coated with Nsp1-S mutant Nups. A black cross is shown when no translocation events could be measured (e.g. because the nanopore clogged upon addition of Kap95 or tCherry). No clear differences in selectivity are observed between the smaller and larger pores.
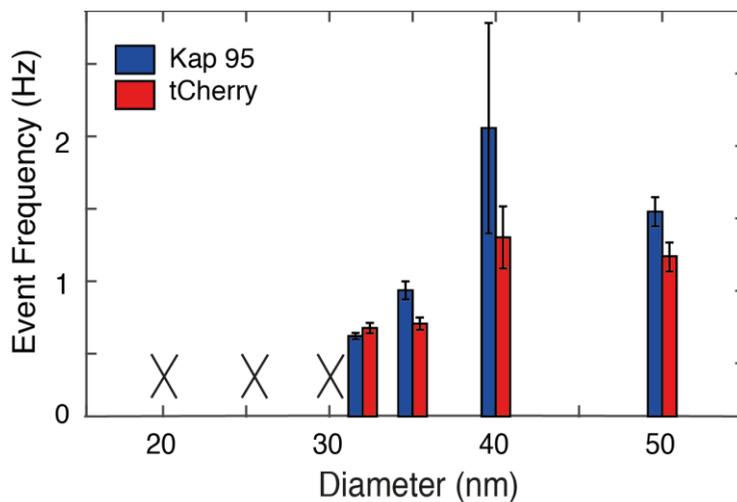
Figure S2.9: Event frequency versus diameter for Kap95 and tCherry through Nsp1-S coated nanopores. The event frequencies are averaged over different pores (n=3). The error bars indicate standard deviations.

SI 2.8. Coating the nanopores in the presence of Guanidine hydrochloride (3M).

As a further confirmation that the grafting density of Nsp1 and Nsp1-S are similar, we coated the nanopores (~50 nm) with proteins in the presence of 3M Guanidine hydrochloride. Under these conditions both Nsp1 and Nsp1-S will be in the denatured state and one does not expect any FG-FG interaction to be relevant for Nsp1. The pores were washed with PBS and the ionic conductance with measurement buffer. The bare pore conductance dropped from 78 nS to 16 nS after coating with Nsp1, which is about 80% conductance blockade. Interestingly, this is a similar conductance blockade observed in our measurements obtained in the normal assembly protocol. For the case of Nsp1-S, the bare pore conductance dropped from 82 nS to 45 nS, i.e. a conductance blocked of about 45% - again similar. These measurements confirm that the grafting of Nsp1 and Nsp1-S in the presence of 3M Guanidine hydrochloride was not different compared to coating in PBS (see materials and methods.

SI 2.9. Localization of the Nsp1 and Nsp1-S heads in the nanopores
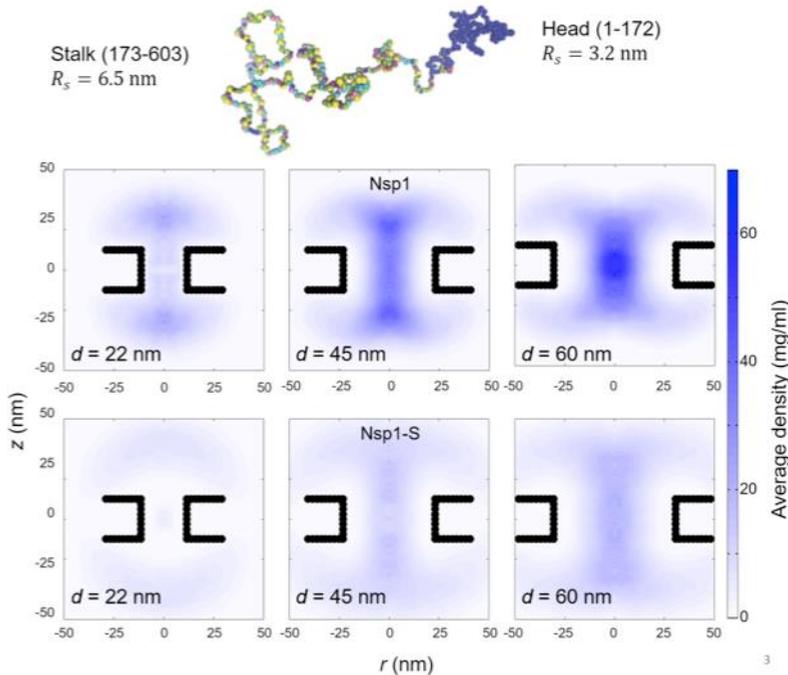
Figure S2.10: **Top: The configuration of Nsp1 consists of a 'collapsed coil' head (in blue) and a 'extended coil' stalk region (multi**-colored; each color represents a different amino acid). Bottom: Two-dimensional *r-z* density distribution of the mass density of the head-region (1-172) of Nsp1, for nanopores with diameters 22 nm, 45 nm and 60 nm (first row). The second row shows the same pores but coated with the Nsp1-S mutant. These data show the much more center-pore localized mass density for the wildtype Nsp1 compared to the Nsp1 mutant.

The Stokes radii (R_s) of the head and stalk region are 3.2 nm and 6.5 nm, respectively, as computed by us (Ghavami *et al.*, 2014) and measured by Yamada and coworkers (Yamada *et al.*, 2010). To investigate the role of these two segments in establishing the high-density structure, we plot the density distribution of only those amino-acids that are part of the N-terminal head region in Fig. S2.10. For the mutant we see a more wide-spread distribution, whereas for Nsp1 the heads are rather localized, forming a cohesive structure around the central pore axis for the largest pore sizes (for the smaller pore size of 22 nm the geometric confinement is so large that the Nsp1 heads are pushed out from the core of the pore). It is interesting to note that the radii of gyration of the head and stalk region in isolation are similar as when they are part of one Nsp1 molecule. However, the radius of gyration of Nsp1 is less than the sum of the radius of gyration of the head

and tail, indicating that the head and tail do interact but retain their individual conformation (see SI Movie 3), even when tethered together (see SI Movie 1). This also carries over to their conformation inside the pore, albeit with one difference: the radius of gyration of the stalk region is enlarged by 30%, whereas the radius of gyration of the head again remains unchanged. This is most likely caused by the stronger lateral constraints of the stalks at the anchor points (C-terminal), while the N-terminal heads have more freedom.

SI 10. Modified conductance relation: details
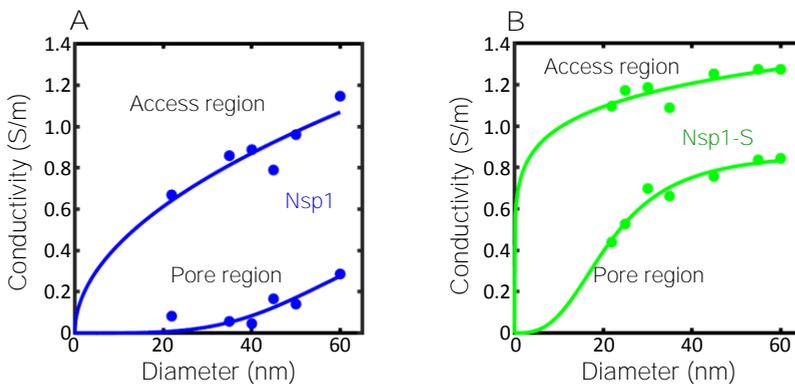
Figure S11: The conductivity in the pore region (σ_{pore}) and access region (σ_{access}) for the simulated nanopores lined with Nsp1 (blue circles; panel A) and Nsp1-S (green circles; panel B) plotted as a function of pore diameter. For σ_{pore} the density distribution is integrated over the pore region $|z| < 10$ nm according to Eq. 3 in the main text. For the conductivity in the access region σ_{access} the density distribution in the range 10 nm < $|z|$ < 40 nm is considered, as the l/d ratio for the nanopore is comparable to 1.5 (Hyun, Rollings and Li, 2012). These serve as input to the conductance relation $G(d)$ in Eq. 2 of the main text. The solid lines are sigmoidal fits to the data. The sigmoid function is of the form $S(x) = d + ((-d)/(1 + (x/c)^b))$. The R² values of σ_{pore} and σ_{access} are 0.85, 0.96 in Nsp1 and 0.98, 0.99 for Nsp1-S.

Hyun and coworkers probed the size of the access region and showed that for nanopores with a similar l/d ratio (1.5) as used here, the access resistance is only affected in a region closer than 40 nm from the center of the pore (Hyun, Rollings and Li, 2012). For smaller values of l/d, the size of the access region was found to decrease. Therefore, we define the access region to extend from 10 nm < $|z|$ < 40 nm, and we use this range to calculated the density distribution as a function of r. We performed a sensitivity analysis for the size of the access region and observed

that by decreasing the size with a factor as large as 3, the maximal change in all computed conductance values was only found to be 13%, showing that the results are not sensitive to changes in the size of the access region.
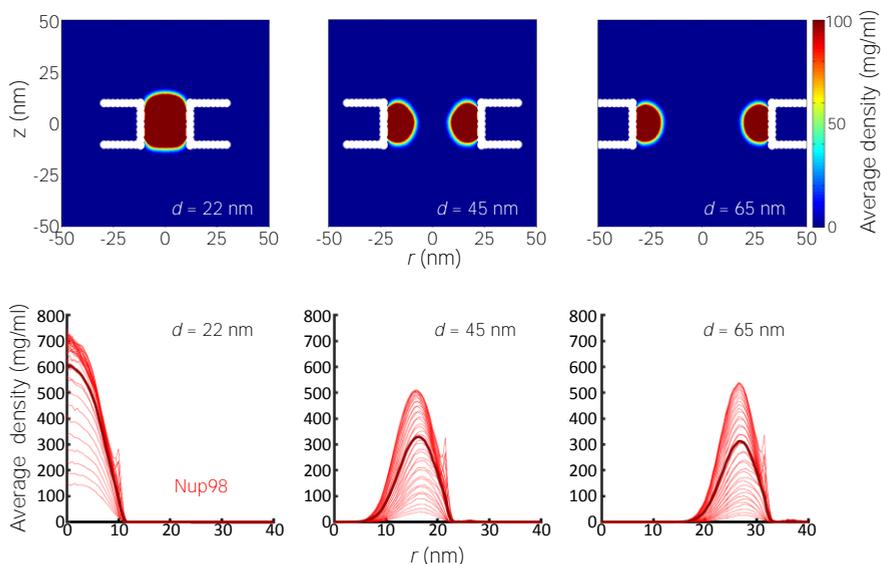
Figure S2.12: Simulation results for the density distribution in Nup98-coated biomimetic pores. Top panel: Two-dimensional r-z density distribution of Nup98-coated pores with diameters 22 nm, 45 nm, and 65 nm. Bottom panel: the corresponding radial density distributions. All data are taken within the height of the cylinder (20 nm; -10 nm $< z <$ 10 nm) that is divided into 20 equally spaced discs of thickness 1 nm each. Each of the 20 curves represented in each panel shows the radial density distribution for that specific z location.
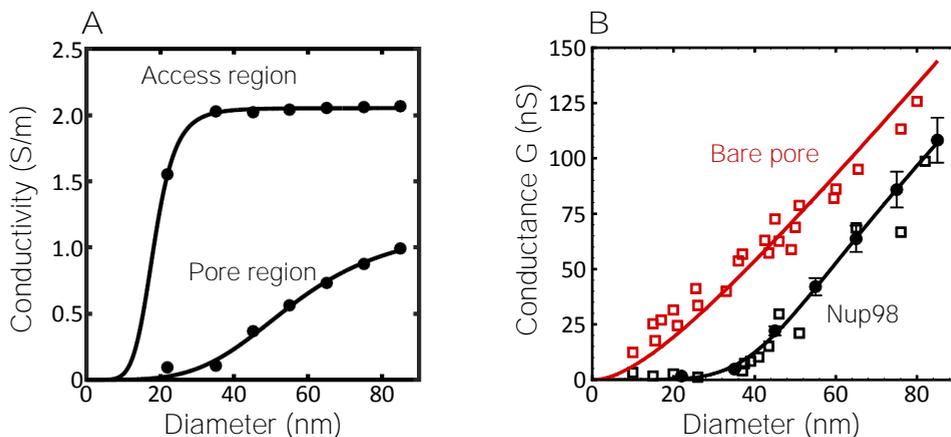
Figure S2.13: A. Based on the radial density distributions $\rho(r)$ of the Nup98 pore (Fig. S2.12, bottom row), we calculated the pore conductivities σ_{pore} and σ_{access} (black circles) for each diameter using Eq. 3 of the main text, with ρ_{crit}=85 mg/ml as fitted to the Nsp1 and Nsp1-S data. For the access region the density distribution in the range 10 nm < |z| < 40 nm is considered, as the l/d ratio for the nanopore is comparable to 1.5 (Hyun, Rollings and Li, 2012). The solid lines are sigmoidal fits to the data. The sigmoid function is of the form $S(x) = d + ((-d)/(1 + (x/c)^b))$. The R^2 values of σ_{pore} and σ_{access} are both equal to 0.99. B. The conductance G of the Nup98-coated pores (black) and bare pores (red) plotted as a function of the pore diameter. The open squares represent experimental data (Kowalczyk *et al.*, 2011), while the closed circles represent the results of the MD simulations. The solid lines are predictions of the conductance relation that describes the conductance G as a function of diameter d for the bare pore (red, see Eq. 1 in the main text with l = 20 nm), resulting in a fitted value of σ_{bare} = 2.13 ± 0.05 nS/nm (with an R^2 value of 0.93). The conductivity results from panel A (σ_{pore} and σ_{access}) are taken as input for the conductance relation of Eq. 2 resulting in the solid black line for the Nup98-coated pores in panel B, showing excellent agreement with the experiments (R^2=0.93).
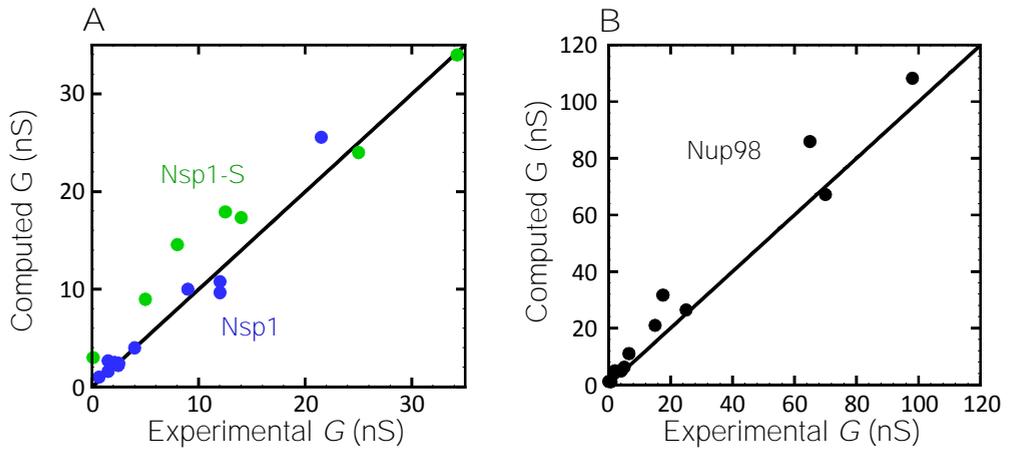
Figure S2.14: Computed conductance vs the experimentally measured conductance, for A: Nsp1 (blue circles) and Nsp1-S (green circles), and B: Nup98 (black circles). The solid lines have a slope of 1, representing a perfect match between experiment and model.

SI 2.11. Molecular characteristics of the FG-Nups

	Nsp1	Nsp1-S	Nup98	Nsp1-head (AA 1-172)	Nsp1-tail (AA 173-637)
#aminoacid (AA)	637	638	498	172	465
#charged AA (pos/neg)	135	135	25	5	130
#hydrophobic AA (F,I,L,V)	72	2	90	19	53
#hydrophobic AA (F,I,L,V,W,Y,A)	146	76	130	30	116
Stokes radius R_S in nm (stand. dev.)	7.4 (0.6)	8.4 (0.6)	4.1 (0.3)	3.2 (0.2)	6.5 (0.5)
Mass in Da	76440	76560	59760	20640	55800
Stokes volume, $4\pi R_S^3/3$ in ml	1.72E-18	2.44E-18	2.88E-19	1.37E-19	1.15E-18
Protein density: mass per Stokes volume in mg/ml	73.9	52.1	344	250	80.9

Table S2.2. Molecular characteristics of Nsp1 (see SI movie 3), Nsp1-S (see SI movie 3) and Nup98 and the computed Stokes radii (in isolation).

SI 2.12. Relating energy barrier to event rate using the Arrhenius relation
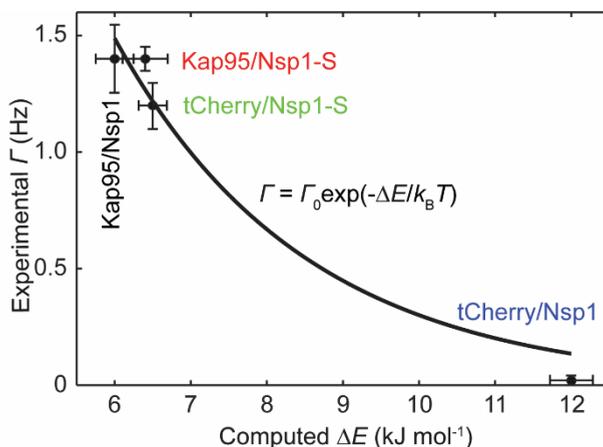
Figure S2.15: Experimental event rate Γ_0 **versus computed energy barrier** Δ□, for tCherry and Kap95 in Nsp1 and Nsp1-S pores. The data points are plotted as black circles and fitted using the Arrhenius relation (see Eq. 4 in the main text). From the fitting we obtain Γ_0 = 16.4 Hz with an R^2 value of 0.96.

SI. 2.13 Stable baseline conductance and increase of the event rate with Kap95 concentration for an Nsp1-coated pore

Figure S2.16A shows the ionic conductance that was measured for Nsp1-coated pores at a varying Kap95 concentration in the measurement buffer. Notably, it was observed that the baseline conductance does *not* vary with increasing Kap95 concentration, in contrast to what would be expected if large numbers of Kap95 would accumulate within the pore.(Lim and Kapinos, 2015; Kapinos *et al.*, 2017) Figure S2.16B shows the event frequency vs Kap95 concentration, measured for single Kap95 translocations through a Nsp1-coated pore. We observe a (trivial) linear increase of the event rate, as more Kap95 proteins traverse the pore for higher concentrations.
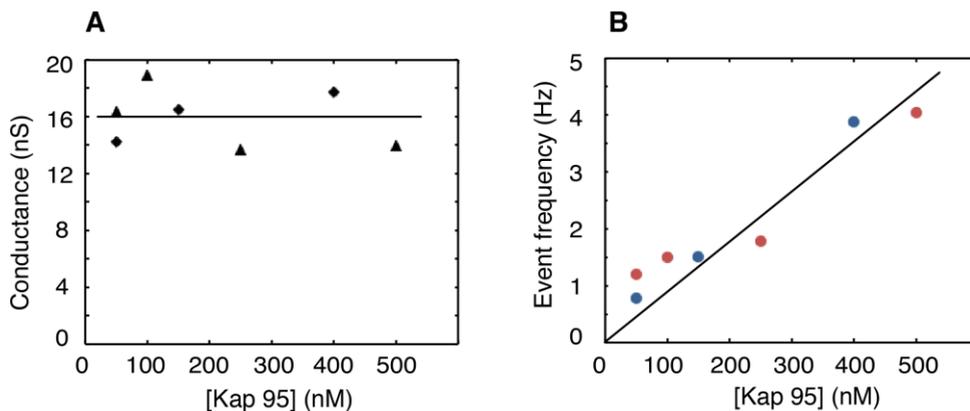
Figure S2.16: Experiments on Nsp1-coated pores with a varying Kap95 concentration in the buffer. A. Baseline ioninc conductance versus Kap95 concentration. Triangles and diamonds denote two independent measurements performed on two different pores. The pore diameter was 49±1nm. The solid line denotes the average conductance of 16 nS. B. Event frequency versus Kap95 concentration. Blue and red data markers denote two independent measurements performed on two different pores. The solid line denotes a linear fit (R^2= 0.89) to all data points.

SI. 2.14 Information on the tCherry control protein

A tCherry protein was chosen as a good reference to Kap95 because of its similar size and because it is a hydrophilic cytosolic protein that is expected to be inert regarding the interactions with hydrophobic Nups. In our study, tCherry, a tetramer of mCherry, was created by restoring the original tetramerization interface of DsRed (a tetrameric parent of mCherry) into mCherry (which originally was intended to be a monomeric derivative of DsRed). This operation results in a constitutively tetrameric protein with fluorescent properties similar to mCherry. According to our data, the protein is very hydrophilic, inert and – in contrast to DsRed itself – very well behaved.

The monomer sequence is:

GTGMASSEDIIKEFMRFKVRMEGSVNGHEFEIEGEGEGRPYEGTQTAKLKVTKGGPLPFAWDILSP
QFMYGSKAYVKHPADIPDYLKLSFPEGFKWERVMNFEDGGVVTVTQDSSLQDGEFIYKVKLIGVNF
PSDGPVMQKKTMGWEASTERMYPRDGVLKGEIHQALKLKDGGHYLAEVKTIYMAKKPVQLPGYY
YVDIKLDITSHNEDYTIVEQYERAEGRHHLFL

References

(1)   Hurt, E.; Beck, M. Towards Understanding Nuclear Pore Complex Architecture and Dynamics in the Age of Integrative Structural Analysis. Curr. Opin. Cell Biol. 2015, 34, 31–38.

(2)   Schwartz, T. U. The Structure Inventory of the Nuclear Pore Complex. Journal of Molecular Biology, 2016, 428, 1986–2000.

(3)   Hoelz, A.; Glavy, J. S.; Beck, M. Toward the Atomic Structure of the Nuclear Pore Complex: When Top down Meets Bottom up. Nat. Struct. Mol. Biol. 2016, 23, 624–630.

(4)   Popken, P.; Ghavami, A.; Onck, P. R.; Poolman, B.; Veenhoff, L. M. Size-Dependent Leak of Soluble and Membrane Proteins Through the Yeast Nuclear Pore Complex. Mol. Biol. Cell 2015, 26, 1386–1394.

(5)   Timney, B. L.; Raveh, B.; Mironska, R.; Trivedi, J. M.; Kim, S. J.; Russel, D.; Wente, S. R.; Sali, A.; Rout, M. P. Simple Rules for Passive Diffusion through the Nuclear Pore Complex. J. Cell Biol. 2016, 215.

(6)   Schmidt, H. B.; Görlich, D. Transport Selectivity of Nuclear Pores, Phase Separation, and Membraneless Organelles. Trends in Biochemical Sciences, 2016, 41, 46–61.

(7)   Pante, N.; Kann, M. Nuclear Pore Complex Is Able to Transport Macromolecules with Diameters of 39 Nm. Mol. Biol. Cell 2002, 13, 425–434.

(8)   Lowe, A. R.; Siegel, J. J.; Kalab, P.; Siu, M.; Weis, K.; Liphardt, J. T. Selectivity Mechanism of the Nuclear Pore Complex Characterized by Single Cargo Tracking. Nature 2010, 467, 600–603.

(9)   Hurt, E. C. A Novel Nucleoskeletal-like Protein Located at the Nuclear Periphery Is Required for the Life Cycle of Saccharomyces Cerevisiae. EMBO J. 1988, 7, 4323–4334.

(10)   Iovine, M. K.; Watkins, J. L.; Wente, S. R. The GLFG Repetitive Region of the Nucleoporin Nup116p Interacts with Kap95p, an Essential Yeast Nuclear Import Factor. J. Cell Biol. 1995, 131, 1699–1713.

(11)   Bayliss, R.; Ribbeck, K.; Akin, D.; Kent, H. M.; Feldherr, C. M.; Görlich, D.; Stewart, M. Interaction between NTF2 and xFxFG-Containing Nucleoporins Is Required to Mediate Nuclear Import of RanGDP. J. Mol. Biol. 1999, 293, 579–593.

(12)   Frey, S.; Görlich, D. A Saturated FG-Repeat Hydrogel Can Reproduce the Permeability Properties of Nuclear Pore Complexes. Cell 2007, 130, 512–523.

(13)   Patel, S. S.; Belmont, B. J.; Sante, J. M.; Rexach, M. F. Natively Unfolded Nucleoporins Gate Protein Diffusion across the Nuclear Pore Complex. Cell 2007, 129, 83–96.

(14)   Rout, M. P.; Aitchison, J. D.; Suprapto, A.; Hjertaas, K.; Zhao, Y.; Chait, B. T. The Yeast Nuclear Pore Complex: Composition, Architecture, and Transport Mechanism. J. Cell Biol. 2000, 148, 635–651.

(15)   Rout, M. P.; Aitchison, J. D.; Magnasco, M. O.; Chait, B. T. Virtual Gating and Nuclear Transport: The Hole Picture. Trends in Cell Biology, 2003, 13, 622–628.

(16)   Lim, R. Y. H.; Fahrenkrog, B.; Köser, J.; Schwarz-Herion, K.; Deng, J.; Aebi, U. Nanomechanical Basis of Selective Gating by the Nuclear Pore Complex. Science 2007, 318, 640–643.

(17)   Peters, R. Translocation through the Nuclear Pore Complex: Selectivity and Speed by Reduction-of-Dimensionality. Traffic 2005, 6, 421–427.

(18)   Schleicher, K. D.; Dettmer, S. L.; Kapinos, L. E.; Pagliara, S.; Keyser, U. F.; Jeney, S.; Lim, R. Y. H. Selective Transport Control on Molecular Velcro Made from Intrinsically Disordered Proteins. Nat. Nanotechnol. 2014, 9, 525–530.

(19)   Ribbeck, K.; Görlich, D. Kinetic Analysis of Translocation through Nuclear Pore Complexes. EMBO J. 2001, 20, 1320–1330.

(20)   Lim, R. Y. H.; Kapinos, L. E. How to Operate a Nuclear Pore Complex by Kap-Centric Control. Nucleus 2015, 6, 366–372.

(21)   Kapinos, L. E.; Huang, B.; Rencurel, C.; Lim, R. Y. H. Karyopherins Regulate Nuclear Pore Complex Barrier and Transport Function. J. Cell Biol. 2017, 216, 3609–3624.

(22)   Yamada, J.; Phillips, J. L.; Patel, S.; Goldfien, G.; Calestagne-Morelli, A.; Huang, H.; Reza, R.; Acheson, J.; Krishnan, V. V; Newsam, S.; et al. A Bimodal Distribution of Two Distinct Categories of Intrinsically Disordered Structures with Separate Functions in FG Nucleoporins. Mol. Cell. Proteomics 2010, 9, 2205–2224.

(23)   Caspi, Y.; Zbaida, D.; Cohen, H.; Elbaum, M. Synthetic Mimic of Selective Transport through the Nuclear Pore Complex. Nano Lett. 2008, 8, 3728–3734.

(24)   Jovanovic-Talisman, T.; Tetenbaum-Novatt, J.; McKenney, A. S.; Zilman, A.; Peters, R.; Rout, M. P.; Chait, B. T. Artificial Nanopores That Mimic the Transport Selectivity of the Nuclear Pore Complex. Nature 2009, 457, 1023–1027.

(25)   Kowalczyk, S. W.; Kapinos, L.; Blosser, T. R.; Magalhães, T.; van Nies, P.; Lim, R. Y. H.; Dekker, C. Single-Molecule Transport across an Individual Biomimetic Nuclear Pore Complex. Nat. Nanotechnol. 2011, 6, 433–438.

(26)   Dekker, C. Solid-State Nanopores. Nat. Nanotechnol. 2007, 2, 209–215.

(27)   Ghavami, A.; van der Giessen, E.; Onck, P. R. Coarse-Grained Potentials for Local Interactions in Unfolded Proteins. J. Chem. Theory Comput. 2013, 9, 432–440.

(28)   Ghavami, A.; Veenhoff, L. M.; van der Giessen, E.; Onck, P. R. Probing the Disordered Domain of the Nuclear Pore Complex through Coarse-Grained Molecular Dynamics Simulations. Biophys. J. 2014, 107, 1393–1402.

(29)   Ader, C.; Frey, S.; Maas, W.; Schmidt, H. B.; Görlich, D.; Baldus, M. Amyloid-like Interactions within Nucleoporin FG Hydrogels. Proc. Natl. Acad. Sci. U. S. A. 2010, 107, 6281–6285.

(30)   Frey, S.; Richter, R. P.; Görlich, D. FG-Rich Repeats of Nuclear Pore Proteins Form a Three-Dimensional Meshwork with Hydrogel-like Properties. Science 2006, 314, 815–817.

(31)   Kowalczyk, S. W.; Grosberg, A. Y.; Rabin, Y.; Dekker, C. Modeling the Conductance and DNA Blockade of Solid-State Nanopores. Nanotechnology 2011, 22, 315101.

(32)   Hall, J. E. Access Resistance of a Small Circular Pore. J. Gen. Physiol. 1975, 66, 531–532.

(33)   Eisele, N. B.; Labokha, A. a.; Frey, S.; Görlich, D.; Richter, R. P. Cohesiveness Tunes Assembly and Morphology of FG Nucleoporin Domain Meshworks - Implications for Nuclear Pore Permeability. Biophys. J. 2013, 105, 1860–1870.

(34)   Bustamante, J. O.; Hanover, J. A.; Liepins, A. The Ion Channel Behavior of the Nuclear Pore Complex. J Membr Biol 1995, 146, 239–251.

(35)   Tonini, R.; Grohovaz, F.; Laporta, C. A.; Mazzanti, M. Gating Mechanism of the Nuclear Pore Complex Channel in Isolated Neonatal and Adult Mouse Liver Nuclei. FASEB J 1999, 13, 1395–1403.

(36)   Plesa, C.; Dekker, C. Data Analysis Methods for Solid-State Nanopores. Nanotechnology 2015, 26, 84003.

(37)   Ghavami, A.; van der Giessen, E.; Onck, P. R. Energetics of Transport through the Nuclear Pore Complex. PLoS One 2016, 11, e0148876.

(38)   Cardarelli, F.; Lanzano, L.; Gratton, E. Fluorescence Correlation Spectroscopy of Intact Nuclear Pore Complexes. Biophys. J. 2011, 101, L27–L29.

(39)   Kersey, P. J.; Staines, D. M.; Lawson, D.; Kulesha, E.; Derwent, P.; Humphrey, J. C.; Hughes, D. S. T.; Keenan, S.; Kerhornou, A.; Koscielny, G.; et al. Ensembl Genomes: An Integrative Resource for Genome-Scale Data from Non-Vertebrate Species. Nucleic Acids Res. 2012, 40, D91--7.

(40)   Tagliazucchi, M.; Peleg, O.; Kröger, M.; Rabin, Y.; Szleifer, I. Effect of Charge, Hydrophobicity, and Sequence of Nucleoporins on the Translocation of Model Particles through the Nuclear Pore Complex. Proc. Natl. Acad. Sci. U. S. A. 2013, 110, 3363–3368.

(41)   Carpenter, T. S.; Kirshner, D. A.; Lau, E. Y.; Wong, S. E.; Nilmeier, J. P.; Lightstone, F. C. A Method to Predict Blood-Brain Barrier Permeability of Drug-Like Compounds Using Molecular Dynamics Simulations. Biophys. J. 2014, 107, 630–641.

(42)   Musser, S. M.; Grünwald, D. Deciphering the Structure and Function of Nuclear Pores Using Single Molecule Fluorescence Approaches. J. Mol. Biol. 2016.

(43)   **Zahn, R.; Osmanović, D.; Ehret, S.; Araya Callis, C.; Frey, S.; Stewart, M.; You, C.;** Görlich, D.; Hoogenboom, B. W.; Richter, R. P. A Physical Model Describing the Interaction of Nuclear Transport Receptors with FG Nucleoporin Domain Assemblies. Elife 2016, 5, e14119.

(44)   Vovk, A.; Gu, C.; Opferman, M. G.; Kapinos, L. E.; Lim, R. Y.; Coalson, R. D.; Jasnow, D.; Zilman, A. Simple Biophysics Underpins Collective Conformations of the Intrinsically Disordered Proteins of the Nuclear Pore Complex. Elife 2016, 5.

(45)   Hülsmann, B. B.; Labokha, A. A.; Görlich, D. The Permeability of Reconstituted Nuclear Pores Provides Direct Evidence for the Selective Phase Model. Cell 2012, 150, 738–751.

(46)   Rout, M. P.; Wente, S. R. Pores for Thought: Nuclear Pore Complex Proteins. Trends Cell Biol 1994, 4, 357–365.

(47)   Bayliss, R.; Leung, S. W.; Baker, R. P.; Quimby, B. B.; Corbett, A. H.; Stewart, M. Structural Basis for the Interaction between NTF2 and Nucleoporin FxFG Repeats. EMBO J. 2002, 21, 2843–2853.

(48)   Port, S. A.; Monecke, T.; Dickmanns, A.; Spillner, C.; Hofele, R.; Urlaub, H.; Ficner, R.; Kehlenbach, R. H. Structural and Functional Characterization of CRM1-Nup214 Interactions Reveals Multiple FG-Binding Sites Involved in Nuclear Export. Cell Rep. 2015, 13, 690–702.

(49)   Isgro, T. A.; Schulten, K. Binding Dynamics of Isolated Nucleoporin Repeat Regions to Importin-β. Structure 2005, 13, 1869–1879.

(50)   Yang, W.; Gelles, J.; Musser, S. M. Imaging of Single-Molecule Translocation through Nuclear Pore Complexes. Proc Natl Acad Sci U S A 2004, 101, 12887–12892.

(51)   Kubitscheck, U.; Grünwald, D.; Hoekstra, A.; Rohleder, D.; Kues, T.; Siebrasse, J. P.; Peters, R. Nuclear Transport of Single Molecules: Dwell Times at the Nuclear Pore Complex. J. Cell Biol. 2005, 168, 233–243.

(52)   Janssen, X. J. a; Jonsson, M. P.; Plesa, C.; Soni, G. V; Dekker, C.; Dekker, N. H. Rapid Manufacturing of Low-Noise Membranes for Nanopore Sensors by Trans-Chip Illumination Lithography. Nanotechnology 2012, 23, 475302.

(53)   Tabard-Cossa, V.; Trivedi, D.; Wiggin, M.; Jetha, N. N.; Marziali, A. Noise Analysis and Reduction in Solid-State Nanopores. Nanotechnology 2007, 18, 305505.

(54)   Wanunu, M.; Meller, A. Chemically Modified Solid-State Nanopores. Nano Lett. 2007, 7, 1580–1585.

3.

Reversible immobilization of proteins in sensors and solid-state nanopores

The controlled functionalization of surfaces with proteins is crucial for many analytical methods in life science research and biomedical applications. Here we establish a coating for silica-based surfaces that enables stable and selective immobilization of proteins with controlled orientation and tunable surface density. The coating is reusable, retains functionality upon long-term storage in air, and is applicable to surfaces of complex geometry. We validate the protein anchoring method on planar SiO_2 and SiN surfaces, and then develop a method to measure the anchoring process in real time using SiN solid-state nanopores. For surface attachment, we exploit polyhistidine (His) tags that are site-specifically introduced into recombinant proteins and use the yeast nucleoporin Nsp1 FG domain as model protein. Contrary to the commonly used covalent thiol chemistry, the anchoring of proteins *via* His tag is reversible, permitting to take proteins off and replace them by other ones. We monitor such switching in real time in experiments on individual nanopores using ion conductivity. Finally, we demonstrate that silica and gold surfaces can be orthogonally functionalized to accommodate His-tagged proteins on silica but prevent protein binding to gold, which extends the applicability of our surface functionalization method to even more complex sensor devices

3.1 Introduction

Functionalization of material surfaces with biomolecules with nanoscale control is required for a wide variety of applications. In biosensing devices, for example, nanopores are very promising tools for DNA sensing,[1] ion detection,[2] macromolecule/protein sensing,[3] DNA sequencing,[4] molecular separation,[5] and biomimetics.[6] Chemical modification of solid-state nanopores is a key task to control the functional groups at surfaces, and to give a specific function to the pores, designed for example for antifouling,[7] or more specifically for target applications.[8] Specific functionalization of the nanopores and other materials with complex surface geometry is challenging, however, partly because of the lack of analytical characterization techniques that can provide detailed information of the physico-chemical properties of the modified nanopores, required to control the degree, quality and spatial arrangement of the functionality.[7b, 9]

Planar surfaces, on the other hand, enable application of a broad range of surface-sensitive characterization techniques which provide a detailed description of the structure and physico-chemical properties of surface-confined biomolecular films and time-resolved information of film formation, reorganization processes, and of biomolecular interactions. This makes them ideal, as we demonstrate here, to tailor and quality control surface functionalization and protein immobilization approaches prior to their translation onto more complex surface geometries.

Nanopores in silicon-derived membranes can be tuned with subnanometer precision in size and shape.[10] The silicon-derived membranes present better mechanical, chemical and thermal characteristics compared with lipid-bilayer-based systems, and can be integrated with electronic or optical readout techniques.[11] SiN is the most popular material because of its low stress and excellent aspect ratio membranes for fabricating single nanopores with well-defined shape and size, as well as high-density nanopore arrays.[5b, 10, 12] SiN pores can be covered with gold in order to use thiol chemistry to attach molecules.[8b, 13] However, silanes are most extensively used for the direct coating of nanopores in silicon-based solid-state membranes. Silanes have been used, for example, to modify the charge of the SiN pore surface for charge-based molecular differentiation.[5b] They can also be used as a platform to further covalently link other organic molecules, such as glutaraldehyde.[8a] Alternatively, the pore walls can be coated with biomolecules such as lipids, nucleic acids, or proteins. Yusko et al [14] showed the advantages of coating a nanopore with a lipid bilayer in terms of tuning protein translocation speeds, preventing non-specific adsorption, and

attaching streptavidin-functionalized molecules by incorporation of biotin into the lipid bilayers. For nucleic acids or proteins, a molecular recognition element, like a single-stranded DNA for the detection of the complementary sequence, or an aptamer for complementary shape recognition, can be directly attached to the pore walls.[15] Sensors with such molecular recognition elements can be very efficient in molecular detection but they are essentially "single use" devices as they are based on strong and irreversible recognition affinities. An alternative recognition element is a chelator, such as the nitrilotriacetic acid (NTA) group, which in complex with a nickel ion enables specific binding of a polyhistidine (His) tagged protein. Wei et al, for example, developed a gold-modified nanopore functionalized with $HS–(CH_2)_{15}–(OC_2H_4)_3–NTA$, and these pores showed a strong increase of the dwell time for His-tagged proteins.[8b] Various NTA-based methods have also been used on planar or macroporous surfaces for protein immobilization (*e.g.* ref. [16]). Recent studies on functionalization of silicon-based and polymeric nanopores with metal-organic chelates emphasized the need for reversible functionalization inside nanopores.[17]

The new strategy for selective and reversible immobilization of proteins that we report here is partly motivated by current efforts to reconstitute the selective permeability of the nuclear pore complex (NPC) in solid state nanopores.[18] NPCs form ~40 nm wide channels in the nuclear membrane and control the exchange of proteins and nucleic acids into and out of the nucleus of eukaryotic cells. Crucial to this function are intrinsically disordered and thus flexible protein domains rich in phenylalanine-glycine dipeptide motifs (nucleoporin FG domains),[19] which are grafted at high density to the NPC channel wall and efficiently preclude the passage of large inert macromolecules. Such macromolecules can, however, efficiently permeate when bound to soluble nuclear transport receptors (NTRs) that engage in low-affinity interactions with FG domains. Given the broad interest in this system, we mostly use an FG domain (from the yeast nucleoporin Nsp1) as a model protein to analyse the quality and features of our surface functionalization strategy. The strategy itself, however, is generic and can be applied to other His-tagged proteins.

In this paper, we establish a protein coating approach for silica-based surfaces of arbitrary geometry that enables stable and selective immobilization of proteins with controlled orientation and tunable surface density. For attachment to the surface, we use site-specific polyhistidine (His) tags in recombinant proteins. Contrary to the common strategies for anchoring proteins, the capture of proteins *via* the His tag is reversible and proteins can be put on and off, which can be monitored in real time in experiments on planar surfaces and individual nanopores. More specifically, whilst FG domain immobilization to nanopore walls in previous studies was covalent, exploiting the binding of cysteines either

directly to gold coated membranes[18a] or to chemically modified SiN,[18b] the method developed here permits the binding of His-tagged proteins in a stable and oriented manner. Importantly, their triggered release enables reversible functionalization, and single nanopores can thus be used for several successive experiments.[16d, 17b, 20] The method can be applied on all silica-based surfaces, such as silica wafers, silicon nitride, or glass, which present a surface that is chemically equivalent to silicon oxide.

As a Ni^{2+} chelator for His tag capture, we use ethylenediaminetetraacetic acid (EDTA) mono amide which has two major advantages over the traditional NTA group. First, its introduction into silica surfaces requires only bulk chemicals (an aminosilane, EDTA and a water-soluble carbodiimide) and follows a simpler chemistry. Second, it binds Ni^{2+} far stronger than an NTA group and is therefore highly resistant against Ni-leakage or -reduction, even in the presence of free chelators or DTT.

In this study, we first present the surface functionalization method and characterize its performance in terms of model protein immobilization on planar surfaces with quartz crystal microbalance (QCM-D) and spectroscopic ellipsometry (SE). Then, the versatility of the method is demonstrated by three application examples:

i. The analysis of molecular interactions and protein film morphologies on planar surfaces.
ii. The combination of the His-tag capturing function on silica with passivation for the selective chemical modification of dual gold /silica-based substrates, which are suitable candidates for the fabrication of selective functional patterned platforms or three-dimensional topographic structures[7b, 9] required for advanced biosensing and sieving applications[21] and nanoporous plasmonic sensors.[22]
iii. The implementation of the functionalization method to the more complex topology of SiN nanopores, where we monitor the reversible immobilization of model proteins and the reuse of nanopores *in situ* through ion current measurements.
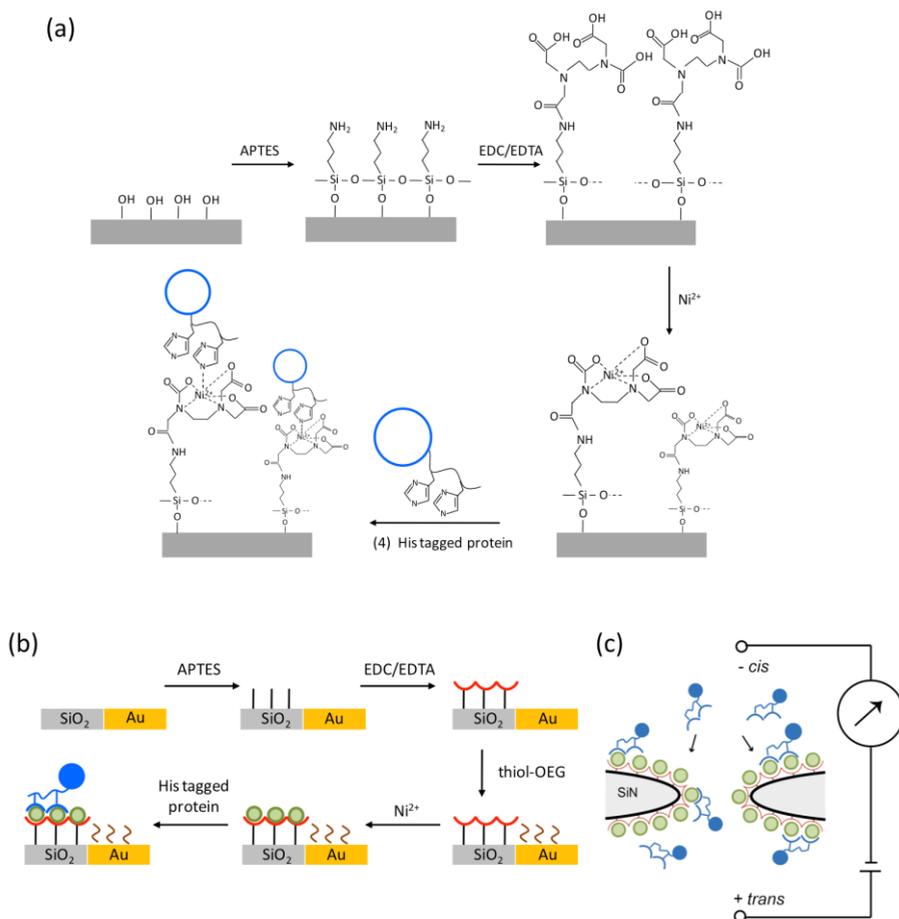
Figure 3.1. Functionalization of planar surfaces and nanopores. (a) Schematic representation of the surface functionalization method for specific immobilization of His-tagged proteins on silica-based surfaces. (b) Schematic representation of the orthogonal functionalization of silica (for specific immobilization of His-tagged proteins, as in (a)) and gold (for passivation against protein adsorption). (c) Schematic representation of a functionalized nanopore (as in (a)) for immobilization of His-tagged proteins and conductance measurements to monitor ion fluxes through the pore. Stable immobilization of His-tagged proteins is thought to require multivalent attachment, illustrated in (b) and (c) as anchorage to two EDTA moieties.

3.2 Results and discussion

3.2.1 Functionalization of silicon oxide surfaces for selective, oriented, and reversible immobilization of His-tagged proteins

The functionalization of silicon oxide surfaces contained two sequential chemical conjugation steps: surface OH groups first reacted with the aminosilane APTES, and subsequently EDTA was coupled to the resulting dense layer of primary amines (Figure 3.1a). The EDTA mono amide (EDTA for short in the following) thus generated was used to chelate nickel ions which can specifically coordinate with histidine moieties and thus enable the selective and oriented immobilization of His-tagged proteins.

Quartz crystal microbalance with dissipation monitoring (QCM-D) was used to monitor protein binding and assess the quality of immobilization (Figure 3.2a). **Strong shifts in resonance frequency, Δf, and dissipation, ΔD**, were achieved upon incubation of the model protein Nsp1-H_{10}, demonstrating the formation of a soft and hydrated film of this nucleoporin FG domain. The proteins remained stably bound upon rinsing in buffer (typically > 90% were retained over rinsing periods of 30 min) but could be fully released by incubation with 500 mM imidazole (for at least 20 min; longer times had no additional effect) which competes with the His tag for the coordination of the nickel ions. Moreover, an equivalent protein construct that lacked the His tag hardly bound to the Ni^{2+}-EDTA functionalized surfaces (Figure S3.1). These results demonstrate that the proteins bind exclusively *via* their His tag, thus enabling immobilization in a well-defined orientation through a specifically tailored site (here the C terminus) on the protein. The affinity of individual interactions between an EDTA-coordinated Ni^{2+} and a histidine is expected to be of rather low affinity. The high stability of Nsp1-H_{10} against elution in buffer thus indicates that anchorage is realized through multiple histidine-Ni^{2+}-EDTA complexes.

The protein surface density was quantified by spectroscopic ellipsometry (SE). A surface density of 5 pmol/cm^2 (320 ng/cm^2) was easily reached with the typical incubation conditions (Figure 3. 23.b). This density corresponds to a root-mean-square distance between anchor points of approximately 6 nm, comparable to the size of proteins (*e.g.* streptavidin has dimensions around 5 nm at a molecular mass of 60 kDa) and illustrating that a dense protein coating can readily be achieved. Lower film densities can be produced by adjusting the concentration and time of protein incubation, and quantitatively controlled thanks to the kinetic information which is also provided by SE (Figure 3. 3.2b). The surfaces showed a good batch-to-batch reproducibility in protein binding (Figure S3.2). Moreover,

functionalized SiN substrates performed similar to functionalized silica wafers (Figure 3. S3.2). Both types of substrate are expected to be covered with a thin film of silicon oxide, and indeed they appeared chemically identical for the purpose of the here-presented surface modification.
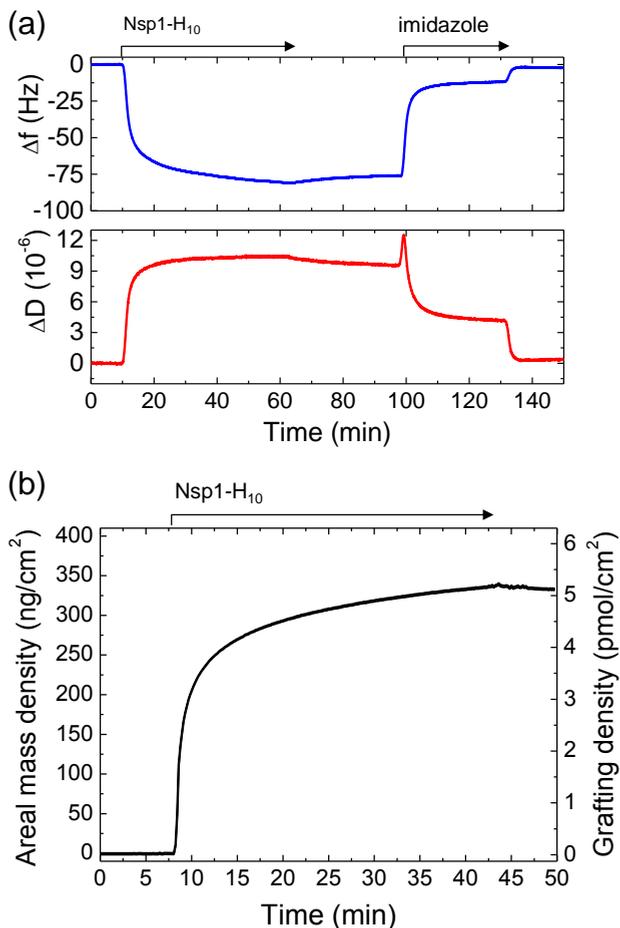
Figure 3.2. Characterization and quantification of the immobilization of His-tagged proteins on planar silica surfaces. (a) Immobilization of Nsp1 with a C-terminal His tag (Nsp1-H_{10}), and triggered release with imidazole, monitored by QCM-D. Arrows on top of the graph indicate the start and duration of incubation with different sample solutions; **remaining times correspond to rinsing with working buffer. Changes in Δf and ΔD** upon exchange from imidazole-containing solution to buffer do not reflect any changes on the surface but result from a change in the viscosity and density of the surrounding solution owing to the presence of imidazole. (b) Areal surface densities upon immobilization of Nsp1-H_{10} quantified by SE. Conditions: buffer – 10 mM HEPES, 150 mM NaCl, pH 7.4; Nsp1-H_{10} – **1.5 µM; imidazole –** 0.5 M; silica surfaces were functionalized with EDTA and loaded with $NiCl_2$ (2 mM, 15 min) prior to the measurements.

The SE data in Figure 3.3a demonstrate that the functional surfaces can be regenerated and re-used multiple times without an appreciable loss in activity. Across three successive Nsp1-H$_{10}$ incubations on the same surface, the areal protein mass densities reached after 30 min of exposure agreed to well within 5% (337 ± 8 ng/cm^2). We also found the surfaces to remain functional upon repeated wetting with aqueous solution and subsequent drying. Figure 3. 3.3b evaluates the performance of two sensors that were used many times and stored in air at room temperature between measurements. In this plot, the efficiency of protein immobilization is quantified by the QCM-D frequency shift reached after 1 h of Nsp1-H$_{10}$ incubation relative to the response obtained during the first incubation of Nsp1-H$_{10}$ right after surface functionalization (day 0) under otherwise identical conditions. This parameter is a measure of the relative changes in areal protein mass density. The data show that the His-tag binding capacity is retained at a level above 70% during the first month (comprising 6 uses) and remains above 60% after 3.5 months (9 uses). This demonstrates that the surfaces also retain very good activity when stored over several months.
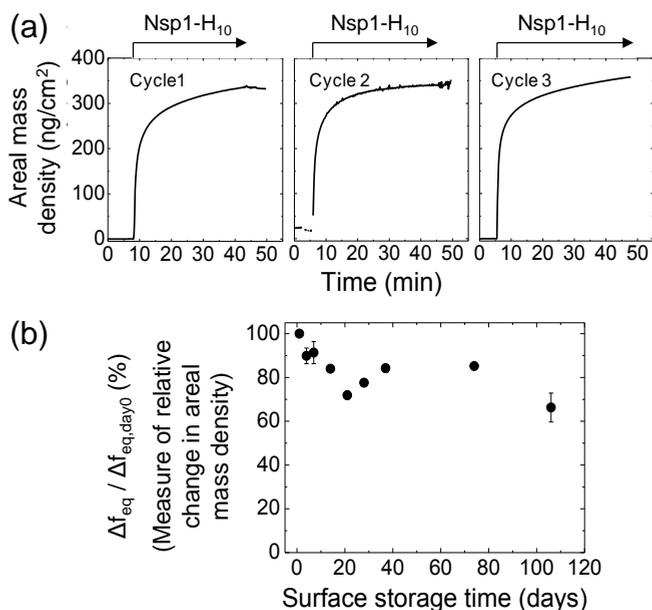
Figure 3.3. Multiple use of His-tag capturing surfaces, and stability upon storage. (a) Three cycles of Nsp1-H$_{10}$ immobilization on the same surface monitored by SE. The second cycle was performed immediately after the first, and the third cycle one week later; surface regeneration steps are not shown, yet the quality of surface regeneration is reflected by the proximity to zero of the baseline prior to the subsequent protein injections. Conditions: buffer – 10 mM HEPES, 150 mM NaCl, pH 7.4; Nsp1-H$_{10}$– 1.9 µM; the silica surface was functionalized with EDTA, and after each incubation cycle, the surface was regenerated with a solution of 0.5 M imidazole and 1 M GuHCl (for 40 min, not shown);

the surface was loaded with $NiCl_2$ (2 mM for 15 min) prior to each protein incubation step. (b) QCM-D frequency shifts upon incubation with Nsp1-H_{10} (1.5 μM for 60 min) are shown as a function of storage time relative to the response at day 0; the parameter $\Delta f_{eq}/\Delta f_{eq, day\ 0}$ is an approximate measure of the changes in areal mass density relative to day 0, and reflects the conservation of His-tag binding capacity. Before each measurement, the surfaces were re-loaded with $NiCl_2$; after each measurement, the surfaces were regenerated with 0.5 M imidazole and 1 M GuHCl (30 min), rinsed with buffer and water, blow-dried in nitrogen gas and stored dry in the dark at room temperature until the next measurement. Error bars represent standard deviations for two measurements with two different sensors; the same sensors were repeatedly used to acquire all data shown in (b).

3.2.2 Aplication example I. Analysis of molecular interactions and protein film morphology on planar surfaces

To illustrate the versatility of the Ni^{2+}-EDTA functionalized surface for protein immobilization, we analyzed the binding of three different His-tagged proteins with distinct structural properties (Figure 3. 3.4a). Next to the wild type form of the FG domain of Nsp1 (Nsp1-H_{10}), we used a mutant form (Nsp1-H_{10} FILV→S) of identical size in which all hydrophobic amino acids where replaced by serines.[19d] Nsp1 and Nsp1 FILV→S are both intrinsically disordered, but the mutant exhibits a reduced inter- and intra-chain attraction (cohesiveness) compared to the wild type Nsp1.[19a] We have previously shown that the reduced cohesiveness affects the morphology of one-end grafted FG domains considerably, leading to less dense and softer films.[19d] Finally, we also used green fluorescent protein with an N-terminal His tag (H_{14}-GFP) as an example of a 'conventional' folded, globular protein.

Figure 3.4a-b demonstrates that all three proteins can be stably immobilized, and also almost fully released with 0.5 M imidazole confirming specific and oriented binding *via* the His tag. Moreover, the effective surface regeneration achieved by the imidazole rinse (typically to within 10% of the total protein binding, *cf.* Figs. 2.2a, 2.3a, 2.4a-b and S2.2b) enabled sequential studies with the different proteins on the same sensor surface.
Planar surfaces enable characterization of proteins and protein films with surface sensitive techniques at a level of detail that is difficult to achieve on more complex surface geometries. This makes them attractive as tools to study biomolecular interactions and self-organization. Moreover, it also makes them ideal to tailor and quality control surface functionalization and protein immobilization methods prior to their application on more complex surface geometries. To illustrate both aspects, we here briefly compare the QCM-D responses for the three proteins on

Ni^{2+}-EDTA functionalized surfaces with each other, and with earlier works where we had used another functionalization platform – supported lipid bilayers with nickel-loaded nitrilotriacetic acid (Ni^{2+}-NTA SLBs) – for anchorage of the same proteins.[19d, 23] As the Ni^{2+}-EDTA surfaces, the Ni^{2+}-NTA SLB platform also provides for the selective and reversible binding of His-tagged proteins. Differences are that the SLBs retain the protein anchors laterally mobile and that they are not stable upon drying, which limits their use in certain sensor applications.
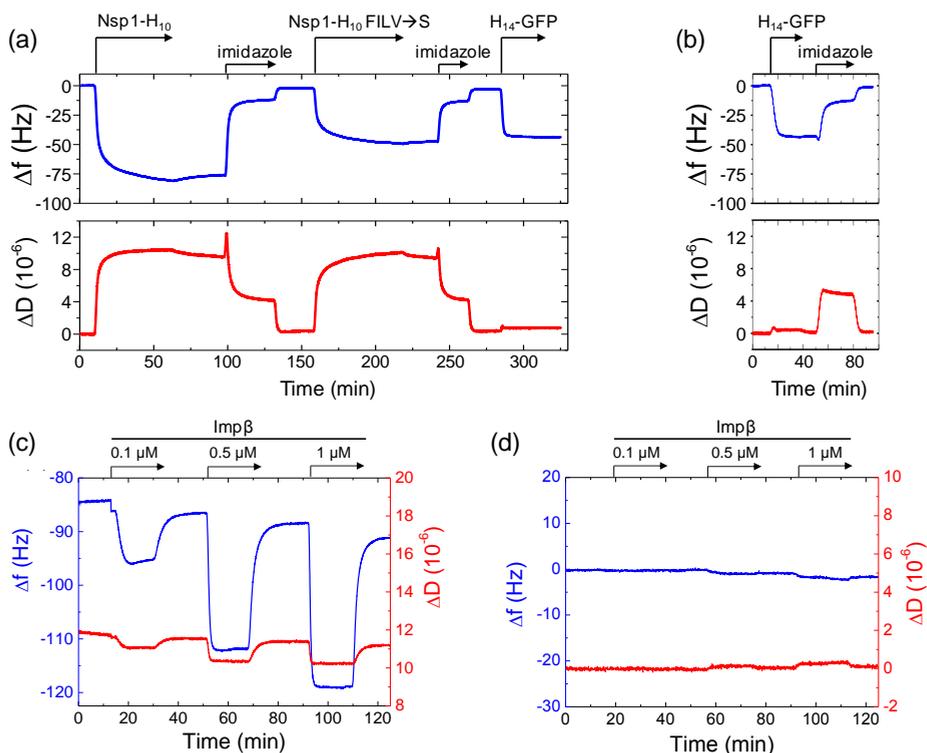
Figure 3.4. Versatile use of the His-tag capturing surface and selective protein-protein interactions, studied by QCM-D. (a) Consecutive immobilization of three different His-tagged proteins – Nsp1-H$_{10}$, a FILV→S mutant of Nsp1-H$_{10}$, and H$_{14}$-GFP. Conditions: buffer – 10 mM HEPES, 150 mM NaCl, pH 7.4; all proteins – 1.5 µM; between incubation cycles, proteins were released and the surface was thus regenerated by 0.5 M imidazole (as shown). Data are presented analogous to Fig. 2.2a. (b) Immobilization of H$_{14}$-GFP to a virgin His-tag capturing surface, and triggered release (conditions as in (a)). (c) The nuclear transport receptor **Impβ** reversibly binds to a film of immobilized Nsp1-H$_{10}$ in a dose-dependent manner (decrease in Δf) and rigidifies the Nsp1 film (decrease in ΔD). (d) In the absence of Nsp1-H$_{10}$, there is only minor **Impβ** binding, confirming that **Impβ**

binding to the Nsp1-H$_{10}$ film is specific. Conditions: buffer – 10 mM HEPES, 150 mM NaCl, pH 7.4. Silica surfaces were functionalized with EDTA and loaded with NiCl$_2$ (2 mM for 15 min) prior to the measurements in (a) to (d); in addition, an Nsp1-H$_{10}$ film was formed in (c), as shown in 3.2a.

The QCM-D responses in Figure 3.4a reveal characteristic differences in the morphology of the protein films that mirror the structural features of the proteins. The frequency shift for H$_{14}$-GFP **at saturation (Δf = -40 Hz)** corresponds to a film thickness of approximately 6 nm [24] which is consistent with the size of the **protein, while the small dissipation shift (ΔD = 0.6 × 10^{-6})** reflects the globular (and thus rigid) nature of the protein. The two Nsp1 constructs generate a much higher dissipation, reflecting the formation of soft films. A detailed analysis of the $\Delta D / -\Delta f$ ratio, which is a measure of the elastic compliance of thin films,[24] reveals that the FILV→S mutant forms softer films than the wild type protein, as expected given its reduced cohesiveness (Figure S3.3). Moreover, Figure S3.3 also shows a gradual rigidification of the Nsp1 films as the protein surface coverage increases. The one-end grafted Nsp1 forms a continuous film of flexible, interpenetrating protein chains (also **called 'brush') and the rigidification is the expected** consequence of an increase in film density with surface coverage.[19d, 23] Notably, all these observations are consistent with previous studies in which the same three proteins had been anchored to Ni^{2+}-NTA SLBs[19d, 23] instead of Ni^{2+}-EDTA surfaces (see Figure S3.3), demonstrating that the morphology of the protein films is similar and independent of the exact surface chemistry used for His-tag anchorage.

Comparison of Figure 3.4a-b with the previous work also shows that the kinetics of protein binding on the Ni^{2+}-EDTA surfaces is comparable to the Ni^{2+}-NTA SLBs. Binding is limited by mass transport at low coverages, but steric constraints slow down the binding as the surface is increasingly populated with proteins. Here, the packing constraints of the globular H$_{14}$-GFP are relatively weak and the equilibrium state of a dense protein monolayer is reached rather rapidly (within 10 min; on Ni^{2+}-EDTA surfaces, Fig. 3.4a-b, and on Ni^{2+}-NTA SLBs, Fig. 3.2 in ref. [23]). The barrier to binding imposed by the film of interpenetrating Nsp1 chains is more severe, particularly so for the less cohesive FILV→S mutant,[19d] and as a consequence, binding of the Nsp1 constructs does not saturate over 1 h of protein incubation. It is notable that the maximal frequency shifts obtained for H$_{14}$-GFP on Ni^{2+}-EDTA (Figure 3.4a) and on Ni^{2+}-NTA SLBs (ref. [23]) were identical, confirming formation of a dense protein monolayer. For Nsp1-H$_{10}$ and Nsp1-H$_{10}$ FILV→S, the final frequency shifts were somewhat lower (20 to 30%) on Ni^{2+}-EDTA than on Ni^{2+}-NTA SLBs.[19d] The reason for this difference is not entirely clear, but it suggests that the density of His-tag immobilization sites on Ni^{2+}-EDTA is

somewhat smaller than what can be attained on Ni^{2+}-NTA SLBs. It appears also possible that the lateral mobility of the anchoring points on the SLBs facilitates local rearrangements and thus protein binding.

Figure 3. 4c-d illustrates the application of Ni^{2+}-EDTA functionalized surfaces for biomolecular interaction studies. Specifically, we measured the selective interaction between a nuclear transport receptor (NTR) and an FG domain film. Interaction between NTRs and FG domains are known to be essential for the facilitated permeation of large macromolecules through nuclear pore complexes (NPCs). Here, we selected importin β (Impβ) from yeast as the NTR to interact with the Nsp1-H_{10} FG domain. Titration measurements by QCM-D demonstrated Impβ binding to Nsp1 films in a dose-dependent manner (Figure 3.4c). A control on bare Ni^{2+}-EDTA surfaces (Figure 3.4d) showed no appreciable Impβ binding, confirming that genuine Impβ-Nsp1 interactions are being probed. Binding and unbinding of Impβ was rapid, indicating fast and reversible interactions with Nsp1. It is notable that the shifts in dissipation upon Impβ binding are negative though generally small relative to the total dissipation shift of the Nsp1 film. These observations are again consistent with previous reports for Nsp1-H_{10} brushes on Ni^{2+}-NTA SLBs.[19b, 19c] Following the detailed analysis in ref. [19b], we can conclude from the frequency and dissipation data that NTR binding promotes a minor increase in film thickness and a moderate increase in film rigidity whereas the data is inconsistent with an NTR-induced film collapse. Taken together, these examples demonstrate that the developed planar His-tag capturing surfaces are versatile to study interactions between biomolecules in general, and between FG domains and NTRs in particular.

3.2.3 Application example II. Orthogonal functionalization of silica and gold surfaces

Sensing techniques increasingly rely on the use of structured surfaces that exhibit chemical (next to topographical) contrast on the nanometer or micrometer scale, or on the use of fluidic devices that expose the sample fluid to surfaces with various chemistries. The presence of multiple surface chemistries in one device entails the need to develop methods for selective functionalization of one or another surface. Gold in particular is commonly used in sensors, because it is stable as an electrode in aqueous solution and also of interest for surface plasmon resonance (SPR) sensing. Silicon-based materials are also very attractive because of their optical transparency (quartz or borosilicate glass) and their versatile use in the semiconductor industry (silicon wafers). Here we combine orthogonal silane and thiol chemistries to functionalize silica and gold surfaces such that His-tagged proteins are selectively immobilized on silica while the gold remains inert to protein binding.

The method builds on the APTES/EDTA functionalization of silica (Figure 3.1a) but includes the deposition of thiol-terminated oligo(ethylene glycol) (thiol-OEG) on gold as an additional step prior to nickel loading (Figure 3. 1b). The quality and orthogonality of the functionalization steps was evaluated by QCM-D using sets of two sensors, one coated with silica and the other with gold, that were jointly exposed to the full set of incubation steps outlined in Figure 3. 1b. Nsp1-H_{10} again served as a model protein. Figure 3.5 shows QCM-D responses upon protein incubation and triggered release on silica that were comparable to those obtained previously (Figure 3.2a), demonstrating that the thiol-OEG incubation step does not affect the quality of the Ni^{2+}-EDTA functionalization.
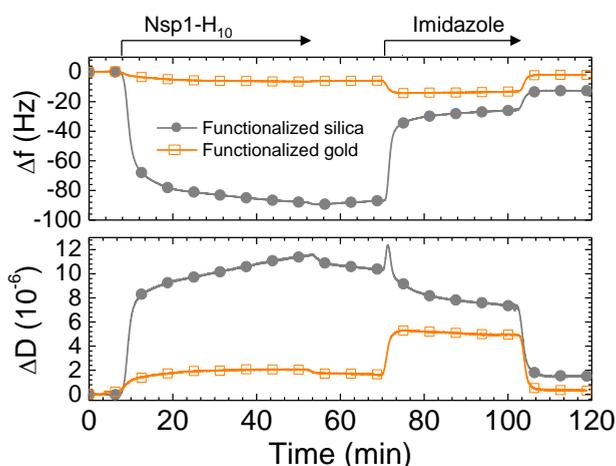
Figure 3.5. Orthogonal functionalization for selective immobilization of His-tagged proteins to silica surfaces whilst passivating gold surfaces. Binding and triggered release of Nsp1-H_{10}, monitored by QCM-D. The magnitudes of the responses on the silica surface (closed symbols) are comparable to data in Figure 3.2a (demonstrating proper silica functionalization) but much lower on the gold surface (open symbols; indicating effective – yet imperfect – passivation of gold). The over-**proportional change in** ΔD **compared to** Δf on gold reflects that residual Nsp1 adsorbs as a rather soft film. Conditions: buffer – 10 mM HEPES, 150 mM NaCl, pH 7.4; Nsp1-H_{10} – **1.5 μM; imidazole** – 0.5 M; prior to the measurement, silica and gold surfaces were exposed together to the functionalization steps outlined in Figure 3.1b.

At the same time, protein binding to gold induced a 90% smaller frequency shift than on silica (Figure 3. 5), and also a 90% smaller frequency shift than on bare gold and on gold that had been exposed to APTES and EDTA but not to thiol-OEG (Figure S3.4), indicating effective passivation of the gold surface. We also tested gold that had been exposed to thiol-OEG (but not to APTES or EDTA) and found no detectable binding of Nsp1-H$_{10}$ (Figure S3.4). The residual binding to gold treated with orthogonal functionalization (Figure 3.5) thus indicates that the APTES and/or EDTA conjugation steps perturb the formation of the thiol-OEG layer, although to a minor degree. It is notable that the residually bound Nsp1-H$_{10}$ can be fully released with imidazole, indicating that protein binds to the gold through the His tag. This suggests that a residue of EDTA is retained on the gold surface even after thiol-OEG deposition. Binding of APTES to gold has previously been reported,[21b, 25] and it might be that this also entails the retention of EDTA. We found that the surfaces exposed to orthogonal functionalization also showed good retention of their activity during repeated use over the course of at least one month (Figure S3.5).

3.2.4 Application example III. *In-situ* reversible protein attachment to solid-state nanopores

To evaluate the applicability of the Ni^{2+}-EDTA functionalization on more complex surface geometries, we tested its performance with solid-state nanopores (Figure 3.1c). The procedure for functionalizing SiN membranes (20 nm thickness) containing a single nanopore (approximately 45 nm diameter) was identical to what we established above on planar surfaces, and was performed *ex situ*. The process of protein grafting on the inner surface of the pore was, however, subsequently done *in situ*. To this end, the nanopore was mounted into a custom-made flow cell for measurements of the ion current. The channels of the flow cell were flushed with working buffer, and care was taken to keep the membrane wet throughout the measurement. Current *versus* voltage (*I/V*) curves were recorded from -200 mV to +200 mV to test the quality of the pore. A minority of the tested Ni^{2+}-EDTA functionalized pores (6 out of 17) were found to be either asymmetric in the *I/V* characteristics (indicating an asymmetric pore or functionalization), or to have increased conductance (indicating pore growth) or very low conductance (indicating clogging by the multi-step chemical treatment). By contrast, most pores (11 out of 17) yielded the expected conductance level of marginally less than bare pores (95 ± 4 %, mean ± s.d.) at the given measurement conditions, and these pores were used for protein-binding studies.

After setting up the experiment, the baseline current across the nanopore was recorded at -100 mV. The model protein Nsp1-H$_{10}$ was then flushed into the *cis* chamber of the nanopore assembly (cf. Figure 3.1c) while the current was

continuously monitored. Figure 3.6a shows a gradual decrease in the conductance during protein exposure (1 to 7 min) starting from the baseline level (75 nS) until a new equilibrium is reached at 24 nS. This lowering of the conductance is consistent with the formation of a film of $Nsp1-H_{10}$ proteins that are anchored at the nanopore walls and enhance the pore resistance. The binding of $Nsp1-H_{10}$ is specific to the Ni^{2+}-EDTA functionalization: no significant changes in conductance were observed when bare SiN pores were exposed to $Nsp1-H_{10}$ constructs (Figure S3.6).

Comparative transmission electron microscopy of the nanopore before and after coating with $Nsp1-H_{10}$ (Figure S3.7) provided further evidence for protein attachment. Next, the nanopore was subjected to a regeneration protocol, which consisted of incubation with a regeneration mixture (1 M imidazole and 1 M GuHCl; 20 min) followed by washing with ultrapure water, then a 1:1 (*v*/*v*) mixture of ethanol and water, and finally with measurement buffer to complete one cycle. This led to a recovery of the conductance to a level of 67 nS, *i.e.*, close to the starting conductance value.

To assess the possibility of reusing the same pore, we performed additional cycles of protein incubation and pore regeneration. The representative data in Figure 3.6a (>28 min) shows clear conductance shifts for both $Nsp1-H_{10}$ FILV→S (2nd cycle) and $Nsp1-H_{10}$ (3rd cycle), indicating successful immobilization of the protein and regeneration of the pore. The *I*/*V* curves after coating the pore with proteins were found to be linear (Figure 3.6b-c, red and green traces). The pores filled with protein thus retain the ohmic behaviour of the bare Ni^{2+}-EDTA functionalized pores (Figure 3.6b-c, blue traces), as expected, although the slope of the *I*/*V* curves is smaller due to the reduced conductance with the proteins. Notably, the effect of the FILV→S mutant on the conductance was significantly smaller than that of wild type Nsp1, which is understood from the different organization of these mutant FG domains in the pore.[18c] The protein attachment and regeneration cycles were performed on different pores (n = 3; average size 45 ± 4 nm as measured by transmission electron microscopy; Figure S3.7) and the conductance dropped from 65 ± 7 nS to 21 ± 4 nS (by 67 %) upon attachment of $Nsp1-H_{10}$, and from 65 ± 7 nS to 35 ± 6 nS (by 46 %) for $Nsp1-H_{10}$ FILV→S. These conductance values are in good agreement with our previous work on the same proteins, which showed 80% and 50% conductance blockage for Nsp1 and Nsp1 FILV→S, respectively, that were immobilized by cysteine maleimide chemistry.[18c] The Nsp1 FILV→S mutant has a reduced cohesiveness compared to wild type Nsp1, and we have previously shown that this leads to the formation of a less dense biopolymer meshwork[19d] (see also Figure S3.3). The smaller effect of the FILV→S mutants on conductivity as compared to wild type Nsp1 reflects an enhanced permeability of monovalent ions and is consistent with a less dense meshwork

(see refs. [18c, 26] for the biophysical relevance of the different ion conduction through Nsp1 and Nsp1 FILV→S).
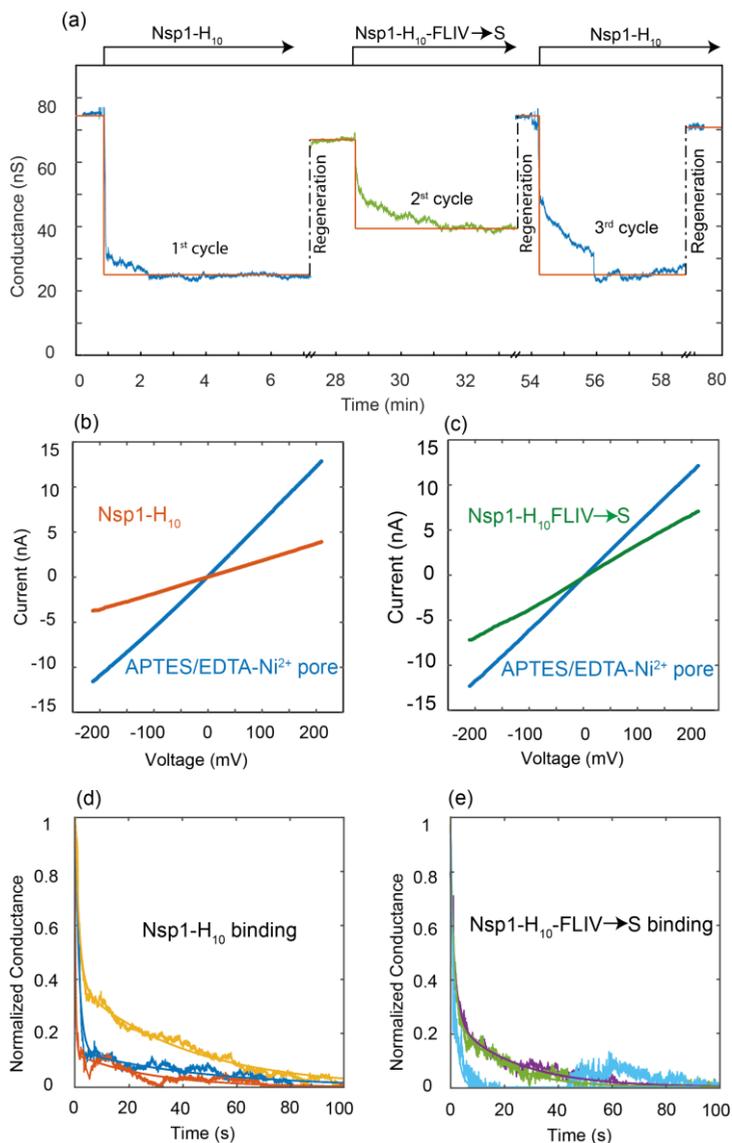
Figure 3. 6. Real time monitoring of protein immobilization in solid-state nanopores. (a) Ion current I, continuously recorded at an applied voltage $V = -100$ mV across a Ni^{2+}-EDTA-functionalized nanopore of 40 nm diameter, during sequential cycles of protein injection (Nsp1-H_{10} – blue, Nsp1-H_{10} FILV→S – green) and surface regeneration (regeneration steps not shown). The red line is a guide to the eye, and the plotted current traces were low-pass filtered at 1 kHz and down-sampled 100 times. (b-c) Current *vs.*

voltage (I/V) curves for a nanopore functionalized with Ni^{2+}-EDTA (blue), and incubated with Nsp1-H_{10} (red) or Nsp1-H_{10} FILV→S (green). Data correspond to the first and second cycle in (a). (d-e) Conductance *vs.* time for injection of Nsp1-H_{10} (d) and Nsp1-H_{10} FILV→S (e). Three representative binding curves are shown for each case, and the conductance was normalized by the conductance prior to protein injection to facilitate comparison. Conditions: buffer – 10 mM Tris, 150 mM KCl, pH 7.4; Nsp1-H_{10} and Nsp1-H_{10} FILV→S – 1.5 **µM; regeneration** – 1 M imidazole and 1 M GuHCl, 20 min. Conductance traces were low-pass filtered at 1 kHz and down sampled 100 times.

Upon surface regeneration, we regained the baseline conductance level to 93±5 % (n = 4), suggesting that the self-assembled monolayer underneath is retained without damage. The ability to selectively bind and detach proteins at will thus provide the flexibility to tether whichever protein with a polyhistidine tag, in much the same way as we have shown in more detail above for planar surfaces. The used nanopores were later subjected to oxygen plasma treatment, yielding an increase of the pore conductance by 6 ± 3 % (n = 2) compared to the protein-free Ni^{2+}-EDTA functionalized pores. This difference was in agreement with the conductance decrease of 5 ± 4 % (n = 11) observed upon Ni^{2+}-EDTA functionalization.

The time-resolved conductance measurements also shed light on the kinetics of protein binding to the modified nanopore. Close examination (Figure 3.6d-e) reveals two distinct response regimes upon incubation of the Nsp1 constructs: conductance decreases rapidly during the first seconds of incubation and then more slowly over several minutes before changes become comparable with the noise and a plateau is effectively attained. Similarly, two regimes can also be observed for the binding of the Nsp1 constructs to planar surfaces (by QCM-D and SE, cf. Figure S3.2, 3.3a and 3.4a). We have previously shown that the initial binding of FG domains to planar surfaces is limited by mass transport from the solution, and that a kinetic barrier arises once a continuous polymer film has formed that gradually slows further binding.[19d] Equivalently, two binding regimes would be expected inside the nanopores, and we suggest that this explains the two conductance regimes observed in Figure 3. 6.

3.3 Conclusions

We have established a surface functionalization method that uses Ni^{2+}-loaded EDTA moieties to selectively immobilize His-tagged proteins on materials that present silicon oxide on their surfaces (such as silicon or silicon nitride wafers and quartz or borosilicate glass) at well-defined orientation and tuneable surface density (Figure 3. 2). The method should be particularly attractive for biosensing applications because the method requires only bulk chemicals and follows a simple chemistry, and the coating can be regenerated and reused multiple times and retains functionality upon storage for several months (Figure 3.3). Importantly, the method can be applied to surfaces of complex geometry, as demonstrated here for nanopores (Figure 3.6). Moreover, the silane chemistry used to form the EDTA coating on silica can be combined with thiol chemistries on gold (here demonstrated with the passivation of gold, Figure 3.5), making it possible to apply the reversible immobilization of proteins on silica with an orthogonal surface chemistry on gold in the same device.

We demonstrated the benefits of first establishing the surface functionalization on planar surfaces, because these enable detailed, time-resolved and quantitative characterization of protein films (including morphology, surface density, stability of immobilization and triggered release, binding and reorganization processes, and protein-protein interactions; Figures 3.2-3.4) with surface sensitive techniques such as QCM-D and SE. The optimized surface functionalization and protein immobilization method was then translated to more complex surfaces such as solid-state membranes with nanopores. Such a two-step approach should also be useful for the establishment of other surface functionalization methods in the context of biosensor development and other applications requiring well-defined surface biofunctionalization.

We have directly demonstrated successful functionalization of nanopores using *in situ* ion current measurements (Figure 3.6). An attractive target for future efforts will be the functionalization of gold-coated nanoporous SiN membranes, in such a way that His-tagged proteins are selectively coating the inside of the nanopores (silica) whilst the outer membrane scaffold (gold) remains inert to protein adsorption. This functionalization approach would focus recognition processes to the interior of nanopores. Such functionalization should be useful for advancement in nanopore-based sensing (*e.g.* of biomarkers[27] and antibodies[14]), and also for highly selective filtration and sieving applications.

3.4 Experimental Section

Functionalization of silicon-based surfaces.

(3-aminopropyl)triethoxysilane (APTES), N-(3-dimethylaminopropyl)-N'-ethylcarbodiimide hydrochloride (EDC) and ethylenediaminetetraacetic acid tetrasodium salt hydrate (EDTA) were purchased from Sigma-Aldrich. Four different silicon-based substrates were used: (a) silicon wafers (BT Electronics, Les Ulis, France; for SE measurements), (b) QCM-D sensors with a reactively sputter-coated film of silica (QSX303; Biolin Scientific, Västra Frölunda, Sweden; for QCM-D measurements), (c) Silicon wafers with a 20 nm low-pressure chemical vapour-deposited silicon nitride coating (Dimes Technology Centre, Delft, The Netherlands; for control SE measurements), and (d) silicon nitride membranes (20 nm thickness) with a single nanopore (45 ± 4 nm diameter).[28] Silicon and silicon **nitride form a thin layer of 'native' silicon oxide upon exposure to air, and all four** surfaces thus effectively present OH groups. Substrates (a) to (c) were cleaned by immersion in an aqueous solution of 2 % sodium dodecyl sulphate (SDS; Carl Roth, Germany; 30 min), followed by rinsing with ultrapure water, ethanol and ultrapure water, blow-drying with nitrogen gas and exposure to UV/ozone (BioForce Nanosciences, Ames, IA; 30 min). Substrate (d) was cleaned by rinsing in ultrapure water, ethanol, acetone and isopropanol followed by gentle blow-drying with nitrogen gas and exposure to oxygen plasma (Pico; Diener Electronic GmbH, Nagold, Germany; 30 s).

Surface functionalization with APTES was performed in the vapour phase, adapting a method previously described by Wang et al.[29] We found this method to reproducibly generate homogeneous silane layers that were stable in aqueous medium, whereas functionalization in the liquid phase may lead to less homogenous and less stable coatings.[30] Specifically, a clean desiccator of approximately 2 L volume was conditioned by purging with argon (5 min), **deposition of a drop (30 µL) of APTES, and additional 2 min of argon flow. Freshly** cleaned surfaces were then placed inside the desiccator and following an argon purge for 3 min the desiccator was sealed with parafilm and the sample left to incubate for 1 h. After APTES treatment, samples were sequentially immersed in aqueous solutions containing 0.5 M EDTA and 25 mM EDC at pH 8 (adjusted with HCl) at room temperature, first once for 3 h, then twice for 2 h, and eventually once overnight, rinsed in ultrapure water and blow-dried with nitrogen gas. The solutions were prepared freshly before each incubation step, and the large excess of EDTA over EDC ensured that only one carboxyl group per EDTA reacted with a primary amine on the solid phase.[31] Prior to use, the EDTA on the solid phase was

loaded with nickel ions through immersion in an aqueous solution of 2 mM NiCl$_2$ (15 min).

Functionalization of gold surfaces. A linear oligo (ethylene glycol) derivative containing 7 ethylene glycol units, and with a thiol group on one end and an OH group on the other (thiol-OEG), was obtained from Polypure (Oslo, Norway). QCM-D sensors with a gold coating (QSX301; Biolin Scientific) were used as substrates and cleaned as the silicon-based surfaces described above. For functionalization, gold surfaces were incubated with 1 mM thiol-OEG in ultrapure water for at least 18 h, rinsed with ultrapure water and blow-dried with nitrogen gas.

Proteins. The main protein used was the FG domain (amino acids 2 to 601) of the yeast nucleoporin Nsp1 with a C-terminal polyhistidine tag (Nsp1-H$_{10}$; 64.1 kDa). We also used an equivalent mutant construct in which all phenylalanines, isoleucines, leucines and valines were replaced by serines (Nsp1-H$_{10}$ FILV→S; 60.4 kDa), and the wild type Nsp1 FG domain lacking a histidine tag (Nsp1; 62.1 kDa). FG domain constructs were purified as described earlier[19b] and stored at 10 mg mL^{-1} concentration in 50 mM Tris, pH 8 and 6 M guanidine hydrochloride (GuHCl) at -80°C. Green fluorescent protein with an N-terminal polyhistidine tag (H$_{14}$-GFP; 27 kDa) was stored at 2.7 mg mL^{-1} concentration in 40 mM Tris, pH 7.5, 260 mM NaCl, 4 mM magnesium acetate, 0.4 mM EDTA, 250 mM saccharose, and 2 mM dithiothreitol at -80°C. The nuclear transport receptor importin β from *Saccharomyces cerevisiae* (Impβ, 95 kDa) was purified as described earlier,[19b] and stored at 9.5 mg mL^{-1} concentration in 40 mM Tris pH 7.5, 260 mM NaCl, 4 mM magnesium acetate, 0.4 mM EDTA, 250 mM saccharose, and 10 mM β-mercaptoethanol at -80 °C. Before use, proteins were diluted in working buffer to desired concentrations; the dilutions of the Nsp1 constructs were chosen such that the residual concentration of GuHCl in the final solutions was below 75 mM.

Buffers. For measurements on planar surfaces, we used a working buffer containing 10 mM HEPES and 150 mM NaCl at pH 7.4. For measurements with nanopores, the working buffer contained 10 mM Tris and 150 mM KCl at pH 7.4. These buffers were chosen according to established routines for the characterization of each substrate; in a comparative QCM-D control measurement on planar surfaces, we verified that Nsp1-H$_{10}$ FILV→S films of comparable surface density and morphology are formed in both buffers (Figure S3.8).

Quartz crystal microbalance with dissipation monitoring (QCM-D). QCM-D monitors changes in resonance frequency Δ*f* and dissipation Δ*D* of a sensor crystal upon interaction of (soft) matter with its surface. The QCM-D response is sensitive to the mass, including hydrodynamically coupled water, and the mechanical properties of the surface-bound layer.[24] To a first approximation,

a decrease in Δf indicates an increase in film areal mass density, and high (low) values of $\Delta D/\text{-}\Delta f$ indicate a soft (rigid) film. QCM-D measurements were performed with a Q-Sense E4 system equipped with Flow Modules (Biolin Scientific). The system was operated in flow mode with a flow rate of 10 µL min^{-1} using a syringe pump (KD Scientific, Holliston, MA, USA), and the working temperature was 23°C. Δf and ΔD were measured with a time resolution of around 1s at the fundamental (i = 1) and six overtones (i = 3, 5, ...,13), corresponding to resonance frequencies $f_i \approx$ 5, 15, 25, ..., 65 MHz. Normalized frequency shifts, $\Delta f = \Delta f_i/i$, and dissipations shifts, $\Delta D = \Delta D_i$, for i = 5 are presented; any other overtone would have given qualitatively similar information.

Spectroscopic ellipsometry (SE). SE measures changes in light polarization upon reflection on a sample surface. The ellipsometric angles Δ and Ψ were measured as a function of time and modelled to quantify the surface density of immobilized proteins. A spectroscopic ellipsometer (M2000V; Woollam, Lincoln, NE, USA; wavelength range λ = 380 to 1000 nm) with a horizontal plane of incidence was used, as described in detail elsewhere.[19b, 19c] Briefly, the binding of biomolecules to functionalized silicon wafers was followed in working buffer using a custom-made open-cuvette liquid cell (200 µL volume) with continuously stirred sample solution[19b] at 70° angle of incidence. Sample solutions were injected directly into the buffer-filled cuvette and excess sample was removed by repeatedly diluting the cuvette content in buffer.

Data were fitted with CompleteEASE software (Woollam) using a model of optically homogeneous layers as described in detail in previous work.[19b] Specifically, the SiO_2 (or SiN) layer with APTES/EDTA functionalization, and the protein film, were treated as two distinct transparent Cauchy layers each with an optical thickness h_{SE} and a wavelength-dependent refractive index $n = A + B/\lambda^2$. The surrounding working buffer was also treated as a transparent Cauchy medium with $n_{buffer} = 1.325 + 0.00322/(\lambda/\mu m)^2$, and the dispersion parameter B of the protein film was assumed to be identical to that of the buffer. Protein surface densities were determined using de Feijter's equation,[32] $\Gamma = h_{SE}\,\Delta n/(M_w \times dn/dc)$, where Δn is the difference between the refractive indices of the solvated protein film and the surrounding buffer solution, M_w is the protein molecular weight, and dn/dc is the refractive index increment (0.18 cm^{3}g^{-1} for proteins[33]).

Nanopore fabrication and measurements. Nanopores were fabricated on silicon nitride (SiN) membranes deposited on silicon wafers as described elsewhere in detail.[28] In brief, nanopore chips were built-up on a 100 silicon wafer by adding supporting layers of silicon dioxide and low-stress SiN. By employing UV-lithography, reactive-ion etching and chemical etching, these supporting layers were etched away to produce a free-standing SiN window of 10 × 10 µm^2

surface area and 20 nm thickness. A nanopore was drilled into the SiN membrane window by transmission electron microscopy (Tecnai 200STEM-FEG; FEI, Eindhoven, The Netherlands) operated at 300 kV. Membranes with a nanopore were stored in a solution containing 50% (v/v) ethanol in ultrapure water until further use.

For protein immobilization and conductance measurements, a membrane with nanopore was loaded in a custom-made poly (methyl methacrylate) flow cell with 30 μL liquid volume on each side of the membrane (*cis* and *trans*), and the flow cell was flushed with working buffer (at least 3 times the cell's volume). Ag/AgCl electrodes were used to apply electric fields and measure the ionic current across the nanopore. The ionic current was recorded with an electrophysiology patch clamp setup Axopatch 200B amplifier at 100 kHz bandwidth and digitized at 500 KHz (Digidata 1322A DAQ; Molecular Devices, CA, USA). The data was analysed with a custom-made Matlab script.

3.5 Supporting Information
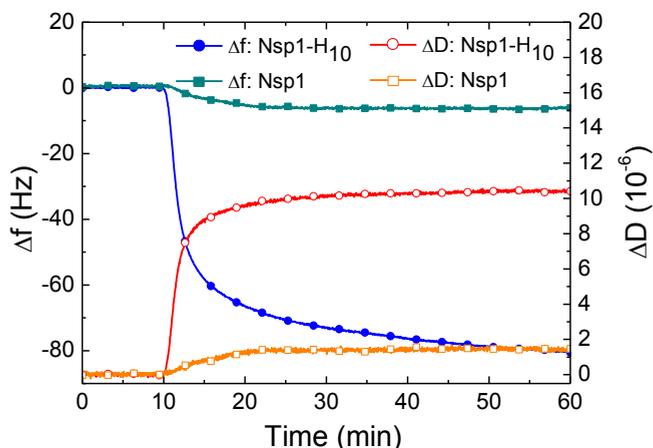
Figure S3.1. Selectivity for His-tagged proteins. The selective anchoring via the His tag was evaluated by comparing the binding of Nsp1-H_{10} with an identical Nsp1 construct that lacks the His tag. While Nsp1-H_{10} binding is comparable to Figure 3.2, only minor binding is observed for Nsp1. Conditions: buffer – 10 mM HEPES, 150 mM NaCl, pH 7.4; Nsp1-H_{10} and Nsp1 –1.5μM; surfaces were functionalized with EDTA and loaded with $NiCl_2$ (2 mM for 15 min) prior to the measurements.

Figure S3.2. Functional coatings on SiN and SiO_2 have comparable propensity to immobilize His-tagged proteins. (a) SE data of Nsp1-H_{10} binding and triggered release on functionalized SiN with a solution of 0.5 M imidazole and 1 M GuHCl (for 50 min, not shown). The maximal bound amount, binding stability and specificity of binding is comparable to SiO_2 (cf. Figure 3.2). (b) Averaged areal mass density of immobilized Nsp1-H_{10}, measured by SE after 50 min of incubation at 1.5 μM (grey bars) and after surface regeneration as in (a) (white bars) for functionalized SiO_2 and SiN surfaces. Error bars are standard deviations of independent measurements with 8 different SiO_2 surfaces and 4

different SiN surfaces. Conditions: buffer – 10 mM HEPES, 150 mM NaCl, pH 7.4; Nsp1-H_{10}–
1.5 μM; surfaces were functionalized with EDTA and loaded with $NiCl_2$ (2 mM for 15 min)
prior to the measurements.

Figure S3.3. Morphology of protein films. **The parameter** ΔD/-Δf was derived from QCM-
D data and is a measure for the softness of the protein films; -Δf is a measure for the surface
coverage. Because film mechanical properties and morphology are linked, this parametric
plot provides insight into the evolution of the overall film morphology with protein
coverage.[23-24] Data for proteins on Ni^{2+}-EDTA on aminosilane are taken from Fig.3.4a. For
comparison, data on supported lipid bilayers (SLBs) displaying Ni^{2+}-loaded nitrilotriacetic
acid (Ni^{2+}-NTA) for capture of His-tagged proteins are also shown (Nsp1-H_{10} and Nsp1-H_{10}
FILV→S from Fig. 4 in ref. [19d], H_{14}-GFP from Fig. 2 in ref. [23]). Proteins on aminosilane
exhibit the same trends as on SLBs: Nsp1-H_{10} FILV→S films are softer than Nsp1-H_{10} films
owing to the reduced cohesiveness of the mutant protein, and both films become more
rigid as protein coverage increases and the films become denser. It is notable that Nsp1
FG domain films appear slightly more rigid when formed on aminosilanes as compared to
SLBs. We tentatively attribute this to differences in the anchorage: when anchored to the
SLBs, proteins are laterally mobile but when anchored to aminosilanes they are not. As
expected, the monolayer of globular GFP appears much more rigid than the meshwork of
disordered and interpenetrating Nsp1 FG domains. The rigidity of GFP films is comparable
on aminosilanes and on SLBs. For GFP, the decrease in ΔD/-Δf with –Δf is due to
hydrodynamic coupling between proteins, as explained in detail in ref. [23].

Figure S3.2. Functional coatings on SiN and SiO_2 have comparable propensity to immobilize His-tagged proteins. (a) SE data of Nsp1-H_{10} binding and triggered release on functionalized SiN with a solution of 0.5 M imidazole and 1 M GuHCl (for 50 min, not shown). The maximal bound amount, binding stability and specificity of binding is comparable to SiO_2 (cf. Figure 3.2). (b) Averaged areal mass density of immobilized Nsp1-H_{10}, **measured by SE after 50 min of incubation at 1.5 μM (gr**ey bars) and after surface regeneration as in (a) (white bars) for functionalized SiO_2 and SiN surfaces. Error bars are standard deviations of independent measurements with 8 different SiO_2 surfaces and 4 different SiN surfaces. Conditions: buffer – 10 mM HEPES, 150 mM NaCl, pH 7.4; Nsp1-H_{10}–**1.5 μM; surfaces were functionalized with EDTA and loaded with $NiCl_2$ (2 mM for 15 min)** prior to the measurements.

Figure S3.3. Morphology of protein films. **The parameter** ΔD/-Δf was derived from QCM-D data and is a measure for the softness of the protein films; -Δf is a measure for the surface coverage. Because film mechanical properties and morphology are linked, this parametric plot provides insight into the evolution of the overall film morphology with protein coverage.[23-24] Data for proteins on Ni^{2+}-EDTA on aminosilane are taken from Fig.3.4a. For comparison, data on supported lipid bilayers (SLBs) displaying Ni^{2+}-loaded nitrilotriacetic acid (Ni^{2+}-NTA) for capture of His-tagged proteins are also shown (Nsp1-H_{10} and Nsp1-H_{10} FILV→S from Fig. 4 in ref. [19d], H_{14}-GFP from Fig. 2 in ref. [23]). Proteins on aminosilane exhibit the same trends as on SLBs: Nsp1-H_{10} FILV→S films are softer than Nsp1-H_{10} films owing to the reduced cohesiveness of the mutant protein, and both films become more rigid as protein coverage increases and the films become denser. It is notable that Nsp1 FG domain films appear slightly more rigid when formed on aminosilanes as compared to SLBs. We tentatively attribute this to differences in the anchorage: when anchored to the SLBs, proteins are laterally mobile but when anchored to aminosilanes they are not. As expected, the monolayer of globular GFP appears much more rigid than the meshwork of disordered and interpenetrating Nsp1 FG domains. The rigidity of GFP films is comparable **on aminosilanes and on SLBs. For GFP, the decrease in** ΔD/-Δf with −Δf is due to hydrodynamic coupling between proteins, as explained in detail in ref. [23].

Figure S3.4. OEG-coated gold surfaces are inert to protein adsorption. The QCM-D shift upon exposure of Nsp1-H_{10} to differently functionalized gold surfaces: thiol-OEG, EDTA/APTES, and bare gold (as indicated). No response is observed on thiol-OEG demonstrating full passivation by comparison to the strong QCM-D shift obtained upon Nsp1-H_{10} adsorption on EDTA/APTES functionalized gold and on bare gold. Conditions: buffer – 10 mM HEPES, 150 mM NaCl, pH 7.4; Nsp1-H_{10} – 1.5 µM.
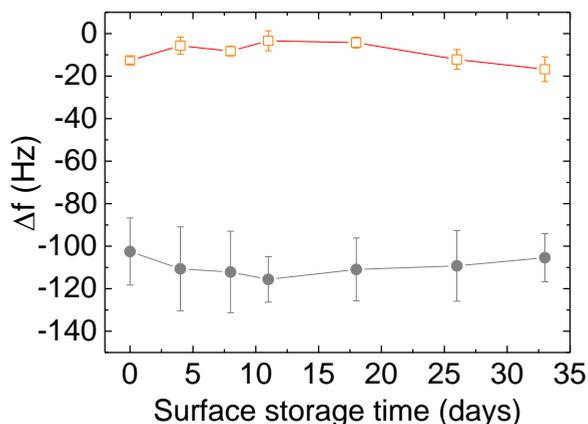
Figure S3.5. Stability upon storage and re-use of orthogonally functionalized surfaces. QCM-D frequency shifts at equilibrium, upon incubation with a His tagged FG domain H_{18}-Mac98 (0.3 μM for 60 min) are shown as a function of storage time. This reflects the conservation of His-tag binding capacity on silica (grey filled circles) and the passivation of gold (orange open squares) over the course of one month. Before each measurement, the surfaces were re-loaded with $NiCl_2$; after each measurement, the surfaces were regenerated with 0.5 M imidazole and 1 M GuHCl (30 min), rinsed with buffer and water, blow-dried in nitrogen gas and stored dry in the dark at room temperature until the next measurement. Error bars represent standard deviations for two measurements with two different sensors; the same sensors were repeatedly used to acquire all data shown. For this set of measurements, the FG domain of Nup98 from *Tetrahymena thermophila* with an N terminal H_{18} tag (H_{18}-Nup98; 61 kDa; see B. Schmidt, D. Görlich. *eLife*. 2015, *4*, e04251 for protein preparation) was used thus demonstrating application to another His tagged protein. Additional tests with Nsp1-H_{10} over a period of 20 days showed comparable stability.
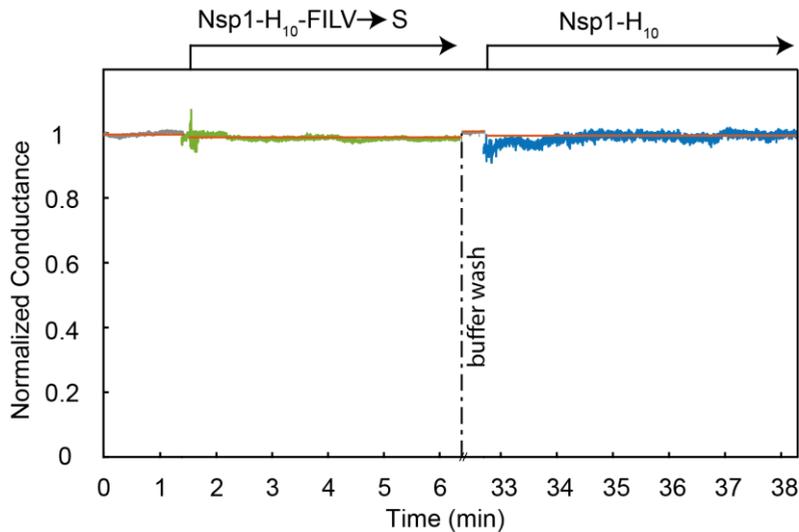
Figure S3.6. Nsp1-H_{10} proteins do not bind to bare SiN nanopores. Shown are representative ion current traces for bare SiN nanopores of 40 nm diameter. Exposure to Nsp1-H_{10} and Nsp1-H_{10} FILV→S (as indicated) does not affect the conductance level significantly compared to the baseline conductance. Data are presented analogous to Figure 3.6a.
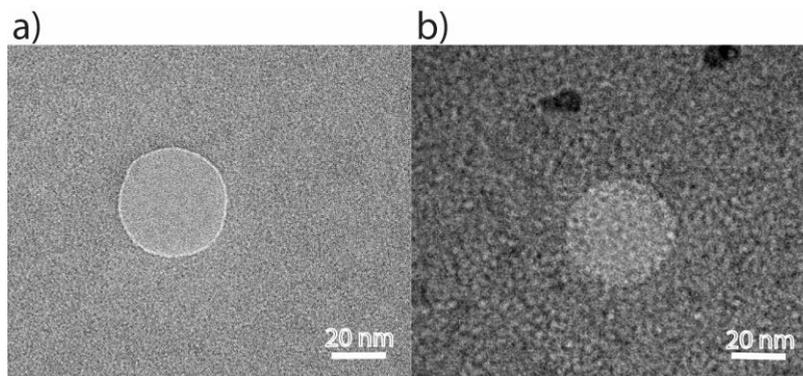
Figure S3.7. Transmission electron micrographs of nanopores. (a) Bare nanopore of 40 nm diameter. (b) The same nanopore after *in situ* Nsp1-H_{10} coating. In (b), the presence of bio-organic material in the pore and on the SiN membrane surface is evidenced by the grainy appearance which is lacking in (a). Similar images have been reported in a previous study for Nsp1-coated solid-state nanopores.[18c] We emphasize that the exact structural arrangement of the Nsp1 cannot be elucidated from such images because the structure of disordered proteins is generally difficult to resolve, and because the sample has been dried and is imaged in high-vacuum imaging conditions.
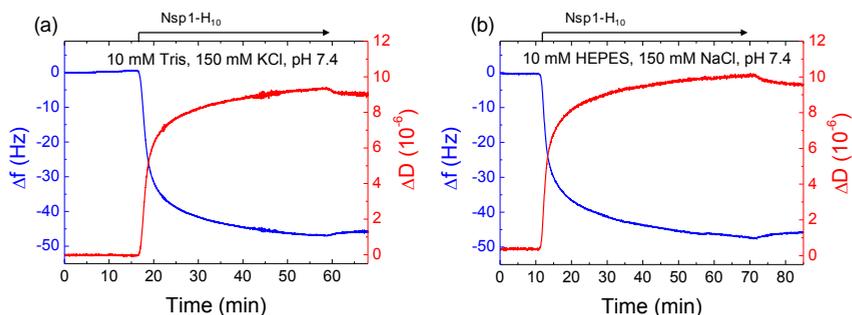
Figure S3.8. Buffer and cation types do not affect Nsp1 immobilization. Binding of Nsp1-H_{10} FILV→S is shown in (a) 10 mM Tris, 150 mM KCl, and in (b) 10 mM HEPES, 150 mM NaCl, both at pH 7.4. Conditions: Nsp1-H_{10} – 1.5 μM; silica surfaces were functionalized with EDTA and loaded with $NiCl_2$ (2 mM for 15 min) prior to the measurements.

References

[1]   a) F. Traversi, C. Raillon, S. M. Benameur, K. Liu, S. .Khlybov, M. Tosun, D. Krasnozhon, A. Kis, A. Radenovic. *Nat. Nanotechnol.* 2013, *8*, 939; b) A. P. Ivanov, E. Instuli, C. M. McGilvery, G. Baldwin, D. W. McComb, T. Albrecht, J. B. Edel. *Nano Lett.* 2011, *11*, 279.

[2]   a) C. E. Korman, M. Megens, C. M. Ajo-Franklin, D. A. Horsley. *Langmuir.* 2013, *29*, 4421; b) C. Duan, A. Majumdar. *Nat. Nanotechnol.* 2010, *5*, 848; c) C. Ho, R. Qiao, J. B. Heng, A. Chatterjee, R. J. Timp, N. R. Aluru, G. Timp. *Proc. Natl. Acad. Sci. U. S. A.* 2005, *102*, 10445.

[3]   a) M. Pastoriza-Gallego, M.-F. Breton, F. Discala, L. Auvray, J.-M. Betton, J. Pelta. *ACS Nano.* 2014, *8*, 11350; b) C. C. Striemer, T. R. Gaborski, J. L. McGrath, P. M. Fauchet. *Nature.* 2007, *445*, 749; c) A. Ivankin, R. Y. Henley, J. Larkin, S. Carson, M. L. Toscano, M. Wanunu. *ACS Nano.* 2014, *8*, 10774.

[4]   Y. Feng, Y. Zhang, C. Ying, D. Wang, C. Du. *Genomics, Proteomics Bioinf.* 2015, *13*, 4.

[5]   a) X. Lin, Q. Yang, L. Ding, B. Su. *ACS Nano.* 2015, *9*, 11266; b) I. Vlassiouk, P. Y. Apel, S. N. Dmitriev, K. Healy, Z. S. Siwy. *Proc. Natl. Acad. Sci. U. S. A.* 2009, *106*, 21039.

[6]   S. W. Kowalczyk, T. R. Blosser, C. Dekker. *Trends Biotechnol.* 2011, *29*, 607.

[7]   a) K. C. Popat, G. Mor, C. A. Grimes, T. A. Desai. *Langmuir.* 2004, *20*, 8035; b) M. Pla-Roca, L. Isa, K. Kumar, E. Reimhult. *ACS Appl. Mater. Interfaces.* 2015, *7*, 6030.

[8]   a) M. Wanunu, A. Meller. *Nano Lett.* 2007, *7*, 1580; b) R. Wei, V. Gatterdam, R. Wieneke, R. Tampe, U. Rant. *Nat. Nanotechnol.* 2012, *7*, 257.

[9]   T. D. Lazzara, T.-T. Kliesch, A. Janshoff, C. Steinem. *ACS Appl. Mater. Interfaces.* 2011, *3*, 1068.

[10]   a) J. Li, D. Stein, C. McMullan, D. Branton, M. J. Aziz, J. A. Golovchenko. *Nature.* 2001, *412*, 166; b) A. J. Storm, J. H. Chen, X. S. Ling, H. W. Zandbergen, C. Dekker. *Nat. Mater.* 2003, *2*, 537.

[11]   B. M. Venkatesan, R. Bashir. *Nat. Nanotechnol.* 2011, *6*, 615.

[12]   a) M. J. Kim, M. Wanunu, D. C. Bell, A. Meller. *Adv. Mater.* 2006, *18*, 3149; b) M.-Y. Wu, D. Krapf, M. Zandbergen, H. Zandbergen, P. E. Batson. *Appl. Phys. Lett.* 2005, *87*, 113106.

[13]   R. Wei, D. Pedone, A. Zürner, M. Döblinger, U. Rant. *Small.* 2010, *6*, 1406.

[14]   E. C. Yusko, J. M. Johnson, S. Majd, P. Prangkio, R. C. Rollings, J. Li, J. Yang, M. Mayer. *Nat. Nanotechnol.* 2011, *6*, 253.

[15]   a) V. Mussi, P. Fanzio, L. Repetto, G. Firpo, P. Scaruffi, S. Stigliani, G. P. Tonini, U. Valbusa. *Nanotechnology.* 2010, *21*, 145102; b) S. M. Iqbal, D. Akin, R. Bashir. *Nat. Nanotechnol.* 2007, *2*, 243.

[16]   a) S. Lata, J. Piehler. *Anal. Chem.* 2005, *77*, 1096; b) A. Tinazli, J. Tang, R. Valiokas, S. Picuric, S. Lata, J. Piehler, B. Liedberg, R. Tampé. *Chem. Eur. J.* 2005, *11*, 5249; c) S. Wijeratne, W. Liu, J. Dong, W. Ning, N. D. Ratnayake, K. D. Walker, M. L.

Bruening. *ACS Appl. Mater. Interfaces.* 2016, *8*, 10164; d) T. Muhammad Nawaz, A. Mubarak, A. Rute, M. Werner E. G., S. Heinz-Christoph, T. Wolfgang, E. Wolfgang. *Chem.Commun.* 2013, *49*, 2210.

[17] a) M. Lepoitevin, M. Bechelany, J.-M. Janot, S. Balme. *Sci. Lett.* 2015, *4*; b) Z. Chen, T. Chen, X. Sun, B. J. Hinds. *Adv. Funct. Mater.* 2014, *24*, 4317; c) M. Ali, P. Ramirez, I. Duznovic, S. Nasir, S. Mafe, W. Ensinger. *Colloids Surf., B.* 2017, *150*, 201.

[18] a) T. Jovanovic-Talisman, J. Tetenbaum-Novatt, A. S. McKenney, A. Zilman, R. Peters, M. P. Rout, B. T. Chait. *Nature.* 2009, *457*, 1023; b) S. W. Kowalczyk, L. Kapinos, T. R. Blosser, T. Magalhaes, P. van Nies, R. Y. H. Lim, C. Dekker. *Nat. Nanotechnol.* 2011, *6*, 433; c) A. N. Ananth, A. Mishra, S. Frey, A. Dwarakasing, R. Versloot, E. v. d. Giessen, D. Görlich, P. Onck, C. Dekker. *eLIFE (2018).*

[19] a) S. Frey, R. P. Richter, D. Gorlich. *Science.* 2006, *314*, 815; b) N. B. Eisele, S. Frey, J. Piehler, D. Gorlich, R. P. Richter. *EMBO Rep.* 2010, *11*, 366; c) N. B. Eisele, F. I. Andersson, S. Frey, R. P. Richter. *Biomacromolecules.* 2012, *13*, 2322; d) N. B. Eisele, A. Labokha, S. Frey, D. Gorlich, R. P. Richter. *Biophys. J.* 2013, *105*, 1860.

[20] a) E. L. Schmid, T. A. Keller, Z. Dienes, H. Vogel. *Anal. Chem.* 1997, *69*, 1979; b) N. Haddour, S. Cosnier, C. Gondran. *J. Am. Chem. Soc.* 2005, *127*, 5752.

[21] a) S. Durán, M. Duch, T. Patiño, A. Torres, O. Penon, R. Gómez-Martínez, L. Barrios, J. Esteve, C. Nogués, L. Pérez-García, J. A. Plaza. *Sens. Actuators, B.* 2015, *209*, 212; b) E. Briand, V. Humblot, J. Landoulsi, S. Petronis, C.-M. Pradier, B. Kasemo, S. Svedhem. *Langmuir.* 2011, *27*, 678.

[22] a) M. P. Jonsson, A. B. Dahlin, L. Feuz, S. Petronis, F. Höök. *Anal. Chem.* 2010, *82*, 2087; b) F. Nicoli, D. Verschueren, M. Klein, C. Dekker, M. P. Jonsson. *Nano Lett.* 2014, *14*, 6917.

[23] D. Johannsmann, I. Reviakine, R. P. Richter. *Anal. Chem.* 2009, *81*, 8167.

[24] I. Reviakine, D. Johannsmann, R. P. Richter. *Anal. Chem.* 2011, *83*, 8838.

[25] D. G. Kurth, T. Bein. *Langmuir.* 1995, *11*, 3061.

[26] M. Mazzanti, J. O. Bustamante, H. Oberleithner. *Physiol. Rev.* 2001, *81*, 1.

[27] J. Shim, G. I. Humphreys, B. M. Venkatesan, J. M. Munz, X. Zou, C. Sathe, K. Schulten, F. Kosari, A. M. Nardulli, G. Vasmatzis, R. Bashir. *Sci. Rep.* 2013, *3*, 1389.

[28] J. A. J. Xander, P. J. Magnus, P. Calin, V. S. Gautam, D. Cees, H. D. Nynke. *Nanotechnology.* 2012, *23*, 475302.

[29] H. Wang, R. Bash, J. G. Yodh, G. L. Hager, D. Lohr, S. M. Lindsay. *Biophys. J.* 2002, *83*, 3619.

[30] N. Aissaoui, L. Bergaoui, J. Landoulsi, J.-F. Lambert, S. Boujday. *Langmuir.* 2012, *28*, 656.

[31] D. Goerlich, S. Frey (imac) *US* 20110071274 A1. 2011.

[32] J. A. De Feijter, J. Benjamins, F. A. Veer. *Biopolymers.* 1978, *17*, 1759.

[33] R. P. Richter, K. B. Rodenhausen, N. B. Eisele, M. Schubert, In *Ellipsometry of Functional Organic Surfaces and Films*, Vol. 52, (Eds: K. Hinrichs,K.-J. Eichhorn), Springer, Berlin, Heidelberg, Germany 2014, Ch. 11.

4.

Ionic permeability and mechanical properties of DNA origami nanoplates on solid-state nanopores

While DNA origami is a popular and versatile platform, its structural properties are still poorly understood. In this study we use solid-state nanopores to investigate the ionic permeability and mechanical properties of DNA origami nanoplates. DNA origami nanoplates of various designs are docked onto solid-state nanopores and measure their ionic conductance. The ionic permeability is found to be high for all origami nanoplates. We observe the conductance of docked nanoplates, relative to the bare nanopore conductance, to increase as a function of pore diameter, as well as to increase upon lowering the ionic strength. The honeycomb lattice nanoplate is found to have slightly better overall performance over other plate designs. After docking, we often observe spontaneous discrete jumps in the current, a process which can be attributed to mechanical buckling. All nanoplates show a non-linear current-voltage dependence with a lower conductance at higher applied voltages, which we attribute to a physical bending deformation of the nanoplates under the applied force. At sufficiently high voltage (force), the nanoplates are strongly deformed and can be pulled through the nanopore. These data show that DNA origami nanoplates are typically very permeable to ions and exhibit a number of unexpected mechanical properties

4.1 Introduction

Solid-state-nanopore research[1, 2] is an area which has been gaining much attention due to its potential applications in sequencing, biosensing, and as a tool for biophysics. In this technique an electric field is applied across a membrane containing a single pore. Charged molecules such as DNA experience an electrophoretic force which pulls them through the pore. Molecules are detected by the temporary reduction (or increase at low salt) in the ionic current which they cause as they pass through the pore. Despite recent advances[1, 2] in solid-state-nanopore research, biological pores still offer several advantages such as a higher signal-to-noise ratio,[3] slower DNA translocation velocity,[4] and the possibility for adding chemical modifications to the channel by creating mutant proteins.[5] In an attempt to combine the advantages of solid-state pores with those of biological pores, in 2010, our group demonstrated that a stable hybrid pore could be built by capturing an α-hemolysin protein pore with a DNA tail into a solid state nanopore.[6] This work subsequently opened up a new stream of research into combining biological structures with solid-state nanopores in order to open up new functionalities.

This approach can be extended to DNA origami, a technique introduced by Paul Rothemund in 2006 which allows complex shapes to be built from DNA by **designing short oligonucleotide "staples" which upon hybridization bring two** defined parts of a large single-stranded DNA template together.[7] Through the rational design of staples, the single-stranded DNA template can thus be folded into any desired shape. Since its introduction, DNA origami has grown into a robust technique capable of reliably producing 3D structures[8, 9] such as boxes, spheroids, and complex objects with curved surfaces.[10, 11]

DNA origami can be used to create DNA origami nanopores. Recent literature has reported the creation of hybrid nanopores by capturing DNA origami nanoplates containing apertures[12] as well as funnel-like structures[13] onto solid state nanopores and glass nanocapillaries.[14] Synthetic lipid membrane channels[15, 16] have also been made using DNA origami nanostructures. The versatile approach, of docking DNA origami nanostructures onto solid-state nanopores, allows great control over both the geometry and the chemical functionality of the pore. Wei *et al* created a square honeycomb-lattice-based DNA-origami nanoplate with a central aperture. Their nanoplate contained a long ssDNA tail extending from the side of the aperture (close to the center of the nanoplate) to facilitate proper insertion. Initial work with this system showed translocation of DNA and protein through a docked nanoplate and stochastic sensing of target molecules using a

bait-prey scheme. Bell *et al* focused on a hollow pyramid type structure with an aperture and a tail at the apex, reminiscent of the structure of α-hemolysin or MspA, with a top side larger than the diameter of the solid-state pore. Their work showed the ability to capture and insert these structures into the pore and subsequently translocate dsDNA through docked nanostructures. These first experiments provided a good proof-of-concept and established that this technique can be used to add additional functionalities to solid-state nanopores. In addition, this approach can be used to study the inherent properties of DNA origami at the single-molecule level and measure properties, such as ionic permeability, which cannot be determined with other methods.

Here, we carry out a fundamental investigation into the ion conduction and mechanical properties of DNA origami nanoplates, by docking them onto solid-state nanopores. The approach begins with electrophoretically capturing an origami plate (without an aperture) by use of a long centrally located DNA tail into a pore, as shown in Figure 4.1. The tail allows the guided insertion of the nanostructure with a well-defined orientation onto a solid-state nanopore. An example 3D cross section of a honeycomb lattice nanoplate docked onto a 20 nm nanopore is shown in Figure 4.1a. The docking of a nanoplate is observed in real time by a reduction in the current level as shown in Figure 4.1b. Once docked, a current-voltage sweep such as shown in Figure 4.1c, reveals a lower conductance when the nanoplate is docked (red curve) compared to the conductance for a bare nanopore (blue) taken before the nanoplate was added. Nanoplates can be undocked from the nanopore by reversing the polarity of the applied voltage or by pulling them through the pore by significantly increasing the voltage, as shown below. The docking time is found not to be an intrinsic property but dependent on the experiment. Most nanoplates would stay docked forever if kept at low voltages.

The ionic permeability of the nanoplate is an important parameter for origami nanopores to optimize because it sets the magnitude of the current blockade in sensing single biomolecules relative to the baseline current. The ideal nanoplate should have minimal leakage of ions through the nanoplate itself, with the majority of the ionic current given by ionic transport through the open aperture, leading to a high ratio between the excluded volume of the translocating molecule and the total volume available to carry ions. This would result in a high signal-to-noise ratio. Secondly, the nanoplate should have a high mechanical stability under any applied voltage. We investigate these issues by experimenting with different nanoplate designs, varying the diameter of the solid-state nanopores, probing a wide range of voltages, and altering buffer conditions. We find that the conductance of the nanoplates is high and increases as a function of

pore diameter and ionic strength. Additionally, we see interesting mechanical effects including deformation, buckling, and structural failure under increasing applied force.

4.2 Results and discussions

First, we investigated how the geometry of the DNA nanoplates influences their ionic permeability. Four different nanoplate designs were used, as shown in Figure 4.2a. None of the designs contained an aperture, to ensure that the measured current was only due to the ionic permeability of the nanoplate itself. The first design (HC) utilized a honeycomb-type DNA-packing architecture and has lateral dimensions of 45 nm x 52 nm with a thickness of 6.75 nm and an ideal spatial filling factor[12] of 0.605. The other designs are all based on the square-lattice rectangular DNA origami nanoplates introduced[7] by Paul Rothemund with varying thicknesses of one, two, or three DNA layers. The filling factor for these plates is expected to be below 0.785, as several studies[17, 18] have shown the DNA helices in the square-lattice are not close packed.

The one-DNA-layer-thick Rothemund rectangle (RR) has lateral dimensions of 98 nm x 54 nm, the two-DNA-layer-thick rectangle (2LL) has 51 nm x 54 nm, and the three-DNA-layer-thick design (3LL) has 40 nm x 45 nm. Since each design is based on oligo-staple hybridization with a standard M13 single-stranded DNA template (RR and HC 7560 bases, 2LL and 3LL 7704 bases), the lateral dimensions of the designs are reduced as the thickness is increased. CanDo[19, 20] finite-element modeling was used to predict the flexibility of each plate (Supplementary Section 8). This revealed that the RR plate should be quite deformed, as evident in Figure 4.2a, due to a large twist along the plate, although thermal fluctuations and surface effects should be able to force it into a flat state. This twist is caused by the square lattice and was compensated for in the 2LL and 3LL designs by designing staples which skip hybridization to some bases of the scaffold.[11]

The predicted plate stiffness, as established from the range of RMS fluctuations (provided in the brackets) over different parts of the structure can be ordered **from highest to lowest as follows: HC (0.3 to 0.8 nm)** $\approx$ 3LL (0.3 to 1.0 nm) > 2LL (0.6 to 1.7 nm) > RR (1.2 to 3.5 nm). In addition to the electrophysiological measurements, which are the main focus of this work, the DNA nanoplates were characterized using TEM and high-speed liquid AFM. Negative-stain TEM was used to verify proper nanoplate assembly with averaged micrographs for each design shown in Figure 4.2c. The high-speed liquid AFM provides high-resolution images of the plates (Figure 4.2b) but also allowed us to confirm the good stability of each design in a variety of buffer conditions. Details of the TEM and AFM characterization have been provided in Supplementary Section 4.5.77.We first

report how the ionic conductance of the nanoplates varies among the different designs, how it depends on the nanopore diameter, and how the observed trends can be reproduced with a simple model. The diameter of the solid-state nanopores onto which nanoplates were docked was varied from 5 nm to 30 nm. Figure 4.3a shows the observed relative conductances (*i.e.* the conductance of the pore with the plate relative to that of the bare pore) for the honeycomb (HC) nanoplate at 200 mV in 1 M KCl. The relative conductance decreases as the diameter on the solid-state nanopore is reduced. We see the relative conductance decrease from about 0.8 in large 30 nm pores down to below 0.6 in small 5 nm pores. Similar plots for the other nanoplate designs and at different voltages are shown in Supplementary Section 4.5.1.

The solid line in Figure 4.3a represents a least-squares fit to the data using the model outlined below, with only one free parameter (a). Experimentally we measure G_{hybrid}, the conductance of the nanopore in series with the conductance of the nanoplate. As in previous work[12] this can be modeled as

$$G_{hybrid} = \left[\frac{1}{G_{pore}} + \frac{1}{G_{plate}} \right]^{-1} , \quad (1)$$

where the conductance of the pore[21] is given by

$$G_{pore} = \kappa \left[\frac{4l_{pore}}{\pi d^2} + \frac{1}{d} \right]^{-1} , \quad (2)$$

where κ is the conductivity of the buffer, l_{pore} is the effective thickness of the solid-state nanopore, and d is its diameter. Note that Eq. 2 also includes the access-resistance[21] contribution which was ignored in previous work.[12] We model the conductance of the nanoplate using

$$G_{plate} = \frac{\pi a \kappa d^2}{4} , \quad (3)$$

where a is a phenomenological parameter with units of inverse length given by

$$\alpha = \frac{f(V)}{l_{plate}} , \quad (4)$$

where l_{plate} **is the nanoplate's thickness** and $f(V)$ is a dimensionless function related to the applied voltage and the filling factor (F). If we ignore the (non-linear) voltage dependence discussed later on, $f(V)$ equals

$$f(V) = 1 - F , \quad (5)$$

where F is the filling factor of the nanoplate. It is useful to examine the limiting behavior of α. When the nanoplate becomes very thick $(l_{plate} \rightarrow \infty)$, α approaches zero. In the other limit of very thin plates, we encounter the minimum plate thickness which is set by the diameter of a single DNA helix (2.25nm). Here, the value of α approaches zero for a fully filled plate (F=1), whereas it goes to 1/(2.25nm) as the filling factor goes to zero. In the context of optimizing the nanoplate design, the value of α should be as low as possible, since this represents the smallest leakage through the nanoplate, thus giving the highest signal-to-noise ratio in DNA translocation experiments through a nanopore in the nanoplate. The nanoplate designs are experimentally best characterized by their relative conductance (RC), the ratio of G_{hybrid} to G_{pore}. Combining equations 1, 2, and 3, we thus obtain

$$RC = \frac{G_{hybrid}}{G_{pore}} = \frac{1}{1+\dfrac{4}{\alpha\left(4l+\pi d\right)}} \quad . \quad (6)$$

This model nicely captures the observed trend of a decreasing relative conductance as the diameter of the solid-state nanopore is reduced, as seen in the solid line of Figure 4.3a. For the example in Figure 4.3a, α = 0.112 ± 0.06 nm^{-1}. Generally, we find values for α in the range from 0.10 to 0.18 nm^{-1}, see Figure S4.7, where we plot the value of the fit parameter α as a function of voltage. We find that the honeycomb nanoplate has the lowest leakage (lowest α). Surprisingly, the one-layer-thick Rothemund rectangle nanoplate has the next best characteristics, while the two and three-layer-thick nanoplates are worst. Although the differences are small, this observation is counterintuitive as we would expect the thicker nanoplates to have less leakage. Even though the higher leakage as the lateral dimensions of the origami nanoplate are decreased could indicate the presence of some leakage currents flowing in between the nanoplate and the solid-state nanopore substrate, we do not believe this to be a significant effect given the small size of the nanopores relative to the large size of the nanoplates involved as well as other factors discussed in detail in
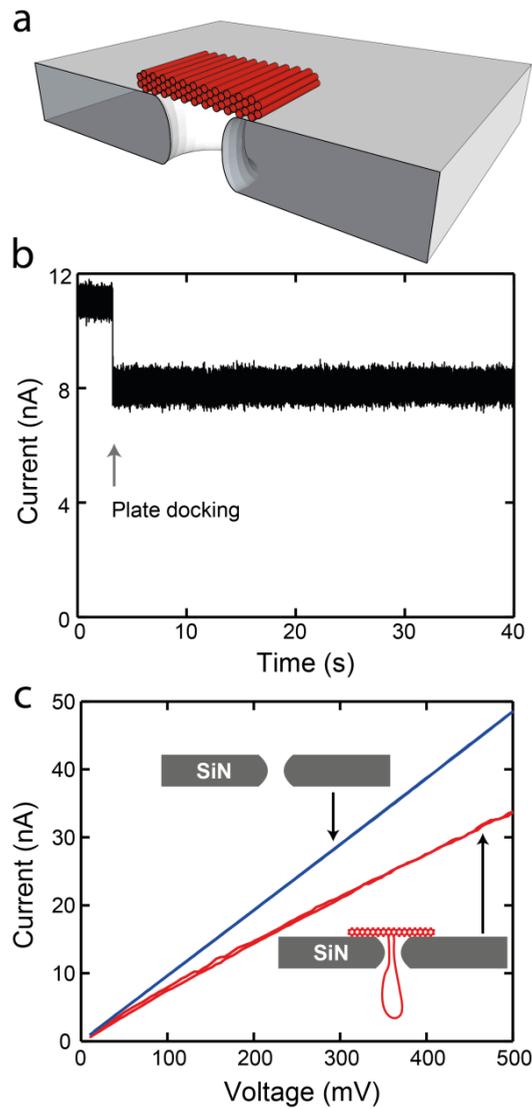
Figure 4.1. a) 3D representation showing a cross-sectional view of a honeycomb lattice DNA nanoplate docked onto a SiN nanopore. The tail has been omitted for visual clarity. b) Current trace of a honeycomb nanoplate captured onto a 14 nm pore at 100 mV. c) IV curve for a bare 14 nm SiN pore (blue) as well as for the same pore after a honeycomb nanoplate was docked (red).
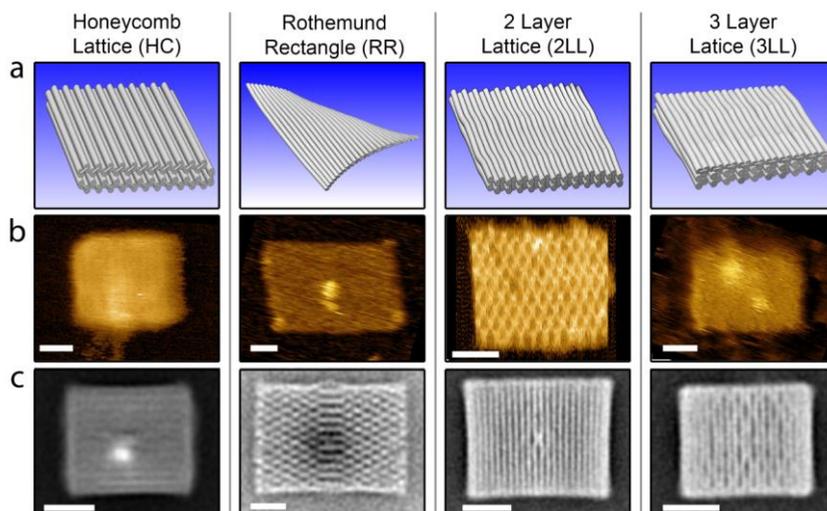
Figure 4.2. Properties of four different DNA origami nanoplates. a) 3D representations of each design. b) Liquid tapping-mode AFM scans for each nanoplate design. Variations in image resolution can be attributed to differences in AFM tip sharpness. c) TEM class averages of negative stain micrographs for each plate (RR adapted from Sobczak *et al.*[30]). All scale bars are 20 nm.

Supplementary Section 4.1. This phenomenon, of the thicker square-lattice plates being leakier, is therefore attributed to differences in the particular design of the nanoplates such as the arrangement of the oligo staples.

The dependence of the RC on the ionic strength of the buffer is shown in Figure 4.3b. The relative conductance is found to increase as the salt concentration is decreased. In other words, the nanoplates appear to become leakier as the salt concentration drops. The relative conductance is observed to increase from around 0.8 at 1 M KCl up to 0.9 at salt concentration of 100 mM KCl or lower. Similar trends are observed for all other nanoplate designs and different pore sizes (see Supplementary Section 2 and 3). For the salt concentrations tested (1 M KCl, 400mM KCl, 100 mM KCl, 40mM KCl, and 10 mM KCl) the Debye screening length is 0.31 nm, 0.47 nm, 0.89 nm, 1.26 nm, and 1.82 nm, respectively. At 100 mM and lower, the Debye layer from neighboring DNA strands should begin to overlap in many areas of the DNA origami nanoplate. As the salt concentration is lowered from the (typically used) 1 M value, the reduced electrostatic screening **could have two effects on a nanoplate's ionic permeability. First, increased** electrostatic repulsion between neighboring strands could increase the size of the holes present in-between the crossover points[17], allowing more ions to pass though the structure, thus increasing the ionic permeability.

This effect is a contributing factor, together with mechanically induced twist, in the diamond-like pattern clearly visible in the AFM and TEM characterization (Figure 4.2) of some plates, and has been observed in previous Cryo-EM[17] and AFM[22] studies of DNA origami structures. The structure swells up to the point where it is constrained by the oligo-staples. In addition to this, the higher effective negative charge and larger Debye screening lengths of the DNA leads to a higher cation selectivity, attracting more positive potassium (K^+) ions while repelling the negatively charged chloride (Cl^-) ions present in the solution.[23] This may result in higher conductivities than the bulk conductivity of the solution, as reported previously for small charged nanopores in low salt conditions.[24] The observed increase at low ionic strengths is likely due to a combination of these two effects.
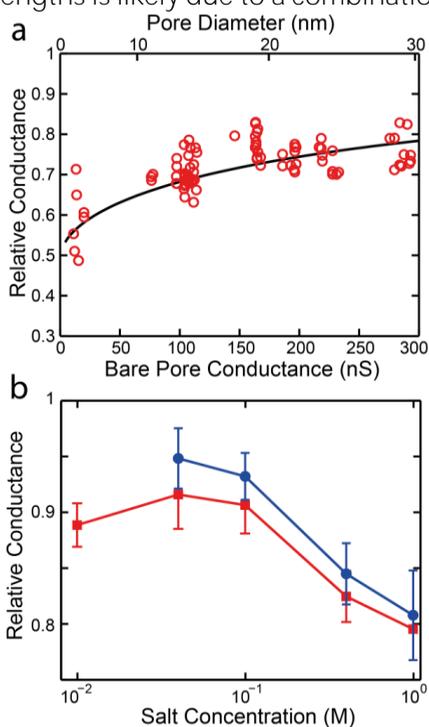
Figure 4.3. a) The relative conductance, G_{hybrid}/G_{pore} for the honeycomb nanoplate design at 200 mV in 1 M KCl buffer plotted *versus* the pore conductance, which scales inversely with pore diameter (see nonlinear scale at the top). Solid line denotes a fit of Eq. 6 giving a = 0.112 ± 0.06 nm^{-1}. b) Salt dependence of the relative conductance for the 2LL nanoplates docked onto 24 nm pores at 300 mV (red squares) and 200 mV (blue circles).

The measurements reveal that, while high salt concentrations should be preferred, the docking of nanoplates into nanopores can be detected in salt concentrations as low as 10 mM, opening up the possibility of conducting measurements on docked nanoplates at physiological conditions.

We found that the presence of magnesium in the buffer was unimportant for the behavior of the nanoplates. Although it has been recently shown that Magnesium divalent cations are not required for proper folding of the DNA origami structures,[25] the need for a divalent cation such as magnesium in the buffer can be rationalized as a means to allow the negatively charged nanoplate to stick to the negatively charged surface (an effect well known from AFM literature) of the SiN surface at pH 8, where all measurements are carried out. All nanoplates were folded in a buffer containing 20 mM Mg. Before measuring, these stock solutions are diluted into the proper salt concentration with new buffers containing 11 mM Mg. As a control, we also diluted some samples into magnesium-free buffer resulting in a final Mg concentration of around 0.5 mM. No differences were observed in the relative conductance measurements for these samples compared to those carried out in buffer with 11 mM Mg (data not shown). Furthermore, no issues were encountered with the docking of the nanoplates, suggesting that the electrophoretic force and van der Waals adhesion are stronger than the electrostatic forces. Over typical experimental timescales of several hours, no deterioration in the stability of the nanoplates was observed. These results show that the presence of high concentrations of magnesium in the buffer is not a stringent requirement for either maintaining nanoplate stability or facilitating the docking of nanoplates into solid-state nanopores.

Next, we report an interesting observation that was not anticipated, namely the effects of mechanical deformation of the nanoplates. We find that docked nanoplates may undergo physical deformation as the voltage is increased and can even be pulled through the pore if sufficient force is applied. Once a nanoplate is docked into a pore, we can subject the nanoplate to a voltage ramp in order to probe its current-voltage (IV) characteristics. Voltage sweeps begin at 10 mV and go to 800 mV in steps of 5 mV (each 103 ms long), and subsequently we ramp back down to 10 mV. Examples of typical IV curves can be seen in Figure 4.1c for a HC nanoplate on a 14 nm pore and in Figure 4.4a for a 2LL nanoplate on a 9 nm pore. All nanoplates exhibit non-linear IV behavior with the conductance of the nanoplate being reduced as the voltage is increased. This trend can also be seen in the decrease of the fit parameter alpha as a function of voltage (Figure S4.7). We attribute this effect to the nanoplate undergoing increased physical deformation as the voltage is increased, which brings more DNA material into the pore (*cf.* sketch in the bottom right inset to Figure 4.4a).
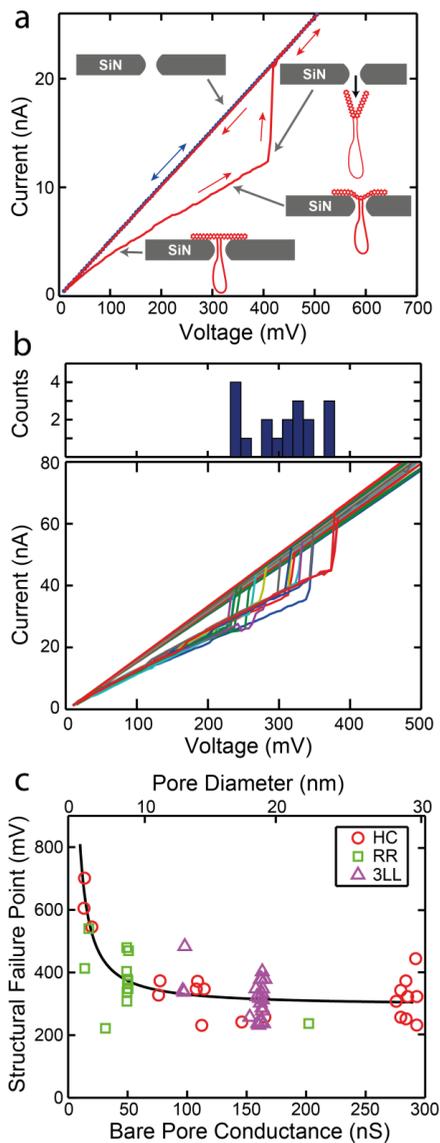
Figure 4.4. a) IV curve (red) showing a 2LL nanoplate undergoing structural failure and being pulled through a 9 nm pore. Once pulled through, the conductance of the pore returns to the level seen for the bare pore (blue dots). b) IV curves of 18 different 3LL nanoplates being pulled through a 19 nm pore. Top panel displays a histogram of the structural failure points. c) The structural failure points for three nanoplate designs docked onto different-diameter pores. It can be seen that smaller pores require a greater force to pull the nanoplate through. The solid line has been added to guide the eyes.

This idea is supported by the fact that beyond a critical voltage value, the current level is observed to suddenly return to the bare pore level as shown in Figure 4.4a, after which the IV curve is linear, reproducible, and back to the conductance value for the bare nanopore, indicating that the nanoplate has been pulled through the pore, as also proven using recapture experiments described below. We term the voltage level at which this occurs the structural failure point (SFP). This effect is quite reproducible, and we are able to repeatedly capture nanoplates and pull them through, as shown in Figure 4.4b, where 18 different 3LL nanoplates are pulled through a 19 nm pore. The histogram at the top shows that the mean SFP is at a voltage of 307 ± 51 mV. If we plot the observed SFP for different nanoplate designs in different pores, as shown in Figure 4.4c, we observe that, not surprisingly, a higher voltage, and thus higher force, is required to pull the nanoplates through smaller pores compared to larger pores. The dependence on pore diameter is in fact even stronger than apparent for Figure 4.4c, since our detection method misses many SFPs with a large value (exceeding our maximum voltage of 800 mV) in small pores and additionally, it misses SFPs with a small value in larger pores. In small pores (~5 nm) it is often very difficult to pull a nanoplate through the pore (as evidenced by the low number of SFP events occurring). Instead, almost all nanoplates docked onto small pores remain stable up to the maximum applied voltage of 800 mV and are not pulled through. In large-diameter pores, some nanoplates are instantly pulled through already at the typical docking voltage (200 mV), thus creating short translocation events that are observed as spikes in the recorded current trace as they pass through the pore. The short spikes are observed to occur most frequently for the most flexible nanoplate, the single-layer Rothemund rectangle. This is expected because more flexible plates will undergo more deformation at a given level of applied force compared to stiffer plates. Figure S4.15 shows the spikes observed from RR nanoplates being pulled through a 24 nm pore at 200 mV and higher. This effect underlies the lack of data collected for the RR nanoplate in large-diameter pores, as evident in Figure 4.4c, Figure S4.1, and elsewhere. In addition to flexible plates, plates containing structural defects, such as those caused by missfolding are likely to be pulled through the pore very quickly.

In order to conclusively prove that the nanoplates were actually being pulled through the pore (rather than undocking back into the cis insertion chamber), we carried out recapture experiments where the electric field was reversed shortly after a spike was observed. If a nanoplate is being pulled through the pore, it should be recaptured if the electric field is reversed quickly enough and thus produce another spike. As shown in Figure S4.16, we indeed were able to recapture many nanoplates. The ability to recapture nanoplates when switching even 3 seconds after the translocation event at an applied voltage of 200 mV

shows that the nanoplates were pulled through and undergo a slow drift-diffusion away from the pore. All our observations thus reveal that the nanoplates undergo mechanical deformation as the force applied on them is increased, and furthermore that the nanoplates can be completely pulled through the pore if sufficient force is applied. Flexible nanoplates can easily be pulled through larger pores, something which should be taken into account in future designs of origami nanopores.

Another surprising observation is that the current through a docked nanoplate can suddenly and randomly jump between discrete levels. Observations of many such spontaneous jumps over time indicate that these jumps occur to and from quantized levels as shown in Figure 4.5a for a RR nanoplate docked in a 20 nm pore. These levels are clearly visible as discrete peaks in the histogram of the current trace, shown on the right. The magnitude of the jumps is up to about 10% of their relative conductance. Examples for other plate designs are provided in Supplementary Section 5. These jumps are also often seen during IV sweeps, as shown in Figure 4.5b. Here an HC nanoplate was docked in a 10 nm pore and subjected to a voltage ramp during which it transitioned through three distinct levels before being pulled through at the SFP. Subsequently another HC plate was docked in the same pore and showed similar behavior when subjected to the same voltage ramp. Interestingly, the conductance switched among the *same* discrete values for these two independent plates (*cf.* dotted green lines). We often observe these level jumps occurring in a docked nanoplate at constant voltage just before a nanoplate is pulled through, as shown in Figure S4.18 and Figure S4.19.

All these observations indicate that the source of these jumps is a physical change in the nanoplate structure. Although not every nanoplate tested exhibits these jumps, statistics at 100 mV on the occurrence reveal the majority (69% of HC, 60% of RR, 44% of 2LL, and 75% of 3LL nanoplates) exhibit these jumps. At 200 mV applied voltage these percentages all increase, to 82%, 80%, 68%, and 76% respectively, as shown in Figure S4.20. The 2LL nanoplate thus appears to exhibit a smaller effect compared to the other plates. We have previously seen that the 2LL nanoplate, unlike the other nanoplates, shows a very weak voltage dependence for its conductance (Figure S4.7). Ideally for origami nanopore experiments, these jumps should be absent or as small as possible in order to distinguish them from the signals produced by translocations.
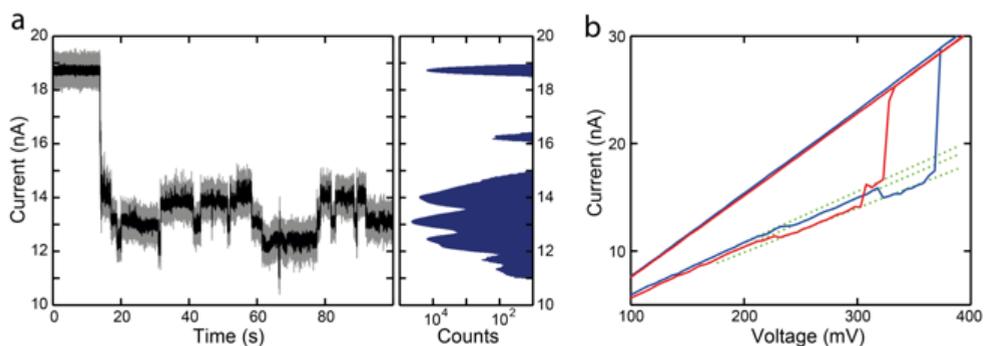
Figure 4.5 a) Current is seen to jump among a number of discrete levels for a Rothemund rectangle nanoplate docked onto a 20 nm pore at 100mV. The black trace shows data filtered at 20 kHz while the gray data is unfiltered. The histogram on the right shows the frequency of all of the current values in the trace on a log scale, with each peak representing a discrete level. b) IV curve of two different honeycomb nanoplates docked onto the same 10 nm pore. As the voltage is ramped up, the two nanoplates each jump through three distinct levels before being pulled through. Three dotted green lines have been added for visualization purposes.

Several different mechanisms could explain the physical origin of these jumps. Jumps occurring right after the nanoplate has docked could be attributed to the nanoplate orienting itself into the most energetically favorable position. We have indeed observed some events, which represent only a small fraction of the total events, where some jumps occurred within a short time after docking, after which the nanoplate remains at a stable current level for a long period of time (minutes) or indefinitely. The majority of jumps, however, continue occurring long after the nanoplate has docked and can be attributed to mechanical buckling of the nanoplate. Such buckling could be associated with various distinct mechanical modes of the plates. Temporary melting of the strands hybridized to the M13 template seems less likely since we see no evidence that ssDNA staples are ripped off of the nanoplates as jumps occur in both directions and will often return to the original conductance level after a number of jumps. It should be noted that Langeker et al[15] attributed part of the current gating they observed in their DNA origami nanochannel to a similar effect. Although melted strands could in principle rehybridize, they are unlikely to do so in the presence of the high electric field of the nanopore where the highly charged melted strand is pulled away from its hybridization counterpart. For unzipping of the strands, the orientation of the staples is also very important, as it is known that a lower force is required to unzip a DNA helix if it is applied to the 5' and 3' ends[26] of complementary strands compared to the 5' and 5' ends.[27] In summary, we see discrete jumps in the current levels in many docked nanoplates, an effect which may be attributed mechanical readjustments such as nanoplate re-orientation and mechanical buckling.

How does the tail of the nanoplates affect the relative conductance measurements? The DNA origami nanostructures tested all contained a tail, 648 bp to 798 bp in length, protruding from the center of the nanoplate in order to facilitate their proper insertion into the solid-state nanopore. Since this single-stranded tail will form a blob of secondary structures, as confirmed by AFM and in previous nanopore experiments,[28] we attempted to investigate if this blob impacts the observed conductance by comparing it to an identical nanoplate design where the single-stranded loop had been hybridized with short oligos into a fully double-stranded loop which due to its large persistence length should stick out far from the pore. Comparison of these two tail designs in a honeycomb nanoplate showed no significant differences (Supplementary Section 6). Based on the observations, we conclude that the tail design does not affect the conductance of the nanoplate.

4.3 Conclusion

The experimental results in this work present a detailed study of ionic permeability through DNA origami objects. The conductance data reveal that the honeycomb structure is the best design for minimizing the leakage through the nanoplate, while the 2LL nanoplate appears to have the best mechanical stability. A number of methods could be explored in the future to reduce the ionic permeability of the nanoplates. For example, groove binders and possibly intercalators could provide an interesting route. We have seen that, counterintuitively, creating a thicker nanoplate (up to 3 DNA helices thick) does not necessarily reduce the resulting ionic leakage through the nanoplate. The availability of ssDNA templates longer than M13 could allow much thicker structures to be created. Such structures could reveal whether there is an inherent minimum ionic permeability of DNA nanostructures which is independent of thickness, as our data suggests. Investigation into the behavior of the nanoplates in different ionic regimes revealed an increased leakage through the nanoplates as the monovalent salt concentration was reduced, whereas the reduction of the magnesium concentration was shown to have no detectable effect.

DNA origami is beginning to move beyond the early static structures towards active machines with advanced functionalities. The design of such machines requires insight into the dynamics of these structures, as explored in this study. We have seen that the force applied on the nanoplates can deform the structures, cause them to buckle, and even pull them through the pore if sufficient voltage is applied. Alternative versions of the designs tested here, with different oligo-

stapling or alternative scaffold routing may reveal how much the observed effects are dependent on minute design details connected to the stapling. Mechanical defects can be designed into plates to observe their effect on the plates mechanical properties such as the SFP. The combination of solid-state nanopores with DNA origami structures promises to open up a number of new possibilities that cannot be realized with other methods, including the ability to simultaneously integrate multiple receptors, binding sites, enzymes, protein, and simple mechanical machines directly within or adjacent to the nanopore.

4.4 Methods and Materials

Nanopore fabrication and measurements. SiN pores were fabricated as described previously.[29] Nanopore membranes were mounted in a PEEK flowcell separating two aqueous chambers into which Ag/AgCl electrodes were inserted. Solutions of nanoplates at approximately 200 pM concentration were added to the CIS reservoir and a voltage was subsequently applied. The measurement buffer (unless otherwise stated) consisted of 1 M KCl, 10 mM Tris, 1 mM EDTA, 11 mM Mg at pH 8. Ionic currents were detected using an Axopatch 200B amplifier at 100 kHz bandwidth and digitized with a DAQ card at 500 kHz. Current traces were analyzed using Matlab and Clampfit.

AFM and TEM. AFM measurements were carried out under solution on a RIBM High-Speed AFM 1.0. Imaging buffers contained 10 mM Tris pH 7.6, 10 mM MgCl and KCl concentrations varying between 10 and 1000 mM. No significant differences were observed between different KCl concentrations (Figure S4.25). Samples were prepared by applying a drop of origami nanostructures in their folding buffer to plates of freshly cleaved muscovite mica. After an incubation time of 10 minutes, unadhered origamis were gently rinsed off with imaging buffer. Without drying, the samples were then transferred to the liquid cell of the AFM and imaged in tapping mode using Nanoworld USC-f1.5-k0.6 cantilevers. The TEM protocol and image processing followed the method described in Wei *et al.*[12]

Nanoplate design and assembly. The structures were designed using caDNAno v 0.2. DNA staple oligonucleotide strands were prepared by solid-phase chemical synthesis (Eurofins MWG) with Eurofins MWG high purity salt-free purification grade. The folding buffer was 5 mM Tris-base, 1 mM EDTA, 20 mM MgCl2 (except for RR 12.5 mM), and 5 mM NaCl at pH8. For the scaffold strand either 7560 (RR & HC) or 7704 (2LL & 3LL) base long M13mp18-phage-derived genomic DNA was

used (20 nM). Staple strands were added with 10x excess (200 nM). The RR plate was folded in a thermocycler by ramping the temperature from 95°C to 25°C at 66 s/°C. For HC, 2LL, 3LL plates the temperature was ramped from 65°C to 60°C at 15 min/°C and then 59°C to 40°C with 3 h steps. All plates were subsequently stored at 4°C. The quality of folding was verified by 2% agarose gel electrophoresis (running buffer 0.5xTBE+11 mM MgCl2) showing that all structures fold with an acceptable yield. All the samples were 4x filter-purified after folding by using the folding buffers indicated above. Briefly, 50 µL of folded sample and 450 µL of buffer were added to Amicon Ultra 0.5 mL filter having molecular weight cutoff of 100 kDa. The sample was centrifuged with 14,000 rcf for 3 minutes. This step was repeated 3 times by adding 450 µL of buffer each round (final round 5 min centrifugation). Then the structures were collected to a fresh tube by placing the filter upside down and centrifuging with 1,000 rcf.

4.5 Supporting information

4.5.1 Nanoplate Conductance in 1M KCl

Here we present the relative conductances for all the nanoplate designs docked onto nanopores of various diameters. First, the data for individual nanoplates is shown at 200 mV (Figures S4.1-S4.3). Subsequently data for all designs is shown at 100 mV, 200 mV, and 300 mV (Figures S4-S6). Relative conductances were determined using the mean value of the current after nanoplate docking divided by the mean value of the bare pore current, as described in Eq. 6. Solid lines represent fits using the model described in the main manuscript. The bottom x-axis is the measured bare pore conductance for that respective data point, while the top x-axis is the estimated diameter of the nanopore based on the formula

$$d = \frac{1}{2\pi\kappa}\left(\pi G_{pore} + \sqrt{\left(\pi G_{pore}\right)^2 + 16\pi\kappa l G_{pore}} \right) \quad . \quad (S4.7)$$

where the measured conductivity of the buffer κ is 13.5 S/m and the effective thickness is taken to be 8.6 nm as previously determined.[1] We observe the relative conductance increase as the nanopore diameter is increased from 5 nm to 30 nm, as predicted by Eq. 6. The voltage dependence of the fit parameter α is shown in Figure S4.7. The value of α is observed to decrease, indicating that the plates become less permeable, as the applied voltage is increased. A number of IV curves for each type of plate, docked onto various size nanopores are shown in Figures S4.8-S4.11.
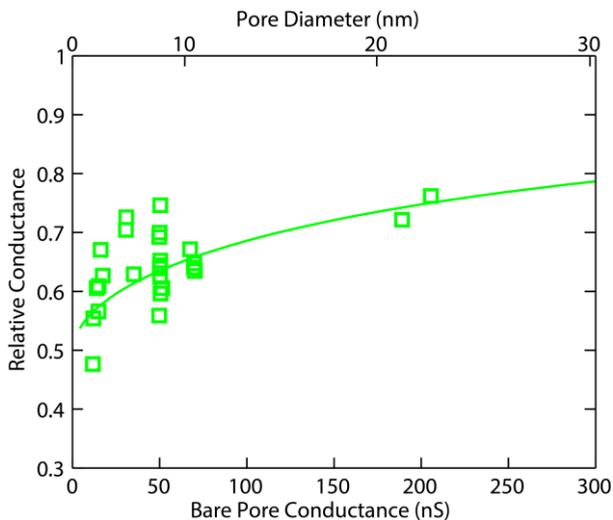
Figure S4.1 - Relative conductance for Rothemund Rectangle (RR) nanoplates at 200 mV in 1M KCl.
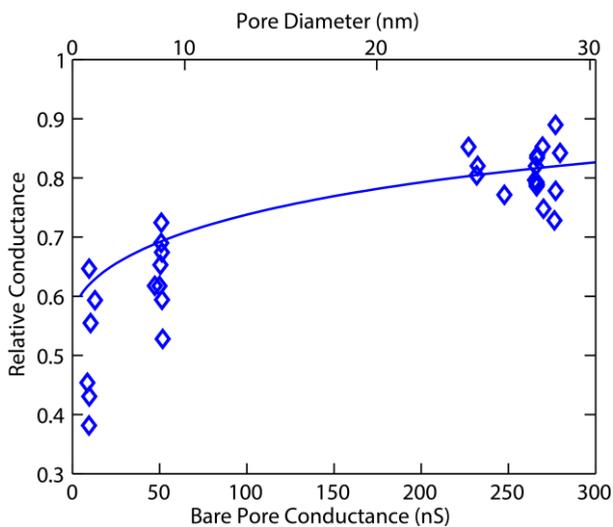
Figure S4.2 - Relative conductance for 2 Layer Lattice (2LL) nanoplates at 200 mV in 1M KCl.
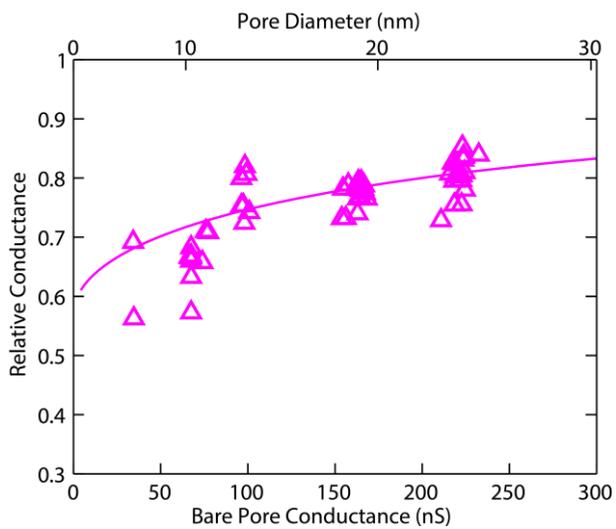
Figure S4.3 - Relative conductance for 3 Layer Lattice (3LL) nanoplates at 200 mV in 1M KCl.
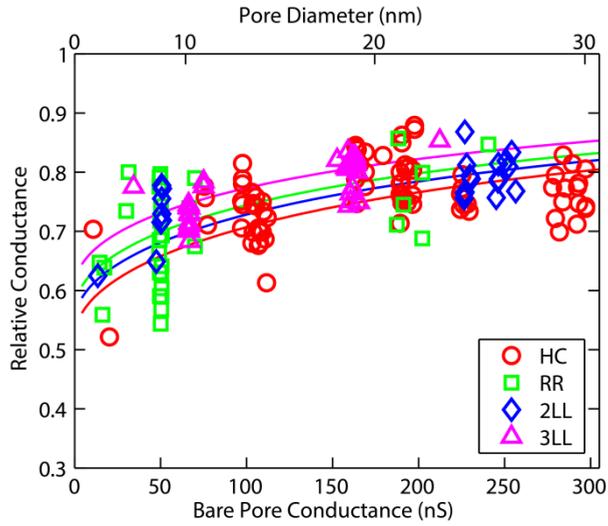
Figure S4.4 - Relative conductances for the four different nanoplate designs at 100 mV in 1M KCl.
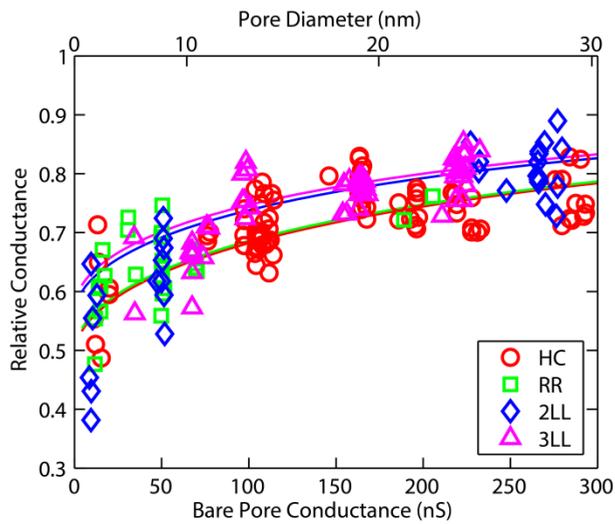
Figure S4.5 - Relative conductances for the four different nanoplate designs at 200 mV in 1M KCl.
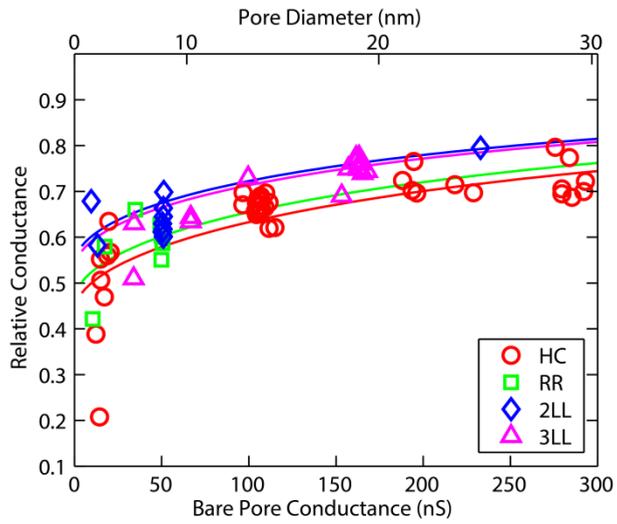
Figure S4.6 - Relative conductances for the four different nanoplate designs at 300 mV.
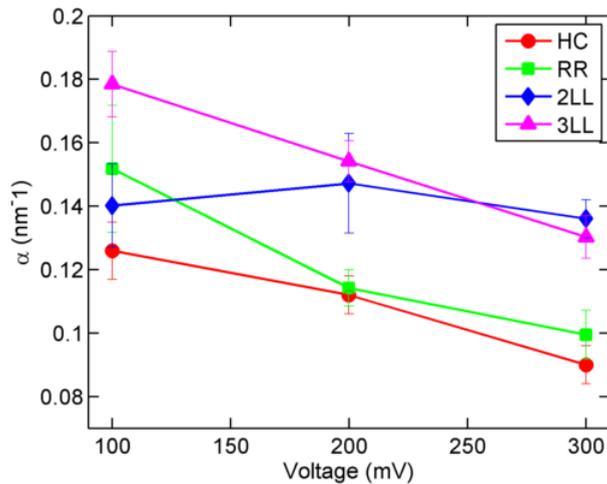
Figure S4.7 – **Dependence of the fit parameter α on the applied voltage. Smaller values of α represent less leakage through the nanoplate. We observe, with the exception of the** 2LL nanoplate, that the leakage decreases as the voltage is increased. Error bars represent 95% confidence intervals, *i.e.* 2 standard deviations from the least squares fit.

In Figure S4.7 we see the counter-intuitive trend that thicker plates seem to have a higher leakage. Several observations and considerations indicate that leakage currents passing underneath the plate do not contribute significantly to the nanopore current: (1) Since the tails that protrude from the center of the DNA nanoplate are used to thread the plate into the pore, it is very unlikely that the nanoplate will be off center by more than the radius of the pore, relative to the axis of the pore. This ensures full coverage of the pore, leaving no path for a leakage current between the SiN surface and the nanoplate in all but the very largest nanopores. Moreover, if an effect of non-complete coverage were present, we would expect our model to underestimate the relative conductance in large pores, since the presence of leakage currents would increase the value of the relative conductance observed. No such effect is observed in our data. (2) We can take a different approach that might lead to leaking currents and assume that the nanoplate is properly centered on the nanopore but that there is a small gap remaining between the SiN surface and the bottom surface of the plate which allows ions to flow through. The leakage current will then involve a surface-current contribution. The ratio between the bulk conduction through the ion permeable nanoplate and the surface leakage component increases as the pore becomes smaller which implies that the leakage currents would have a much larger effect in small pores. As a rough quantitative estimate of this type of effect, **let's assume that a potential leakage current between the plate and the SiN**

surface is due to the contribution of the counterions shielding the surface change. Using equation 1 from Smeets *et al.*[2] we calculate the contribution of the counterion current relative to the bulk ionic current. At 1M KCl for a 20 nm pore, 5.8% of the total current (14nS of 251nS total) is due to the counterion current. If the pore diameter is reduced to 5 nm, the surface contribution increases to 19.6% (3.6nS of 18.3nS total). So we would expect the contribution of a potential leakage current to increase 3.4x between 20 nm and 5 nm. This is not at all what we observe. (3) The presence of leakage currents would have the effect of increasing the relative conductance, and we thus expect that our model would give smaller relative conductances compared to experimental data. Accordingly, the gap between model and experimental values would be largest at the smallest pore values. In fact we see just the opposite: Looking at Fig S4.2, S4.3, S4.4, and S4.5, it seems that the model over-estimates the relative conductance. Hence, also this observation indicates that a significant leakage current is not present.
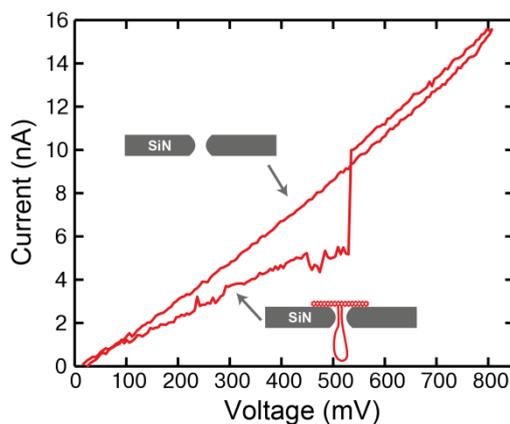
Figure S4.8 – IV curve for an RR nanoplate docked onto a 4.5 nm pore. The nanoplate is pulled through the nanopore at 540 mV, after which the current returns to the bare nanopore values.
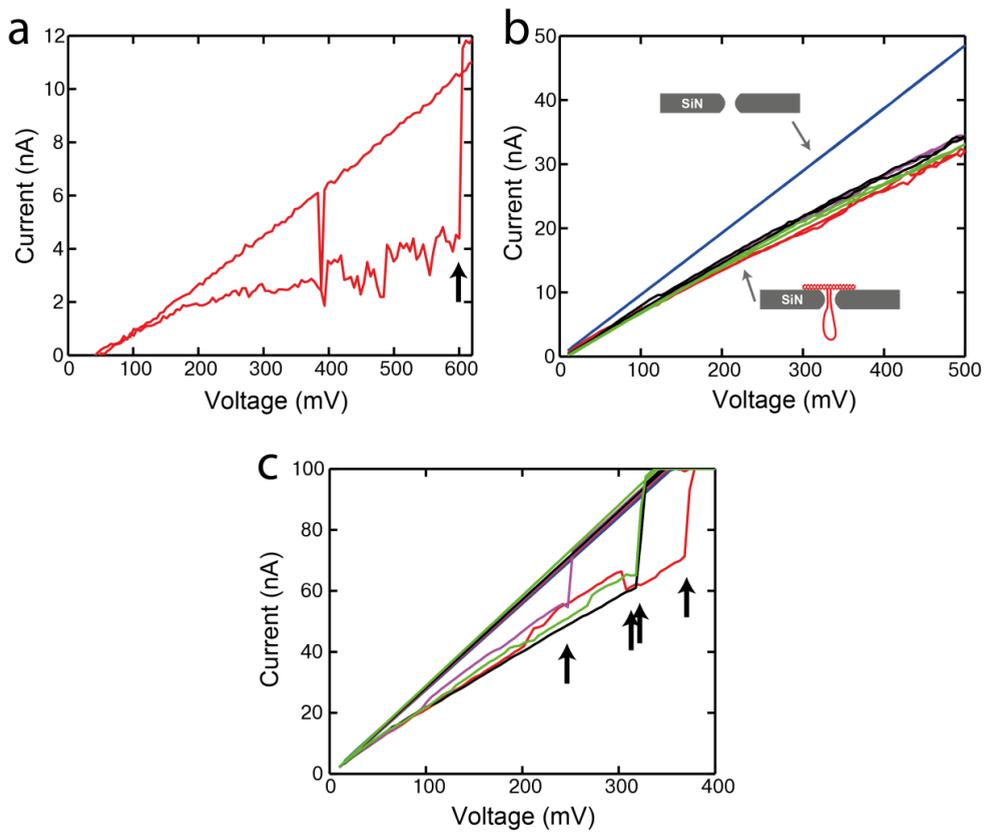
Figure S4.9 – IV curves for HC plates docked onto three different size pores. Black arrows indicate the voltages at which the nanoplates were pulled through the nanopore. The uncertainty in the current data is 0.25 nA (STD). a) A plate on a 4 nm pore. b) Four plates on a 14 nm pore. c) Four plates on a 28 nm pore.
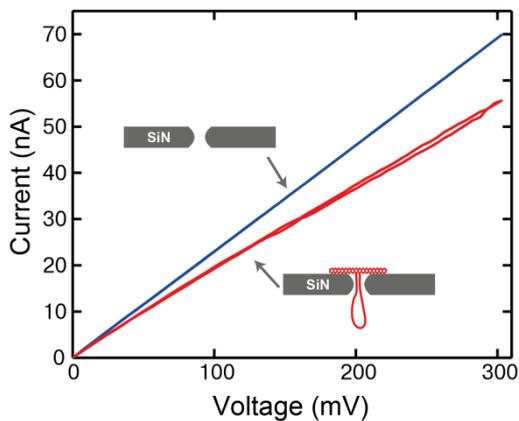
Figure S 4.10 – IV curve of a 2LL plate docked onto a 26 nm pore (red). The blue curve shows the IV characteristics for the bare nanopore.
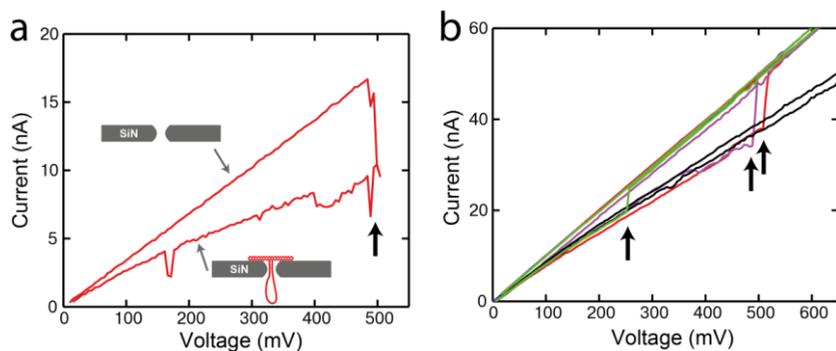
Figure S4.11 – IV curves for 3LL nanoplates docked onto two different size pores. The black arrows indicate the voltage at which a nanoplate was pulled through the pore. a) 6.6 nm pore b) 13 nm pore.

4.6.2 Nanoplate Conductance in 100 mM KCl

The relative conductances for all the nanoplate designs docked into nanopores of various diameters in 100 mM KCl, 10 mM Tris, 1 mM EDTA, and 11 mM Mg^{2+}. The data for all designs is plotted at 200 mV and 300 mV. We observe a similar trend as seen with the data taken in 1M KCl, *i.e.*, a smaller RC for smaller pore diameters. The conductance model used to fit the data at 1M KCl, gives a poor fit at 100 mM KCl. The model should, at low salt, be extended by integrating the contributions of surface charge, similar to previous work by Smeets *et al.*[2]
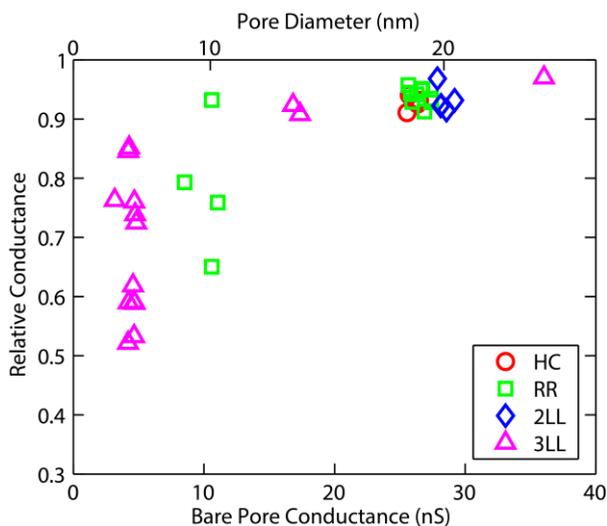
Figure S4.12 - Relative conductances for the different nanoplate designs at 200 mV in 100 mM KCl.
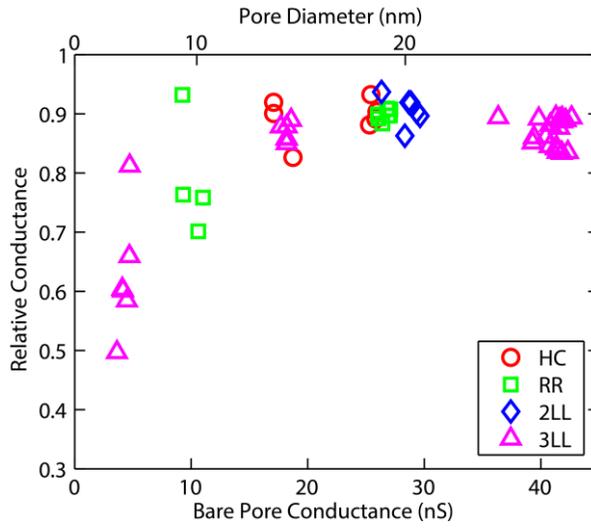
Figure S4.13 - Relative conductances for the different nanoplate designs at 300 mV in 100 mM KCl.

4.6.3 Salt Dependence of a Honeycomb Nanoplate

The relative conductance of all nanoplates is observed to increase as the ionic strength is decreased from 1M to 100 mM. This trend is shown for HC nanoplate data in Figure S4.14 for three different applied voltage levels. Similar trends are observed for 3LL and RR nanoplates (data not shown).
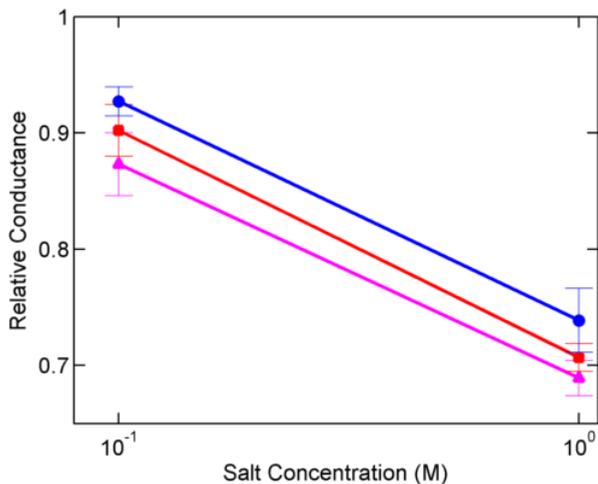
Figure S4.14 – The relative conductance observed at low (100 mM) and high (1M) KCl concentrations for Honeycomb (HC) nanoplates docked onto 20 nm pores at 200 mV (top-blue), 300 mV (middle-red), and 400 mV (bottom-magenta).

4.6.4 Spike Events and Nanoplate Recaptures

   If a nanoplate is very flexible and the nanopore's diameter is sufficiently large, the nanoplate is instantly pulled through the nanopore instead of being docked. These events show up in current traces as fast, high amplitude spikes as shown in Figure S4.15 for RR nanoplates passing through a 24 nm pore at several voltages. We successfully carried out recapture experiments, shown in Figure S4.16, in order to confirm that the nanoplates are being pulled through the nanopores.
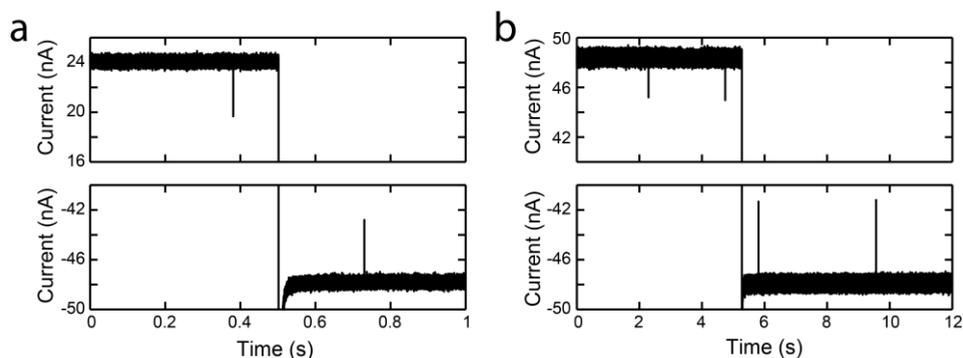
Figure S4.15 – Short spike events observed for RR nanoplates in a 24 nm pore at voltages of 200 mV or higher.
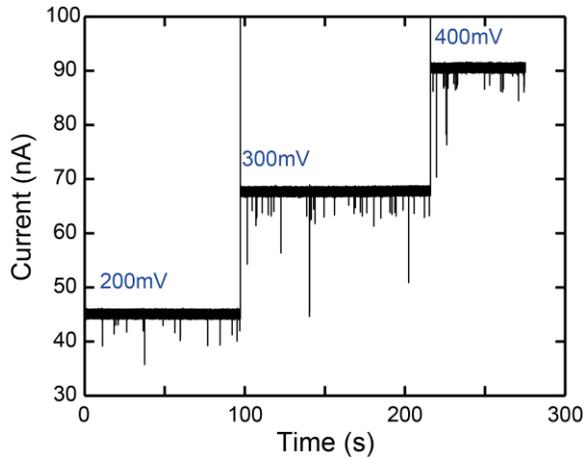
Figure S4.16 - The recapture of RR nanoplates that are pulled through a 24 nm pore. (a) An event is observed at a voltage of 100 mV. The voltage is then switched to -200 mV, 120 ms after the first event. The nanoplate is recaptured 228 ms after switching. (b) Two short events are observed at 200 mV applied voltage. The polarity is reversed 2.98 s after the first event and 530 ms after the second. After reversal two recapture events are observed at 530 ms and 4.29 s after switching.

4.5.5 Multi-Level Conductance in Docked Nanoplates

Current traces from docked nanoplates often exhibit spontaneous sudden jumps in the current level. Examples of this multi-level conductance effect are shown in Figure S4.17 for HC nanoplates in several different pores. The phenomenon of multiple conductance levels was observed with all nanoplate designs, in all pore diameters, at all salt concentrations tested. The source of this effect is attributed to mechanical buckling and re-orientation of the nanoplate. This is supported by the observation that current level jumps are often observed before a docked nanoplate is pulled through the nanopore, as shown in Figure S4.18 and Figure S4.19.

Statistics on docked nanoplates reveal that, except for the 2LL nanoplate, 60% to 75% of docked nanoplates have multiple levels at 100 mV applied voltage, as shown in Figure S4.20. The effect occurs more frequently as the voltage is increased. The magnitude of these jumps, given as the change in relative conductance normalized by the average relative conductance, is shown in Figure S4.21. It varies from 0.05 to 0.07 at 100 mV, and increases to 0.08 to 0.1 at 200 mV.

In considering possible sources for the observed current jumps we also considered the free staple oligos present in the DNA nanoplate solution after purification. The possibility of free staples causing the observed current jumps can be ruled out by several experimental observations. (1) We observe that not all nanoplates show the current jumps, even within the same experiment with the same buffer containing excess staples. For example, in Figure S4.20 at 100 mV, at least 25% of events show no jumping behavior. If excess staples were the cause we would expect all plates to show some jumping behavior. (2) We typically see current jumps occur in both directions, *i.e.* towards higher and towards lower current values. If current jumps were due to staples approaching the plate, the observance of both downward and upward current jumps would mean that staples which are brought to the nanoplate either pass through the plate, which is extremely unlikely, or return back into solution which is also unlikely due to the high electric fields. (3) Let us nevertheless assume that free staples temporarily get stuck to the surface of the DNA nanoplate. What magnitude current drop would we expect? The magnitude of the jumps we observe ranges from 5% to 10% of the baseline value (Figure S4.21). If we assume optimistic values for the hydration volume of the free staples (3 nm radius of gyration) and use the standard volume exclusion formula to calculate the expected current blockade produced by a free staple inside the pore we find values that vary from 1.5% for 20 nm pores, to 36% for 5 nm pores. This does not match our observations which show no significant pore size dependence for the current jumps. Furthermore,

excluded volume analysis states that there should be no voltage dependency for the normalized blockade, while our data shows that the normalized blockade increases with voltage for most plates (Figure S4.21). (4) Using pessimistic retention values of 30% for the low-MW oligos and 95% for the high-MW DNA nanoplates, if we start with 20 nM scaffold DNA and 200 nM staples, we estimate final concentrations of 14 nM nanoplates and 14 nM staples after 4x purification (assuming a retention volume of 58uL). Such a free staple concentration of 14 nM should produce an event rate of ~4Hz. The observation that the frequency of buckling is observed to vary substantially among different plates in the same experiment, suggests that the free staples are not the source of buckling.

Figure S4.17 - Examples of Honeycomb nanoplate docking events in several different pores exhibiting multiple conductance levels.
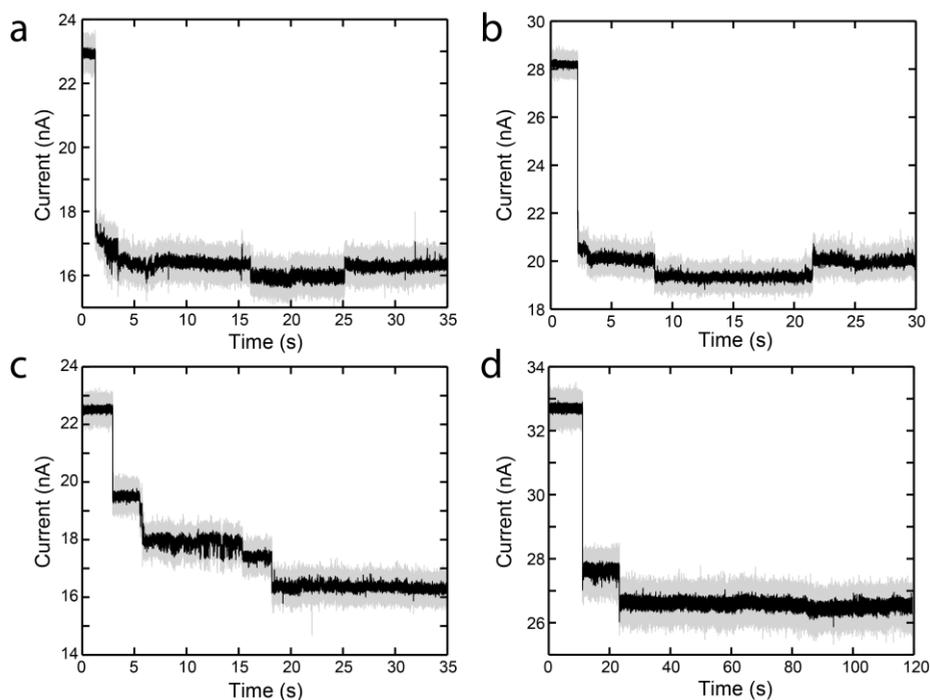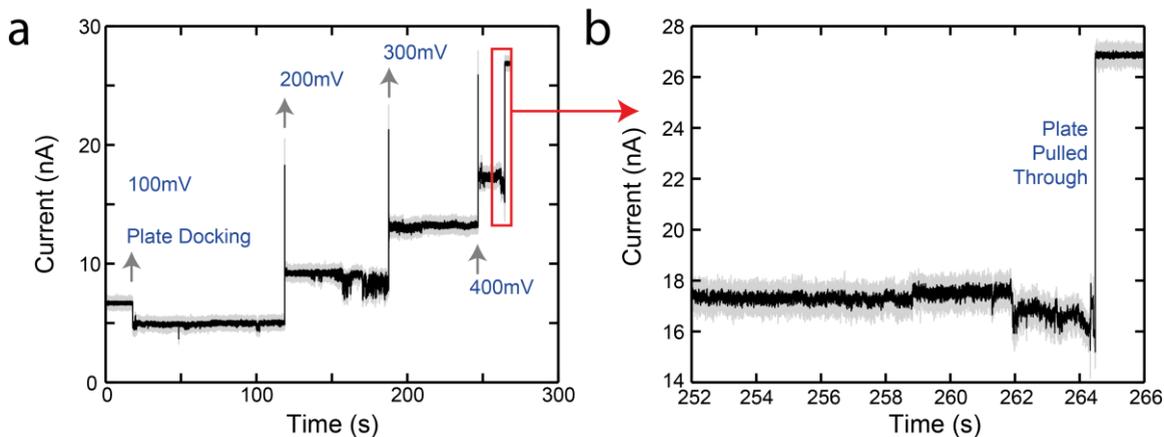
Figure S4.18 - a) A 3 Layer Lattice nanoplate is captured in a 10 nm pore at 100 mV. The applied voltage is then increased to 200 mV, 300 mV, and 400 mV. The nanoplate is finally pulled through the pore after the voltage was set to 400 mV. b) Close-up of the trace in the seconds before the nanoplate is pulled through. The presence of multiple levels in the current trace right before the nanoplate is pulled through (Figures S4.18, S4.19) supports the hypothesis that these levels are related to mechanical buckling of the nanoplates.
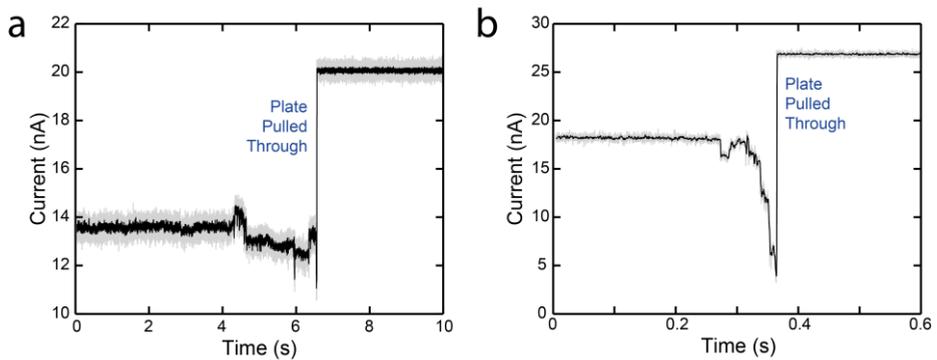
Figure S4.19 – Examples of two other nanoplates exhibiting, similar to the data in Figure S4.18, multiple conductance levels right before being pulled through the pore.
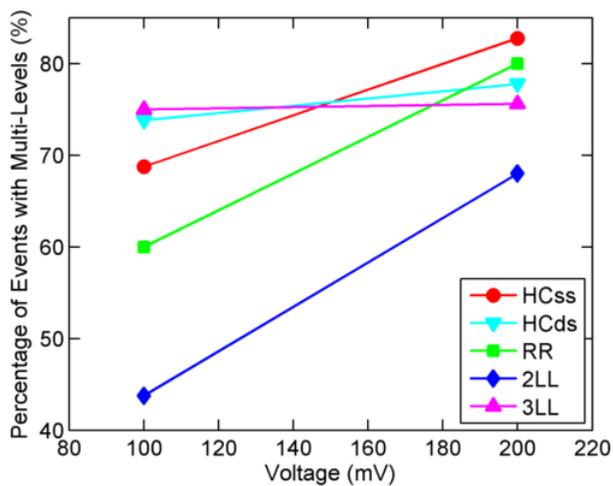
Figure S4.20 – Percentage of events which displayed conductance levels jumps, while docked into a nanopore, as a function of voltage. In all cases we see the percentage of events with jumps to increase as the voltage is increased.
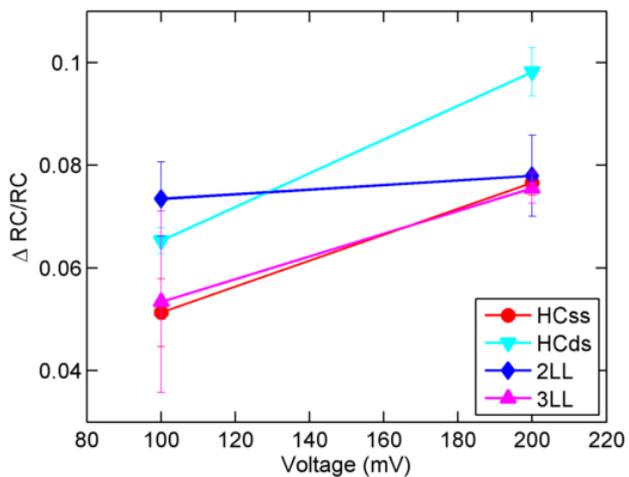
Figure S4.21 – The normalized magnitude of the conductance levels shifts (ΔRC/RC) as a function of voltage. The magnitude of the jumps increases as the voltage is increased, except for the 2LL nanoplate.

4.5.6 Comparison of Single-Stranded and Double-Stranded DNA Tails

Two HC nanoplates, one with a ssDNA tail and another with a fully hybridized dsDNA tail, were compared, as shown in Figure S4.22, in order to determine if the **nanoplate's tail influenced the observed conductance values.** The slightly lower relative conductance seen for the dsDNA tail can be explained by its larger excluded volume, since the tail is threaded through the pore while the nanoplate is docked.
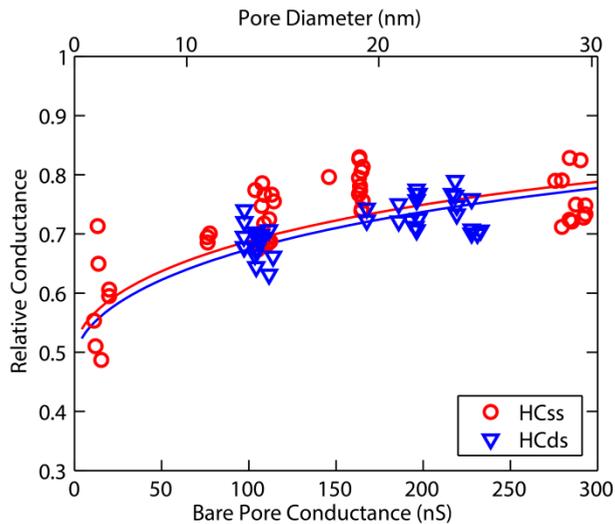
Figure S4.22 - Relative conductance for Honeycomb nanoplates with single-stranded and double-stranded DNA tails docked at 200 mV in 1M KCl. The slightly lower **conductance of the nanoplate with a dsDNA tail is attributed to the tail's higher excluded volume.**

4.5.7 TEM and AFM Characterization

The long single stranded tail forms a large blob above the nanoplate as visible in Figures S4.23 and S4.24. The nanoplates were also scanned with AFM under a variety of different ionic conditions and found to be stable (Figure S4.25).
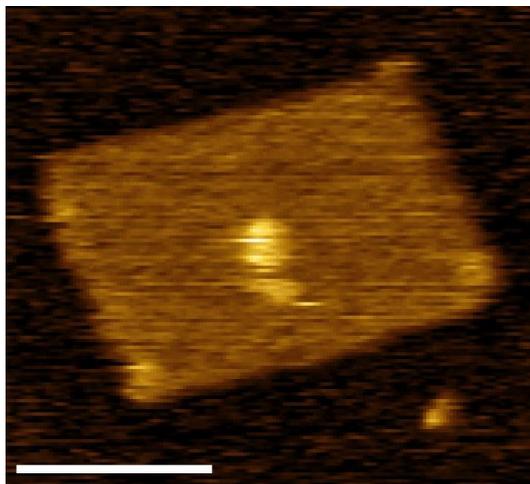
Figure S4.23 – An AFM image of a RR nanoplate with the ssDNA tail visible. The scale bar is 50 nm.
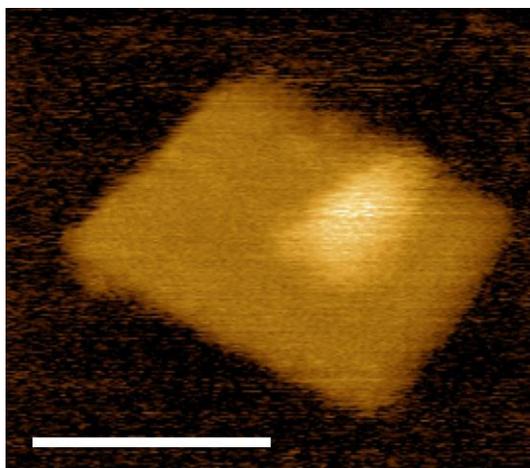
Figure S4.24 - An AFM image of a 2LL nanoplate with the ssDNA tail visible. The scale bar is 50 nm.
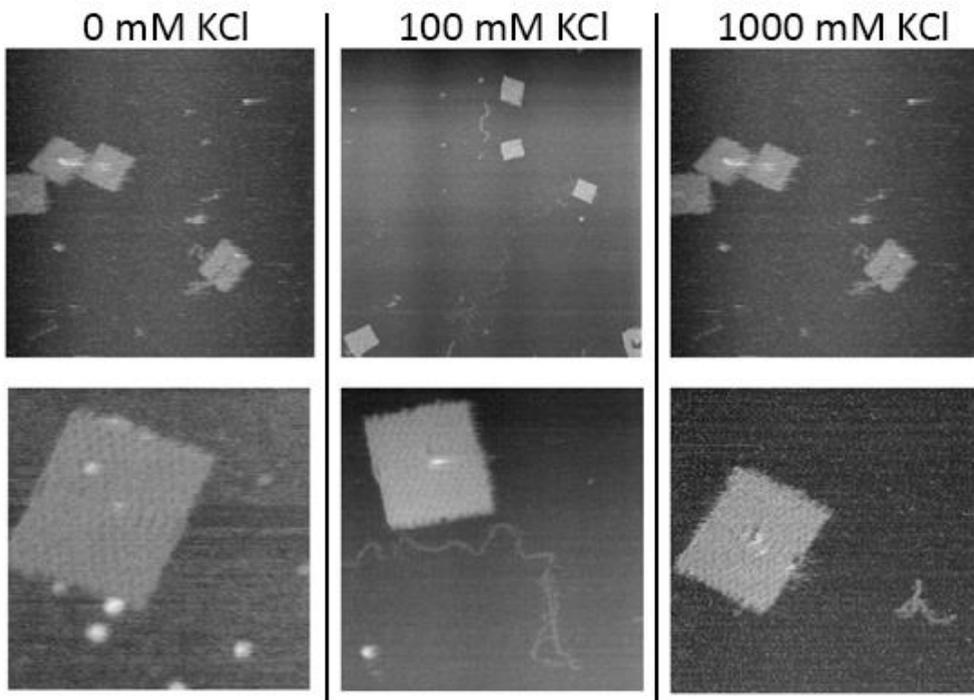
Figure S4.25 - The RR nanoplate imaged at three different ionic strengths. No significant differences are noticeable between the different ionic conditions. Left: 0 mM KCl, Center: 100mM KCl, Right: 1000mM KCl.
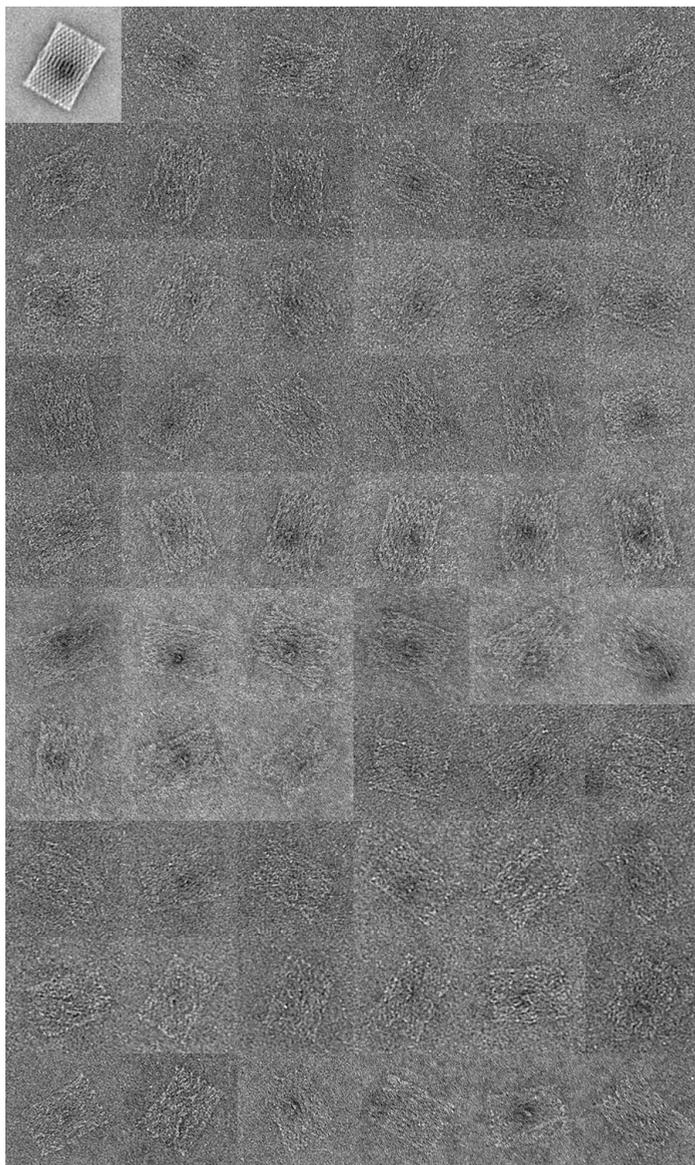
Figure S4.26 – The negative stain micrographs of the RR nanoplate, with the average shown in the top left. Each micrograph is 137nm x 137nm. Adapted from Sobczak *et al.*[3]
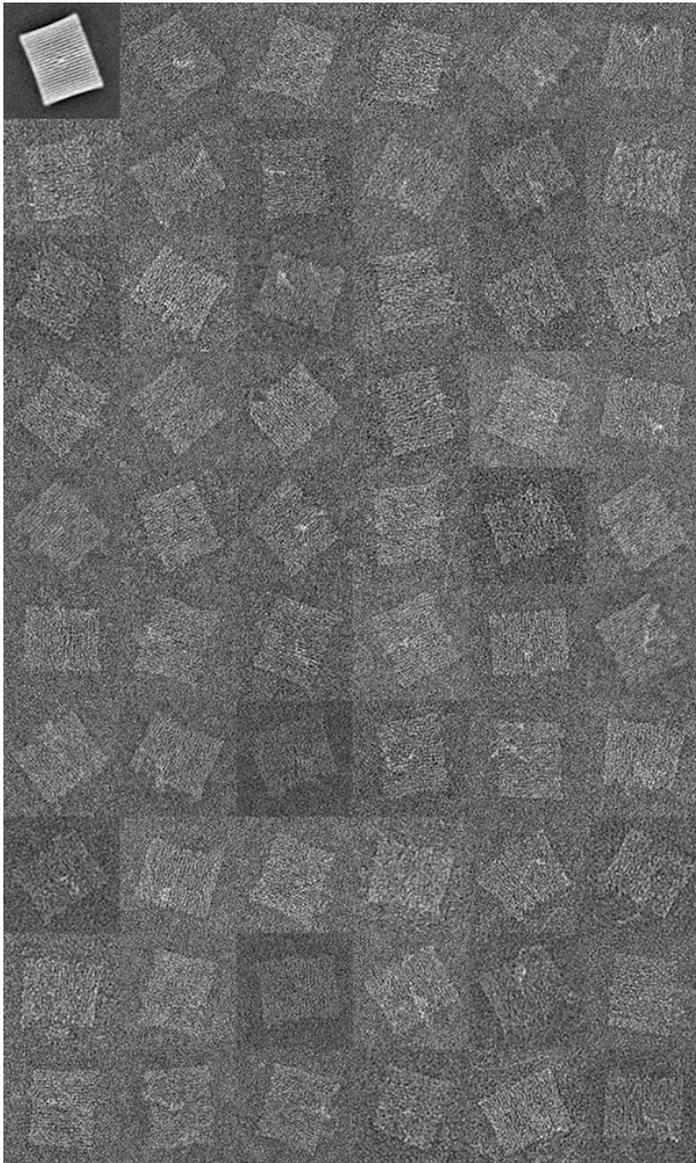
Figure S4.27 – The negative stain micrographs of the 2LL nanoplate, with the average shown in the top left. Each micrograph is 91nm x 91nm.
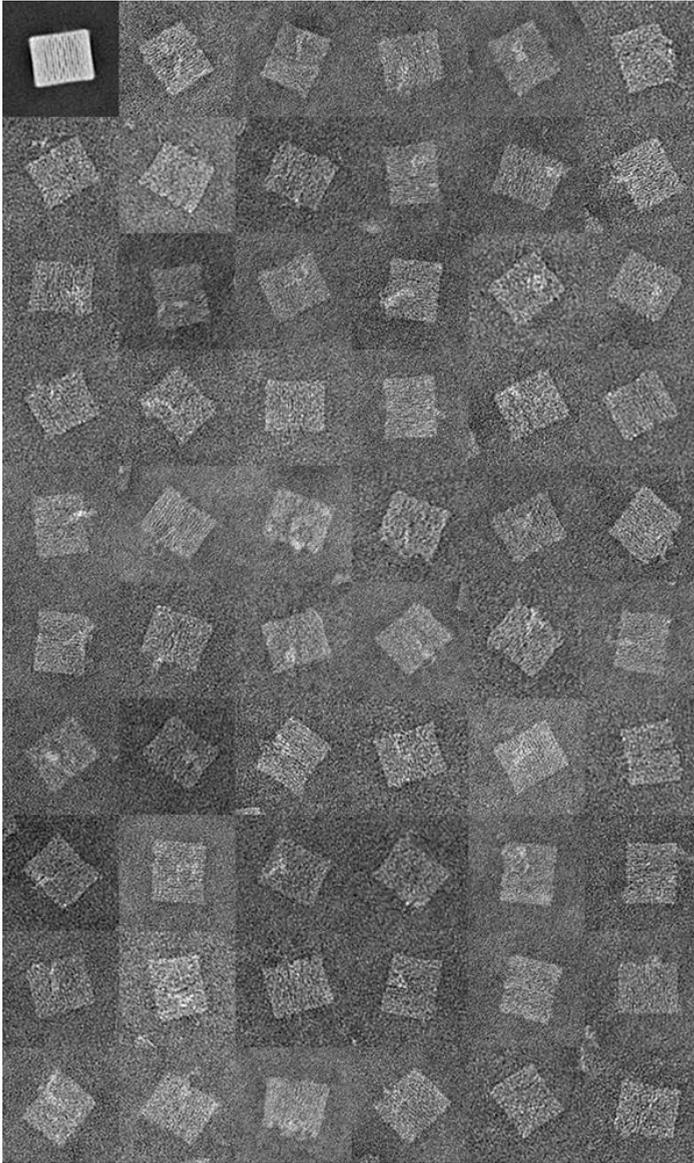
Figure S4.28 – The negative stain micrographs of the 3LL nanoplate, with the average shown in the top left. Each micrograph is 91nm x 91nm.
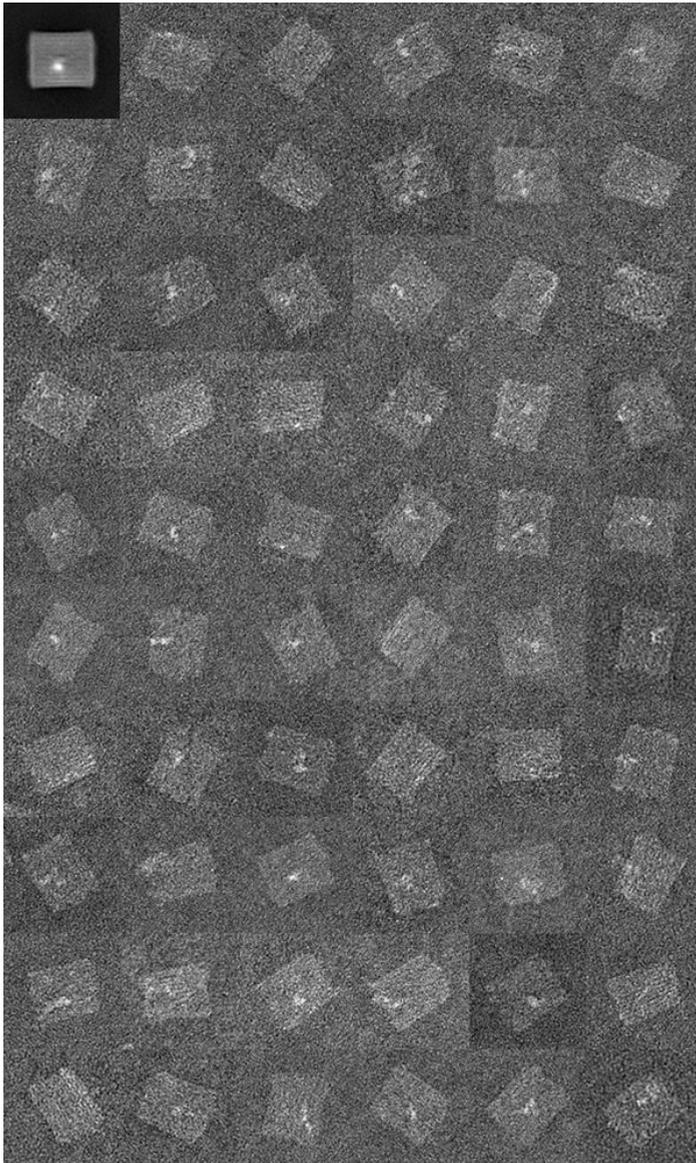
Figure S4.29 – The negative stain micrographs of the HC nanoplate, with the average shown in the top left. Each micrograph is 91nm x 91nm.

4.5.8 Nanoplate Design Details

A detailed description of each nanoplate design is provided. CanDo modeling results are shown for each plate (Figure S4.30 to S33) as heat maps of the RMS fluctuations in different regions of each object. Briefly, these fluctuations are determined by applying external forces to an origami object which has been modeled as a series of elastic rods where cross-overs are rigid constraints and observing the structural relaxation using finite element analysis.[4] The scaffold routing diagrams are provided for each plate design (Figures S4.35 to S4.38) as generated by caDNAno, as well as a gel-electrophoresis characterization of assembled plates (Figure S4.34). Finally, we provide the sequences of all of the oligo-staples used to generate each nanoplate.
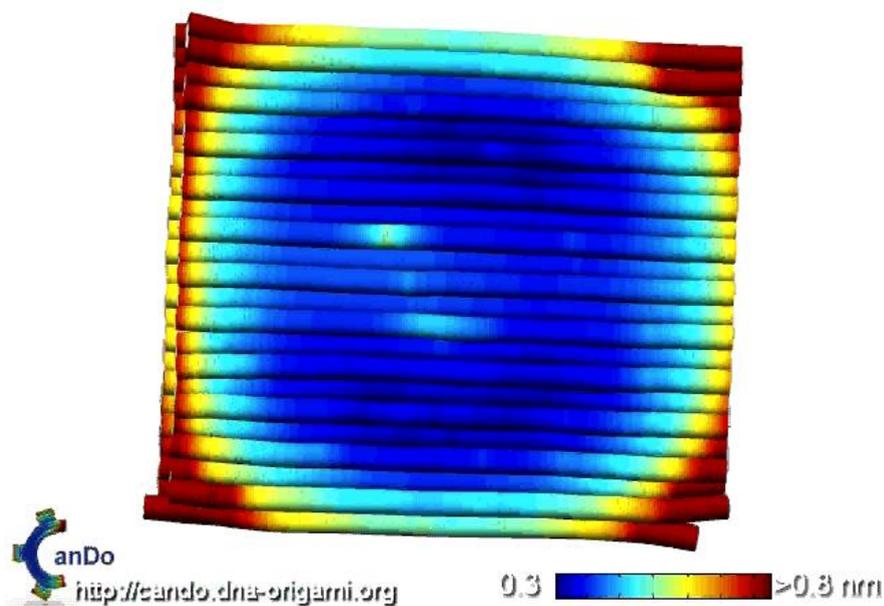
Figure S4.30 – CanDo simulation of the HC plate. This plate is predicted to exhibit the lowest flexibility of all of the designs, as evidenced by the small RMS fluctuations present over much of the plate.
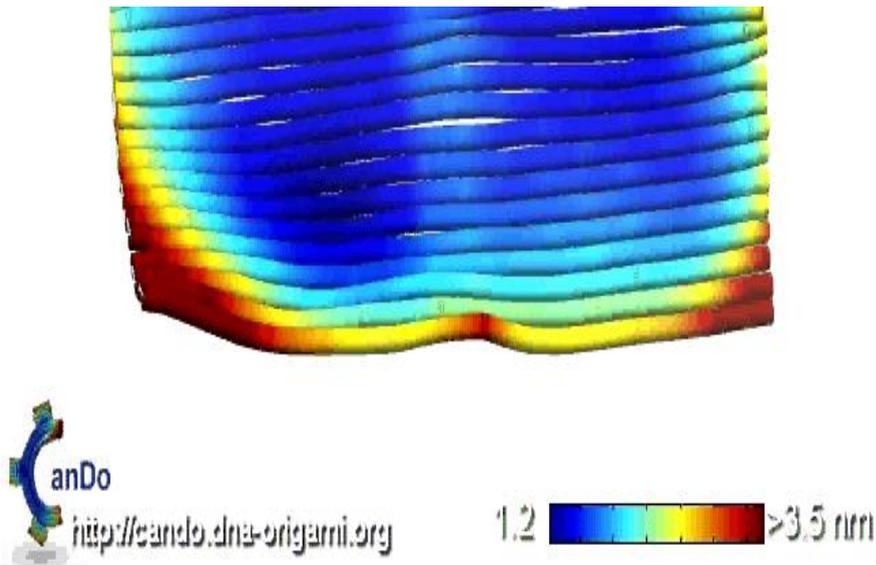
Figure S4.31 – CanDo simulation of the RR plate. This plate is predicted to exhibit the highest flexibility of all of the designs.
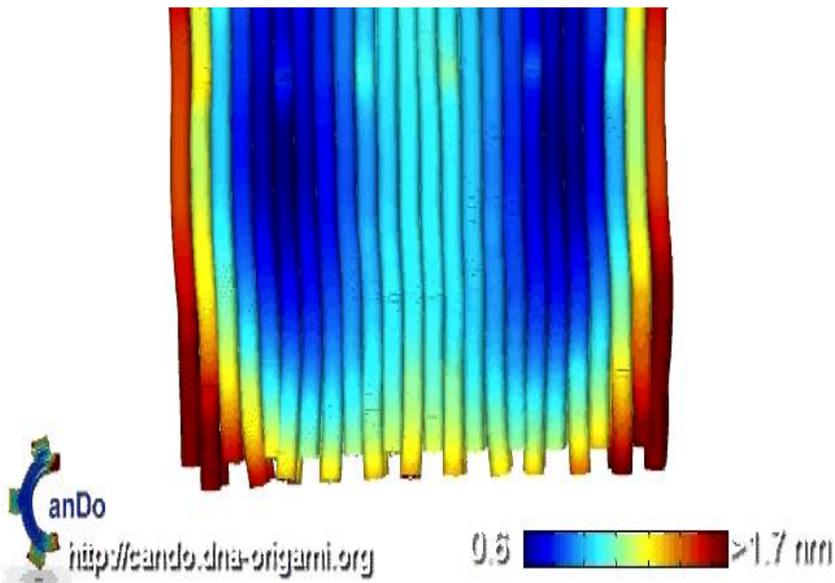
Figure S4.32 – CanDo simulation of a 2LL plate. This plate is predicted to exhibit a lower flexibility than the RR plate, but higher than 3LL or HC.
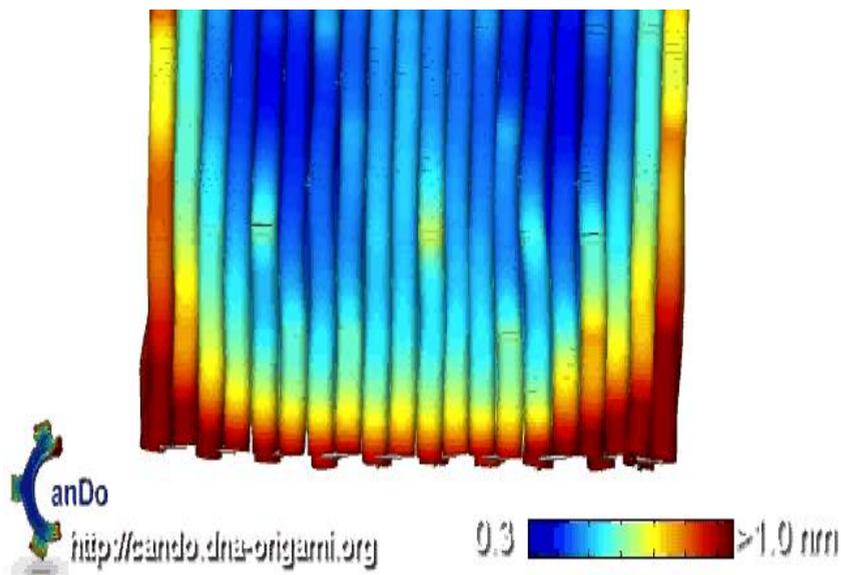
Figure S4.33 – CanDo simulation of a 3LL plate. This plate is predicted to exhibit a low flexibility, slightly larger than the HC.
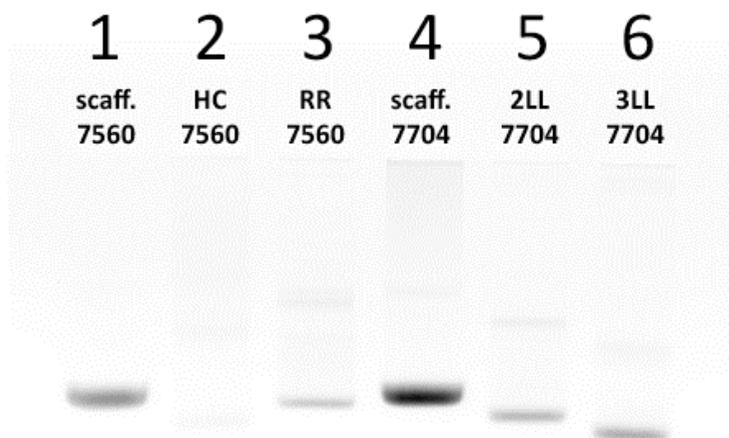
Figure S4.34 – The spin-filtered nanoplates run on a 2 % agarose gel containing EtBr. From left to right: scaffold 7560, HC (7560), RR (7560), scaffold 7704, 2L (7704), 3L (7704). The scaffold is a reference only for the running speed of structures, the concentrations are not comparable. All the excess strands have been filtered out as described in the methods.

References

1.   Wanunu, M., Nanopores: A Journey Towards DNA Sequencing. Physics of Life Reviews 2012, 9, 125-158.

2.   Haque, F.; Li, J.; Wu, H.-C.; Liang, X.-J.; Guo, P., Solid-State and Biological Nanopore for Real-Time Sensing of Single Chemical and Sequencing of DNA. Nano Today 2013, 8, 56-74.

3.   Tabard-Cossa, V.; Trivedi, D.; Wiggin, M.; Jetha, N.; Marziali, A., Noise Analysis and Reduction in Solid-State Nanopores. Nanotechnology 2007, 18, 305505.

4.   Venkatesan, B. M.; Bashir, R., Nanopore Sensors for Nucleic Acid Analysis. Nat Nano 2011, 6, 615-624.

5.   Rotem, D.; Jayasinghe, L.; Salichou, M.; Bayley, H., Protein Detection by Nanopores Equipped with Aptamers. J. Am. Chem. Soc. 2012, 134, 2781-2787.

6.   Hall, A. R.; Scott, A.; Rotem, D.; Mehta, K. K.; Bayley, H.; Dekker, C., Hybrid Pore Formation by Directed Insertion of [Alpha]-Hemolysin into Solid-State Nanopores. Nat Nano 2010, 5, 874-877.

7.   Rothemund, P. W. K., Folding DNA to Create Nanoscale Shapes and Patterns. Nature 2006, 440, 297-302.

8.   Andersen, E. S.; Dong, M.; Nielsen, M. M.; Jahn, K.; Subramani, R.; Mamdouh, W.; Golas, M. M.; Sander, B.; Stark, H.; Oliveira, C. L. P., et al., Self-Assembly of a Nanoscale DNA Box with a Controllable Lid. Nature 2009, 459, 73-76.

9.   Douglas, S. M.; Dietz, H.; Liedl, T.; Hogberg, B.; Graf, F.; Shih, W. M., Self-Assembly of DNA into Nanoscale Three-Dimensional Shapes. Nature 2009, 459, 414-418.

10.   Han, D.; Pal, S.; Nangreave, J.; Deng, Z.; Liu, Y.; Yan, H., DNA Origami with Complex Curvatures in Three-Dimensional Space. Science 2011, 332, 342-346.

11.   Dietz, H.; Douglas, S. M.; Shih, W. M., Folding DNA into Twisted and Curved Nanoscale Shapes. Science 2009, 325, 725-730.

12.   Wei, R.; Martin, T. G.; Rant, U.; Dietz, H., DNA Origami Gatekeepers for Solid-State Nanopores. Angew. Chem., Int. Ed. 2012, 51, 4864-4867.

13.   Bell, N. A. W.; Engst, C. R.; Ablay, M.; Divitini, G.; Ducati, C.; Liedl, T.; Keyser, U. F., DNA Origami Nanopores. Nano Lett. 2012, 12, 512-517.

14.   Hernández-Ainsa, S.; Bell, N. A. W.; Thacker, V. V.; Göpfrich, K.; Misiunas, K.; Fuentes-Perez, M. E.; Moreno-Herrero, F.; Keyser, U. F., DNA Origami Nanopores for Controlling DNA Translocation. ACS Nano 2013, 7, 6024-6030.

15.   Langecker, M.; Arnaut, V.; Martin, T. G.; List, J.; Renner, S.; Mayer, M.; Dietz, H.; Simmel, F. C., Synthetic Lipid Membrane Channels Formed by Designed DNA Nanostructures. Science 2012, 338, 932-936.

16.   Burns, J. R.; Stulz, E.; Howorka, S., Self-Assembled DNA Nanopores That Span Lipid Bilayers. Nano Lett. 2013, 13, 2351-2356.

17.   Bai, X.-c.; Martin, T. G.; Scheres, S. H. W.; Dietz, H., Cryo-Em Structure of a 3d DNA-Origami Object. Proc. Natl. Acad. Sci. U. S. A. 2012, 109, 20012-20017.

18.   Ke, Y.; Douglas, S. M.; Liu, M.; Sharma, J.; Cheng, A.; Leung, A.; Liu, Y.; Shih, W. M.; Yan, H., Multilayer DNA Origami Packed on a Square Lattice. J. Am. Chem. Soc. 2009, 131, 15903-15908.

19.   Castro, C. E.; Kilchherr, F.; Kim, D.-N.; Shiao, E. L.; Wauer, T.; Wortmann, P.; Bathe, M.; Dietz, H., A Primer to Scaffolded DNA Origami. Nat Meth 2011, 8, 221-229.

20.   Kim, D.-N.; Kilchherr, F.; Dietz, H.; Bathe, M., Quantitative Prediction of 3d Solution Shape and Flexibility of Nucleic Acid Nanostructures. Nucleic Acids Res. 2012, 40, 2862-2868.

21.   Kowalczyk, S. W.; Grosberg, A. Y.; Rabin, Y.; Dekker, C., Modeling the Conductance and DNA Blockade of Solid-State Nanopores. Nanotechnology 2011, 22, 315101.

22.   Arbona, J. M.; Aimé, J.-P.; Elezgaray, J., Modeling the Mechanical Properties of DNA Nanostructures. Phys. Rev. E: Stat., Nonlinear, Soft Matter Phys. 2012, 86, 051912.

23.   Schoch, R. B.; Han, J.; Renaud, P., Transport Phenomena in Nanofluidics. Rev. Mod. Phys. 2008, 80, 839-883.

24.   Ho, C.; Qiao, R.; Heng, J. B.; Chatterjee, A.; Timp, R. J.; Aluru, N. R.; Timp, G., Electrolytic Transport through a Synthetic Nanometer-Diameter Pore. Proc. Natl. Acad. Sci. U. S. A. 2005, 102, 10445-10450.

25.   Martin, T. G.; Dietz, H., Magnesium-Free Self-Assembly of Multi-Layer DNA Objects. Nat Commun 2012, 3, 1103.

26.   Essevaz-Roulet, B.; Bockelmann, U.; Heslot, F., Mechanical Separation of the Complementary Strands of DNA. Proc. Natl. Acad. Sci. U. S. A. 1997, 94, 11935-11940.

27.   Strunz, T.; Oroszlan, K.; Schäfer, R.; Güntherodt, H.-J., Dynamic Force Spectroscopy of Single DNA Molecules. Proc. Natl. Acad. Sci. U. S. A. 1999, 96, 11277-11282.

28.   Kowalczyk, S. W.; Tuijtel, M. W.; Donkers, S. P.; Dekker, C., Unraveling Single-Stranded DNA in a Solid-State Nanopore. Nano Lett. 2010, 10, 1414-1420.

29.   Janssen, X. J. A.; Jonsson, M. P.; Plesa, C.; Soni, G. V.; Dekker, C.; Dekker, N. H., Rapid Manufacturing of Low-Noise Membranes for Nanopore Sensors by Trans -Chip Illumination Lithography. Nanotechnology 2012, 23, 475302.30.   Sobczak,   J.-P.   J.; Martin, T. G.; Gerling, T.; Dietz, H., Rapid Folding of DNA into Nanoscale Shapes at Constant Temperature. Science 2012, 338, 1458-1461.

References (SI)

1.   Kowalczyk, S. W.; Grosberg, A. Y.; Rabin, Y.; Dekker, C., Modeling the Conductance and DNA Blockade of Solid-State Nanopores. Nanotechnology 2011, 22, 315101.

2.   Smeets, R. M. M.; Keyser, U. F.; Krapf, D.; Wu, M.-Y.; Dekker, N. H.; Dekker, C., Salt Dependence of Ion Transport and DNA Translocation through Solid-State Nanopores. Nano Lett. 2006, 6, 89-95.

3.   Sobczak, J.-P. J.; Martin, T. G.; Gerling, T.; Dietz, H., Rapid Folding of DNA into Nanoscale Shapes at Constant Temperature. Science 2012, 338, 1458-1461.

4.   Castro, C. E.; Kilchherr, F.; Kim, D.-N.; Shiao, E. L.; Wauer, T.; Wortmann, P.; Bathe, M.; Dietz, H., A Primer to Scaffolded DNA Origami. Nat Meth 2011, 8, 221-229.

5.

DNA origami scaffold for studying intrinsically disordered proteins of the nuclear pore complex

The nuclear pore complex (NPC) is the gatekeeper for nuclear transport in eukaryotic cells. A key component of the NPC is the central shaft lined with intrinsically disordered proteins known as FG-Nups which control the selective molecular traffic through NPCs[1–6]. To shed light on the NPC structural and transport properties, we here present a novel approach to realize artificial NPC-mimics that allow full control of the type and copy numbers of FG-Nups: We designed 34 nm-wide 3D DNA origami rings and attached NSP1or NSP1-S, in different copy numbers within the ring. These DNA-origami-based NPC-mimics enable studying the structure and function of key components of the nuclear pore complex in a controlled fashion. Using (cryo) electron microscopy, we find that NSP1 forms cohesive networks inside the ring with a greater density than the hydrophilic mutant NSP1-S. Consistent with this, the ionic conductance measured through NPC-mimic origami rings docked onto solid-state nanopores is found to be lower for NSP1 than for NSP1-S, and it is reduced for a larger number of FG-Nups in the ring. MD simulations is in good agreement with the experimental data. Our novel approach provides a working experimental platform for deciphering the collective behavior of intrinsically disordered proteins with full control of their type and position.

5.1 Introduction

Nuclear pore complexes (NPCs) mediate all transport to and from the nucleus in eukaryotic cells. A single NPC is a complex protein structure consisting of hundreds of proteins called nucleoporins (Nups), which comprise both structural Nups that build the scaffolding structure of the NPC, and intrinsically disordered Nups[2,3,7]. The latter so-called FG-Nups contain hydrophobic phenylalanine-glycine repeats and are located inside the central NPC channel. The FG-Nups are responsible for the remarkable selective permeability of NPCs[4]. Several models have been proposed for the transport mechanism through NPCs, but, despite much research on the structure and function of NPCs, no consensus has been reached[5,8–11].

Owing to the huge (60-125MDa) size and complexity of the NPC, deciphering its structural and functional properties represents a significant challenge. Probing and manipulating NPC transport *in vivo* is challenging given the complex cellular environment and the demand for true nanoscale resolution. Full *in vitro* reconstitution of the large NPCs would be beneficial as a much larger set of analytical methods could be employed, but has so far not been found to be feasible. Interestingly, various groups have developed biomimetic NPCs where a single type of FG-Nup is attached to nanopores within a polymeric or solid-state SiN membrane[12–14]. While this approach has provided encouraging results for NPC studies, all such previous work relied on random attachment of FG-Nups on nanopore surfaces which inherently precludes full control of the exact number, density, position, and composition of the FG-Nups.

Here, we present a novel type of biomimetic NPCs with superior control over the positioning of NPC components which is based on DNA origami based scaffolds[15]. DNA origami structures have previously been constructed for usage as pores and channels in lipid membranes[16–18] and also as addressable adapters for solid-state nanopores[19,20]. DNA origami technology can also be employed to create ring-like objects with custom-designed curvature[21]. Such rings have previously been employed to template liposome assembly[22]. Our DNA-origami-based NPC mimic features a custom-designed multilayer DNA origami structure that resembles the ring-like shape and diameter of the NPC scaffold. Onto this scaffold, we attach yeast NSP1, an archetypal well-studied FG-Nup, at a number of defined locations on the inner ring surface. With this DNA origami scaffold approach, we gain control over the precise number and position of the FG-Nup attachment points to affect the density of the Nups in the NPC mimic, as the user can choose where exactly to attach what type of Nup. Next to wildtype NSP1, we also study a mutant

Nup, NSP1-S, where the hydrophobic amino acids F, I, L, and V were replaced with hydrophilic S[23]. We report the design of these DNA-origami-based NPC mimics and present electron microscopy, ionic conductance measurements, and molecular dynamics (MD) simulations that characterize their structural and transport properties. Taken together, the data establish these DNA-origami scaffolds as a new platform for studying the NPC.
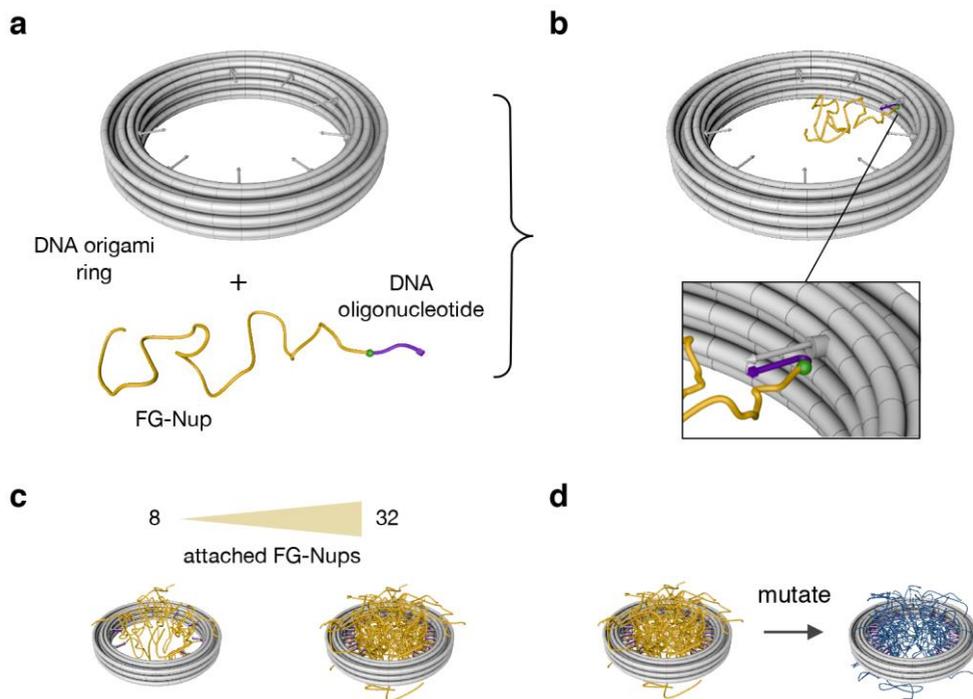
Figure 5.1. Schematics of DNA origami ring with attached FG-Nups. a, DNA ring (see Fig. S1 for design details) and one NSP1 protein with a covalently attached oligonucleotide. b, Ring with attached NSP1 protein. c, DNA ring versions with 8 (left) and 32 (right) NSP1 proteins attached. d, DNA ring with 32 NSP1 (left) and 32 mutated NSP1-S (right) attached.

The origami scaffold (Fig. 5.1; design details in Fig. S5.1 and S5.2) consists of 18 helices that form a ring with an inner diameter of ~34 nm, which is similar to the inner diameter of the central channel of NPCs[3,24]. The ring can host up to 32 attachment sites pointing radially inward. We designed two variants of rings, one with 8 and one with 32 attachment sites, where these copy numbers were inspired by multiple-of-8 protein abundances in NPCs. The attachment anchors contain single-stranded DNA overhangs that can hybridize to targets, which are complementary-sequence oligomers that are covalently bound to a Nup. Each attachment anchor is based on two DNA single-strands protruding from the ring which can partly hybridize in order to form a short double-helical "separator" domain away from the ring (Fig. S5.1e) from which the single-strand anchor emerges. The separator part biases the orientation of the Nup attachment anchors toward the radially inward direction and thereby increases the accessibility for target attachment. To facilitate electrophoretically-driven docking of the ring to solid-state nanopores, we also mounted a double-stranded DNA leash at the bottom of the ring[25]. Electrophoretic mobility analysis (EMA) was used to verify the ring assembly (Fig. S5.3)[26].

5.2 Results and discussions

To probe whether the attachment anchors indeed successfully hybridizes DNA oligomers, we incubated rings with 8 and 32 attachment sites with a complementary oligonucleotide labeled with cyanine-5 (Cy5) dye and analyzed the samples using EMA (Fig. 5.2a). The obtained fluorescence intensity in the Cy5 channel strongly increased with the number of attachment points, yielding a significantly larger (3.2-fold higher) intensity for 32 versus 8 attachment sites. For a quantitative estimate, we counted the number of bleaching steps in TIRF fluorescence microscopy recordings on rings near a surface, which report the number of attached strands in individual NPC rings (Fig. 5.2b and SI methods). For rings with 8 attachment sites, we obtained a skewed distribution with a peak around 7 Cy5 molecules, a tail at lower numbers, and almost no recordings of more than 8 steps. We conclude that the large majority of the targets are successfully incorporated to the attachment anchors.

For attachment of the Nup proteins to the ring, we conjugated NSP1 and NSP1-S with an oligonucleotide with the respective complementary sequence (SI methods). We incubated rings with 32 attachment anchors with NSP1 and NSP1-S (hereafter denoted as '32-NSP1' or '32-NSP1-S') and purified samples from excess protein. We employed negative-stain transmission electron microscopy (TEM) to obtain images of rings without protein, 32-NSP1 and 32-NSP1-S (Fig. 5.2c-e). Images of bare rings without proteins yielded well-defined particles with

circular stripes corresponding to layers of DNA helices within the ring. 32-NSP1 frequently showed rings with a heterogeneous density of proteins inside and less well visible circular stripes. We attribute this to the presence of NSP1 protein that spreads out across the top of the rings (in accordance with the MD simulations discussed below). Rings incubated with NSP1-S show a lower protein density inside the rings, while also exhibiting less well visible circular stripes compared to the rings without proteins.
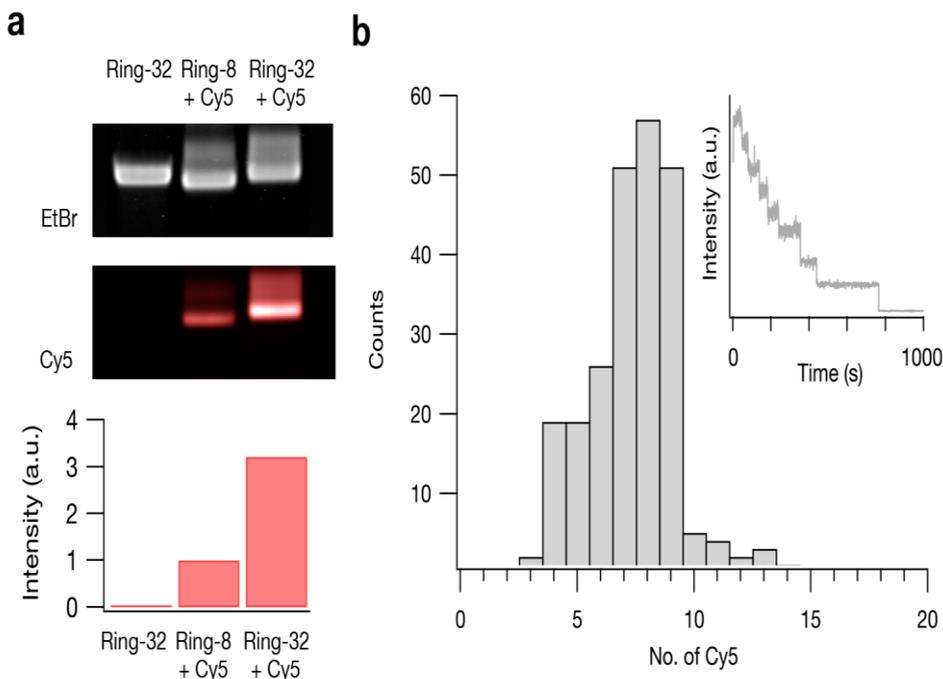
Figure 5.2. Attachment of NSP1 and NSP1-S to the DNA ring. a, Top: laser-scanned EtBr images of a 1% agarose gel on which DNA origami ring samples were electrophoresed. Middle: same gel scanned in Cy5 excitation/emission channels. Cy5-labelled DNA strands were added to FG-Nup attachments where indicated. Bottom: integrated Cy5 band intensity normalized to EtBr intensity. b, Histogram of the number of attached Cy5-labelled oligomers for an 8-attachment ring. Inset shows an exemplary intensity trace of a single-particle recording of a DNA ring with 8 attachment sites incubated with the complementary Cy5-labelled oligonucleotide obtained using total internal reflection microscopy (TIRF) (see SI methods and Fig. S5.4). See Fig. S5.5 for additional intensity traces. Inset: Histogram of the number of bleaching steps of single-particle (N=240).

Quantification of these EM images was done by classifying, in a user-unbiased way (see SI methods), the ring density into three different categories, low/medium/high protein density inside the ring (Fig. 5.2f-h). As expected, over

95% of the bare rings exhibited a low density inside the rings, while upon addition of the NSP1 proteins 80% of the rings contained a medium or high density. In case of NSP1-S around 40% of all rings showed either medium or high density – indicating that NSP1-S forms a less dense structure inside the ring than NSP1. In addition, tomograms obtained from tilt series of negative-stain electron micrographs on 32-NSP1 showed a high density in all slices along the height of the ring, indicating a rather homogenous filling of the rings with NSP1 (Fig. S5.7). Taken together, these results confirm the successful attachment of the proteins to the DNA origami NPC mimic. The intrinsically disordered FG-Nups appear to form a cohesive protein mass inside the origami scaffolds. As the staining agent as well as drying artefacts might complicate quantification, we subsequently employed cryo-electron microscopy (cryo-EM) for a more in-depth analysis.

Cryo-EM average micrographs (Fig. 5.3a-b) were obtained from many single-particle cryo-EM micrographs of empty rings, 32-NSP1 and 32-NSP1-S. The average micrographs clearly indicate protein density inside the ring for both 32-NSP1 and 32-NSP1-S, where the NSP1 intensity is higher than for NSP1-S. To quantitatively compare the densities, we calculated circularly averaged intensity profiles and normalized the background value to 0 (Fig. S5.9). These profiles indicate that the average density inside the 32-NSP1 is ~2.4-fold higher than for 32-NSP1-S. Rotationally aligned 2D class averages for the empty rings showed 19 circularly distributed density spikes that mutually connect the three radial DNA layers (Fig. S5.10), which can be matched to DNA crossovers forming connections between neighboring helices in the DNA ring.

To obtain microscopic insight into the spatial distribution of the FG-Nups inside the pore, we used a coarse-grained (CG) MD model to simulate the FG-Nups[27,28] (see SI methods) and calculated the time-averaged protein density distribution for 32-NSP1 and 32-NSP1-S inside the rings. The average mass density in the 32-NSP1 pore is clearly higher than for 32-NSP1-S (Figs. 5.3c-d and S5.9c-d). Interestingly, we observe that the NSP1 pores feature a strong spatial variation in protein density (middle panel of Fig. 5.3d) with a z-averaged value of ~50 mg/ml at the central axis (Fig. S9c-d). In contrast, the NSP1-S pores show a more uniform protein distribution (bottom panel of Fig. 5.3d) with a considerably reduced density of ~32 mg/ml at the central axis (Fig S5.9c-d). We attribute the higher densities of NSP1 to its high percentage of hydrophobic residues relative to charged residues, consistent with expectations[27]. For both NSP1 and NSP1-S, we observe that proteins are spilling out of the ring (Fig. 5.3d-e), which likely accounts for the cloudy density on top of the rings seen in the cryo-EM data, which also blurs the circular stripes in the origami TEM images. While the density differences between 32-NSP1 and 32-NSP1-S in the simulations match the trend of the experimental intensities obtained by cryo-EM, the absolute mass ratios

quantitatively deviate (2.4 in the measured densities versus 1.2 in the simulated densities integrated over the inner volume of the ring). The difference may be due to excess NSP1 proteins in solution that bind to the rings via hydrophobic interactions with the attached NSP1 proteins and that stay attached upon purification from excess proteins.
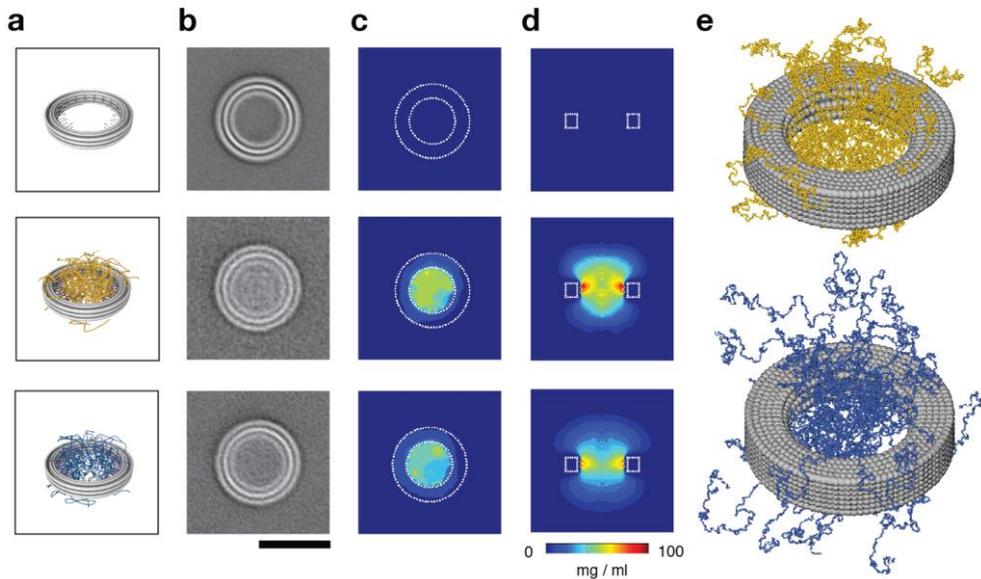
Figure 5.3. Spatial distribution of FG-Nup densities in DNA rings from cryo-EM and MD simulations. a, Schematic representation of (top to bottom): empty ring, 32-NSP1, and 32-NSP1-S. b, Corresponding average micrographs obtained from aligning and summing individual cryo-EM particles. See Fig. S5.8 for exemplary particles. Scale bar = 50 nm. c-d, Time-averaged mass densities of proteins inside the DNA ring obtained from coarse-grained MD simulations averaged in the *z*-direction, shown in top view (c) and side view (d). e, Exemplary snapshot of MD simulations of 32-NSP1 (top) and 32-NSP1-S (bottom), showing that NSP1-S proteins extend further out than NSP1.

We employed nanopore ionic-current measurements[19,20,29–31] to determine the ion conductance of various ring–protein assemblies. DNA origami rings were docked onto solid-state nanopores using the electrophoretic force provided by a 100 mV applied voltage (Fig. 5.4a, see SI methods)[29,30]. Current versus voltage (IV) measurements in 250 mM KCl yielded linear curves (Fig. 5.4b), indicating the stability of the ring in the docked position[29]. To measure the influence of docked rings on the ionic conductance we docked various ring-protein combinations repeatedly on the same nanopore to avoid pore-to-pore variations (exemplary current traces in Fig. 5.4c). For rings without proteins we found a reduction in the conductance of 15 ± 5 % for both 32 and 8 attachment anchors. (Fig. S5.11). A small conductance decrease is expected since the rings partially block the current path in the access region of the solid-state nanopore[29]. To probe for variations in the docking position of a ring on a nanopore, we repeatedly reversed the applied voltage for 10 ms to release and re-dock a single ring multiple times on the same nanopore, which yielded variations of the reduced conductance of ±2 % (Fig. S5.12). We performed experiments for all ring–protein combinations on four different nanopores in which we docked each variant multiple times to obtain reliable statistics, always including a ring variant without attached proteins for comparison[31] (Figs. 45.d-g, S5.11 and S5.13).

We found that increasing the number of attached proteins systematically increases the conductance blockade. For instance, 8-NSP1 results in a reduced conductance of 24 ± 5 %, while 32-NSP1 yields a blockage of 34 ± 6 % on the same nanopore. Moreover, when varying the type of protein, we found that NSP1 blocks the ionic current more strongly than NSP1-S (20 ± 4 % for 8-NSP1 vs. 18 ± 3 % for 8-NSP1-S and 35 ± 5 % for 32-NSP1 vs. 31 ± 9 % for 32-NSP1-S). We can understand these reduced ionic conductances of Nup-filled rings from a simple model that we recently developed (see SI methods and Figs. S5.14 – S5.15). The model assumes a critical protein density, above which no ion conductance is supported. From the spatial protein density distribution found in the simulations (Fig. 5.4h), the ion conductance can then be computed without any further fitting parameters (see SI methods), yielding conductance values that compare well with the experimental results (Fig. 5.4i). While it is gratifying that this simple model captures all trends well, the absolute calculated values are consistently lower than the experimental values which is explained by the fact that experimentally, ions are observed to leak through the DNA ring while such an ionic permeability of the origami structures was not considered in the model.

Figure 5.4. Ionic conductance of rings with FG-Nups docked on a solid-state
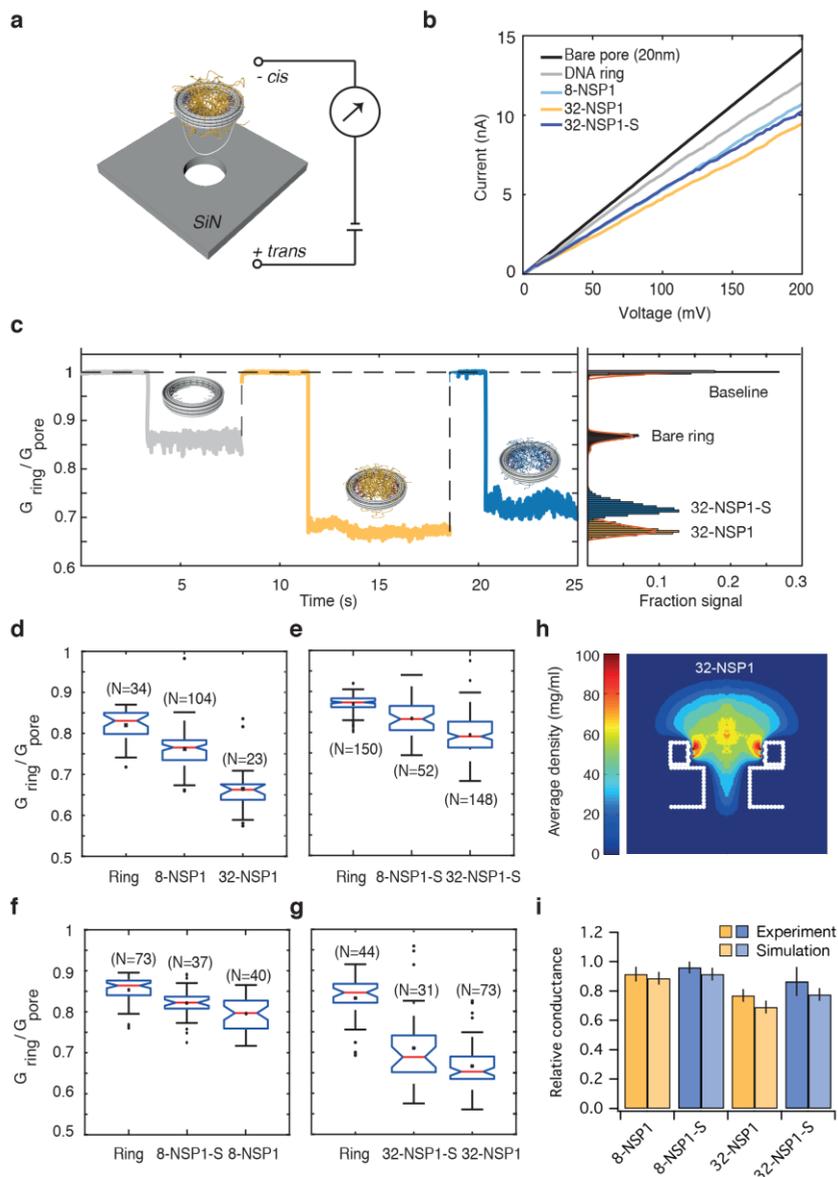
nanopore, from experiments and MD simulations. a, Schematic representation of DNA ring that is docking onto a solid-state nanopore. b, Exemplary current (nA) versus voltage (mV) traces for rings without proteins, 8-NSP1, 32-NSP1 and 32-NSP1-S and the bare nanopore. c, Exemplary relative conductance (G_{ring}/G_{pore}) vs time (s) traces showing the change in conductance upon docking of the ring without protein (gray), 32-NSP1 (yellow), and 32-NSP1-S (blue). d, Box-plot representation of the relative conductance (G_{ring}/G_{pore}) for the empty ring, 8-NSP1 and 32-NSP1. e, Same as d, but for empty ring, 8-NSP1-S and

32-NSP1-S. f, Same as d, but for empty ring, 8-NSP1 and 8-NSP1-S. g, Same as d, but for relative conductance of empty ring, 32-NSP1 and 32-NSP1-S. Each of the panels d-g represents a different nanopore experiment where a series of rings are probed on one particular solid-state nanopore. In the box plot representation in panel (d-g), the blue boxes denote the 25th and 75th percentiles and the red lines represent the median values with the associated wedges representing a 95% confidence interval for the medians. h, Side view (*rz-plane*) average density distribution for 32-NSP1 placed on a 20 nm wide nanopore in a 20 nm thin SiN membrane (see Fig. S5.14 for an exemplary simulation snapshot and Fig. S5.15 for density distributions of other variants). i, Comparison of experimental reduced conductance values and simulation results (see SI methods and Table S5.1 and S5.2).

5.3 Conclusions

Taken together, our experiments demonstrate the successful development of a NPC mimic based on a DNA origami ring as a scaffold to position NSP1 and NSP1-S Nups. This novel approach circumvents major limitations of previous studies by allowing precise control over the number and location of FG-Nup attachment sites which opens the way to high-resolution cryo-EM imaging and transport studies. We find that NSP1 forms a much denser mass distribution compared to NSP1-S, consistent with the reduced hydrophobic interactions in the mutant[23,32].

Our novel approach opens the way to many more sophisticated future experiments on well-controlled NPC mimics. We anticipate that additional NPC components may be integrated into the DNA origami scaffold, for example, different Nups on different anchoring sites, spatial variation along the axial z direction, as well as the modular stacking of multiple rings with different Nups. Such studies will be of interest for disentangling the mechanism of these fascinating natural gatekeepers to the cell nucleus, as well as potentially for applications involving selective membrane pores, for example in synthetic cell systems. On a more general outlook, we note that intrinsically disordered proteins are notoriously difficult to study, yet increasing evidence is amounting their ubiquitous importance in biology. Our DNA origami-based approach is well suited to help elucidate the role of such proteins in other natural biomolecular assemblies.

5.4 Materials and Methods
Design of DNA origami ring

The ring was designed in an iterative procedure of using caDNAno v0.2[1] and CanDo[2,3].

Molecular self-assembly of DNA origami ring.

All reaction mixtures contained single-stranded scaffold DNA at a concentration of 50 nM and oligonucleotide strands (Eurofins MWG, Ebersberg, Germany) at 200 nM each. The reaction buffer includes 5 mM TRIS, 1 mM EDTA, 5 mM NaCl (pH 8) and 20 mM MgCl$_2$. All reaction mixtures were subjected to a thermal annealing ramp using TETRAD (MJ Research, now Biorad) thermal cycling devices. During the annealing, the reaction mixture was exposed to 65ºC for 15 min, then the temperature was decreased with 1º per 2h down to 40ºC.

Gel electrophoresis of self-assembly reactions

Folded DNA-nanostructures were electrophoresed on 2% agarose gels containing 0.5×TBE and 11mM MgCl$_2$ for 2 to 3 h at 70 V bias voltage in a gel box immersed in an iced water-bath. The electrophoresed agarose gels were stained with ethidium bromide and scanned using a Typhoon FLA 9500 laser scanner (GE Healthcare) at a resolution of 50 μm/px.

Total internal reflection microscopy (TIRF)

We annealed the Cy5-oligonucleotides (IDT, Coralville, USA) on origami rings by incubating at a 1:10 ratio of binding spots to oligonucleotides in 250 mM KCl, 10 mM Tris, 1 mM EDTA, and 10 mM MgCl$_2$ at 35°C for 60 min. We did not purify the origami rigs from excess Cy5-oligos as they would be removed during buffer exchange. Flow cells were assembled by sandwiching double-sided tape between PEG passivated microscope quartz slides and cover slips. A small fraction (1:100 ratio) of PEG molecules contained a biotin moiety to facilitate the immobilization and imaging of biotin-labelled DNA origami rings (Fig. S5.4). The flow cell was first incubated with 0.1 mg/ml streptavidin in buffer A (50 mM Tris HCl pH 8.0, 50 mM NaCl, 10 mM MgCl$_2$) for 1 minute. Excess streptavidin was removed with 100 μl of buffer A. Then the Cy5-oligo annealed origami rings of around 50 pM were introduced into the flow cell and incubated for one minute before removing the excess with 100 μl of buffer A. We then introduced an imaging buffer consisting of 40 mM Tris-HCl, pH 8.0, 50 mM NaCl, 10mM MgCl$_2$, 2 mM trolox. We also included an oxygen scavenging system (0.3 mg/ml glucose oxidase and 40 μg/ml catalase with 5% (w/v) glucose as a substrate) for obtaining stable fluorescence from the dye molecules. We used a TIRF-microscope setup that was described earlier[4] for obtaining the bleaching curves of Cy5-labelled rings. We recorded the fluorescence of Cy5 molecules using a 640 nm laser with 30 mW power at a frame rate of 2 Hz until the bright spots reached to the background level. We then plotted the fluorescence intensity from each spot over time. Bleaching of individual fluorophores resulted in a clear step-wise decrease

in fluorescence which facilitated us to count the total number of fluorophores in each ring.

Conjugation of proteins

Nups proteins were a kind gift of S. Frey and D. Görlich. We used a maleimide-cysteine coupling reaction to conjugate the proteins with an oligonucleotide at the single cysteine at the N-terminal tails of both protein variants. The maleimide-modified oligo was produced by Biomers, Ulm, Germany. The proteins were treated with TCEP prior to incubation with the modified oligonucleotides which was subsequently removed using cut off filters (Merck Millipore). The proteins were incubated with the oligonucleotides in the presence of 5M GuHCl-PBS overnight. The protein-oligo mixtures were purified from non-attached oligos by **size exclusion fast protein liquid chromatography (AKTA) with Superdex™ 200** increase columns using the same buffer. First, control samples were analyzed using AKTA. One sample contained only the oligo with a malemide modification **('M-oligo') and one sample contained only NSP1 proteins, to identify the elution** peak for each sample. It is important to mention that the use of GuHCl in the running buffer was essential for this step. GuHCl ensures that NSP1 proteins remain in their unfolded conformation and do not interact with each other, forming aggregates which would result in clogging of the SEC column. The protein was stored at -80°C until it was incubated with the rings.

Preparation of samples for EM imaging

After the folding reaction, excess oligonucleotides were subsequently removed by aagarose gel extraction followed by a PEG precipitation to increase the concentration[7]. DNA rings were incubated with proteins at a ratio of 1:8 per binding site at a $MgCl_2$ concentration of 20 mM and 2 M GuHCl at room temperature for 6 –10 h. Excess proteins were subsequently removed by two rounds of PEG precipitations[7]. The pellet was resuspended in a buffer containing 5 mM Tris, 1 mM EDTA, 5 mM NaCl and 5 mM $MgCl_2$. Shortly before applying the sample to the EM grids the $MgCl_2$ concentration was increased to 20 mM.

TEM imaging

Purified sample of DNA rings with or without attached proteins were adsorbed on glow-discharged formvar-supported carbon-coated Cu400 TEM grids (Science Services, Munich, Germany) and stained using a 2% aqueous uranyl formate solution containing 25 mM sodium hydroxide. Imaging was performed using a Philips CM100 electron microscope operated at 100 kV. Images were acquired

using a AMT 4 Megapixel CCD camera at a magnification of x28,500. Tomography tilt series were acquired using a FEI Tecnai Spirit electron microscope operating at 120 kV. Tilt series were acquired using a TemCam-F416 (Tietz, Gauting, Germany) camera at magnification of x42,000 with tilt angles between -50° and 50° in steps of 1°. Tomography calculations were performed using IMOD[8].

The manual classification of particles shown in Fig. 5.2f-h was performed by pooling all particles of all three samples together and subsequently randomizing the order to avoid any bias. Classification of all particles was performed by P.K. and E.B. independently and the results were averaged.

Cryo-EM imaging and image processing

Samples of DNA rings with or without attached proteins (in 20 mM $MgCl_2$, 5 mM tris base, 1 mM EDTA, and 5 mM NaCl) were incubated for 120 s on glow-discharged lacey carbon grids with ultrathin carbon film (Ted Pella, 01824) and vitrified using a freeze-plunging device (Vitrobot Mark IV, FEI). Samples were imaged at liquid nitrogen temperatures using a Titan Krios TEM (FEI) operating at 300 kV with a Falcon II detector (FEI) set to a magnification of ×29,000 and a **defocus around −2 μm. 2D averaging was performed with a custom script written** in MathWorks MATLAB (R2013b; 8.2.0.701). The particles used for all three averages shown in Fig. 3b were selected by choosing particles with high intensity inside the ring relative to the mean intensity of the particle image. Rationally-aligned reference-free class averages were calculated (Fig. S5.10) using Relion2[9] and Ctffind v4.0[10] for ctf-correction.

Preparation of samples for nanopore measurements

All samples were prepared and measured at a concentration of 200-300 pM of rings in a buffer containing 250 mM KCl, 50 mM $MgCl_2$ and 10 mM TE. The (8 or 32) rings were incubated in 250 mM KCl, 2.5 M GuHCL, 50 mM $MgCl_2$ and 10 mM TE overnight overnight with oligo-NSP1(-S) in 30x excess per binding site in the shaker at 300 rpm and 35°C. Next, free oligo-NSP1(-S) was removed by incubating the sample with magnetic beads (MB, 6.25 mg/pmol) for at least 30 min in the shaker at 300 rpm and 35°C. The final concentration of GuHCl in samples containing rings with NSP1(-S) was 150 mM. At least 150 mM GuHCl was also added to rings without NSP1(-S) to adjust the baseline current correspondingly. The magnetic beads have oligos attached that are complementary to the oligo attached to NSP1(-S).

Ionic conductance measurements with solid-state nanopores

Samples of DNA rings at approximately 200 pM in measurement buffer (250 mM KCl, 10 mM Tris, 1 mM EDTA and 50 mM $MgCl_2$) were added to the *Cis*-chamber of the flowcell (Fig. 45.a). When applying a voltage (100 mV), the electrophoretic force acts on the negatively charged DNA rings and pulls them onto the nanopore. Multiple DNA ring samples were loaded per nanopore experiment for comparable results. The custom made PMMA-flowcell chamber with sample was washed with 3-fold excess buffer between loading samples[11,12]. The current vs. voltage (IV) characteristics of the bare pore were determined, to confirm a linear IV dependence without intercept and the stability of the nanopore. IV-curves were recorded from -200 to +200 mV with steps 2.5 mV (Fig. 5.4b). Data acquisition was performed at room temperature, with +100 mV applied voltage (unless stated otherwise). Ionic currents were detected using a patch clamp amplifier (Axopatch 200B, Axon Instruments) at 100 kHz bandwidth, digitized with a DAQ card at 500 kHz and recorded with Clampex 9.2 (Axon Instruments).

Efforts to detect translocation events of importer proteins were hampered by a significant level of noise in the ionic current signal upon docking the rings to the nanopores (Fig. S5.14). Such translocation measurements may be feasible in future work when using a lipid bilayer instead of a solid-state nanopore.

Conductance blockade analysis

Current traces were analysed with a custom Matlab script. The files were loaded into Matlab and filtered (1 kHz low-pass Gaussian) with Transalyzer[13]. The filtered traces were separated between zaps into ring traces for each DNA ring with zap residues removed. Each ring trace was further analysed as follows. A histogram was fit to the current trace over time (1000 bins/nS). The histogram was smoothened, and peaks were selected (minimal peak distance 0.75 nS/peak) using build-in Matlab functions. The baseline conductance was selected, and the ring conductance was calculated from the averaged remaining peaks. Finally, the rings were selected with a baseline within 0.75 nS of the estimated average baseline and a minimal event length (0.3 s). The boxplots were created with build-in Matlab functions from the fractions of the ring and baseline conductance for each ring. The boxplot notches provide a 95% confidence interval for the median, confidence interval that are disjoint are different at the 5% significance level. The vertical and horizontal black bars denote the whiskers extending to the most extreme data points; the individual black dots represent outliers. The boxplot whiskers in Fig. 4d-g (black) correspond to approximately ±2.7σ

Salt concentrations

We note that the interactions between the Nups potentially may depend slightly on the salt concentration and the corresponding screening length. For the cryo-EM measurements, we used 20 mM $MgCl_2$ + 5 mM NaCl which yields a screening length of ~1.5 nm. For the conductivity measurements, we used 250 mM KCl + 50 mM $MgCl_2$, yielding a shorter screening length of ~0.5 nm. The screening length in cells is ~0.8 nm (150 mM monovalent salt concentration).

Molecular Dynamics (MD) simulations

The one-bead-per-amino-acid MD model used here accounts for the exact amino-acid sequence of the FG-Nups, with each bead centered at the C_α positions of the polypeptide chain[14,15]. The average mass of the beads is 120 Da. Each bond is represented by a stiff harmonic spring potential with a bond length of 0.38 nm[14]. The bending and torsion potentials for this model were extracted from the Ramachandran data of the coiled regions of protein structures. Solvent polarity is incorporated through a distance-dependent dielectric constant, and ionic screening is accounted for through Debye screening with a screening length that is consistent with the salt concentrations used in the cryo-EM and conductance experiments as described in the previous section. The hydrophobic interactions among the amino-acids are incorporated through a modified Lennard-Jones potential accounting for hydrophobicity scales of all 20 amino-acids through normalized experimental partition energy data renormalized in a range of 0 to 1. For details of the method and its parametrization, the reader is referred to reference[15]. The DNA ring was modelled as a cylinder of height 13.85 nm and diameter of 36 nm constructed from inert beads of diameter 2.6 nm. The DNA ring is modelled in detail and the FG domains are anchored to the scaffold at the specified attachment sites given by the origami design (see Figs. 5.3e, S5.1b-c and S5.14).

MD simulations were carried out using GROMACS 4.5.1. First, the systems were energy minimized to remove any overlap of the amino acid beads. Then the long-range forces were gradually switched on. The simulations were carried out for over $5x10^7$ steps (with the first $5x10^6$ steps ignored for extracting the end-result data), which was found to be long enough to have converged results in the density distribution inside the pores. The time-averaged density calculations presented in the main text were carried out by centering the nanopore in a 100 nm x 100 nm x 140 nm box, which was divided into discrete cells of volume $(0.5 nm)^3$ and the number density in each cell was recorded as a function of simulation time. Finally, the number density was averaged over the simulation time and multiplied with the mass of each bead to get the time-averaged 3D density

profile. The 3D density in cylindrical coordinates $\rho(r, \theta, z)$ was averaged in the circumferential (θ) direction to obtain two-dimensional (2D) $\rho(r, z)$ density plots (as shown in Fig. 5.3d and 5.4h). The 3D density was also averaged in the z-direction (extending out to $|z| = 25$ nm, where the density was found to be zero) to obtain 2D $\rho(r, \theta)$ density distributions (Fig. 5.3c). Finally, the radial density distribution $\rho(r)$ was obtained by averaging the 2D $\rho(r, z)$ density maps in the vertical direction ($|z| < 25$ nm) and shown in Fig. S5.9c-d. For comparison with the cryo-EM data, we integrated the circularly averaged 2D $\rho(r, z)$ density profile (Fig. 5.3d) over radii corresponding to the inside of the ring ($r = 18$ nm) and over $|z| < 25$ nm, giving the total mass M of proteins inside the ring.

Density-based conductance calculation

We previously developed a model to calculate the conductance from the density of the FG-Nups in a separate study in which NSP1 and NSP1-S were directly attached to solid-state nanopores[16]. **Here, we briefly recapitulate the model's** essentials, before describing its extension to account for the DNA ring. The ionic conductance $G(d)$ for cylindrical bare solid-state (SiN) nanopores of diameter d can be expressed as[17,18]

$$G(d) = \sigma_{bare}[4l/(\pi d^2) + 1/d]^{-1}, \qquad (1)$$

where the first and second terms in the denominator account for the pore resistance and the access resistance, respectively. Here, $l = 20$ nm is the height of the pore and σ_{bare} is the ionic conductivity through the bare pore. In order to probe the conductance of the nanopores coated with FG-Nups, we developed a density-based conductance relation by assuming that the presence of protein reduces the conductivity in the pore and access region by means of volume exclusion[16]:

$$G(d) = \left[\left(4l/(\pi d^2 \sigma_{pore})\right) + (1/(d\sigma_{access}))\right]^{-1}. \qquad (2)$$

To calculate the effective conductivity σ_{pore} for a specific pore diameter d, we make use of the radial density distributions $\rho(r)$ of the Nups inside the pore, i.e., averaged over the range -10 nm $< z <$ 10 nm. The ion conductivity is taken equal to σ_{bare} for regions where the Nup density is zero. The conductivity is assumed to decrease linearly with the local protein density as $\sigma(r) = \sigma_{bare}(1 - \rho(r)/\rho_{crit})$, where ρ_{crit} is taken equal to 85 mg/ml[16], and set to zero at and beyond that critical density. Then by radially integrating $\sigma(r)$, the conductivity of the pore can be calculated as

$$\sigma_{\mathbf{pore}} = (4/\pi d^2) \int_{r=0}^{r=\frac{d}{2}} 2\pi r \sigma(r) dr. \qquad (3)$$

A similar expression is also used to calculate the access conductivity ($\sigma_{\mathbf{access}}$), but with the radial density distribution $\rho(\mathbf{r})$ obtained by integrating over z-values in the access region i.e., 10 nm $< |z| <$ 40 nm[19]. The conductance results for the bare pore as well as for SiN nanopores coated with NSP1 or NSP1-S were shown to be in excellent agreement with the experimentally observed sconductances.[16]

In the study presented here, we extended the model to FG-Nups tethered inside a DNA ring which is placed on top of a bare nanopore (Fig. S5.14). The conductance experiments for the Nup-coated DNA ring on top of a bare pore were carried out at a salt concentration of 250 mM KCl + 50 mM MgCl$_2$ leading to a bulk conductivity of $\sigma_{\mathbf{bare}}$ = 4.30 ± 0.13 nS/nm (from bulk conductivity measurements at these conditions). For the system with the DNA ring shown in Fig. S5.14, z = 0 nm is chosen to be the centre of the DNA ring so that the SiN nanopore region corresponds to -27 nm $< z <$ 7 nm (Fig. S5.15). In Fig. S5.15 it can be observed that outside the SiN nanopore the protein has non-zero density towards the ring side (top) and zero density on the other (bottom) side. Therefore, the access resistance contains contributions from the top side with non-zero protein density in the region -7 nm $< z <$ 33 nm and from the bottom side in the region $z <$ -27 nm with zero density. Therefore, we modified the access resistance term in Eqn. 2 to differentiate between the top and bottom access resistance, resulting in the conductance relation for FG-Nup coated DNA rings placed on a SiN pore, as

$$G(d) = \left[4l/\left(\pi d^2 \sigma_{\mathbf{pore}}\right) + 1/(2d\sigma_{\mathbf{access}}) + 1/(2d\sigma_{\mathbf{bare}}) \right]^{-1} \qquad (4)$$

5.5 Supporting information
Details of NSP1 and NSP1-S

The NSP1 (67.5 kDa) and NSP1-S (62.1 kDa) were purified as described in Frey et al.[5,6].

Sequence of NSP1

MSKHHHHHSGHHHTGHHHHSGSHHHTGENLYFQGSNFNTPQQNKTPFSFGTANNNSN
TTNQNSSTGAGAFGTGQSTFGFNNSAPNNTNNANSSITPAFGSNNTGNTAFGNSNPTS
NVFGSNNSTTNTFGSNSAGTSLFGSSSAQQTKSNGTAGGNTFGSSSLFNNSTNSNTTKP
AFGGLNFGGGNNTTPSSTGNANTSNNLFGATANANKPAFSFGATTNDDKKTEPDKPAF
SFNSSVGNKTDAQAPTTGFSFGSQLGGNKTVNEAAKPSLSFGSGSAGANPAGASQPEPT
TNEPAKPALSFGTATSDNKTTNTTPSFSFGAKSDENKAGATSKPAFSFGAKPEEKKDDNS
SKPAFSFGAKSNEDKQDGTAKPAFSFGAKPAEKNNNETSKPAFSFGAKSDEKKDGDASK
PAFSFGAKPDENKASATSKPAFSFGAKPEEKKDDNSSKPAFSFGAKSNEDKQDGTAKPA
FSFGAKPAEKNNNETSKPAFSFGAKSDEKKDGDASKPAFSFGAKSDEKKDSDSSKPAFSF
GTKSNEKKDSGSSKPAFSFGAKPDEKKNDEVSKPAFSFGAKANEKKESDESKSAFSFGSK
PTGKEEGDGAKAAISFGAKPEEQKSSDTSKPAFTFGAQKDNEKKTETSC.

Sequence for NSP1-S

MSKHHHHHSGHHHTGHHHHSGSHHHTGENLYFQGSNSNTPQQNKTPSSSGTANNNSN
TTNQNSSTGAGASGTGQSTSGSNNSAPNNTNNANSSSTPASGSNNTGNTASGNSNPTS
NSSGSNNSTTNTSGSNSAGTSSSGSSSAQQTKSNGTAGGNTSGSSSSSNNSTNSNTTKP
ASGGSNSGGGNNTTPSSTGNANTSNNSSGATANANKPASSSGATTNDDKKTEPDKPAS
SSNSSSGNKTDAQAPTTGSSSGSQSGGNKTSNEAAKPSSSSGSGSAGANPAGASQPEPT
TNEPAKPASSSGTATSDNKTTNTTPSSSSGAKSDENKAGATSKPASSSGAKPEEKKDDNS
SKPASSSGAKSNEDKQDGTAKPASSSGAKPAEKNNNETSKPASSSGAKSDEKKDGDASK
PASSSGAKPDENKASATSKPASSSGAKPEEKKDDNSSKPASSSGAKSNEDKQDGTAKPA
SSSGAKPAEKNNNETSKPASSSGAKSDEKKDGDASKPASSSGAKSDEKKDSDSSKPASSS
GTKSNEKKDSGSSKPASSSGAKPDEKKNDESSKPASSSGAKANEKKESDESKSASSSGSK
PTGKEEGDGAKAASSSGAKPEEQKSSDTSKPASTSGAQKDNEKKTESTSC.

System	G(d) nS	Stand. dev (G(d)) (nS)	Relative Conductance (RC)	Error (RC)
Bare ring	37.80	1.20	1.00	0.03
8-NSP1	33.53	1.01	0.89	0.04
8-NSP1-S	34.60	1.05	0.92	0.04
32-NSP1	26.15	0.79	0.69	0.04
32-NSP1-S	29.36	0.89	0.78	0.04

Supplementary Table S5.1. Computed conductance for DNA ring coated with 8 and 32 copies of NSP1 and NSP1-S.

Table S5.1 shows the computed absolute conductance for the system with FG-nups tethered inside the DNA ring placed on a SiN nanopore (calculated using Eqn. 4) and bare DNA ring on a SiN nanopore (using Eqn. 1). The standard deviation in $G(d)$ accounts for the standard deviation in bare pore conductivity (σ_{bare}). We obtain the relative conductance and corresponding error by normalizing with the bare ring system. In order to compare the computational conductance with the experiments shown in Fig. 5.4d-g, we normalized the experimental relative conductance (mean of different realizations from Fig. 5.4d-g) with the bare ring on a SiN nanopore results as shown in Table S5.2.

System	G_{ring}/G_{pore}	Error	Relative Conductance (RC)	Error (RC)
Bare ring	0.85	0.03	1.00	0.04
8-NSP1	0.78	0.03	0.91	0.05
8-NSP1-S	0.83	0.02	0.97	0.04
32-NSP1	0.66	0.02	0.77	0.04
32-NSP1-S	0.74	0.07	0.87	0.10
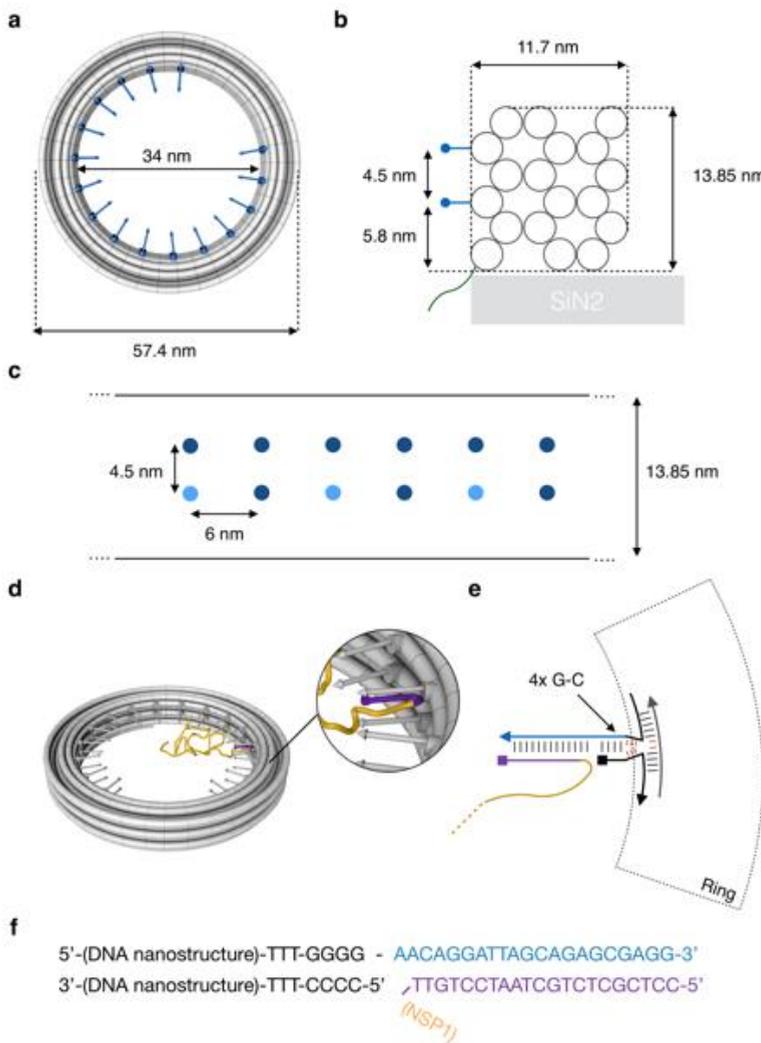
Supplementary Figure 5.1. Geometry of DNA origami ring and protein attachment. a, Schematic representation of DNA origami ring with indicated dimensions. Attachment anchors depicted in blue. b, Schematic cross section of the ring. Attachment anchors are depicted in blue and the starting position of the leash in green. c, Schematic view onto a part of the inner surface of the ring indicating the geometry of the attachment anchors. Light blue circles indicate anchors used for the 8 attachment sites variant, dark blue and light blue circles indicate positions of all 32 attachment anchors. d, Schematic representation of DNA ring with one protein bound. DNA oligonucleotide attached to the protein is depicted in purple. e, Schematic sketch of the design of one attachment anchor. Red lines indicate unpaired nucleotides. f, Attachment anchor sequences.

Leash
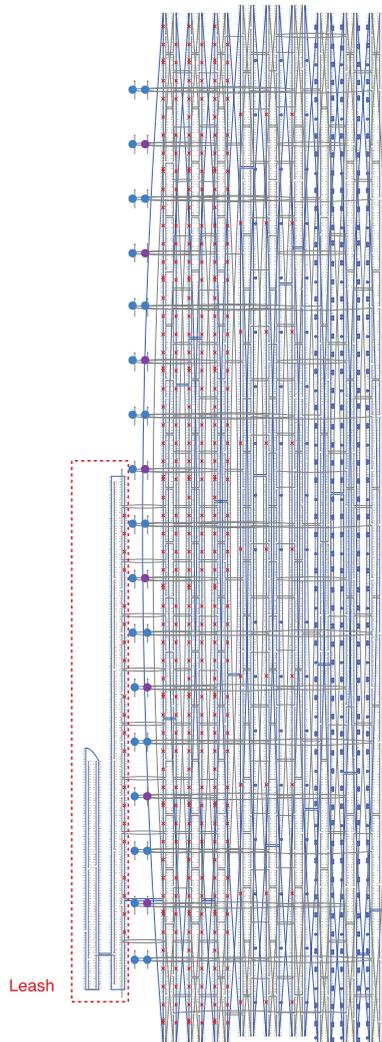
Supplementary Figure 5. 2. Scaffold / staple layout of the DNA ring. Generated with caDNAno v0.2. Purple dots indicate positions of attachment anchors of the variant with 8 anchors, blue and purple dots indicate positions of all 32 attachment anchors.

\
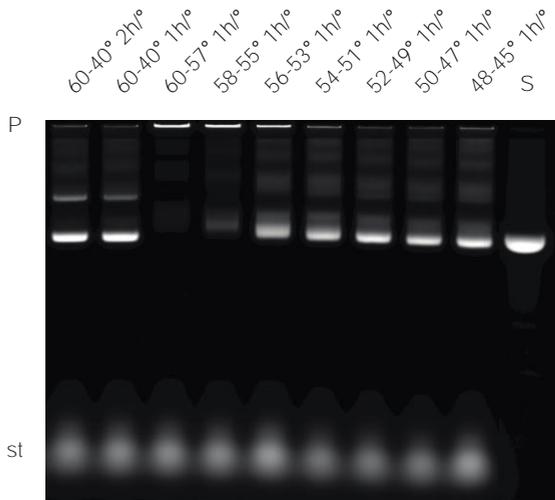
Supplementary Figure 5.3. Electrophoretic mobility analysis of the ring. Laser-scanned image of a 2% agarose gel with 11mM MgCl$_2$ run on an iced water-bath. **S=scaffold DNA, folding ramps as indicated. 'P' denotes the pockets and 'st' the excess** staple oligonucleotides. Image was globally auto-levelled below the pockets.
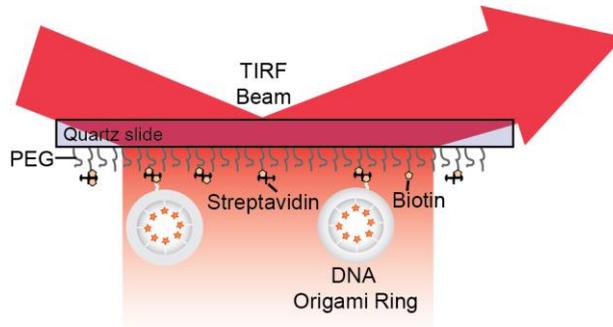
Supplementary Figure 5.4. Schematic diagram showing TIRF imaging of Cy5-labelled DNA origami rings. The rings are attached to the Quartz surface by biotin-streptavidin-biotin interactions.
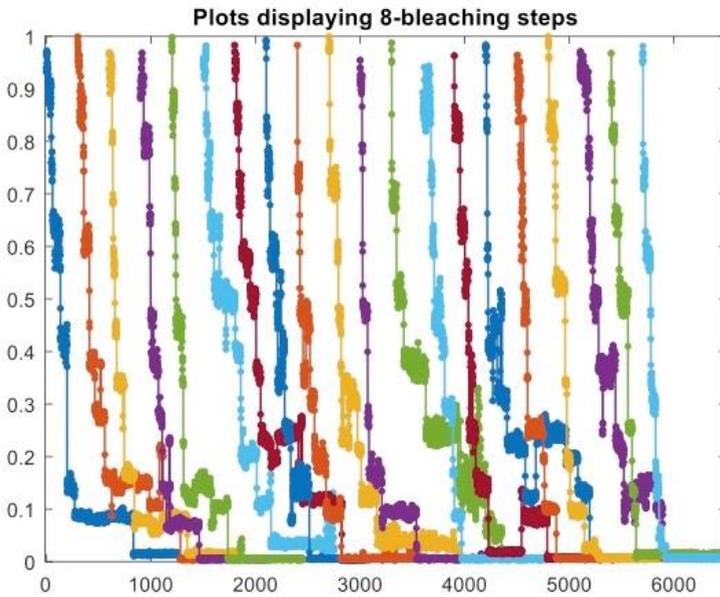
Supplementary Figure 5.5. Exemplary TIRF bleaching curves showing 8 bleaching steps. Every plot is shifted in time by 300s for visualization. Intensity is normalized to the maximum intensity.
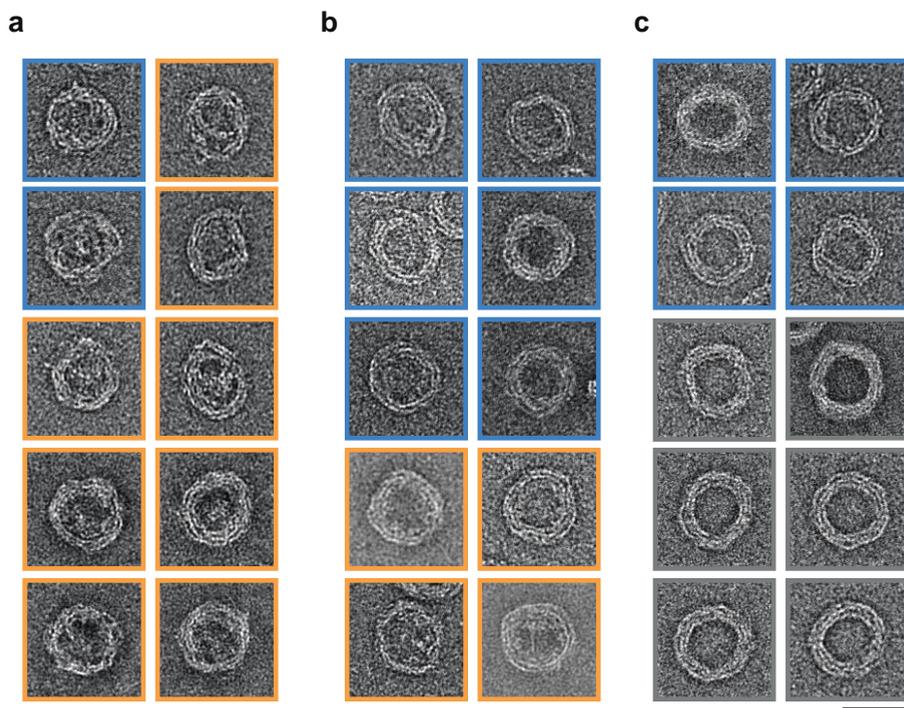
Supplementary Figure 5.6. Exemplary negative-stain TEM particles. Samples: DNA ring with 32-NSP1 (a), with 32-NSP1-S (b), and with no protein (c). Scale bar = 50 nm
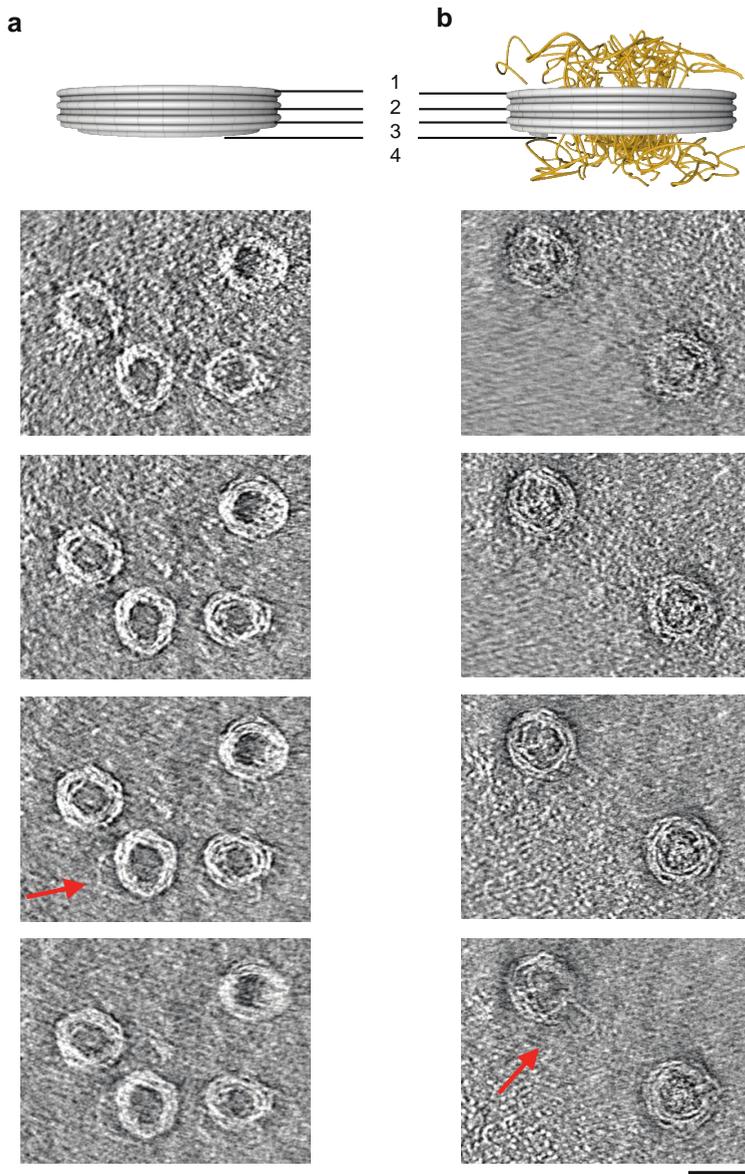
Supplementary Figure 5.7. Tomography of bare ring without proteins and of 32-NSP-1. Schematic representation of DNA ring without (a) and with NSP1 (b). Numbers indicate positions of slices of reconstruction from tomography data shown below top images at position 1; bottom images at position 4). Red arrows indicate the bottom leash of DNA rings. Scale bar = 50 nm.
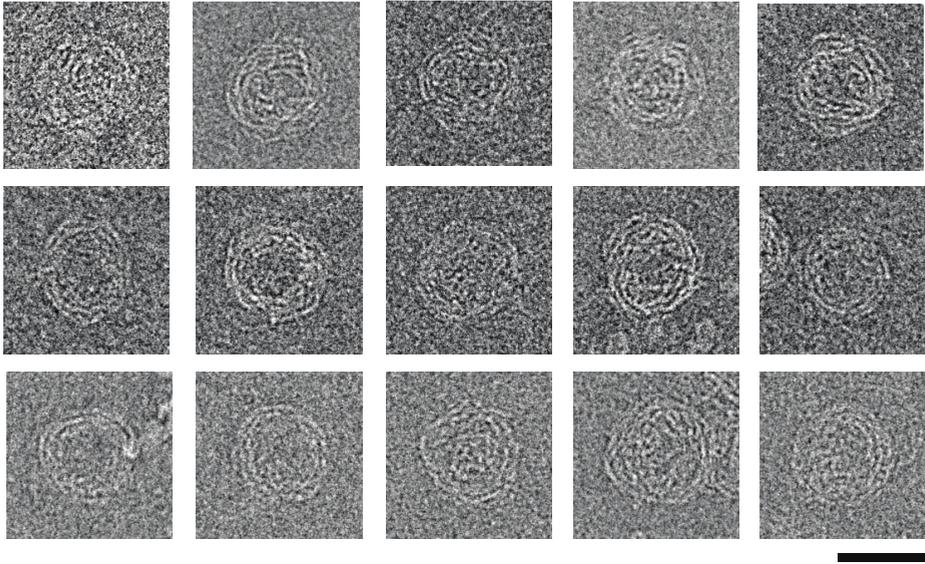
Supplementary Figure 5.8. Exemplary cryo-EM single particles of the sample 32-NSP1. Scale bar = 50 nm.
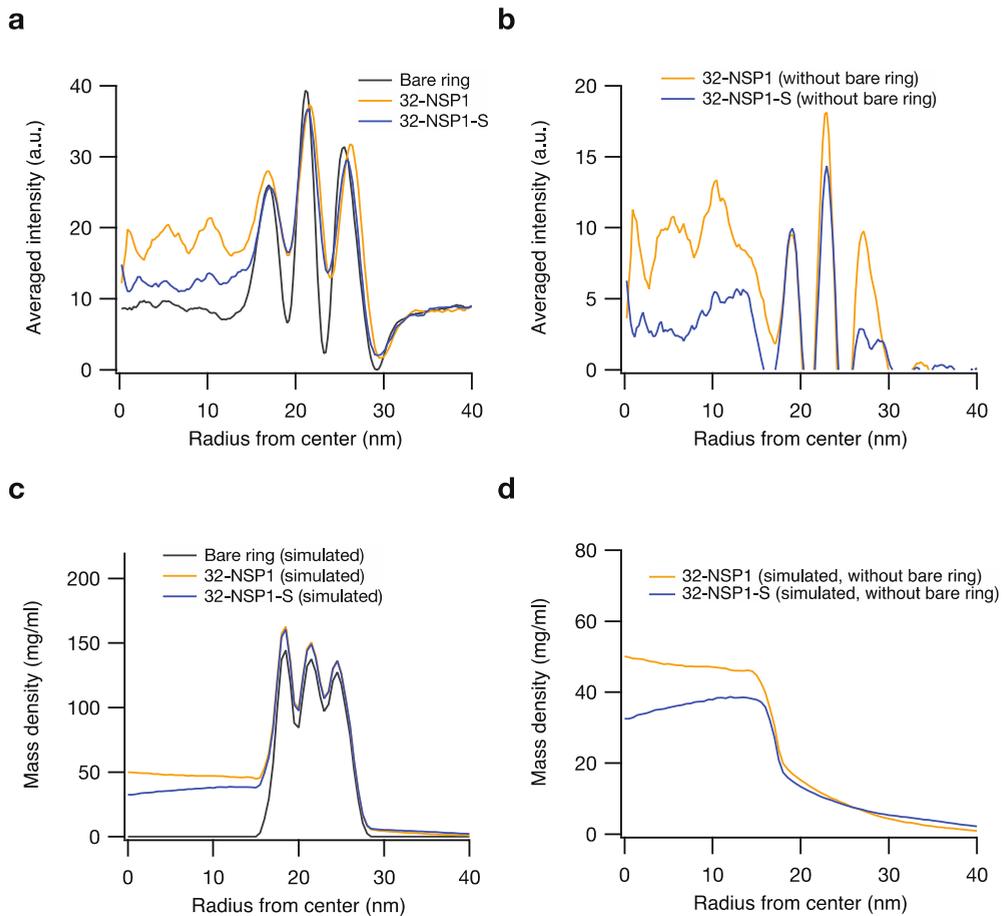
Supplementary Figure 5.9. Comparison of densities from cryo-EM and MD simulations. a, Circularly averaged radial intensity profiles obtained from the cryo-EM average micrographs shown in Fig. 5.3b containing the ring as well as the proteins. b, As in a, but the profile of the bare ring was subtracted from the profiles with proteins. Note that residual density oscillations for radii 17-28 nm are observed as these are difference signals from strongly oscillating intensities (see a) that are slightly misaligned. c, Time-averaged radial density distribution of the ring-nanopore system with NSP1 and NSP1-S, averaged in the circumferential direction and axial direction for $|z| < 25$ nm. The bare ring density was calculated from a pdb file obtained from a CanDo simulation. d, As in c, but only the protein density is shown. The data shows a higher mass density for rings with NSP1 compared to rings with NSP1-S for the same number (32) of FG-Nup copies.

a

b
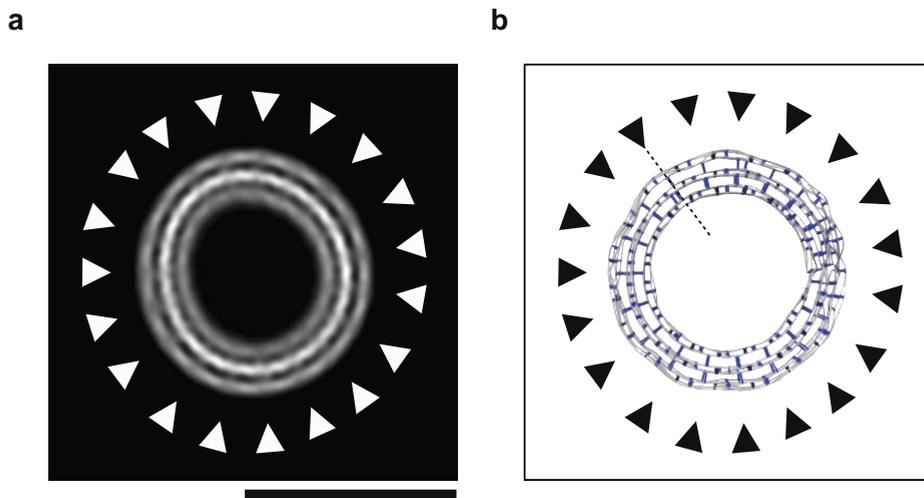
Supplementary Figure 5.10. Comparison of cryo-EM 2D class averages with predicted structure. a, Rotationally aligned reference-free class average of DNA ring with 32 attachment sites without attached protein calculated with Relion2[9]. Number of averaged particles is 2757. White arrows indicate density spikes. Scale bar = 50 nm. b, CanDo simulation of DNA ring. Crossovers are depicted in blue; arrows indicate their positions. c, Other class averages obtained from the same measurement as in a. Numbers of averaged particles are (f.l.t.r.) 2670, 1228, and 551. Scale bar = 50 nm.
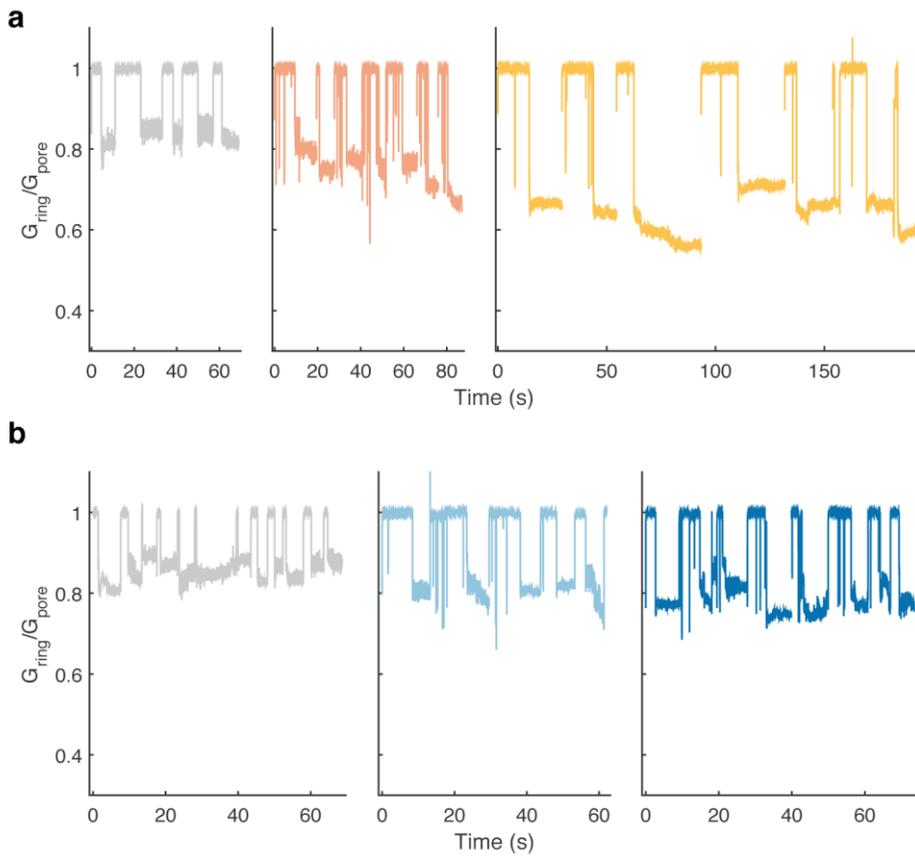
Supplementary Figure 5.11. Exemplary ionic current traces for ring-docking events. Reduced conductance (G_{ring}/G_{pore}) traces over time for DNA rings that are docked onto a nanopore (see methods). a, Data for bare ring (gray), 8-NSP1 (red), 32-NSP1 (yellow). b, bare ring (gray), 8-NSP1-S (lightblue), 32-NSP1-S (blue).

a

b
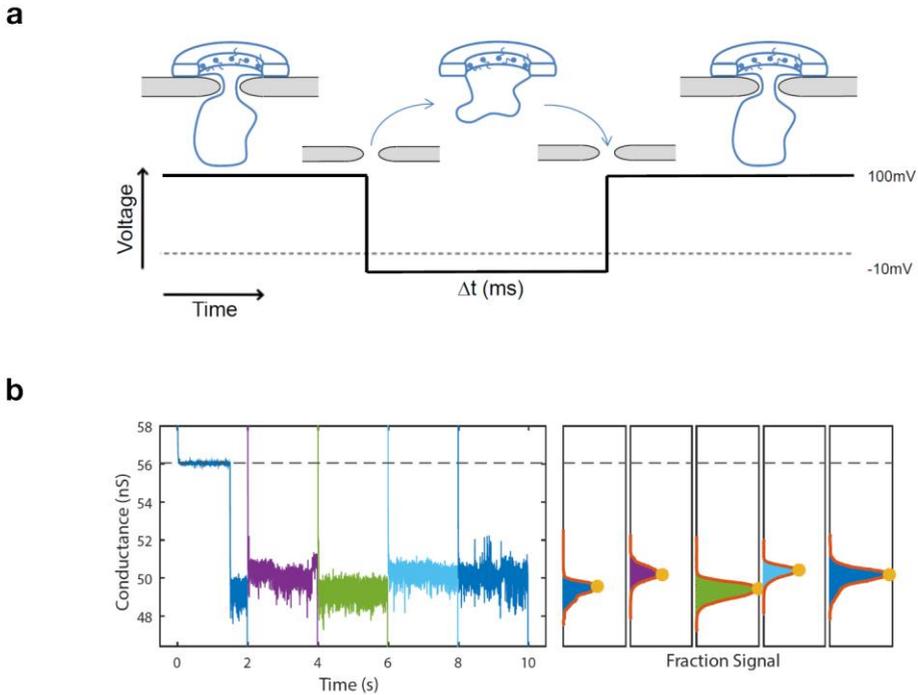
Supplementary Figure 5.12. Ionic current traces of multiple re-docking of a DNA ring on a nanopore. a, Schematic representation showing the DNA ring re-docking on the nanopore by temporarily switching the applied voltage from 100 mV to -10 mV for Δt = 10 ms (every 2 s). b, Left: Filtered (1kHz low-pass Gaussian) continuous ionic current trace showing the conductance of the DNA ring, displayed in different colors after each re-docking. Right: Smoothened trace histogram (red) and fitted histogram peaks (yellow) for the data plotted on the left. Gray dotted line indicates the average nanopore conductance at the moment just before the ring is first docked.

a

b
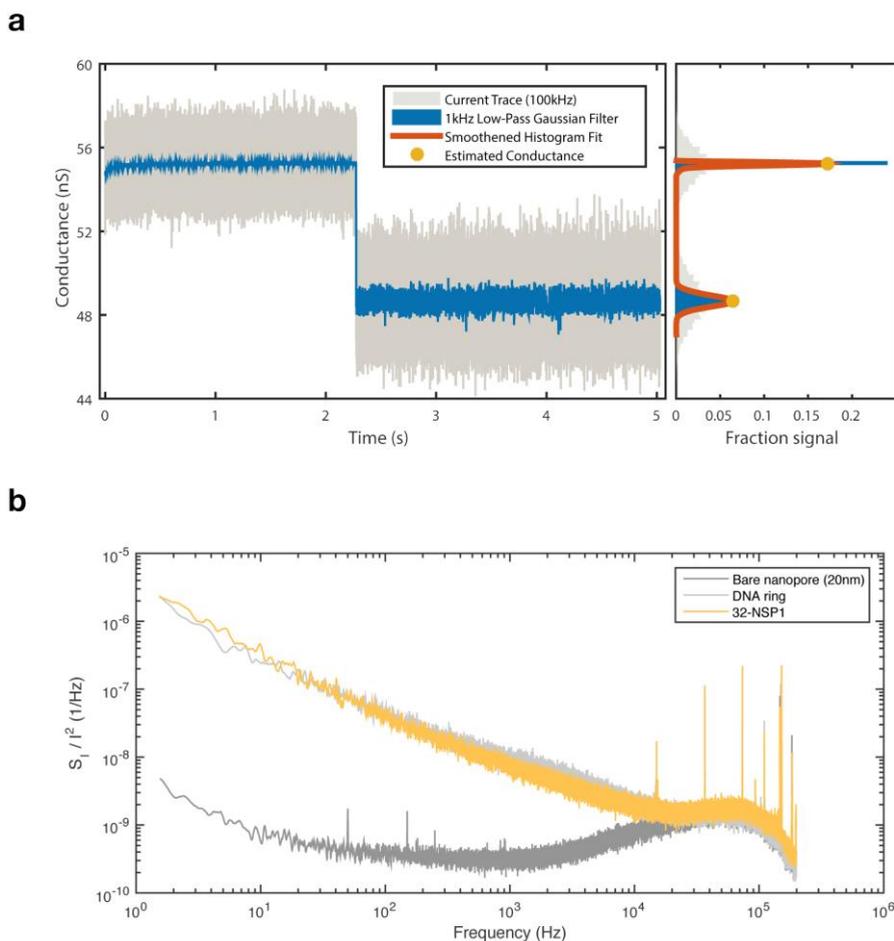
Supplementary Figure 5.13. Noise comparison of the bare nanopore and DNA ring docked on a nanopore. a, Raw ionic current trace of the bare nanopore and of a docked DNA ring, showing the filtered (1 kHz low-pass Gaussian, blue) and full bandwidth (100 kHz, gray) data, together with a smoothened trace histogram and fitted histogram peaks (yellow). The bare nanopore conductance is 55.23 nS and the docked DNA ring conductance is 48.65 nS. b, Normalized power spectral density of the measured ionic current trace for a bare nanopore (dark gray), a nanopore with docked bare ring (light gray), and a docked 32-NSP1 ring (yellow). Typical translocation events are observed near 1 kHz. The noise spikes at frequencies above 20 kHz are inherent to the system setup and shared among all three traces.

a

b

DNA Ring

SiN pore
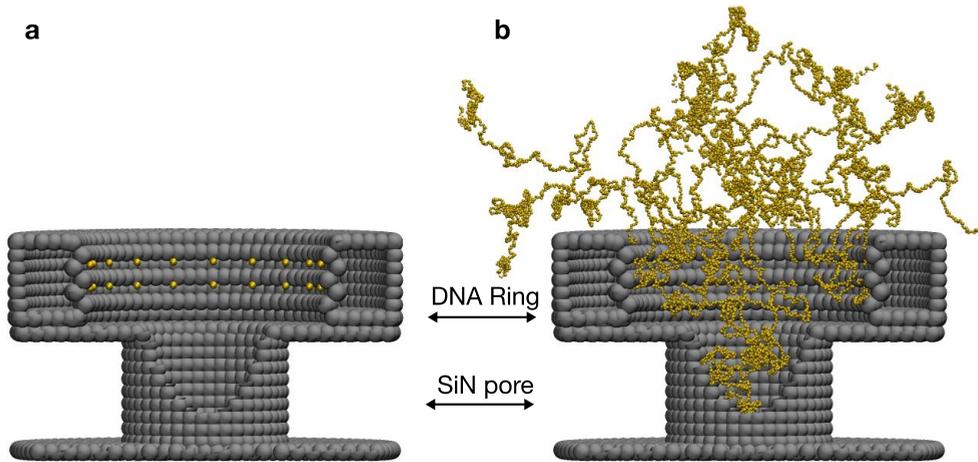
Supplementary Figure 5.14. MD simulations of DNA ring with attached Nups on a solid-state nanopore. a, Cut-through of the DNA ring model with a height of 13.85 nm and a diameter of 36 nm, placed on top of a solid-state nanopore with a height and diameter of 20 nm. The positions of the attachment anchors for the Nups are indicated in yellow. b, Cut-through of a snapshot of a MD simulation with in total 32 NSP1 proteins tethered inside the DNA ring.
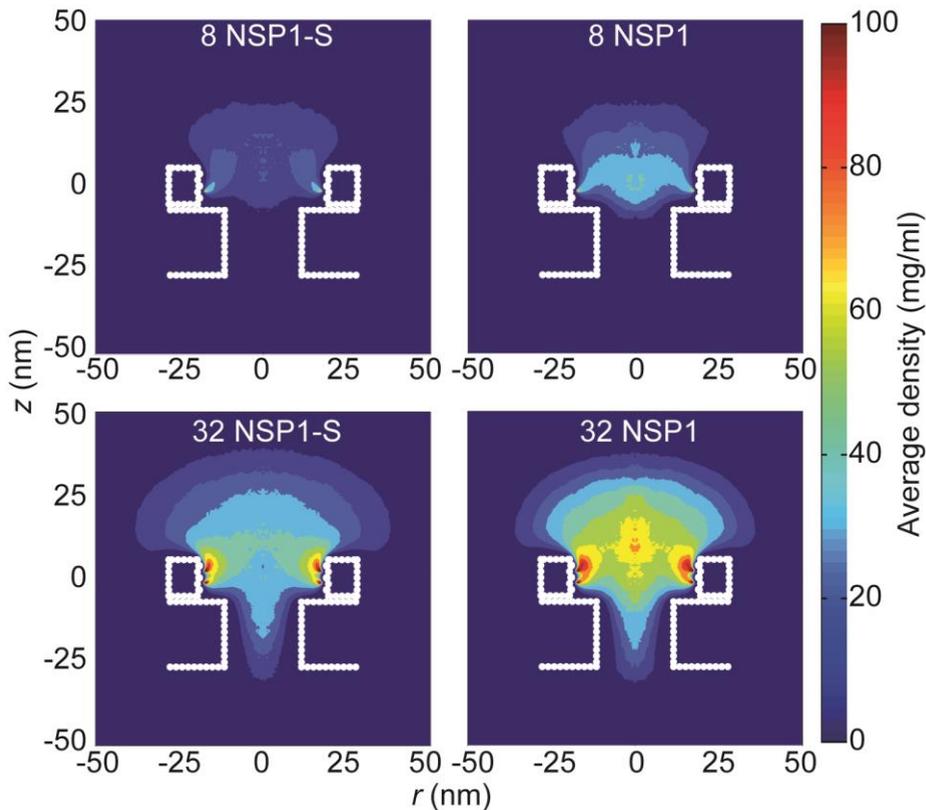
Supplementary Figure 5.15. Time-averaged *r-z* density distribution of rings with 8 (top row) or 32 (bottom row) copies of NSP1 (right column) or NSP1-S (left column) docked on a nanopore. This data shows denser structures of NSP1 inside the nanopores compared to NSP1-S for the same number of copies.

References

(1)   Cronshaw, J. M.; Krutchinsky, A. N.; Zhang, W.; Chait, B. T.; Matunis, M. J. Proteomic Analysis of the Mammalian Nuclear Pore Complex. *J. Cell Biol.* 2002, *158*, 915–927.

(2)   Beck, M.; Hurt, E. The Nuclear Pore Complex: Understanding Its Function through Structural Insight. *Nat. Rev. Mol. Cell Biol.* 2016, *18*, 73–89.

(3)   Alber, F.; Dokudovskaya, S.; Veenhoff, L. M.; Zhang, W.; Kipper, J.; Devos, D.; Suprapto, A.; Karni-Schmidt, O.; Williams, R.; Chait, B. T.; *et al.* The Molecular Architecture of the Nuclear Pore Complex. *Nature* 2007, *450*, 695–701.

(4)   Rout, M. P.; Aitchison, J. D.; Suprapto, A.; Hjertaas, K.; Zhao, Y.; Chait, B. T. The Yeast Nuclear Pore Complex. *J. Cell Biol.* 2000, *148*, 635–652.

(5)   Patel, S. S.; Belmont, B. J.; Sante, J. M.; Rexach, M. F. Natively Unfolded Nucleoporins Gate Protein Diffusion across the Nuclear Pore Complex. *Cell* 2007, *129*, 83–96.

(6)   Shahin, V. Cellular Transport: Gatekeepers of the Nucleus. *Nat Nano* 2016, *11*, 658–659.

(7)   Lim, R. Y. H.; Fahrenkrog, B.; Köser, J.; Schwarz-Herion, K.; Deng, J.; Aebi, U. Nanomechanical Basis of Selective Gating by the Nuclear Pore Complex. *Science (80-.).* 2007, *318*, 640–643.

(8)   Yamada, J.; Phillips, J. L.; Patel, S.; Goldfien, G.; Calestagne-Morelli, A.; Huang, H.; Reza, R.; Acheson, J.; Krishnan, V. V; Newsam, S.; *et al.* A Bimodal Distribution of Two Distinct Categories of Intrinsically Disordered Structures with Separate Functions in FG Nucleoporins. *Mol. Cell. Proteomics* 2010, *9*, 2205–2224.

(9)   Frey, S.; Görlich, D. A Saturated FG-Repeat Hydrogel Can Reproduce the Permeability Properties of Nuclear Pore Complexes. *Cell* 2007, *130*, 512–523.

(10)   Schleicher, K. D.; Dettmer, S. L.; Kapinos, L. E.; Pagliara, S.; Keyser, U. F.; Jeney, S.; Lim, R. Y. H. Selective Transport Control on Molecular Velcro Made from Intrinsically Disordered Proteins. *Nat. Nanotechnol.* 2014, *9*, 525–530.

(11)   Rout, M. Virtual Gating and Nuclear Transport: The Hole Picture. *Trends Cell Biol.* 2003, *13*, 622–628.

(12)   Jovanovic-Talisman, T.; Tetenbaum-Novatt, J.; McKenney, A. S.; Zilman, A.; Peters, R.; Rout, M. P.; Chait, B. T. Artificial Nanopores That Mimic the Transport Selectivity of the Nuclear Pore Complex. *Nature* 2009, *457*, 1023–1027.

(13)   Caspi, Y.; Zbaida, D.; Cohen, H.; Elbaum, M. Synthetic Mimic of Selective Transport through the Nuclear Pore Complex. *Nano Lett.* 2008, *8*, 3728–3734.

(14)   Kowalczyk, S. W.; Kapinos, L.; Blosser, T. R.; Magalhães, T.; van Nies, P.; Lim, R. Y. H.; Dekker, C. Single-Molecule Transport across an Individual Biomimetic Nuclear Pore Complex. *Nat. Nanotechnol.* 2011, *6*, 433–438.

(15)   Rothemund, P. W. K. Folding DNA to Create Nanoscale Shapes and Patterns. *Nature* 2006, *440*, 297–302.

(16)   Howorka, S. Building Membrane Nanopores. *Nat Nano* 2017, *12*, 619–630.

(17)   Krishnan, S.; Ziegler, D.; Arnaut, V.; Martin, T. G.; Kapsner, K.; Henneberg, K.; Bausch, A. R.; Dietz, H.; Simmel, F. C. Molecular Transport through Large-Diameter DNA Nanopores. 2016, *7*, 12787.

(18)   Langecker, M.; Arnaut, V.; Martin, T. G.; List, J.; Renner, S.; Mayer, M.; Dietz, H.; Simmel, F. C. Synthetic Lipid Membrane Channels Formed by Designed DNA Nanostructures. *Science* 2012, *338*, 932–936.

(19)   Wei, R.; Martin, T. G.; Rant, U.; Dietz, H. DNA Origami Gatekeepers for Solid-State Nanopores. *Angew. Chem. Int. Ed. Engl.* 2012, *51*, 4864–4867.

(20)   Bell, N. a W.; Engst, C. R.; Ablay, M.; Divitini, G.; Ducati, C.; Liedl, T.; Keyser, U. F. DNA Origami Nanopores. *Nano Lett.* 2012, *12*, 512–517.

(21)   Dietz, H.; Douglas, S. M.; Shih, W. M. Folding DNA into Twisted and Curved Nanoscale Shapes. *Science* 2009, *325*, 725–730.

(22)   Yang, Y.; Wang, J.; Shigematsu, H.; Xu, W.; Shih, W. M.; Rothman, J. E.; Lin, C. Self-Assembly of Size-Controlled Liposomes on DNA Nanotemplates. *Nat. Chem.* 2016, *8*, 476–483.

(23)   Frey, S.; Richter, R. P.; Görlich, D. FG-Rich Repeats of Nuclear Pore Proteins Form a Three-Dimensional Meshwork with Hydrogel-like Properties. *Science* 2006, *314*, 815–817.

(24)   Lowe, A. R.; Siegel, J. J.; Kalab, P.; Siu, M.; Weis, K.; Liphardt, J. T. Selectivity Mechanism of the Nuclear Pore Complex Characterized by Single Cargo Tracking. *Nature* 2010, *467*, 600–603.

(25)   Hall, A. R.; Scott, A.; Rotem, D.; Mehta, K. K.; Bayley, H.; Dekker, C. Hybrid Pore Formation by Directed Insertion of α-Haemolysin into Solid-State Nanopores. *Nat. Nanotechnol.* 2010, *5*, 874–877.

(26)   Wagenbauer, K. F.; Engelhardt, F. A. S.; Stahl, E. K.; Hechtl, V. K.; Stömmer, P.; Seebacher, F.; Meregalli, L.; Ketterer, P.; Gerling, T.; Dietz, H. How We Make DNA Origami. *ChemBioChem* 2017.

(27)   Ghavami, A.; Veenhoff, L. M.; van der Giessen, E.; Onck, P. R. Probing the Disordered Domain of the Nuclear Pore Complex through Coarse-Grained Molecular Dynamics Simulations. *Biophys. J.* 2014, *107*, 1393–1402.

(28)   Ghavami, A.; van der Giessen, E.; Onck, P. R. Coarse-Grained Potentials for Local Interactions in Unfolded Proteins. *J. Chem. Theory Comput.* 2013, *9*, 432–440.

(29)   Plesa, C.; Ananth, A. N.; Linko, V.; Gülcher, C.; Katan, A. J.; Dietz, H.; Dekker, C. Ionic Permeability and Mechanical Properties of DNA Origami Nanoplates on Solid-State Nanopores. *ACS Nano* 2014, *8*, 35–43.

(30)   Hernández-Ainsa, S.; Misiunas, K.; Thacker, V. V.; Hemmig, E. A.; Keyser, U. F. Voltage-Dependent Properties of DNA Origami Nanopores. *Nano Lett.* 2014, *14*, 1270–1274.

(31)   Dekker, C. Solid-State Nanopores. *Nat. Nanotechnol.* 2007, *2*, 209–215.

(32)   Eisele, N. B.; Labokha, A. a.; Frey, S.; Görlich, D.; Richter, R. P. Cohesiveness Tunes Assembly and Morphology of FG Nucleoporin Domain Meshworks - Implications for Nuclear Pore Permeability. *Biophys. J.* 2013, *105*, 1860–1870.

(33)   Douglas, S. M.; Marblestone, A. H.; Teerapittayanon, S.; Vazquez, A.; Church, G. M.; Shih, W. M. Rapid Prototyping of 3D DNA-Origami Shapes with caDNAno. *Nucleic Acids Res.* 2009, *37*, 5001–5006.

(34)   Castro, C. E.; Kilchherr, F.; Kim, D.; Shiao, E. L.; Wauer, T.; Wortmann, P.; Bathe, M.; Dietz, H. PERSPECTIVE A Primer to Scaffolded DNA Origami. 2011, *8*, 221–229.

(35)   Kim, D. N.; Kilchherr, F.; Dietz, H.; Bathe, M. Quantitative Prediction of 3D Solution Shape and Flexibility of Nucleic Acid Nanostructures. *Nucleic Acids Res.* 2012, *40*, 2862–2868.

(36)   Ganji, M.; Docter, M.; Le Grice, S. F. J.; Abbondanzieri, E. A. DNA Binding Proteins Explore Multiple Local Configurations during Docking via Rapid Rebinding. *Nucleic Acids Res.* 2016, *44*, 8376–8384.

(37)   Stahl, E.; Martin, T. G.; Praetorius, F.; Dietz, H. Facile and Scalable Preparation of Pure and Dense DNA Origami Solutions. *Angew. Chemie - Int. Ed.* 2014, *53*, 12735–12740.

(38)   Mastronarde, D. N. Dual-Axis Tomography: An Approach with Alignment Methods That Preserve Resolution. *J. Struct. Biol.* 1997, *120*, 343–352.

(39)   Kimanius, D.; Forsberg, B.; Scheres, S.; Lindahl, E. Accelerated Cryo-EM Structure Determination with Parallelisation Using GPUs in RELION-2. *Elife* 2016.

(40)   Rohou, A.; Grigorieff, N. CTFFIND4: Fast and Accurate Defocus Estimation from Electron Micrographs. *J. Struct. Biol.* 2015, *192*, 216–221.

(41)   Plesa, C.; Dekker, C. Data Analysis Methods for Solid-State Nanopores. *Nanotechnology* 2015, *26*, 84003.

(42)   Krzywinski, M.; Altman, N. Points of Significance: Visualizing Samples with Box Plots. *Nat. Methods* 2014, *11*, 119–120.

(43)   Ananth, A. N.; Mishra, A.; Frey, S.; Dwarakasing, A.; Versloot, R.; van der Giessen, E.; Görlich, D.; Onck, P.; Dekker, C. Spatial Structure of Disordered Proteins Dictates Conductance and Selectivity in Nuclear Pore Complex Mimics. *eLIfe,* 2018.

(44)   Kowalczyk, S. W.; Grosberg, A. Y.; Rabin, Y.; Dekker, C. Modeling the Conductance and DNA Blockade of Solid-State Nanopores. *Nanotechnology* 2011, *22*, 315101.

(45)   Hall, J. E. Access Resistance of a Small Circular Pore. *J. Gen. Physiol.* 1975, *66*, 531 LP-532.

(46)   Hyun, C.; Rollings, R.; Li, J. Probing Access Resistance of Solid-State Nanopores with a Scanning Probe Microscope Tip.(Supporting Information). *Small* 2012, *8*, 385–392.

Risk Analysis and Technology Assessment (RATA)

The RATA* part of this thesis contains evaluation of risks associated with the handling of materials used, as well as the implication of future risks (if any) based on current results reported in this thesis. The section also dwells upon the impact of this thesis on the advancement of technology for welfare and benefits to human civilization in both short and long-term.

During the execution of this thesis, all the personnel involved were trained with adequate safety and handling procedures. The purified biological **materials** (DNA and proteins) poses no risks. Nevertheless, the biological materials used in this study were handled as ML-1 waste in accordance with the national biosafety standards. During the experiments, adequate precautions and safety measures were enforced for handling the biomaterials mainly, by using gloves, lab coats, and safety goggles. All the waste generated from the fabrication of solid-state nanopores were treated as per the regulations set up by Kavli Nanolab in accordance with EU and Dutch safety standards. In this study, genetically modified organisms and live animal were not used for any experiments or observation.

The technological output from this thesis will impact the areas of medicine in foreseeable future. To enumerate few examples, the selectivity of nuclear pore complex (NPC) mimic pores can be harnessed to develop selective filters for nuclear proteins. Apart from that, the NPC mimic pores can be utilized for testing the efficacy of targeting gene therapy vectors.

Summary

Nuclear pore complexes acts as a gatekeeper for molecular transport between the nucleus and the cytoplasm in eukaryotic cells. The central NPC channel is filled with intrinsically disordered FG domains (phenylalanine (F), glycine (G)) that are responsible for the fascinating selectivity of NPCs, for which the underlying mechanism is still under considerable debate. In this thesis, a minimalistic mimic of (NPCs) was constructed using solid-state nanopore and DNA origami to study the spatial arrangement and transport process.

In chapter 2, we investigated the transport of ions and transport receptors through biomimetic NPCs consisting of Nsp1 (yeast nucleoporin) domains attached to the inner wall of solid-state nanopores. We studied both wildtype FG domains and Nsp1-S variants whose hydrophobic residues were mutated to the hydrophilic serine. FG nanopores showed a clear selectivity as transport receptors (Kap95) could translocate across the pore whereas other protein (tCherry) could not. However, Nsp1-S mutant pores lacked such selectivity. To understand this behavior the coarse-grained simulations of FG pores exhibit a high-density protein distribution with a noticeable maximum at the pore center, in contrast to the uniform and drastically less-dense protein distribution of the Nsp1-S mutant pore. We conclude that the density distribution of the disordered proteins inside the nuclear pore plays a vital role as it dictates the ion conductivity and selective permeability.

The controlled functionalization of surfaces and nanopore with proteins is crucial for many analytical methods in life science research and biosensor applications. In Chapter 3, we establish a reversible coating protein strategy for silica-based surfaces that enables stable and selective immobilization of proteins. For surface attachment, we exploit polyhistidine (His) tags that are site- specifically introduced into recombinant proteins, and use the Nsp1 and Nsp1-S as model protein. We observe reversible binding of proteins for multiple cycles both on nanopore and planar surface.

DNA origami technique is an versatile tool to place biomolecules with nanometer precision. In chapter 4 of this thesis, we investigate and characterize DNA origami nanoplates using solid-state nanopores to the ionic permeability and mechanical

properties. DNA origami nanoplates of various designs are docked onto solid-state nanopores where we subsequently measure their ionic conductance. The ionic permeability is found to be high for all origami nanoplates. We observe the conductance of docked nanoplates, relative to the bare nanopore conductance, to increase as a function of pore diameter, as well as to increase upon lowering the ionic strength. All nanoplates show non-linear current-voltage dependence with a lower conductance at higher applied voltages, which we attribute to a physical bending of the nanoplates under the applied force. At sufficiently high voltage (force), the nanoplates are strongly deformed and can be pulled through the nanopore. The data shown in Chapter 4 concludes that DNA origami nanoplates are typically very permeable to ions and exhibit a number of unexpected mechanical properties which are interesting in their own right, but also need to be considered in the future design of DNA origami nanostructures. The honeycomb lattice nanoplate is found to have slightly better overall performance over other plate designs.

To build an NPC mimic with controlled density of FG Nups in the nanopore, we exploited the DNA origami platform. In chapter 5, we present a novel approach to realize artificial NPC-mimics that allow full control of the type and copy numbers of FG-Nups: We constructed 34 nm-wide 3D DNA origami rings and attached Nsp1 and NSP1-S, in different copy numbers within the ring. Using nanopores, we show the ionic conductance measured through NPC-mimic origami rings docked onto solid-state nanopores is found to be lower for Nsp1 than for Nsp1-S, and it is reduced for a larger number of FG-Nups in the ring. Electron microscopy (cryo) and MD simulations supports the nanopore experiments; where we find that Nsp1 forms cohesive networks inside the ring with a greater density than the hydrophilic mutant Nsp1-S. Our innovative method opens up an experimental platform for deciphering the collective behavior of FG Nups with full control of their type and position for building higher order mimics.

The methodology and results presented in this thesis demonstrated that minimalistic mimicking of biology enables us to understand processes, which are complicated otherwise. In future, we can expect an increase in combination of DNA origami and FG-nups projects. The impact of these results can be exploited for number of follow-ups work such as to create synthetic nups , building higher-order NPC mimics with DNA-origami scaffold, FG-Nups based selective filters for nuclear proteins, FG-pore platform for testing gene therapy vector transport, and selective channels for artificial/synthetic cell systems.

Samenvatting

Eukaryotische cellen slaan hun genetisch materiaal (het DNA) op in een cellulair compartiment dat de celkern heet. De celkerninhoud is omgeven door een lipide membraan: de nucleaire envelop. Dit membraan reguleert de celkerninhoud zoals de signaaleiwitten voor genexpressie, ionen, energiemoleculen en mRNA transcripten, enz. Een direct gevolg van de compartimentalisatie in cellen is de noodzaak voor een streng gereguleerd, selectief en efficiënt transportsysteem tussen de celkern en het cytoplasma. Het Nucleaire Porie Complex (NPC) functioneert als een poortwachter voor het moleculaire transport tussen de celkern en het cytoplasma. Het centrale kanaal van het NPC is gevuld met intrinsiek wanordelijke eiwitten, de zogenaamde nucleoporinen of FG-Nups, vernoemd naar de aminozuren phenylalanine (F) en glycine (G). Deze **nucleoporinen zijn verantwoordelijk voor de fascinerende selectiviteit van NPC's,** waarvan het mechanisme nog ter discussie staat.

In dit proefschrift is een minimalistische imitatie van het NPC gebouwd met behulp van vaste-stof nanoporiën, gepurificeerde FG-Nups en DNA-origami om de ruimtelijke organisatie en transportprocessen te bestuderen. Het inleidende hoofdstuk 1 **geeft een uitgebreide en gedetailleerde beschrijving van NPC's,** nanoporiën en DNA-origami.

In hoofdstuk 2 hebben we onderzocht hoe ionen en transportreceptoreiwitten worden getransporteerd door een biomimetische NPC, bestaande uit Nsp1 (gist-nucleoporine) die aan de binnenmuur van een vaste-stof nanoporie zijn bevestigd. We hebben zowel de wildtype FG-Nups als SG-varianten getest, waarbij hydrofobe residuen gemuteerd zijn naar het hydrofiele serine. FG-nanoporien lieten een duidelijke selectiviteit zien, blijkende uit de translocatie van het transportreceptoreiwit Kap95 door de nanoporie, terwijl dit bij een ander eiwit (tCherry) niet gebeurde. De nanoporie met de mutant Nsp1-S vertoonde geen selectiviteit. Om deze observatie te begrijpen zijn simulaties van de **biomimetische NPC's uitgevoerd. Deze simulaties demonstreerden dat** nanoporiën bedekt met ongemuteerde FG-Nups een eiwitdichtheidsdistributie hebben met een duidelijk maximum in het midden van de porie. Nanoporiën bedekt met de mutant Nsp1-S, daarentegen, vertonen een meer uniforme eiwitdichtheidsdistributie. Hieruit concluderen we dat de dichtheidsdistributie

van de wanordelijke eiwitten aan de binnenkant van de nanoporie een belangrijke rol speelt bij de ionengeleiding en de selectieve permeabiliteit.

De gecontroleerde functionalisatie van oppervlakken en nanoporiën met eiwitten is cruciaal voor vele analytische methoden in de levenswetenschappen en voor biosensoren. In hoofdstuk 3 introduceren we een reversibele coatingstrategie om eiwitten op silicaoppervlakken selectief en stabiel te immobiliseren. Voor de oppervlaktebevestiging gebruiken we polyhistidine-ankers (His-anker) die we op specifieke plekken inbrengen binnen een recombinant eiwit (Nsp1 en Nsp1-S). We observeren voor meerdere cycli de omkeerbare binding van eiwitten aan zowel een nanoporie als een vlak oppervlak.

DNA-origami structuren zijn veelzijdige substraten waarop biomoleculen met een precisie van enkele nanometers kunnen worden geplaatst. In hoofdstuk 4 bestuderen we DNA-origami nanoplaten met behulp van vaste-stof nanoporiën om de ionenpermeabiliteit en mechanische eigenschappen te achterhalen. Nanoplaten met verschillende ontwerpen worden gekoppeld aan een vaste-stof nanoporie en de ionengeleiding wordt gemeten. Hieruit blijkt dat de ionenpermeabiliteit hoog is voor alle nanoplaatontwerpen. We meten dat de geleiding van gekoppelde nanoplaten, in vergelijking met de kale nanoporiegeleiding, toeneemt zowel evenredig met de poriediameter als na verlaging van de ionenconcentratie. Alle nanoplaten vertonen een niet-lineaire stroom-spanningsafhankelijkheid, waarbij we een lagere geleiding bij hogere spanningen observeren, wat kan worden toegeschreven aan de mechanische deformatie van de nanoplaat door de aangelegde kracht. Bij voldoende hoge spanningen (en daarmee krachten), worden de nanoplaten zo sterk vervormd dat ze door de nanoporie getrokken worden. Uit de resultaten van hoofdstuk 4 concluderen we ten eerste dat DNA-origami nanoplaten zeer permeabel zijn voor ionen en verder dat ze enkele onverwachte mechanische eigenschappen vertonen, die op zichzelf al interessant zijn, maar waarmee in toekomstige origamiontwerpen rekening gehouden moet worden. De nanoplaat met de honingraatstructuur presteert over het algemeen beter dan de andere nanoplaatontwerpen.

Om een NPC-imitatie te construeren met een gecontroleerde FG-Nupsdichtheid in de nanoporie, hebben we een DNA-origami nanoplaat gebruikt. In hoofdstuk 5 tonen we een nieuwe techniek om een NPC-imitatie te maken, waarbij we volledige controle hebben over het type en aantal FG-Nups. Hiervoor hebben we DNA-origamiringen met een doorsnede van 34 nm ontworpen, waaraan we verschillende hoeveelheden Nsp1 en Nsp1-S vastzetten in de binnenkant van de ring. We laten zien dat de ionengeleiding door de origamiringen met FG-Nups,

die in een nanoporie gekoppeld zijn, lager is voor Nsp1 dan voor Nsp1-S. Daarnaast leidt een groter aantal FG-Nups in de origamiring tot een lagere ionengeleiding. Elektronenmicroscopie en MD-simulaties ondersteunen de nanoporie-experimenten: we observeren dat Nsp1 in de origamiring een samenhangend netwerk vormt met een hogere eiwitdichtheid dan de hydrofiele mutant Nsp1-S. Deze innovatieve methode vormt de basis voor een experimenteel platform om het collectieve gedrag van FG-Nups te achterhalen met volledige controle over het eiwittype en positionering. Met deze kennis kunnen steeds complexere NPC-imitaties worden gebouwd.

De methodologie en resultaten in dit proefschrift demonstreren dat de minimalistische imitatie van biologische structuren ons in staat stelt om processen te begrijpen die anders te complex zouden zijn. In de toekomst kunnen we een toename verwachten van het aantal projecten waarbij DNA-origami en FG-Nups worden gecombineerd. Onze resultaten kunnen worden gebruikt als de basis voor verscheidene projecten: NPC-imitaties met synthetische Nups, hogere-orde NPC-imitaties met een DNA-origami als substraat, op FG-Nups gebaseerde selectieve filters voor nucleaire eiwitten, FG-Nups-poriën voor het testen van vectortransport in de context van gentherapie, en ten slotte selectieve kanalen voor kunstmatige celsystemen.

Adithya N. Ananth

Maart 2018

List of publications

1. <u>A.N. Ananth</u>*, M. Genua*, N. Aissaoui*, L. Díaz, N. B. Eisele, S. Frey, C.Dekker, R.P. Richter and D. Görlich. Reversible immobilization of proteins in sensors and solid-state nanopores, Small, 03357 (2018).

2. P. Ketterer*, <u>A.N. Ananth</u>,*, D. Lamen Trip, A. Mishra, E. Bertosin, M. Ganji, J. vd. Torre, Dirk Görlich, P. Onck, H. Dietz and C. Dekker. DNA origami scaffold for studying intrinsically disordered proteins of the nuclear pore complex, Nature Communications, 9, 902 (2018).

3. <u>A.N. Ananth</u>*, A. Mishra*, S. Frey, A. Dwarakasing, R. Versloot, E. vd. Giessen, D. Görlich, P. Onck, C. Dekker. Spatial structure of disordered proteins dictates conductance and selectivity in nuclear pore complex mimics, eLIFE (2018). DOI: <u>10.7554/eLife.31510</u>

4. Y. Kabiri, <u>A.N. Ananth</u>, J. vd. Torre, A. Katan, J. Hong, S. Malladi, J. Kong, H. Zandbergen and C. Dekker. Distortion of DNA origami on graphene imaged with advanced TEM techniques, Small, 31, 1700876 (2017).

5. C. Plesa, <u>A.N. Ananth</u>, V. Linko, C. Gülcher, A. J. Katan, H. Dietz, and C. Dekker. Ionic permeability and mechanical properties of DNA origami nanoplates on solid-state nanopores, ACS Nano, 8 , 35 (2014).

6. W. Xi*, A.A. Solovev*,<u>A.N.Ananth</u>, S. Sanchez, D. Gracias and O. G. Schmidt. Rolled-up magnetic microdrillers: towards remotely controlled minimally invasive surgery, Nanoscale, 5, 1294 (2013).

7. S. Sanchez, <u>A. N. Ananth</u>, V. M. Fomin, M. Viehrig and O. G. Schmidt. Superfast motion of catalytic microjet engines at physiological temperature, Journal of the American Chemical Society, 133,14860 (2011).

*Equal contribution

Curriculum Vitae

Adithya. N. Ananth

10-10-1985	Born in Hosanagar, India
2001	Indian Certificate of Secondary Education (ICSE)
	SSRS, Hattiangady, India
2001-2003	Pre-university college
	S.B.P.U college, Karkala, India
2003-2007	Bachelor of Engineering, *with Distinction*
	Visvesvaraya Technological University,
	Belagavi, India
2009-2011	Master of Science, Nanobiophysics
	Technische Universität Dresden, Germany
2012-2018	Doctor of Philosophy,
	Technische Universiteit Delft, The Netherlands
	Title: "Mimicking the nuclear pore complex using nanopores"
	Promoter: Prof. dr. C. Dekker